frontiers | Research Topics

Novel translational advances in hemodynamics for the diagnosis and treatment of cardiovascular diseases

Edited by
Gaoyang Li, Aike Qiao, Hitomi Anzai and Xuelan Zhang

Published in
Frontiers in Cardiovascular Medicine

FRONTIERS EBOOK COPYRIGHT STATEMENT

The copyright in the text of individual articles in this ebook is the property of their respective authors or their respective institutions or funders. The copyright in graphics and images within each article may be subject to copyright of other parties. In both cases this is subject to a license granted to Frontiers.

The compilation of articles constituting this ebook is the property of Frontiers.

Each article within this ebook, and the ebook itself, are published under the most recent version of the Creative Commons CC-BY licence. The version current at the date of publication of this ebook is CC-BY 4.0. If the CC-BY licence is updated, the licence granted by Frontiers is automatically updated to the new version.

When exercising any right under the CC-BY licence, Frontiers must be attributed as the original publisher of the article or ebook, as applicable.

Authors have the responsibility of ensuring that any graphics or other materials which are the property of others may be included in the CC-BY licence, but this should be checked before relying on the CC-BY licence to reproduce those materials. Any copyright notices relating to those materials must be complied with.

Copyright and source acknowledgement notices may not be removed and must be displayed in any copy, derivative work or partial copy which includes the elements in question.

All copyright, and all rights therein, are protected by national and international copyright laws. The above represents a summary only. For further information please read Frontiers' Conditions for Website Use and Copyright Statement, and the applicable CC-BY licence.

ISSN 1664-8714
ISBN 978-2-8325-5667-2
DOI 10.3389/978-2-8325-5667-2

About Frontiers

Frontiers is more than just an open access publisher of scholarly articles: it is a pioneering approach to the world of academia, radically improving the way scholarly research is managed. The grand vision of Frontiers is a world where all people have an equal opportunity to seek, share and generate knowledge. Frontiers provides immediate and permanent online open access to all its publications, but this alone is not enough to realize our grand goals.

Frontiers journal series

The Frontiers journal series is a multi-tier and interdisciplinary set of open-access, online journals, promising a paradigm shift from the current review, selection and dissemination processes in academic publishing. All Frontiers journals are driven by researchers for researchers; therefore, they constitute a service to the scholarly community. At the same time, the *Frontiers journal series* operates on a revolutionary invention, the tiered publishing system, initially addressing specific communities of scholars, and gradually climbing up to broader public understanding, thus serving the interests of the lay society, too.

Dedication to quality

Each Frontiers article is a landmark of the highest quality, thanks to genuinely collaborative interactions between authors and review editors, who include some of the world's best academicians. Research must be certified by peers before entering a stream of knowledge that may eventually reach the public - and shape society; therefore, Frontiers only applies the most rigorous and unbiased reviews. Frontiers revolutionizes research publishing by freely delivering the most outstanding research, evaluated with no bias from both the academic and social point of view. By applying the most advanced information technologies, Frontiers is catapulting scholarly publishing into a new generation.

What are Frontiers Research Topics?

Frontiers Research Topics are very popular trademarks of the *Frontiers journals series*: they are collections of at least ten articles, all centered on a particular subject. With their unique mix of varied contributions from Original Research to Review Articles, Frontiers Research Topics unify the most influential researchers, the latest key findings and historical advances in a hot research area.

Find out more on how to host your own Frontiers Research Topic or contribute to one as an author by contacting the Frontiers editorial office: frontiersin.org/about/contact

Novel translational advances in hemodynamics for the diagnosis and treatment of cardiovascular diseases

Topic editors

Gaoyang Li — Tohoku University, Japan

Aike Qiao — Beijing University of Technology, China

Hitomi Anzai — Tohoku University, Japan

Xuelan Zhang — University of Science and Technology Beijing, China

Citation

Li, G., Qiao, A., Anzai, H., Zhang, X., eds. (2024). *Novel translational advances in hemodynamics for the diagnosis and treatment of cardiovascular diseases*. Lausanne: Frontiers Media SA. doi: 10.3389/978-2-8325-5667-2

Table of contents

frontiers | Frontiers in Cardiovascular Medicine

TYPE Original Research
PUBLISHED 15 December 2023
DOI 10.3389/fcvm.2023.1292647

Check for updates

OPEN ACCESS

EDITED BY
Xuelan Zhang,
University of Science and Technology Beijing, China

REVIEWED BY
Zhehao Dai,
The University of Tokyo, Japan
Erberto Carluccio,
Heart Failure Unit, Italy

*CORRESPONDENCE
Xumin Hou
hxmchest@163.com
Xin Pan
panxin805@126.com
Ruogu Li
13564565961@163.com

RECEIVED 11 September 2023
ACCEPTED 04 December 2023
PUBLISHED 15 December 2023

CITATION
Huang J, Zhang W, Fu W, Le J, Qi Y, Hou X, Pan X, Li R and He B (2023) Noninvasive evaluation of pulmonary hypertension using the second heart sound parameters collected by a mobile cardiac acoustic monitoring system.
Front. Cardiovasc. Med. 10:1292647.
doi: 10.3389/fcvm.2023.1292647

COPYRIGHT
© 2023 Huang, Zhang, Fu, Le, Qi, Hou, Pan, Li and He. This is an open-access article distributed under the terms of the Creative Commons Attribution License (CC BY). The use, distribution or reproduction in other forums is permitted, provided the original author(s) and the copyright owner(s) are credited and that the original publication in this journal is cited, in accordance with accepted academic practice. No use, distribution or reproduction is permitted which does not comply with these terms.

Noninvasive evaluation of pulmonary hypertension using the second heart sound parameters collected by a mobile cardiac acoustic monitoring system

Jingjuan Huang[1], Weiwei Zhang[1], Wenxia Fu[2], Jiawei Le[2], Yiding Qi[1], Xumin Hou[1]*, Xin Pan[1]*, Ruogu Li[1]* and Ben He[1]

[1]Department of Cardiology, Shanghai Chest Hospital, Shanghai Jiao Tong University School of Medicine, Shanghai, China, [2]Department of Cardiac Function, Shanghai Chest Hospital, Shanghai Jiao Tong University School of Medicine, Shanghai, China

Background: Pulmonary hypertension (PH) is linked to higher rates of morbidity and mortality worldwide. Early diagnosis of PH is important for clinical treatment. The estimated pulmonary artery systolic pressure (ePASP ≥ 35 mmHg) measured by echocardiography helps screen PH patients. In this paper, we report a novel PH screening method through a mobile cardiac acoustic monitoring system.
Methods: In the retrospective study, patients admitted to our hospital between January 2022 and April 2023 were classified into PH and control groups using ePASP and compared with acoustic cardiographic parameters. According to ePASP, PH severity was classified as mild, moderate, and severe. We analyzed the first and second heart sound (S1, S2) characteristics, including amplitude (S1A, S2A), energy (S1E, S2E), and frequency (S1F, S2F).
Results: The study included 209 subjects, divided into PH (n = 121) and control (n = 88) groups. Pearson correlation analysis confirmed the positive correlation between S2F and ePASP. The diagnostic performance of S2F as assessed by the area under the ROC curve was 0.775 for PH. The sensitivity and specificity of diagnosing ePASP ≥ 35 mmHg when S2F ≥ 36 Hz were found to be 79.34% and 67.05%, respectively, according to ROC analysis. Severity classification was performed using S2F, the area under the ROC curve was 0.712–0.838 for mild PH, 0.774–0.888 for moderate PH, and 0.826–0.940 for severe PH.
Conclusions: S2F collected by the mobile cardiac acoustic monitoring system offers a convenient method for remote PH screening, potentially improving PH management and outcomes.

KEYWORDS

acoustic cardiography, the second heart sound frequency, a mobile cardiac acoustic monitoring system, pulmonary hypertension (PH), estimated pulmonary artery systolic pressure (ePASP)

1. Introduction

Pulmonary hypertension (PH) is a devastating progressive disease characterized by elevated pulmonary artery pressure along with pulmonary vascular resistance that ultimately leads to right heart failure and premature death (1). With the expansion of PH treatment options, the requirement for precise and non-invasive techniques to allow regular and safe estimation of

pulmonary arterial pressure (PAP) has increased. PH is defined as an increase in mean pulmonary arterial pressure (mPAP) beyond the threshold of 20 mmHg during a resting state, evaluated using right heart catheterization (RHC) (2). RHC is recognized as the gold standard for the diagnosis of PH; nonetheless, the procedure is complex, invasive, and carries inherent risks, making it unsuitable for early diagnosis, routine screening, and sustained, longitudinal monitoring (3). Transthoracic echocardiography (TTE) is advocated as a non-invasive substitute for the screening of PH. The assessment of estimated pulmonary artery systolic pressure (ePASP) via TTE has demonstrated a robust association with measurements obtained through RHC (4, 5). Resting-state ePASP values of ≥35 mmHg measured by echocardiography indicate PH, with severity ranging from mild (35–45 mmHg) to moderate (45–60 mmHg) to severe (>60 mmHg) (6). Nonetheless, accurate TTE results require experienced and skilled staff. Consequently, it is necessary to develop new non-invasive methods to frequently and accurately assess ePASP and screen potential PH patients.

Acoustic cardiography is a noninvasive, safe, inexpensive, continuous monitoring method that quantifies the state of the heart and lung by synchronously analyzing phonocardiogram (PCG) and electrocardiogram (ECG) (7). In recent years, studies on acoustic cardiography have suggested that the characterization of the second heart sound (S2) can be used to estimate PAP (8, 9). The S2 consists of two audible components, the pulmonic closure sound (P2) and the aortic closure sound (A2). Thus, the S2 component is generated by hemodynamic events that occur immediately following the closure of the aortic and pulmonary valves. The vibrations of S2 occur at the end of ventricular contraction, identifying the beginning of ventricular relaxation and the end of mechanical contraction (10). As PAP increases, a notable elevation emerges in the pulmonary component of S2, establishing an interdependent relationship between PAP and the acoustic characteristics of heart sounds (8). However, the relationship between ePASP and S2 is not yet fully clarified, and whether the cut-off value of S2 can be applied to screen patients with PH remains to be investigated.

The objective of this study is to evaluate the correlations between ePASP and S2 using a mobile cardiac acoustic monitoring system, and to determine the value of S2 features in PH screening.

2. Methods

2.1. Study participants and design

This was a retrospective observational cohort study. Based on TTE findings, patients admitted to our ward were consecutively selected from January 2022 to April 2023 and divided into two groups as per the ePASP: PH group (ePASP ≥35 mmHg) and control group (ePASP <35 mmHg). This cut-off value was based upon the values suggested by the American Academy of Family Physicians (AAFP), which proposes that an ePASP of 35–40 mmHg or greater on echocardiography is suggestive of PH (6). The demographic and clinical baseline data were recorded for all subjects, including age, gender, medical history, the types of PH, and the severity of PH. Prior to enrollment, all participants voluntarily signed written informed consent. The study protocol was reviewed and approved by the Ethics Committee of the Shanghai Chest Hospital of Shanghai Jiao Tong University and conducted in accordance with the Declaration of Helsinki.

2.2. Inclusion and exclusion criteria

Inclusion criteria were patients aged ≥ 18 years hospitalized due to cardiovascular diseases. All subjects underwent echocardiography and acoustic cardiography on the same day. Participants were excluded from this study if they met any of the following criteria: severe valvular heart disease, severe ventricular arrhythmia, acute coronary syndrome, severe liver dysfunction, severe chronic obstructive pulmonary disease, constrictive pericarditis, end-stage renal failure, and psychological issues limiting adherence.

2.3. Acoustic cardiography

Acoustic cardiography was performed using the WENXIN® device (Wenxin Tech. and Bayland Scientific, Beijing, China and California, USA), and the details have been described previously (11). The device can simultaneously record PCG, ECG and frequency from the precordial V4 locations after patients have rested in a supine position for 5–10 min. The parameters of the first and second heart sounds (S1and S2) were analyzed, including amplitude (S1A, S2A), energy (S1E, S2E), frequency (S1F, S2F), S2/S1 amplitude ratio (S2/S1A), S2/S1 energy ratio (S2/S1E), and S2/S1 frequency ratio (S2/S1F) were measured by an automatic analysis software. The heart sound frequency is the frequency of maximal amplitude, which is obtained by the wavelet transform of the PCG signal (11). The sound spectrogram is a visual representation of an acoustic signal, with varying amplitude over time at different frequencies (10). **Figures 1A,B** shows the typical acoustic signals and spectral displays from a control and a PH patient. The heart sound audio of two patients is stored in **Supplementary Videos S1, S2**.

2.4. Estimated pulmonary arterial systolic pressure (ePASP)

TTE was used to detect ePASP by measuring the tricuspid regurgitation velocity (TRV) doppler signal (Vivid E95 or Vivid E9, GE Medical Systems, Horten, Norway). Briefly, ePASP was determined by calculating the estimated trans-tricuspid regurgitation gradient (equivalent to $4 \times TRV^2$) and adding the estimated right atrial pressure (12). TTEs were reviewed by an experienced echocardiographer blinded to all clinical data and acoustic cardiography findings.

2.5. Statistical analysis

The SPSS software package (Version 22.0, SPSS, Chicago, IL, USA) was used to perform statistical analysis. Descriptive

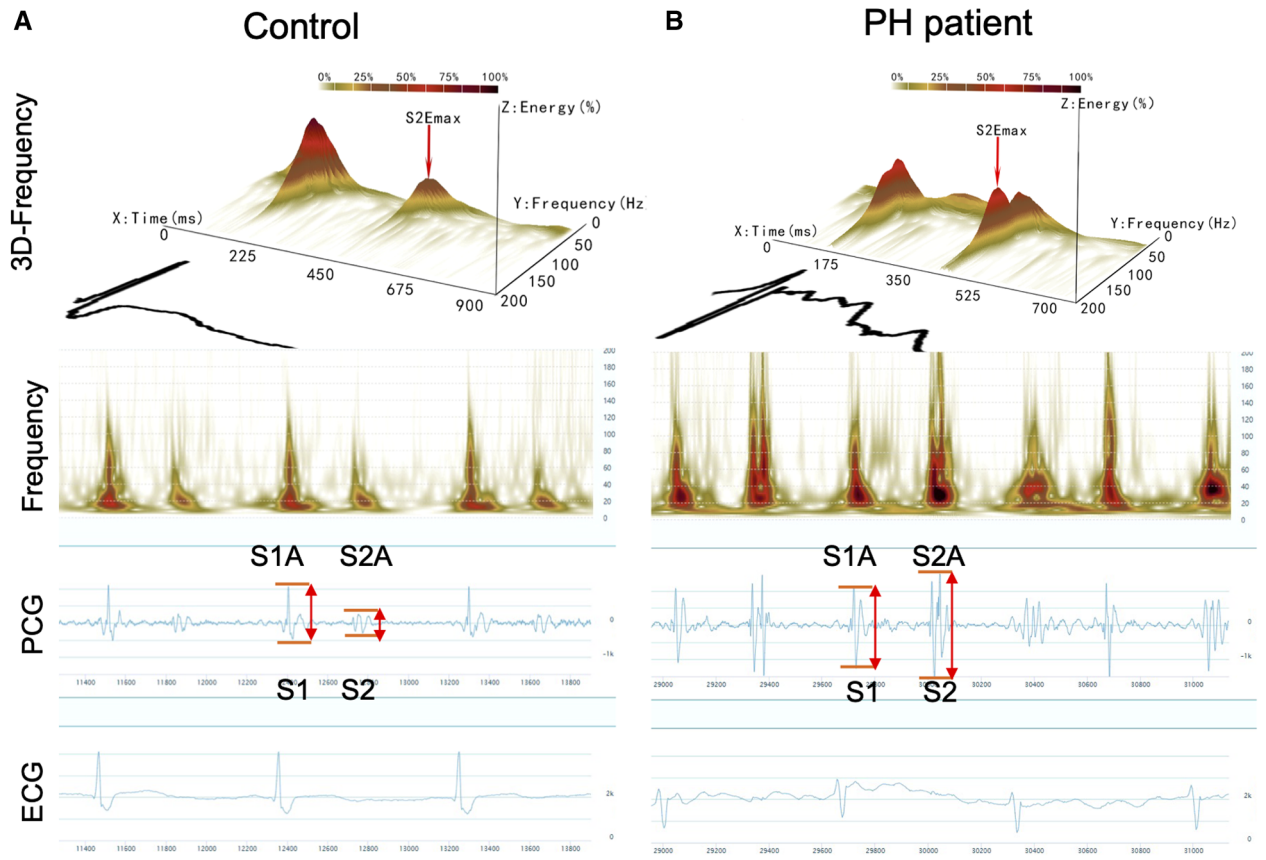

FIGURE 1
Acoustic cardiographic output for a control patient (A) and a patient with PH (B) showing frequency, PCG, and ECG. The scalogram time-frequency representation shows frequency on the vertical axis on a logarithmic scale from 0 to 200 Hz and time on the horizontal axis. The squared magnitude of the wavelet transform energy at each frequency is represented by colors ranging from light yellow to deep red. S1, the first heart sound; S2, the second heart sound; S1A, the first sound amplitude; S1E, the first sound energy; S1F, the first sound frequency; S2A, the second sound amplitude; S2E, the second sound energy; S2F, the second sound frequency.

statistics include the numbers and percentages for categorical data, and continuous data was represented by the mean ± standard error (SE). We tested the null hypothesis for any difference between groups using the one-way ANOVA or unpaired *t*-test for continuous data and chi-square analysis for dichotomous data. Univariate and multivariate logistic analyses were used to determine the predictive factors of heart sound parameters related to elevated ePASP. Linear logistic regression was performed to test the relationship between ePASP and the heart sounds parameters. Receiver operating characteristic (ROC) curve analysis was performed to explore the predictive value of heart sound parameters in detecting different degrees of ePASP elevation. The areas under the curve (AUC) and the optimal cut-off value of each parameter with the highest sensitivity and specificity were obtained from ROC analysis. Intraclass correlation coefficient (ICC) was calculated between ePASP measured by echocardiography and acoustic sound characteristics. All results were considered statistically significantly different at P-value < 0.05.

3. Results

3.1. Comparison of baseline clinical characteristics, ePASP in PH patients and controls

A total of 209 adult patients were included in this retrospective study between January 2022 and April 2023. Participants were divided into the PH group ($n = 121$) and control group ($n = 88$), according to whether the ePASP ≥ 35 mmHg by transthoracic echocardiography or not. Patients' baseline demographic characteristics and ePASP were presented in Tables 1, 2.

3.2. Acoustic cardiography measurements

The acoustic characteristics of S1 and S2 in the PH and control groups were shown in Figure 1 and Table 3. Heart rate and PR intervals were similar between the two groups. Patients with PH

TABLE 1 Baseline clinical characteristics and ePASP of PH patients and controls.

Baseline clinical characteristics	PH ($n = 121$)	Controls ($n = 88$)	*P*-value
Male [*n* (%)]	45 (37.19%)	49 (55.68%)	0.008
Age (years)	67.55 ± 1.39	66.10 ± 1.40	0.474
BMI (kg/m^2)	21.75 ± 0.25	22.24 ± 0.25	0.188
Hypertension [*n* (%)]	54 (44.6%)	40 (45.5%)	0.906
Diabetes [n (%)]	19 (15.7%)	13 (14.8%)	0.854
Coronary artery disease [*n* (%)]	27 (22.3%)	15 (17.00%)	0.348
Atrial fibrillation	46 (38.0%)	23 (26.10%)	0.071
NYHA class	2.45 ± .056	1.97 ± .069	<0.001
BNP (pmol/L)	417.77 ± 27.17	226.70 ± 19.64	<0.001
ePASP (mmHg)	50.26 ± 1.51	30.02 ± 0.32	<0.001

Values are given as mean ± SE unless otherwise indicated.
PH, pulmonary hypertension; LVEF, left ventricular ejection fraction; ePASP, estimate pulmonary artery systolic pressure; BMI, body mass index; BNP, B-type natriuretic peptide.

TABLE 2 Baseline clinical characteristics of PH patients.

Baseline clinical characteristics	PH ($n = 121$)
Clinical classification of PH	
Group 1	17
Group 2	96
Group 3	1
Group 4	4
Group 5	3
Severity of PH	
Mild (35-45 mm Hg)	63
Moderate (45–60 mm Hg)	34
Severe (>60 mm Hg)	24
Medications	
Endothelin receptor antagonists	16
Calcium channel antagonists	11
Phosphodiesterase 5 inhibitors	4
Prostacyclin analogues	5
Prostacyclin receptor agonist	2
Soluble guanylate cyclase stimulator	1

NYHA, New York Heart Association; PH, pulmonary hypertension; Group 1, pulmonary arterial hypertension (PAH); Group 2, PH due to left-sided heart disease; Group 3, PH due to chronic lung disease; Group 4, chronic thromboembolic PH (CTEPH); Group 5, PH with an unclear and/or multifactorial mechanisms.

exhibited a slightly greater QRS duration. Among the PH patients, both the amplitude and frequency of S2 were increased compared with the controls. Hence, the S2/S1 amplitude and frequency ratios were significantly different between the two groups. Although there was no significant difference in S2 energy between the two groups, the S2/S1 energy ratio risen markedly in the PH patients compared with the controls.

3.3. Relationship between acoustic cardiographic parameters and ePASP

As the acoustic cardiographic parameters of S2A, S2F, S2/S1A, S2/S1E, and S2/S1F were remarkably increased in the PH group, we investigated the relationship between ePASP and acoustic

TABLE 3 Acoustic cardiographic parameters of PH patients and controls.

Parameters	PH ($n = 121$)	Controls ($n = 88$)	*P*-value
Heart rate (bpm)	70.84 ± 1.16	72.82 ± 1.11	0.234
PR interval (ms)	151.84 ± 2.04	146.38 ± 1.96	0.063
QRS duration (ms)	118.53 ± 1.17	110.74 ± 1.16	<0.001
S1A (mv)	1,222.93 ± 94.59	1,094.78 ± 78.74	0.324
S1E	1,557.22 ± 116.78	1,579.13 ± 131.01	0.901
S1F (Hz)	29.67 ± 1.12	27.45 ± 1.23	0.188
S2A (mv)	979.78 ± 78.12	767.17 ± 69.93	0.044
S2E	1,061.31 ± 80.51	953.18 ± 94.80	0.385
S2F (Hz)	51.42 ± 2.09	32.57 ± 1.27	<0.001
S2/S1A	0.95 ± 0.06	0.78 ± 0.05	0.043
S2/S1E	0.81 ± 0.05	0.65 ± 0.04	0.012
S2/S1F	1.93 ± 0.11	1.34 ± 0.07	<0.001

Values are given as mean ± SE unless otherwise indicated.
PH, pulmonary hypertension; LVEF, left ventricular ejection fraction; ePASP, estimate pulmonary artery systolic pressure; S1A, the first sound amplitude; S1E, the first sound energy; S1F, the first sound frequency; S2A, the second sound amplitude; S2E, the second sound energy; S2F, the second sound frequency; S2/S1A, S2/S1 amplitude ratio; S2/S1E, S2/S1 energy ratio; S2/S1F, S2/S1 frequency ratio.

TABLE 4 Multiple logistic regression analysis for elevated ePASP predictors of acoustic cardiographic parameters.

Parameters	Odds ratio	95% confidence limits	*P*-value
S2A, every 1mv increase	1.000	1.000–1.001	0.466
S2F, every 1 Hz increase	1.076	1.043–1.111	<0.001
S2/S1A, every 1unit increase	0.320	0.790–1.298	0.111
S2/S1E, every 1unit increase	5.780	1.092–30.593	0.039
S2/S1F, every 1unit increase	1.068	0.583–1.956	0.832

PH, pulmonary hypertension; ePASP,estimate pulmonary artery systolic pressure; S2A, the second sound amplitude; S2F, the second sound frequency; S2/S1A, S2/S1 amplitude ratio; S2/S1E, S2/S1 energy ratio; S2/S1F, S2/S1 frequency ratio.

cardiographic variables including S2A, S2F, S2/S1A, S2/S1E, and S2/S1F across the cohort (Table 4). S2F and S2/S1E were independent multivariate predictor for ePASP, and S2F performed better than S2/S1E. As shown in Figure 2A, S2F was significantly correlated with increasing the severity of ePASP ($R = 0.645$, $P < 0.001$). In contrast to S2F, we observed that the correlation between S2/S1E and ePASP was only 0.201, $P = 0.004$ (Figure 2B).

3.4. S2 frequency has strong diagnostic accuracy in identifying different degrees of PH

We assessed the predictive performance of S2 frequency as a cut-off value to detect PH (ePASP ≥ 35 mmHg) by constructing ROC curves using echocardiographic data from 121 PH cases and 88 controls. Figure 3 showed that the AUC ROC curve for S2F was 0.775 ($P < 0.001$), indicating the ability of S2F to identify PH (ePASP ≥ 35 mmHg). The optimum cut-off S2F for distinguishing PH was 36 Hz (sensitivity 79.34%, specificity 67.05%, likelihood ratio 2.408) according to Table 5. The ICC was 0.62 (95% confidence interval, 0.53–0.70) between echocardiography estimated ePASP and acoustic cardiography measured S2F.

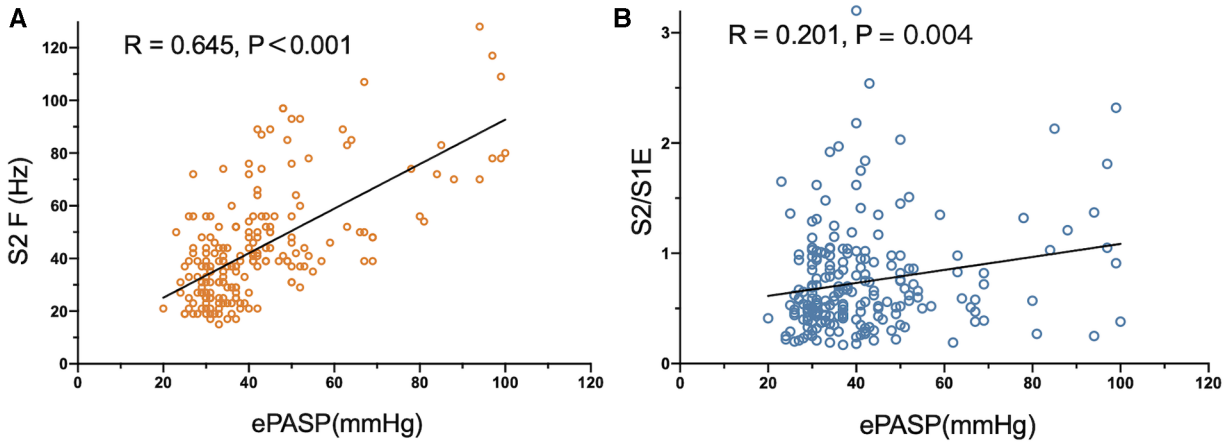

FIGURE 2
Correlation between S2 frequency, S2/S1 energy ratio and ePASP. ePASP, estimate pulmonary artery systolic pressure; S2F, the second sound frequency; S2/S1E, S2/S1 energy ratio.

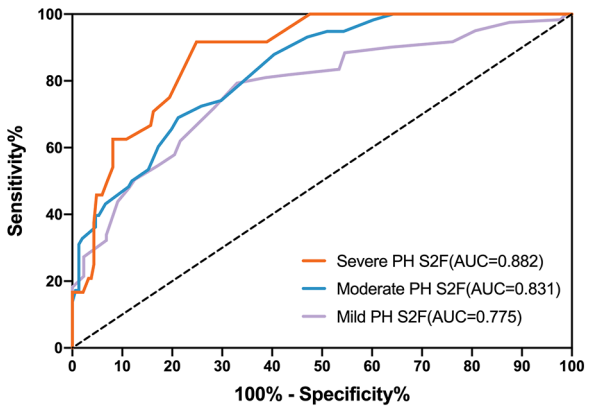

FIGURE 3
Receiver operator characteristic curves (ROC) for S2F as predictors of different severity of PH. PH, pulmonary hypertension; ePASP, estimate pulmonary artery systolic pressure; S2F, the second sound frequency.

Diagnostic accuracy using S2F for the three degrees of PH through ROC analysis was presented in **Table 5**. S2F correctly identified mild PH from the other levels with the AUC range from 0.712 to 0.838, and sensitivity and specificity ranges from 0.713 to 0.856 and from 0.567 to 0.760, respectively. For moderate PH identification by S2F, the AUC range was from 0.774 to 0.888, with sensitivity and specificity varying from 0.562 to 0.794 and from 0.716 to 0.846, respectively. The AUC range for identifying severe PH through S2F was 0.826–0.940, with sensitivity ranging from 0.742 to 0.985 and specificity ranging from 0.684 to 0.881.

4. Discussion

As far as we know, this study first presents the evidence that analyzing S2 frequency collected by the mobile cardiac acoustic monitoring system is a reliable and speedy diagnostic tool for screening PH. Our retrospective cohort study explored the quantitative correlation between S2 acoustic features and PH severity. The frequency of S2 was observed to rise in the PH group, concomitant with increased ePASP levels. Moreover, the diagnostic cut-off value for S2 frequency increases with degree of ePASP elevation among the PH patients.

4.1. Increased loudness of S2 is a typical feature of heart sounds in patients with PH

The prevailing and widely accepted theory regarding the origin of heart sounds is the "cardiohemic model". According to this paradigm, the sounds are produced by the vibration of the entire structure and internal components of the heart (13). This vibration is stimulated by specific cardiac valve closure, with the mitral valve governing the genesis of S1 and the combined interaction of the aortic and pulmonic valves dictating the origin of S2. S2 arises from a complex interplay involving the dynamic processes accompanying the relaxation of the left and right ventricles, the closure of the aortic and pulmonary valves, and the compliance of the aorta and main pulmonary artery (14, 15). The onset of S2 implies the end of mechanical ventricular systole as well as the beginning of ventricular diastole. The aggravation of the pulmonic component of S2 reflects strong closure of the pulmonary valve, suggesting RV pressure overload. Considering A2 and P2 of S2 are usually very close in the time axis, clinical indicators of PH can be concluded as the increased loudness of P2 of S2 and increased transmission of P2 to the cardiac apex. However, it should be noted that a small percentage of cases where only increased A2 loudness causes false positives (i.e., LV systolic dysfunction or left-to-right shunting). The presence of abnormal auscultatory observations manifested as notable frequency was documented in the Primary Pulmonary Hypertension Registry supported by the National Institutes of Health. Specifically, a discernible augmentation in the second

TABLE 5 Diagnostic accuracy of S2F by the severity of PH.

Severity of PH	ePASP (mmHg)	AUC	95% Confidence interval	Cut-off value	Sensitivity	Specificity	PPV	NPV
Mild	39.30 ± 0.35	0.775	0.712–0.838	36	0.793	0.671	0.768	0.702
Moderate	50.12 ± 0.59	0.831	0.774–0.888	45	0.690	0.788	0.556	0.869
Severe	79.25 ± 2.83	0.883	0.826–0.940	47	0.917	0.751	0.324	0.986

Values are given as mean ± SE unless otherwise indicated. PH, pulmonary hypertension; ePASP, estimate pulmonary artery systolic pressure; AUC, area under the curve S2F, the second sound frequency; PPV, positive predictive value, NPV, negative predictive value.

component (P2) of S2 was documented in a substantial majority, accounting for 93%, among a cohort of 187 individuals diagnosed with PH (16). However, conventional cardiac auscultation is a challenging process and can be impacted by various factors, such as patient characteristics and the clinical experience of the physicians, leading to inconsistent results obtained by different observers (17, 18). In this research, the wavelet-based signal processing analysis was utilized for handling continuous digital acoustic data, which yielded the measurements of amplitude, energy, and frequency, thereby resulting in more objectively and realistically reflecting characteristics of the heart sounds.

4.2. S2 frequency, as an inherent characteristic of sound waves, can better reflect the changes in PH

Using acoustic cardiography, the auscultatory heart sounds were collected, quantified, and recorded as sound waveforms. The waveform characteristics of increased loudness of S2 were then reflected as amplitude, frequency, and energy (10, 19). The sounds' amplitude depends on the force generated by valve closure, which in turn relies on the pressure gradient across the valve during the closing. The volume and contents of the heart are also important, in determining the resonance of the cardiohemic system (20). As previously demonstrated, the frequencies of heart sounds can be determined by the volume of the vibrating mass and the tension produced in the walls of the heart and great vessels (21). As the pressure rises, the resonant frequency also increases. The energy value calculated based on the heart sound waveform is coupled with the influence of both amplitude and frequency factors. The greater the amplitude, the higher the energy value; and the greater the frequency, the higher the energy level (22). The amplitude varies with the body weight, acquisition position, and posture. However, as an inherent feature of sound waves, the frequency does not change with the influence of the acquisition conditions or the environment, thus can better reflect the changes in heart sounds.

The subjects were classified into the PH and control groups, depending on whether ePASP was greater than 35 mmHg, which was consistent with the current definition and diagnostic recommendations for PH (4). There was a significant statistical difference in the echocardiography-measured ePASP between the two groups (50.26 ± 1.51 vs. 30.02 ± 0.32 mm Hg; $P < 0.001$) in **Table 1**. In the current study, we analysed the acoustic characteristics of S1 and S2 in both groups, and the results indicated that S1A, S1E, S1F, and S2E were similar between the PH and control groups (see **Table 3**).

The high-frequency components of S2 may be caused by increased wall tension in the right heart and pulmonary artery. In **Table 3**, we found a significant increase in the frequency of S2 in patients with PH (51.42 ± 2.09 vs. 32.57 ± 1.27 Hz, $P < 0.001$), which aligned with the previous observation of S2 frequently being perceived as abnormal in this condition (23). It is encouraging to distinguish subjects with PH from patients with normal ePASP by extracting the constituent features of S2 in the frequency domain.

It has been shown that the amplitude of heart sounds is directly related to myocardial contractility in adult patients undergoing stress testing (24). In our study, the S2 amplitude increased in PH patients (979.78 ± 78.12 vs. 767.17 ± 69.93mv; $P = 0.044$). There was a gradual increase in the size of the amplitude waveforms associated with PH as shown in **Figure 1B**. This phenomenon can be effortlessly clarified by the established impact of elevated ePASP on myocardial contractility. The increased rate of PAP during right ventricle during systole may lead to an increased force of tricuspid valve closure, thus resulting in a higher amplitude of S2.

The control group had a relatively small sample size, and there was an absence of age or sex matching with the PH group. Nevertheless, we adjusted for possible intersubject anthropomorphic differences by calculating the S2/S1 amplitude, frequency, and energy ratios. The results of this study demonstrated that the S2/S1A, S2/S1F, and S2/S1E in the PH group were markedly higher than that in controls, and all the differences were statistically significant (**Table 3**).

4.3. S2 frequency is reliable and effective in assisting PH screening

We examined the correlation between ePASP and digitally recorded precordial acoustic characteristics in PH and control groups. In this study, we found S2A, S2/S1A, and S2/S1F were not strong indicators of PH. As shown in **Table 4**, only S2F and S2/S1E were considered significant independent predictors of PH based on the multivariate analysis. Furthermore, the Pearson correlation analysis indicated that ePASP correlated more strongly with S2F than with S2/S1E in **Figure 2**. S2F and ePASP had a significantly positive correlation ($R = 0.645$, $P < 0.001$). This can be explained based on the differences in mechanism. The amplitude is mainly determined by the closing force of the heart valves, while the frequency can be affected by the closing force, cardiac volume, and the resonance frequencies of the heart and the great vessels. Therefore, differences in pressure and intravascular volume could lead to more variation of frequency than amplitude and

energy in PH patients, thus resulting in a more significant statistical correlation between S2F and ePASP. Other scholars have discussed the use of frequency components as measures of intravascular pressure and wall tension (25, 26). However, to our knowledge, there have been no reports that frequency can characterize the PAP state of the heart. In addition, we found a reciprocal link between S2 and S1 that may relate to ventricular interaction in PH patients. We observed that S2/S1E was an independent multivariate predictor of ePASP, which was in line with other researches examining S2 acoustic properties and pulmonary artery pressure determined from TTE or RHC (27, 28). The QRS duration was shorter in subjects with PH (118.53 ± 1.17 vs. 110.74 ± 1.16 ms; $P < 0.001$). A widened QRS duration or delayed right heart conduction time might influence the splitting interval between A2 and P2 but not the frequency of S2. Age, BMI, and concurrent disorders were not statistically significantly different between the two groups, indicating that these factors were not the cause of the disparities in S2 frequency.

These findings support the established conception that elevated PAP leads to forceful closure of the pulmonic valve and indicate the reliability and validity of S2F in assisting PH screening.

4.4. Different cut-off values of S2 frequency in patients with different severity of PH

We found significant variations in S2F regardless of the severity of PH. According to **Figure 3** and **Table 5**, the accuracy for S2F's PH severity varied from 0.712 to 0.838 for mild PH, 0.774–0.888 for moderate PH, and 0.826–0.940 for severe PH. These findings were comparable to those obtained using echocardiographic monitoring, where it was noted that the diagnosis accuracy for PH type ranged from 0.689 to 0.8 (29–31).

Due to the relatively high NPV values found in severe PH (NPV = 0.9858), S2F may also have the potential to identify individuals with less severe PH (ePASP<60 mmHg). There are various situations when S2F can be employed in clinical settings. For instance, an individual who has S2F greater than or equal to 47 Hz is suspected to have severe PH. S2F greater than or equal to 37 Hz, and smaller than 45 Hz indicates possible mild PH (**Table 5**).Outpatient use of S2F as a screening tool can selectively separate patients for further examinations like echocardiographic measurement or RHC.

4.5. The superiority of acoustic cardiography in evaluating PH

The advantages of applying acoustic cardiography in screening for PH patients include relatively low cost, non-invasiveness, ease of use, and early identification of elevated ePASP.

Since acoustic cardiographic parameters can be easily obtained through non-invasive devices equipped with ECG and PCG sensors (32), they can serve as useful indicators for screening PH. Patients can conveniently record their daily acoustic cardiography on their own terms due to the portability and usability features of these devices. The long-term trend of these data provides valuable insight to detect PH deterioration prior to adverse events, allowing physicians to consider preventative interventions proactively. However, further evaluation of this technology is required to assess its actual efficacy in remote monitoring of diverse patient ranges.

4.6. Limitations of the study

There are still some limitations to acoustic cardiography. First, the quality of data may be compromised by both endogenous and exogenous noises, such as respiratory and background noise. During the heart sound recording process, keeping quiet and breathing calmly as much as possible helps to ensure high-quality data collection. Second, we only studied the association of ePASP estimated by echocardiography and acoustic variables and did not further investigate the relationship between RHC parameters and heart sound parameters. Finally, the 2022 ESC/ERS Guidelines for the diagnosis and treatment of PH suggested using the peak tricuspid regurgitation velocity (TRV) as a crucial factor to determine the echocardiographic likelihood of PH. A peak TRV above 2.8 m/s could suggest the possible presence of PH; nevertheless, the presence of PH cannot be reliably determined by TRV alone, and ePASP is the most used parameter for screening PH in clinical practice.

5. Conclusions

In summary, we demonstrated that S2F was associated with elevated ePASP and had different cut-off points in patients with different severity of PH. Using the mobile cardiac acoustic monitoring system, S2F measurements offer a convenient ambulatory method for PH screening, making it more user-friendly than the standard examination.

Data availability statement

The raw data supporting the conclusions of this article will be made available by the authors, without undue reservation.

Ethics statement

The studies involving humans were approved by the Institutional Review Board of Shanghai Chest Hospital, Shanghai Jiao Tong University School of Medicine. The studies were conducted in accordance with the local legislation and institutional requirements. The participants provided their written informed consent to participate in this study.

Author contributions

JH: Conceptualization, Data curation, Funding acquisition, Methodology, Writing – original draft, Writing – review & editing.

WZ: Conceptualization, Writing – review & editing. WF: Data curation, Writing – review & editing. JL: Data curation, Writing – review & editing. YQ: Data curation, Formal analysis, Software, Writing – review & editing. XH: Supervision, Writing – review & editing. XP: Project administration, Supervision, Writing – review & editing. RL: Conceptualization, Funding acquisition, Supervision, Writing – review & editing. BH: Supervision, Writing – review & editing.

Funding

The author(s) declare financial support was received for the research, authorship, and/or publication of this article.

The work was supported by the National Natural Science Foundation of China (grant nos. 81974051 and 82070262).

Conflict of interest

The authors declare that the research was conducted in the absence of any commercial or financial relationships that could be construed as a potential conflict of interest.

Publisher's note

All claims expressed in this article are solely those of the authors and do not necessarily represent those of their affiliated organizations, or those of the publisher, the editors and the reviewers. Any product that may be evaluated in this article, or claim that may be made by its manufacturer, is not guaranteed or endorsed by the publisher.

Supplementary material

The Supplementary Material for this article can be found online at: https://www.frontiersin.org/articles/10.3389/fcvm.2023.1292647/full#supplementary-material

SUPPLEMENTARY AUDIO S1
The heart sound audio of the control patient.

SUPPLEMENTARY AUDIO S2
The heart sound audio of the PH patient

References

1. Hoeper MM, Humbert M, Souza R, Idrees M, Kawut SM, Sliwa-Hahnle K, et al. A global view of pulmonary hypertension. *Lancet Respir Med*. (2016) 4(4):306–22. doi: 10.1016/S2213-2600(15)00543-3

2. Humbert M, Kovacs G, Hoeper MM, Badagliacca R, Berger RMF, Brida M, et al. 2022 ESC/ERS guidelines for the diagnosis and treatment of pulmonary hypertension. *Eur Heart J*. (2022) 43(38):3618–731. doi: 10.1093/eurheartj/ehac237

3. Hoeper MM, Lee SH, Voswinckel R, Palazzini M, Jais X, Marinelli A, et al. Complications of right heart catheterization procedures in patients with pulmonary hypertension in experienced centers. *J Am Coll Cardiol*. (2006) 48(12):2546–52. doi: 10.1016/j.jacc.2006.07.061

4. D'Alto M, Di Maio M, Romeo E, Argiento P, Blasi E, Di Vilio A, et al. Echocardiographic probability of pulmonary hypertension: a validation study. *Eur Respir J*. (2022) 60(2):2102548. doi: 10.1183/13993003.02548-2021

5. Naeije R, Torbicki A. More on the noninvasive diagnosis of pulmonary hypertension: doppler echocardiography revisited. *Eur Respir J*. (1995) 8(9):1445–9. doi: 10.1183/09031936.95.08091445

6. Dunlap B, Weyer G. Pulmonary hypertension: diagnosis and treatment. *Am Fam Physician*. (2016) 94(6):463–9.

7. Wen YN, Lee AP, Fang F, Jin CN, Yu CM. Beyond auscultation: acoustic cardiography in clinical practice. *Int J Cardiol*. (2014) 172(3):548–60. doi: 10.1016/j.ijcard.2013.12.298

8. Chan W, Woldeyohannes M, Colman R, Arand P, Michaels AD, Parker JD, et al. Haemodynamic and structural correlates of the first and second heart sounds in pulmonary arterial hypertension: an acoustic cardiography cohort study. *BMJ Open*. (2013) 3(4):e002660. doi: 10.1136/bmjopen-2013-002660

9. Yamakawa N, Kotooka N, Kato T, Kuroda T, Node K. Cardiac acoustic biomarkers as surrogate markers to diagnose the phenotypes of pulmonary hypertension: an exploratory study. *Heart Vessels*. (2022) 37(4):593–600. doi: 10.1007/s00380-021-01943-7

10. Chen Y, Hou A, Wu X, Cong T, Zhou Z, Jiao Y, et al. Assessing hemorrhagic shock severity using the second heart sound determined from phonocardiogram: a novel approach. *Micromachines (Basel)*. (2022) 13(7):1027. doi: 10.3390/mi13071027

11. Huang J, Zhang W, Pan C, Zhu S, Mead RH, Li R, et al. Mobile cardiac acoustic monitoring system to evaluate left ventricular systolic function in pacemaker patients. *J Clin Med*. (2022) 11(13):3862. doi: 10.3390/jcm11133862

12. Brugger N, Lichtblau M, Maeder M, Muller H, Pellaton C, Yerly P, et al. Two-dimensional transthoracic echocardiography at rest for the diagnosis, screening and management of pulmonary hypertension. *Swiss Med Wkly*. (2021) 151:w20486. doi: 10.4414/smw.2021.20486

13. Rangayyan RM, Lehner RJ. Phonocardiogram signal analysis: a review. *Crit Rev Biomed Eng*. (1987) 15(3):211–36.

14. Resnekov L. A physical and physiological basis for the interpretation of cardiac auscultation: evaluations based primarily on the second sound and ejection murmurs. *JAMA*. (1982) 247(16):2299. doi: 10.1001/jama.1982.03320410073044

15. Hamilton B. Understanding heart sound and murmurs with an Introduction to lungs sound. *J Cardiovasc Nurs*. (1993) 8(1):84. doi: 10.1097/00005082-199310000-00010

16. Rich S, Dantzker DR, Ayres SM, Bergofsky EH, Koerner SK. Primary pulmonary hypertension: a national prospective study. *Ann Intern Med*. (1987) 107(2):216. doi: 10.7326/0003-4819-107-2-216

17. Marcus G, Vessey J, Jordan MV, Huddleston M, Mckeown B, Gerber IL, et al. Relationship between accurate auscultation of a clinically useful third heart sound and level of experience. *Arch Intern Med*. (2006) 166(6):617–22. doi: 10.1001/archinte.166.6.617

18. Prielipp RC, Kelly JS, Roy RC. Use of esophageal or precordial stethoscopes by anesthesia providers: are we listening to our patients? *J Clin Anesth*. (1995) 7(5):367–72. doi: 10.1016/0952-8180(95)00027-F

19. Debbal SM, Bereksi-Reguig F. Computerized heart sounds analysis. *Comput Biol Med*. (2008) 38(2):263–80. doi: 10.1016/j.compbiomed.2007.09.006

20. Plesinger F, Viscor I, Halamek J, Jurco J, Jurak P. Heart sounds analysis using probability assessment. *Physiol Meas*. (2017) 38(8):1685–700. doi: 10.1088/1361-6579/aa7620

21. Langley P, Murray A. Heart sound classification from unsegmented phonocardiograms. *Physiol Meas*. (2017) 38(8):1658–70. doi: 10.1088/1361-6579/aa724c

22. Nath M, Srivastava S, Kulshrestha N, Singh D. Detection and localization of S(1) and S(2) heart sounds by 3rd order normalized average shannon energy envelope algorithm. *Proc Inst Mech Eng H*. (2021) 235(6):615–24. doi: 10.1177/0954411921998108

23. Sutton G, Harris A, Leatham A. Second heart sound in pulmonary hypertension. *Heart*. (1968) 30(6):743–56. doi: 10.1136/hrt.30.6.743

24. Luisada A, Singhal A, Knighten V. New index of cardiac contractility during stress testing with treadmill. *Acta Cardiol*. (1986) 41(1):31–9.

25. Tranulis C, Durand LG, Senhadji L, Pibarot P. Estimation of pulmonary arterial pressure by a neural network analysis using features based on time-frequency representations of the second heart sound. *Med Biol Eng Comput*. (2002) 40(2):205–12. doi: 10.1007/BF02348126

26. Arnott PJ, Pfeiffer GW, Tavel ME. Spectral analysis of heart sounds: relationships between some physical characteristics and frequency spectra of first

and second heart sounds in normals and hypertensives. *J Biomed Eng*. (1984) 6 (2):121–8. doi: 10.1016/0141-5425(84)90054-2

27. Chen D, Pibarot P, Honos G, Durand LG. Estimation of pulmonary artery pressure by spectral analysis of the second heart sound. *Am J Cardiol*. (1996) 78 (7):785–9. doi: 10.1016/S0002-9149(96)00422-5

28. Michaels AD, Karabsheh S, Neuharth RM, Masood S, Arand P. Noninvasive computerized acoustic cardiographic prediction of pulmonary hypertension. *J Electrocardiol*. (2009) 42(6):617–8. doi: 10.1016/j.jelectrocard.2009.08.037

29. Opotowsky AR, Ojeda J, Rogers F, Prasanna V, Clair M, Moko L, et al. A simple echocardiographic prediction rule for hemodynamics in pulmonary hypertension. *Circ Cardiovasc Imaging*. (2012) 5(6):765–75. doi: 10.1161/CIRCIMAGING.112.976654

30. D'Alto M, Romeo E, Argiento P, Pavelescu A, Mélot C, D'Andrea A, et al. Echocardiographic prediction of pre- versus postcapillary pulmonary hypertension. *J Am Soc Echocardiogr*. (2015) 28(1):108–15. doi: 10.1016/j.echo.2014.09.004

31. Venkateshvaran A, Hamade J, Kjellström B, Lund LH, Manouras A. Doppler Estimates of pulmonary vascular resistance to phenotype pulmonary hypertension in heart failure. *Int J Cardiovasc Imaging*. (2019) 35(8):1465–72. doi: 10.1007/s10554-019-01591-z

32. Dillier R, Zuber M, Arand P, Erne S, Erne P. Assessment of systolic and diastolic function in asymptomatic subjects using ambulatory monitoring with acoustic cardiography. *Clin Cardiol*. (2011) 34(6):384–8. doi: 10.1002/clc.20891

frontiers | Frontiers in Cardiovascular Medicine

TYPE Original Research
PUBLISHED 21 December 2023
DOI 10.3389/fcvm.2023.1301619

Check for updates

OPEN ACCESS

EDITED BY
Gaoyang Li,
Tohoku University, Japan

REVIEWED BY
Boyan Mao,
Beijing University of Chinese Medicine, China
Johannes Uhlig,
University Medical Center Goettingen, Germany

*CORRESPONDENCE
Robin F. Gohmann
robin.gohmann@gmx.de

†These authors have contributed equally to this work and share first authorship

‡These authors have contributed equally to this work and share senior authorship

RECEIVED 25 September 2023
ACCEPTED 13 November 2023
PUBLISHED 21 December 2023

CITATION
Gohmann RF, Schug A, Pawelka K, Seitz P, Majunke N, El Hadi H, Heiser L, Renatus K, Desch S, Leontyev S, Noack T, Kiefer P, Krieghoff C, Lücke C, Ebel S, Borger MA, Thiele H, Panknin C, Abdel-Wahab M, Horn M and Gutberlet M (2023) Interrater variability of ML-based CT-FFR during TAVR-planning: influence of image quality and coronary artery calcifications.
Front. Cardiovasc. Med. 10:1301619.
doi: 10.3389/fcvm.2023.1301619

COPYRIGHT
© 2023 Gohmann, Schug, Pawelka, Seitz, Majunke, El Hadi, Heiser, Renatus, Desch, Leontyev, Noack, Kiefer, Krieghoff, Lücke, Ebel, Borger, Thiele, Panknin, Abdel-Wahab, Horn and Gutberlet. This is an open-access article distributed under the terms of the Creative Commons Attribution License (CC BY). The use, distribution or reproduction in other forums is permitted, provided the original author(s) and the copyright owner(s) are credited and that the original publication in this journal is cited, in accordance with accepted academic practice. No use, distribution or reproduction is permitted which does not comply with these terms.

Interrater variability of ML-based CT-FFR during TAVR-planning: influence of image quality and coronary artery calcifications

Robin F. Gohmann[1,2*†], Adrian Schug[1,2†], Konrad Pawelka[1,2], Patrick Seitz[1], Nicolas Majunke[3], Hamza El Hadi[3], Linda Heiser[1], Katharina Renatus[1,2], Steffen Desch[3], Sergey Leontyev[4], Thilo Noack[4], Philipp Kiefer[4], Christian Krieghoff[2], Christian Lücke[2], Sebastian Ebel[1,2], Michael A. Borger[4,5], Holger Thiele[3,5], Christoph Panknin[6], Mohamed Abdel-Wahab[3], Matthias Horn[7‡] and Matthias Gutberlet[1,2,5‡]

[1]Department of Diagnostic and Interventional Radiology, Heart Center Leipzig, Leipzig, Germany, [2]Medical Faculty, University of Leipzig, Leipzig, Germany, [3]Department of Cardiology, Heart Center Leipzig, University of Leipzig, Leipzig, Germany, [4]Department of Cardiac Surgery, Heart Center Leipzig, University of Leipzig, Leipzig, Germany, [5]Helios Health Institute, Leipzig, Germany, [6]Siemens Healthcare GmbH, Erlangen, Germany, [7]Institute for Medical Informatics, Statistics and Epidemiology (IMISE), University of Leipzig, Leipzig, Germany

Objective: To compare machine learning (ML)-based CT-derived fractional flow reserve (CT-FFR) in patients before transcatheter aortic valve replacement (TAVR) by observers with differing training and to assess influencing factors.
Background: Coronary computed tomography angiography (cCTA) can effectively exclude CAD, e.g. prior to TAVR, but remains limited by its specificity. CT-FFR may mitigate this limitation also in patients prior to TAVR. While a high reliability of CT-FFR is presumed, little is known about the reproducibility of ML-based CT-FFR.
Methods: Consecutive patients with obstructive CAD on cCTA were evaluated with ML-based CT-FFR by two observers. Categorization into hemodynamically significant CAD was compared against invasive coronary angiography. The influence of image quality and coronary artery calcium score (CAC) was examined.
Results: CT-FFR was successfully performed on 214/272 examinations by both observers. The median difference of CT-FFR between both observers was −0.05 (−0.12-0.02) ($p < 0.001$). Differences showed an inverse correlation to the absolute CT-FFR values. Categorization into CAD was different in 37/214 examinations, resulting in net recategorization of Δ13 (13/214) examinations and a difference in accuracy of Δ6.1%. On patient level, correlation of absolute and categorized values was substantial (0.567 and 0.570, $p < 0.001$). Categorization into CAD showed no correlation to image quality or CAC ($p > 0.13$).

Abbreviations

AS, aortic valve stenosis; CAC, coronary artery calcium score; CAD, coronary artery disease; CAD^{-}, negative for coronary artery disease; CAD^{f-}, negative for hemodynamically significant coronary artery disease; CAD^{f+}, negative for hemodynamically significant coronary artery disease; cCTA, coronary CT-angiography; CFD, computational fluid dynamics; CI, confidence interval; CNR, contrast to noise ratio; CT-FFR, CT-derived fractional flow reserve; FN, false negative; FP, false positive; HU, Hounsfield unit; ICA, invasive coronary angiography; ICC, intra-class correlation coefficient; LAD, left anterior descending artery; LCX, circumflex artery; LM, left main coronary artery; LV, left ventricular; ML, machine learning; MM, mismatched coronary artery disease categorizations; NN, remained negative; NP, negative to positive; NPV, negative predictive value; PN, positive to negative; PP, remained positive; PPV, positive predictive value; QCA, quantitative coronary angiography; RCA, right coronary artery; SCCT, Society of Cardiovascular Computed Tomography#; Sen, sensitivity; Spe, specificity; TAVR, transcatheter aortic valve replacement; TP, true positive.

Conclusion: Differences between CT-FFR values increased in values below the cut-off, having little clinical impact. Categorization into CAD differed in several patients, but ultimately only had a moderate influence on diagnostic accuracy. This was independent of image quality or CAC.

KEYWORDS

aortic stenosis, computed tomography coronary angiography, coronary angiography, coronary artery disease, transcatheter aortic valve implantation, diagnostic accuracy, machine learning, computed tomography fractional flow reserve

1. Introduction

Patients evaluated to be treated with transcatheter aortic valve replacement (TAVR) are generally elderly and have a high prevalence of coronary artery disease (CAD) (1–3). CAD is recommended to be excluded and if needed to be treated before the procedure (3–7). Coronary computed tomography angiography (cCTA) is the first line diagnostic tool for the exclusion of CAD in other patient groups (7) and its high negative predictive value (NPV) is known to be preserved also in patient before TAVR (3, 6, 8). Thus, its use is increasingly recognized as part of the standard CT evaluation protocol for TAVR-planning (3–8). However, cCTA remains limited by its low specificity, particularly in this patient group. CT-derived fractional flow reserve (CT-FFR) has been described as a promising tool to mitigate this limitation by non-invasively predicting hemodynamic relevance (9–11) also in patients prior to TAVR (12–16).

Machine learning (ML)-based CT-FFR is a computationally less demanding approach, which makes on-site computation of CT-FFR feasible on standard workstations and is known to correlate well with the more conventional computational fluid dynamics (CFD) approach (17). As opposed to the commercial off-site approaches, where the exact segmentation process is unknown, the user himself performs the segmentation in ML-based CT-FFR. While a high reliability of segmentation is presumed, the significance of the segmentation process and observer experience on the reliability of CT-FFR has not been well examined (18, 19), with no systematic analysis as of now.

In this study, we systematically compared the ML-based CT-FFR measurements carried out by two observers with differing expertise, on segment, vessel and patient level in a large group of patients before TAVR. Furthermore, we analyzed the frequency of conflicting categorizations and the influence of image quality and coronary artery calcium score (CAC).

2. Material and methods

2.1. Study design and patient population

The patient population and study design have previously been reported on (8, 13). In short, consecutive examinations with retrospectively ECG-gated CT for TAVR-planning over a period of 7 months were screened. Only patients having undergone invasive coronary angiography (ICA) within 3 months of CT were considered for the current analysis. Of the 388 patients, 272 had at least one coronary stenosis (≥50%) on cCTA being of interest for CT-FFR evaluation (**Figure 1**).

2.2. CT acquisition

The scan protocol has previously been described in detail (8). Briefly, a retrospectively ECG-gated helical CT of the heart was performed from caudal to cranial, immediately followed by a high-pitch helical CT in the opposite direction for depiction of the aorta and iliofemoral access route using a single bolus of 70 ml iodinated contrast medium. All patients were examined with the same scanner (Somatom Definition Flash; Siemens). No beta blockers or nitrates were given. The ECG-gated scan of the heart was used for computation of the ML-based CT-FFR.

2.3. cCTA and CT-FFR analysis

Coronary arteries were analyzed morphologically by segment according to the 18-segment model (20). When a stenosis of ≥50% diameter was identified on cCTA, CT-FFR values were obtained approximately 2 cm distal to the stenosis (21). The standard of reference was ICA with quantitative coronary analysis (QCA) with the same threshold and ≥70% for a secondary evaluation.

ML-based CT-FFR (cFFR version 3.2.0, Siemens; not commercially available) was performed by observer B on all examinations previously analyzed by observer A (13). The ML-based prototype used for this study has been described in detail before (13, 17, 22). The computationally less demanding process enabled on-site computation on a desktop workstation.

Per-segment interpretations were combined to form per-vessel and per-patient ratings, considering the respective worst segment (highest grade of stenosis; lowest CT-FFR value). CT-FFR values of ≤0.80 were considered as hemodynamically significant CAD (CAD^{ft+}) (23).

Both observers received the same instructions for segmentation and measurement of CT-FFR. Observer A had received several weeks of training in coronary artery imaging, including formal reading of cCTA and case discussions with correlation to ICA. Observer B only received comprehensive instructions on coronary artery segmentation and handling of the CT-FFR

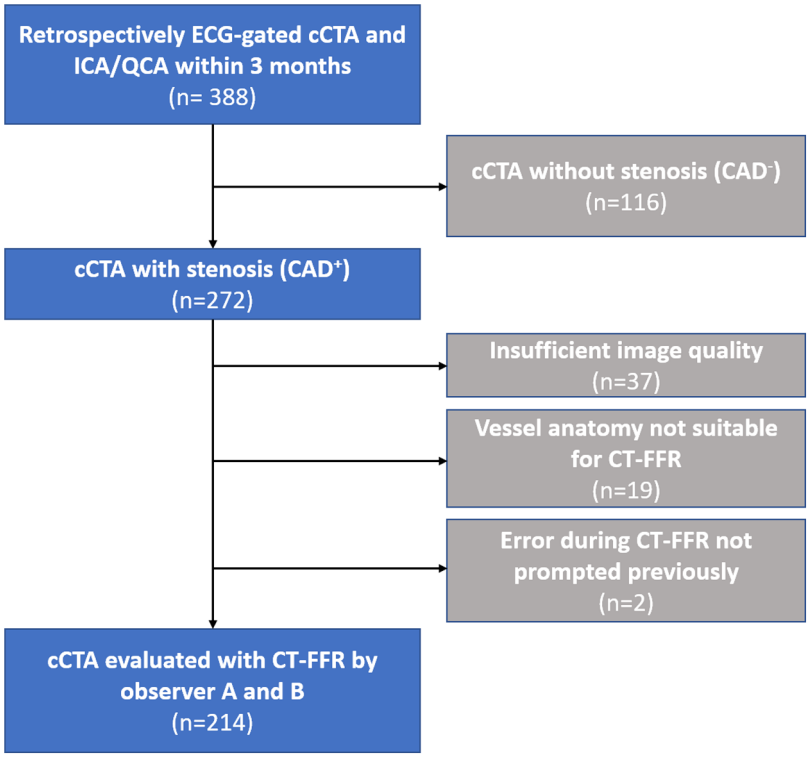

FIGURE 1
Flowchart of the study population. Flowchart of the study population and reasons for exclusion. CAD, coronary artery disease; cCTA, coronary computed tomography angiography; CT-FFR, CT-derived-fractional-flow-reserve; ECG, electrocardiogram; ICA, invasive coronary angiography; QCA, quantitative coronary angiography.

prototype at hand. Both measurements were taken within 18 months. The methods adopted for this study comply with the Guidelines for Reporting Reliability and Agreement Studies (GRRAS) (24).

2.4. Statistical analysis

Continuous variables are presented as median and [interquartile range (IQR)]. Differences between the two observers in CT-FFR values and evaluation times were assessed using the Wilcoxon signed-rank test. Interobserver agreement for CT-FFR values was evaluated using intra-class correlation (ICC) type ICC (1, 3) according to the convention proposed by Shrout and Fleiss (25). For interpretation of ICC coefficients, we followed the guidelines given by Cicchetti, which identify values <0.5 as a poor, 0.5–0.75 as moderate, 0.75–0.9 as a good, and >0.9 as an excellent correlation (26). Interobserver agreement with respect to categorization into hemodynamically significant CAD according to CT-FFR was assessed using Cohen's kappa and interpreted as proposed by Landis and Koch, which classifies correlation as follows: <0.2 slight, 0.2–0.4 fair, 0.4–0.6 moderate, 0.6–0.8 substantial, >0.8 almost perfect (27). Correlation between CT-FFR differences and covariates was calculated using Spearman's rank correlation (quantitative image quality measures and calcium burden) or Kendall's rank correlation (qualitative image quality). Correlation between mismatched coronary artery disease categorization and covariates was determined using the point-biserial correlation (quantitative image quality and CAC) or rank-biserial correlation (qualitative image quality). A p value of <0.05 was considered statistically significant. Statistical analysis was performed using R (version 4.1.2; R Foundation for Statistical Computing, Vienna, Austria).

3. Results

3.1. (Re)evaluation with ML-based CT-FFR

In total, 214 of the 272 examinations with signs of CAD on cCTA were successfully evaluated with ML-based CT-FFR by observer A and B (**Figure 1**). Two patients could not be reevaluated by observer B, because of an error with the prototype not prompted earlier. Reasons for initial exclusion were insufficient or borderline image quality hindering continuous segmentation of the coronary tree, and anatomical variants outside the model boundaries of the CT-FFR prototype (13). Evaluation time was significantly lower for observer A (observer A: 24 (18–32) min; observer B: 28 (22–35) min; $p < 0.001$).

Of the included patients 90 (42.1%) were female and the mean body mass index was 29.2 ± 5.5 kg/m^2.

TABLE 1 Interobserver variability of absolute CT-FFR values.

Level of observation		*n*	Difference	95% CI	*p*	ICC	95% CI	*p*
Patient		214	−0.05 (−0.12–0.02)	−0.065, −0.035	<0.001	0.567	0.469, 0.651	<0.001
Vessel	RCA	115	−0.03 (−0.09–0.03)	−0.055, −0.010	0.003	0.616	0.489, 0.718	<0.001
	LM	13	−0.03(−0.05–0.01)	−0.065, −0.005	0.04	0.427	−0.137, 0.782	0.064
	LAD	177	−0.04 (−0.12–0.05)	−0.06, −0.020	<0.001	0.558	0.447, 0.652	<0.001
	LCX	114	−0.04 (−0.09–0.03)	−0.055, −0.010	0.003	0.423	0.260, 0.563	<0.001

Values are median and (IQR) of the difference of CT-FFR values of the two observers. The first *p* value column (and 95% CI) corresponds to the difference of interobserver differences from zero while the second *p* value column (and 95% CI) corresponds to the difference of the ICC coefficient from zero. *P* values <0.05 were statistically significant. ICC, intra-class correlation coefficient; IQR, interquartile range; LAD, left anterior descending artery; LM, left main coronary artery; LCX, circumflex artery; RCA, right coronary artery.

3.2. Differences in CT-FFR values

CT-FFR values were significantly different between observer A and B with the largest median differences on patient level ($n = 214$; −0.05[−0.12–0.02]; $p < 0.001$). Median differences on vessel level were also significantly different between the observers (left anterior descending artery [LAD] >left circumflex artery [LCX] >right coronary artery [RCA]). The LM had a much lower number of stenoses ($n = 13$) and thus could not be considered for analyses (Table 1).

Patients recategorized as false negative (FN) from true positive (TP) by either observer showed CT-FFR values closest to the cut-off of ≤0.80 (observer A: $n = 17$, 0.85 [0.83–0.87]; observer B: $n = 28$, 0.84 [0.82–0.89]). The distribution of CT-FFR values of both observers is shown in Figure 2. Observer A measured more outliers, particularly in the RCA and LCX. Discrepancies of CT-FFR values between the observers were smaller for high CT-FFR values, and larger for low values (Figure 3).

3.3. Interobserver variability

Analysis on patient level showed fair-good agreement between both observers (ICC coefficient: 0.567; $p < 0.001$). On vessel level, correlation between both observers was fair-good in the RCA and LAD. Agreement of measured values in the LCX was fair (Table 1).

Categorization into hemodynamically significant CAD according to CT-FFR correlated between both observers. On patient level, interobserver agreement was moderate-substantial (Cohen's kappa: 0.570; $p < 0.001$). Correlation in the RCA was moderate-substantial, in the LAD fair, and in the LCX fair (Table 2).

Observer B recategorized 14/214 patients from negative to positive and 23 patients from positive to negative, with 13 recategorizations being incorrect in regard to the standard of reference, resulting in a difference of diagnostic accuracy of Δ−6.07%. Specificity and negative predictive value (NPV) on patient level were decreased by Δ−1.82% and Δ−12.84%, respectively. On patient and vessel level, more recategorizations occurred from positive to negative than vice versa (Table 3). Gross frequency of different categorizations on vessel level was LCX: 38.6% >LAD: 23.2% >RCA: 20.9%, resulting in a net difference of Δ−3.34% in accuracy. On vessel level, specificity was slightly higher for observer B (Δ+0.73%), while other test metrics were slightly lower (Table 3). There was no discernable trend towards a differing frequency in discrepant categorizations on segment level, e.g., in the distal segments. The gross rate of discrepant categorizations into $CADf^{+}$ or CAD^{f-}on segment level is shown in Appendix 1. On segment level the difference in accuracy was Δ+1.46%.

3.4. Standard of reference and diagnostic performance

Overall, observer B rated fewer stenoses CAD^{f+} on patient level, resulting in a lower specificity, NPV and diagnostic accuracy compared to observer A (Table 3). If the ICA cut-off were changed to ≥70% diameter lumen narrowing, the overall differences between observer A and B became much smaller (specificity: Δ+2.08 vs. Δ−1.82; NPV: Δ−6.56 vs. Δ−12.84; accuracy: Δ−1.40 vs. Δ−6.07) (Table 3).

3.5. Influence of image quality and coronary artery calcifications

Absolute CT-FFR values did not correlate with quantitative image quality (CNR, HU). CT-FFR values correlated weakly with qualitative image quality on patient level and in the RCA (patient: $r = -0.116$; RCA: $r = -0.16$; $p < 0.03$). CT-FFR values correlated weakly with CAC on patient level and in the LAD (patient: $r = 0.18$; LAD: $r = 0.206$; $p < 0.009$).

Categorization into CAD was independent of quantitative or qualitative image quality and of CAC (Table 4).

4. Discussion

Interobserver variability of ML-based CT-FFR has not been studied extensively on a large patient cohort with a high prevalence of CAD. This study on patients before TAVR was carried out by observers with differing levels of experience and rendered somewhat different results. This led to occasional differences in categorization of hemodynamically significant CAD

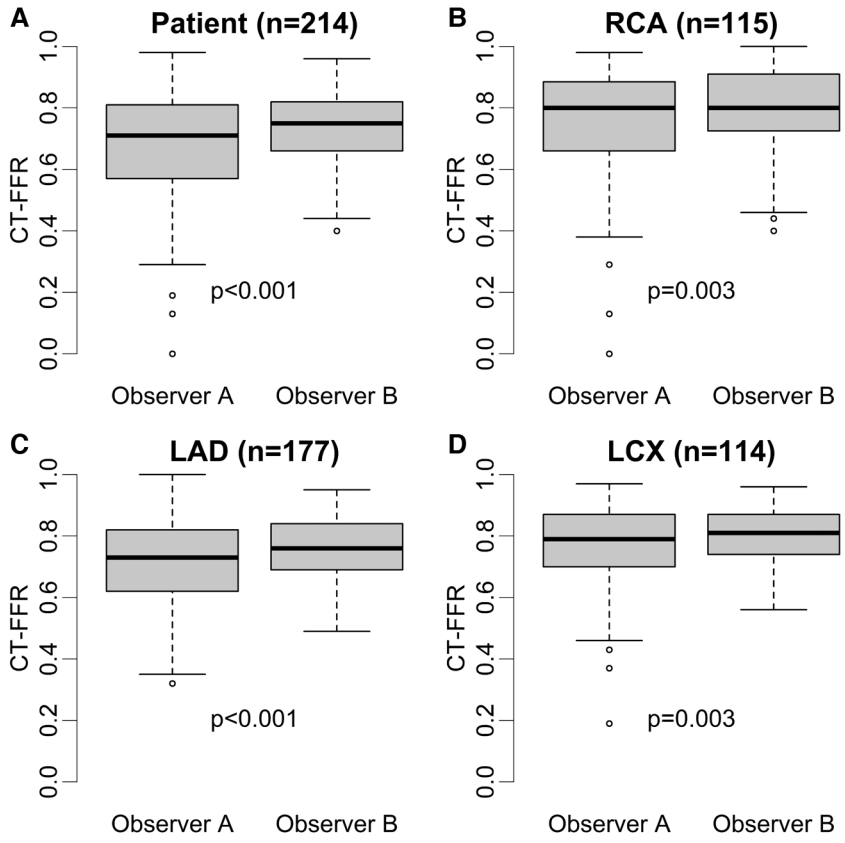

FIGURE 2
Distribution of absolute CT-FFR values. Box plots of CT-FFR values measured by two observers on patient (**A**) and vessel level (**B–D**). Observer B measured higher median CT-FFR values with a smaller interquartile range on patient and vessel level ($p \leq 0.003$) (**A–D**). The difference between both observers were larger on patient level (**A**) compared to vessel level (patient: 0.05> RCA: 0.05; LAD: 0.04; CX: 0.04) (**B–D**). Observer A shows more outliers, especially in RCA and LCX (**B**,**C**). CT-FFR, CT-derived fractional flow reserve; LAD, left anterior descending artery; LCX, left circumflex artery; RCA, right coronary artery.

and moderate changes in diagnostic performance. Recategorization of patients was independent of image quality or CAC.

Absolute values of CT-FFR showed significant differences between the observers from 0.03 to 0.04 on vessel and 0.05 on patient level (**Table 1**). This led to occasional recategorizations into hemodynamically significant CAD when CT-FFR values fell close to the cut-off [grey zone 0.75–0.80 (28)] and likely was the most relevant reason for differences in diagnostic performance between both observers. No observer was clearly superior to the other, with observer A having higher diagnostic accuracy on patient and vessel level and observer B performing slightly better on segment level. The difference in measured values between the observers was lower for high CT-FFR values and much larger for low values. There is no clear cut-off for all levels of observation, but differences are higher below the clinical cut-off CT-FFR ≤0.80 (**Figure 3**). A possible explanation for this observation could be that segmentation of larger vessel lumina is easier and thus more reproducible; while the opposite is true for small vessels. This is consistent with our observation of the smallest vessel, the LCX, having the weakest interobserver agreement. The higher discrepancy of small values is of little concern, as values far below the common cut-off (0.80 or 0.75) are of little to no significance for clinical decision-making (21, 29). Absolute CT-FFR values measured by the more experienced observer (observer A) had higher variance compared to observer B (**Figure 2**). A possible reason for this may be a more conservative segmentation of the contrasted lumen, while observer B may have tried to extrapolate the lumen in the presence of blooming artifacts at heavily calcified lesions in a more generic way (30).

Correlation of CT-FFR values in RCA and LAD and on patient level was moderate or borderline-good. Regardless, overall correlation in our patient cohort was lower than that reported in other patient groups. Ko et al. reported a median difference of 0.03 on patient level vs. 0.05 in this study. Studies with more experienced observers reported good-to-excellent interobserver agreement (18, 19, 31). Observers with less training showed higher discrepancies and moderate agreement (32, 33). The studies consisted of much younger patient groups (60.0 ± 8.5 years; 64.6 ± 8.9 years; 61.8 ± 10.2 years; 62.7 ± 8.9 years vs. 78.9 ± 9.7 years) with fewer stenoses per patient [0.53; 1.47; 0.33; 1.22 (stenosed vessels) vs. 1.6 stenoses per patient] (18, 19, 32, 34). Median evaluation time was vastly different (Ko et al.: 27 min; Donnelly et al.: 9 min; Yang et al.: 50 min; Ihdayhid et al.: 24–38 min; current study: 24 and 28 min). In addition to

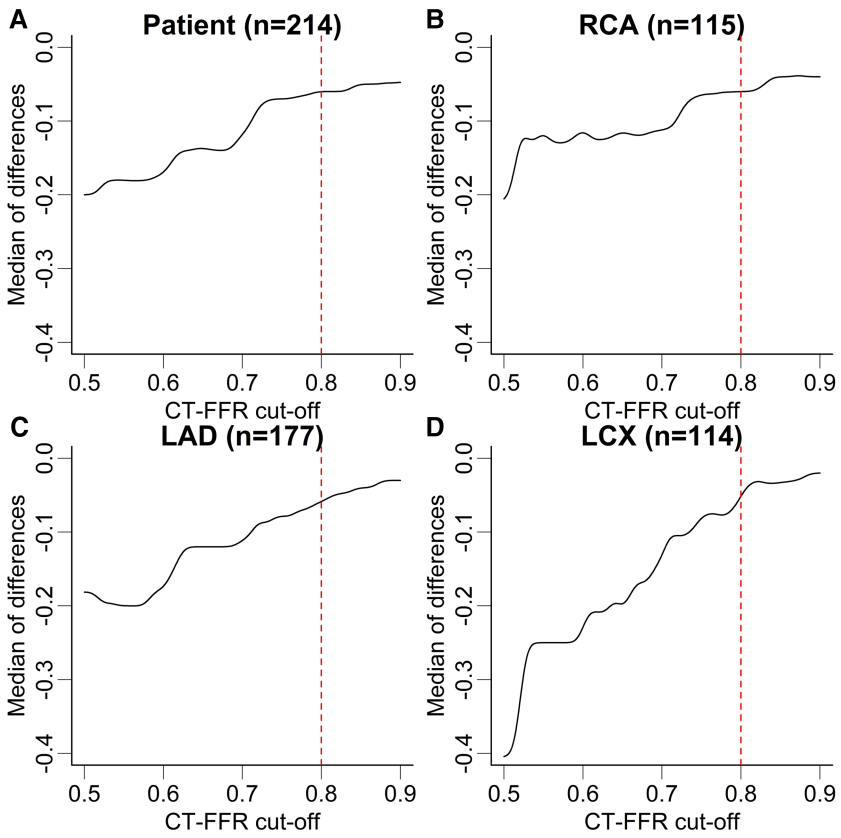

FIGURE 3
Median difference of CT-FFR values in dependence of absolute values. Median difference of CT-FFR values at different cut-offs between both observers at patient (A) and vessel level (B–D). The median difference of CT-FFR values is higher for low absolute values and lower for high values. Note, there is no discrete cut-off for all levels of observation, but differences are higher below the clinical cut-off CT-FFR ≤0.80. The dashed red lines correspond to the CT-FFR cut-off used to characterize hemodynamically significant CAD. The lines of the graph have been smoothed with a Gaussian filter to help avoid over-interpretation of small steps. CT-FFR, CT-derived fractional flow reserve; LAD, left anterior descending artery; LCX, left circumflex artery; RCA, right coronary artery.

TABLE 2 Interobserver agreement of categorization according to CT-FFR.

Level of observation		*n*	Cohen's kappa	95% CI	*p*
Patient		214	0.570	0.444, 0.696	<0.001
Vessel	RCA	115	0.582	0.434, 0.731	<0.001
	LAD	177	0.468	0.325, 0.611	<0.001
	LCX	114	0.230	0.052, 0.408	0.01

Interobserver agreement of categorized CT-FFR values. *P* values <0.05 were statistically significant. The threshold for hemodynamically significant CAD was ≤0.80. LAD, left anterior descending artery; LCX, circumflex artery; RCA, right coronary artery.

the lower experience of the observers, the most likely cause for the weaker interobserver agreement in our study lies in the much different and more challenging patient group of patients prior TAVR with more frequent and perhaps higher grade and frequently calcified stenoses. Overall, more experienced observers had better agreement, while less experience only had moderate agreement between the observers (18, 32, 33). This is a direct result of differences in lumen segmentation by the user himself in ML-based CT-FFR. Resulting differences are thus no different from the reproducibility of other techniques e.g., of cCTA with good interobserver and intraobserver agreement between trained observers, and moderate agreement between untrained observers (35, 36), or even ICA interpretation (37). Other CT-FFR solutions, namely the only commercially available and FDA approved CFD-based technique has not publish data concerning observer experience and reliability. Overall, observer experience seems to have a large influence on reliable CAD diagnosis. Standardized training and certification may likely improve reliability of ML-based CT-FFR further.

Interobserver agreement of categorization of patients into hemodynamically significant CAD was similar to the correlation of absolute values with moderate and sometimes moderate-to-good correlation for the RCA, LAD and patient level. This may be reassuring as in clinical decision making most commonly a discreet cut-off is used. Despite the agreement between the observers not being optimal, it can be considered fair, taking into account the observer's differing experience (**Table 2**). Notably, the LCX had the lowest correlation of absolute values and lowest agreement between categorized values. Although there is no definitive answer for this observation, the LCX is generally the smallest vessel with relatively few and short segments and the second highest rate of motion during the cardiac cycle (38). This

TABLE 3 Differences in categorization and changes in diagnostic performance.

Recategorizations							Changes in diagnostic performance				
Level of observation		*n*	NN	NP	PP	PN	Δ Sen., %	Δ Spe., %	Δ PPV, %	Δ NPV, %	Δ Acc., %
QCA ≥50%	Patient	214	41	14	136	23	−10.58%	−1.82%	−4.05%	−12.84%	−6.07%
	RCA	115	43	10	48	14	−10.96%	+0.73%	−3.71%	−6.07%	−3.34%
	LM	13	12	0	0	1					
	LAD	177	36	17	100	24					
	LCX	114	34	19	36	25					
QCA ≥70%	Patient	214	41	14	136	23	−8.57%	+2.08%	−1.77%	−6.56%	−1.40%
	Vessel	419	125	46	184	64	−10.99%	+2.44%	−2.23%	−3.95%	−0.48%

(Re)categorization into hemodynamically significant CAD and differences in diagnostic performance of CT-FFR between the observer A and B. Thresholds for significant CAD were ≥50% and ≥70% diameter for QCA and ≤0.80 for CT-FFR, respectively. Acc, accuracy; LAD, left anterior descending artery; LCX, circumflex artery; LM, left main coronary artery; NN, remained negative; NP, negative-to-positive; NPV, negative predictive value; PN, positive-to-negative; PP, remained positive; PPV, positive predictive value; RCA, right coronary artery; Sen., sensitivity; Spe., specificity.

TABLE 4 Influence of image quality and coronary arterial calcifications.

Level of observation			*n*	Image quality									Calcium burden		
				r CNR	95% CI	*p*	r HU	95% CI	*p*	r QIQ	95% CI	*p*	r CAC	95% CI	*p*
Absolute differences	Patient		214	−0.060	−0.192, 0.075	0.385	−0.06	−0.194, 0.076	0.384	−0.116	−0.218, −0.010	0.030	0.180	0.037, 0.313	0.009
	Vessel	RCA	115	−0.038	−0.218, 0.141	0.683	−0.103	−0.270, 0.070	0.274	−0.16	−0.290, −0.021	0.030	0.094	−0.099, 0.279	0.323
		LAD	177	0.021	−0.124, 0.167	0.778	−0.046	−0.195, 0.104	0.539	−0.095	−0.199, 0.011	0.110	0.206	0.059, 0.345	0.006
		LCX	114	−0.019	−0.201, 0.168	0.837	−0.023	−0.216, 0.175	0.805	−0.059	−0.208, 0.093	0.428	0.012	−0.183, 0.205	0.901
Categorization mismatch	Patient		214	−0.003	−0.137, 0.131	0.963	0.000	−0.134, 0.134	1.000	0.060	−0.144, 0.259	0.542	−0.104	−0.235, 0.031	0.131
	Vessel	RCA	115	−0.138	−0.313, 0.047	0.142	−0.114	−0.291, 0.071	0.225	0.171	−0.088, 0.408	0.170	−0.005	−0.190, 0.180	0.955
		LAD	177	0.083	−0.065, 0.228	0.269	0.004	−0.144, 0.151	0.958	0.016	−0.184, 0.215	0.870	0.011	−0.137, 0.158	0.888
		LCX	114	0.125	−0.061, 0.302	0.187	0.091	−0.095, 0.270	0.337	−0.007	−0.144, 0.259	0.946	0.058	−0.127, 0.239	0.540

Correlation of CNR, HU, qualitative image quality and CAC with absolute CT-FFR differences between the two observers and mismatch of categorization into hemodynamically significant CAD. The first *p* value column (and 95% CI) corresponds to the influence of CNR, the second to HU, the third to QIQ while the fourth *p* value column (and 95% CI) corresponds to the influence of calcium burden. *P* values <0.05 were considered statistically significant. Thresholds for significant CAD were ≥50% diameter for QCA and ≤0.80 for CT-FFR, respectively. CNR, contrast to noise ratio; CAC, coronary artery calcium score; HU, Hounsfield unit; LAD, left anterior descending artery; LCX, circumflex artery; QIQ, qualitative image quality; RCA, right coronary artery.

10.3389/fcvm.2023.1301619

may contribute to motion- and step-artefacts consequently decreasing diagnostic performance (39) and ultimately making segmentation the most challenging in this vessel.

Observer B showed lower diagnostic performance on patient level, with especially lower sensitivity (Δ−10.58%). However, on vessel level, specificity of observer B was higher (Δ+0.73%) (**Table 3**). A possible explanation may be a different, more conservative segmentation approach for the less experienced observer B, e.g., when encountering artifacts. The much lower NPV on all levels of observation might be caused by observer B's lack of clinical experience, possibly leading to a generic extrapolation of the lumen in calcified lesions and failure to differentiate plaque from artifact and vice versa. Thus, more hemodynamically relevant stenoses were missed (higher false-negative count). However, it must be kept in mind that the standard of reference in this study was anatomical (ICA with QCA). The hemodynamic significance of stenosis in ICA, especially in the context of aortic valve stenosis (AS) and subsequent left ventricular (LV) hypertrophy, is unclear. Because CT-FFR is derived from the vessel cross-section and dependent on specific vessel anatomy and LV mass, AS may influence this technique and generate different values than in patients without AS and none of the resulting adaptations.

The change in diagnostic performance and specificity (Δ−1.82%) on patient level is dependent on the standard of reference. The very conservative cut-off of ≥50% for QCA might not be optimal for clinical decision-making, as it likely includes many stenoses without hemodynamic relevance. Meanwhile, CT-FFR may have classified these as not hemodynamically relevant causing false-negative categorizations. A higher ICA cut-off (e.g., QCA ≥70%) would lead to fewer false-negative categorizations by CT-FFR. Changing the standard of reference to this more stringent cut-off would decrease sensitivity, potentially increase specificity and may decrease the differences in diagnostic performance between both observers (accuracy: Δ−6.07–Δ−1.40; **Table 3**).

Overall, observer A likely evaluated stenoses more strictly, which explains the higher sensitivity. More clinical experience is the most probable reason for the better performance on the clinically relevant levels of observation, namely patient and vessel level. Minute differences in segmentation of the lumen may lead to different categorization into CAD whenever values fall close to the cut-off. Notably, specificity remains very similar between the observers. This can be explained by many true-negative categorizations of values relatively clearly above the cut-off. The patients that are categorized as false-negative presented CT-FFR values closer to the grey zone (0.75–0.80) than other patients (Observer A: 0.85; Observer B: 0.84). These borderline cases are prone to recategorization between both observers. As many recategorizations are correct in regard to ICA and cancel each other out, their influence on diagnostic performance is much smaller than their number leads to believe. This is supported by the number of differing CAD categorizations being larger than the actual change in diagnostic performance (recategorizations: 37/214; accuracy: Δ−6.07).

Image quality and calcium burden may interfere with the correct assessment of coronary arteries. However, the categorization into hemodynamically relevant CAD with CT-FFR was independent of CAC and image quality, which is encouraging for the use of CT-FFR in the group of patients prior to TAVR. Small, likely not clinically relevant correlations of absolute CT-FFR values and image quality and CAC were noted. Considering the number of tests performed, these findings should not be overestimated. Our findings with little to no influence of CAC on CT-FFR are consistent with the literature, with only Tesche et al. finding a degrading effect CAC on CT-FFR with very high scores (18, 19, 30, 39, 40), even though also patients with much higher CAC were included in our study. The virtual lack of correlation of CT-FFR values to image quality suggests that once a certain threshold of image quality is reached, CT-FFR may be expected to be performed reliably. Even a new deep learning algorithm for the improvement of image quality was not able to increase diagnostic performance of CT-FFR further (30).

Patients prior to TAVR assessed with ML-based CT-FFR by two observers with differing experience were sometimes categorized differently into having hemodynamically relevant CAD or not. This was independent of image quality or CAC. This can easily be understood if values fall close to the cut-off and CT-FFR is only measured at a single point in a fixed distance distal to the stenoses (**Figure 4**). However, hemodynamical implications of luminal narrowing can manifest distal to that point of measurement (21). On the other hand, diffuse arteriosclerosis without a distinct stenosis may have a cumulative effect (41) additive to or independent of the stenosis measured. Instead of a single measurement with a fixed cut-off, a relative decrease of CT-FFR values along the coronary tree could perhaps prove more representative for the global hemodynamic situation (21, 41–44) of the coronary arterial vasculature.

4.1. Limitations

Several important limitations to our study must be noted. First, the standard of reference in this study was morphological, not functional with the conservative cut-off of ≥50% diameter on QCA. We explored how discrepancies with a more stringent cut-off would change. But ultimately, a functional standard of reference like invasive FFR would be desirable, particularly in the patient group before TAVR with hemodynamical changes, likely also in coronary artery physiology. Independently of the applied standard, the observed differences in CT-FFR values between the observers are real and likely to be similar in practical application and should be considered whenever performing CT-FFR for clinical decision making. Furthermore, patients before TAVR generally have severe AS with subsequent LV-hypertrophy. As ML-based CT-FFR also considers LV-mass in addition to vessel cross section and specific vessel anatomy for its computation, AS and underling secondary changes may influence computed CT-FFR values. Though different, clinical

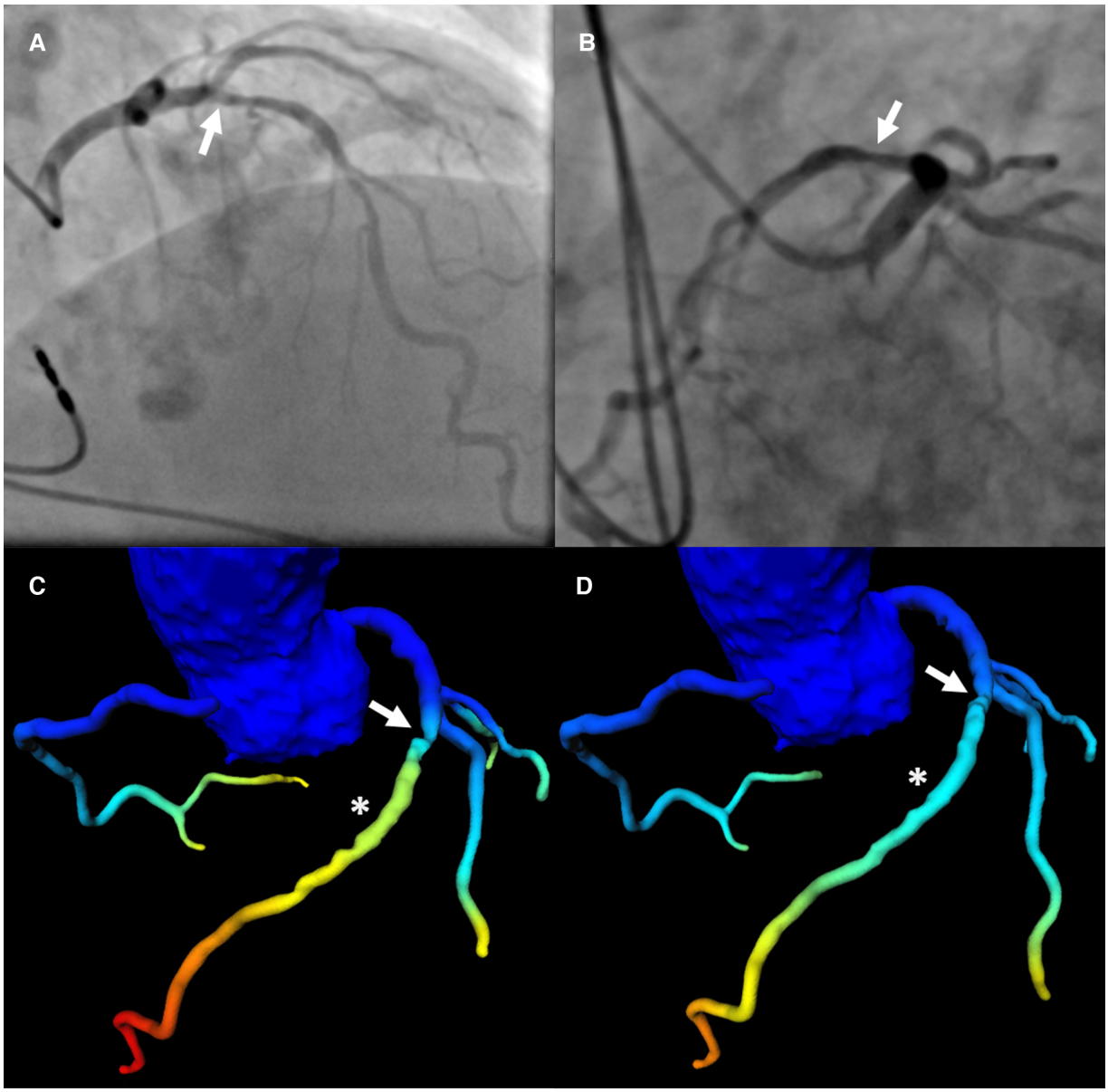

FIGURE 4
Patient with severe LAD stenosis and discrepant categorization according to CT-FFR values. Patient with severe stenosis (arrow in a-d) in the middle LAD (S7) on ICA (QCA: 78%) (**A**,**B**) and results of CT-FFR of observer A (**C**) and observer B (**D**) CT-FFR values were taken approximately 2 cm distal to the stenosis (asterisk in **C**,**D**). The CT-FFR value measured by observer A was 0.79, indicating hemodynamically significant CAD (**C**), the value measured by observer B was 0.86, indicating non-significant CAD (**D**) The threshold for hemodynamically significant CAD was ≤0.80. CAD, coronary artery disease; CT-FFR, CT-derived fractional flow reserve; ICA, invasive coronary angiography; LAD, left anterior descending artery; QCA, quantitative coronary analysis.

experience of both observer A and B was limited and may not reflect clinical practice at academic centers with dedicated experts performing such analysis, it can be assumed that expert observers are more consistent (18, 19). However, so far no data is available about the segmentation process of the commercially available off-site solution. Furthermore, the limited experience of the observers likely amplified the differences in read values, perhaps even allowing for a better evaluation of the potential disturbing factors of image quality and CAC.

5. Conclusion

Measurement of ML-based CT-FFR in patients prior to TAVR by observers with different clinical experience lead to discrepancies in CT-FFR values and CAD categorization, with larger discrepancies in low values and smaller discrepancies in high values. This caused a moderate difference in diagnostic accuracy. Image quality and CAC appear not to influence categorization according to CT-FFR. It seems advisable for segmentation to be

performed by expert observers, particularly when values around the "grey zone" are to be expected.

Data availability statement

The raw data supporting the conclusions of this article will be made available by the authors, without undue reservation.

Ethics statement

The studies involving humans were approved by the local ethics committee of the University of Leipzig (reference number: 435/18-ek). The study was conducted in accordance with the local legislation and institutional requirements. The ethics committee/institutional review board waived the requirement of written informed consent for participation from the participants or the participants' legal guardians/next of kin because of the retrospective design and no identifiable data was being used.

Author contributions

RG: Conceptualization, Data curation, Formal analysis, Investigation, Methodology, Supervision, Writing – original draft, Writing – review & editing. AS: Conceptualization, Data curation, Formal analysis, Investigation, Writing – original draft, Writing – review & editing. KP: Data curation, Investigation, Writing – review & editing. PS: Conceptualization, Data curation, Investigation, Methodology, Writing – review & editing. NM: Investigation, Writing – review & editing. HH: Investigation, Validation, Writing – review & editing. LH: Investigation, Writing – review & editing. KR: Investigation, Writing – review & editing. SD: Investigation, Writing – review & editing. SL: Investigation, Writing – review & editing. TN: Investigation, Writing – review & editing. PK: Investigation, Writing – review & editing. CK: Investigation, Writing – review & editing. SE: Investigation, Writing – review & editing. MB: Writing – review & editing. HT: Investigation, Writing – review & editing. CP: Methodology, Software, Writing – review & editing. MA-W: Data curation, Resources, Validation, Writing – review & editing. MH: Formal analysis, Writing – original draft, Writing – review & editing. MG: Conceptualization, Funding acquisition, Methodology, Project administration, Resources, Software, Supervision, Visualization, Writing – review & editing.

Funding

The author(s) declare financial support was received for the research, authorship, and/or publication of this article.

We acknowledge support from Leipzig University for Open Access Publishing.

Conflict of interest

CP was employed by Siemens Healthcare GmbH.

The remaining authors declare that the research was conducted in the absence of any commercial or financial relationships that could be construed as a potential conflict of interest.

The reviewer JU declared a past co-authorship with the author RFG to the handling editor.

Publisher's note

All claims expressed in this article are solely those of the authors and do not necessarily represent those of their affiliated organizations, or those of the publisher, the editors and the reviewers. Any product that may be evaluated in this article, or claim that may be made by its manufacturer, is not guaranteed or endorsed by the publisher.

References

1. Mack MJ, Leon MB, Thourani VH, Makkar R, Kodali SK, Russo M, et al. Transcatheter aortic-valve replacement with a balloon-expandable valve in low-risk patients. *N Engl J Med*. (2019) 380:1695–705. doi: 10.1056/NEJMOA1814052

2. Popma JJ, Deeb GM, Yakubov SJ, Mumtaz M, Gada H, O'Hair D, et al. Transcatheter aortic-valve replacement with a self-expanding valve in low-risk patients. *N Engl J Med*. (2019) 380:1706–15. doi: 10.1056/NEJMOA1816885

3. Francone M, Budde RPJ, Bremerich J, Dacher JN, Loewe C, Wolf F, et al. CT and MR imaging prior to transcatheter aortic valve implantation: standardisation of scanning protocols, measurements and reporting—a consensus document by the European society of cardiovascular radiology (ESCR). *Eur Radiol*. (2020) 30:2627–50. doi: 10.1007/S00330-019-06357-8

4. Otto CM, Nishimura RA, Bonow RO, Carabello BA, Erwin JP, Gentile F, et al. 2020 ACC/AHA guideline for the management of patients with valvular heart disease: a report of the American college of cardiology/American heart association joint committee on clinical practice guidelines. *J Am Coll Cardiol*. (2021) 77: e25–e197. doi: 10.1016/J.JACC.2020.11.018

5. Grover FL, Vemulapalli S, Carroll JD, Edwards FH, Mack MJ, Thourani VH, et al. 2016 annual report of the society of thoracic surgeons/American college of cardiology transcatheter valve therapy registry. *J Am Coll Cardiol*. (2017) 69:1215–30. doi: 10.1016/J.JACC.2016.11.033

6. Blanke P, Weir-McCall JR, Achenbach S, Delgado V, Hausleiter J, Jilaihawi H, et al. Computed tomography imaging in the context of transcatheter aortic valve implantation (TAVI)/transcatheter aortic valve replacement (TAVR): an expert consensus document of the society of cardiovascular computed tomography. *JACC Cardiovasc Imaging*. (2019) 12:1–24. doi: 10.1016/J.JCMG.2018.12.003

7. Vahanian A, Beyersdorf F, Praz F, Milojevic M, Baldus S, Bauersachs J, et al. 2021 ESC/EACTS guidelines for the management of valvular heart disease. *Eur Heart J*. (2022) 43:561–632. doi: 10.1093/EURHEARTJ/EHAB395

8. Gohmann RF, Lauten P, Seitz P, Krieghoff C, Lücke C, Gottschling S, et al. Combined coronary CT-angiography and TAVI-planning: a contrast-neutral routine approach for ruling-out significant coronary artery disease. *J Clin Med*. (2020) 9:1623. doi: 10.3390/jcm9061623

9. Patel MR, Nørgaard BL, Fairbairn TA, Nieman K, Akasaka T, Berman DS, et al. 1-year impact on medical practice and clinical outcomes of FFRCT: the ADVANCE registry. *JACC Cardiovasc Imaging*. (2020) 13:97–105. doi: 10.1016/J.JCMG.2019.03.003

10. Fairbairn TA, Nieman K, Akasaka T, Nørgaard BL, Berman DS, Raff G, et al. Real-world clinical utility and impact on clinical decision-making of coronary computed tomography angiography-derived fractional flow reserve: lessons from the ADVANCE registry. *Eur Heart J*. (2018) 39:3701–11. doi: 10.1093/EURHEARTJ/EHY530

11. Nørgaard BL, Leipsic J, Gaur S, Seneviratne S, Ko BS, Ito H, et al. Diagnostic performance of noninvasive fractional flow reserve derived from coronary computed tomography angiography in suspected coronary artery disease the NXT trial (analysis of coronary blood flow using CT angiography: next steps). *JACC*. (2014) 63:1145–55. doi: 10.1016/j.jacc.2013.11.043

12. Gutberlet M, Krieghoff C, Gohmann R. Werden die karten der CT-koronarangiographie mit der FFR CT neu gemischt? *Herz*. (2020) 45:431–40. doi: 10.1007/s00059-020-04944-w

13. Gohmann RF, Pawelka K, Seitz P, Majunke N, Heiser L, Renatus K, et al. Combined cCTA and TAVR planning for ruling out significant CAD: added value of ML-based CT-FFR. *JACC Cardiovasc Imaging*. (2022) 15:476–86. doi: 10.1016/J.JCMG.2021.09.013

14. Brown AJ, Michail M, Ihdayhid A-R, Comella A, Thakur U, Cameron JD, et al. Circulation: cardiovascular interventions feasibility and validity of computed tomography-derived fractional flow reserve in patients with severe aortic stenosis the CAST-FFR study. *Circ Cardiovasc Interv*. (2021) 14:9586. doi: 10.1161/CIRCINTERVENTIONS.120.009586

15. Hamdan A, Wellnhofer E, Konen E, Kelle S, Goitein O, Andrada B, et al. Coronary CT angiography for the detection of coronary artery stenosis in patients referred for transcatheter aortic valve replacement. *J Cardiovasc Comput Tomogr*. (2015) 9:31–41. doi: 10.1016/j.jcct.2014.11.008

16. Peper J, Becker LM, van den Berg H, Bor WL, Brouwer J, Nijenhuis VJ, et al. Diagnostic performance of CCTA and CT-FFR for the detection of CAD in TAVR work-up. *JACC Cardiovasc Interv*. (2022) 15:1140–9. doi: 10.1016/J.JCIN.2022.03.025

17. Coenen A, Kim Y-H, Kruk M, Tesche C, de Geer J, Kurata A, et al. Diagnostic accuracy of a machine-learning approach to coronary computed tomographic angiography–based fractional flow reserve. *Circ Cardiovasc Imaging*. (2018) 11:1–11. doi: 10.1161/CIRCIMAGING.117.007217

18. Donnelly PM, Kolossváry M, Karády J, Ball PA, Kelly S, Fitzsimons D, et al. Experience with an on-site coronary computed tomography-derived fractional flow reserve algorithm for the assessment of intermediate coronary stenoses. *Am J Cardiol*. (2018) 121:9–13. doi: 10.1016/J.AMJCARD.2017.09.018

19. Yang DH, Kim YH, Roh JH, Kang JW, Ahn JM, Kweon J, et al. Diagnostic performance of on-site CT-derived fractional flow reserve versus CT perfusion. *Eur Heart J Cardiovasc Imaging*. (2017) 18:432–40. doi: 10.1093/ehjci/jew094

20. Leipsic J, Abbara S, Achenbach S, Cury R, Earls JP, Mancini GJ, et al. SCCT guidelines for the interpretation and reporting of coronary CT angiography: a report of the society of cardiovascular computed tomography guidelines committee. *J Cardiovasc Comput Tomogr*. (2014) 8:342–58. doi: 10.1016/j.jcct.2014.07.003

21. Nørgaard BL, Fairbairn TA, Safian RD, Rabbat MG, Ko B, Jensen JM, et al. Coronary CT angiography-derived fractional flow reserve testing in patients with stable coronary artery disease: recommendations on interpretation and reporting. *Radiol Cardiothorac Imaging*. (2019) 1:e190050. doi: 10.1148/ryct.2019190050

22. Itu L, Rapaka S, Passerini T, Georgescu B, Schwemmer C, Schoebinger M, et al. A machine-learning approach for computation of fractional flow reserve from coronary computed tomography. *J Appl Physiol*. (2016) 121:42–52. doi: 10.1152/japplphysiol.00752.2015.-Frac

23. Chinnaiyan KM, Akasaka T, Amano T, Bax JJ, Blanke P, De Bruyne B, et al. Rationale, design and goals of the HeartFlow assessing diagnostic value of non-invasive FFRCT in coronary care (ADVANCE) registry. *J Cardiovasc Comput Tomogr*. (2017) 11:62–7. doi: 10.1016/J.JCCT.2016.12.002

24. Kottner J, Audigé L, Brorson S, Donner A, Gajewski BJ, Hróbjartsson A, et al. Guidelines for reporting reliability and agreement studies (GRRAS) were proposed. *J Clin Epidemiol*. (2011) 64:96–106. doi: 10.1016/J.JCLINEPI.2010.03.002

25. Shrout PE, Fleiss JL. Intraclass correlations: uses in assessing rater reliability. *Psychol Bull*. (1979) 86:420–8. doi: 10.1037//0033-2909.86.2.420

26. Cicchetti DV. Guidelines, criteria, and rules of thumb for evaluating normed and standardized assessment instruments in psychology. *Psychol Assess*. (1994) 6:284–90. doi: 10.1037/1040-3590.6.4.284

27. Landis JR, Koch GG. The measurement of observer agreement for categorical data. *Biometrics*. (1977) 33:159. doi: 10.2307/2529310

28. Tang CX, Liu CY, Lu MJ, Schoepf UJ, Tesche C, Bayer RR, et al. CT FFR for ischemia-specific CAD with a new computational fluid dynamics algorithm: a Chinese multicenter study. *JACC Cardiovasc Imaging*. (2020) 13:980–90. doi: 10.1016/j.jcmg.2019.06.018

29. Brandt V, Schoepf UJ, Aquino GJ, Bekeredjian R, Varga-Szemes A, Emrich T, et al. Impact of machine-learning-based coronary computed tomography angiography-derived fractional flow reserve on decision-making in patients with severe aortic stenosis undergoing transcatheter aortic valve replacement. *Eur Radiol*. (2022) 32:6008–16. doi: 10.1007/S00330-022-08758-8

30. van Hamersvelt RW, Voskuil M, de Jong PA, Willemink MJ, Išgum I, Leiner T. Diagnostic performance of on-site coronary CT angiography–derived fractional flow reserve based on patient-specific lumped parameter models. *Radiol Cardiothorac Imaging*. (2019) 1:1–9. doi: 10.1148/ryct.2019190036

31. Fujii Y, Kitagawa T, Ikenaga H, Tatsugami F, Awai K, Nakano Y. The reliability and utility of on-site CT-derived fractional flow reserve (FFR) based on fluid structure interactions: comparison with FFRCT based on computational fluid dynamics, invasive FFR, and resting full-cycle ratio. *Heart Vessels*. (2023) 38(9):1095–107. doi: 10.1007/S00380-023-02265-6

32. Ihdayhid AR, Sakaguchi T, Kerrisk B, Hislop-Jambrich J, Fujisawa Y, Nerlekar N, et al. Influence of operator expertise and coronary luminal segmentation technique on diagnostic performance, precision and reproducibility of reduced-order CT-derived fractional flow reserve technique. *J Cardiovasc Comput Tomogr*. (2020) 14:356–62. doi: 10.1016/J.JCCT.2019.11.014

33. Kumamaru KK, Angel E, Sommer KN, Iyer V, Wilson MF, Agrawal N, et al. Inter- and intraoperator variability in measurement of on-site CT-derived fractional flow reserve based on structural and fluid analysis: a comprehensive analysis. *Radiol Cardiothorac Imaging*. (2019) 1:1–7. doi: 10.1148/RYCT.2019180012

34. Ko BS, Cameron JD, Munnur RK, Wong DTL, Fujisawa Y, Sakaguchi T, et al. Noninvasive CT-derived FFR based on structural and fluid analysis: a comparison with invasive FFR for detection of functionally significant stenosis. *JACC Cardiovasc Imaging*. (2017) 10:663–73. doi: 10.1016/J.JCMG.2016.07.005

35. Nicol ED, Stirrup J, Roughton M, Padley SPG, Rubens MB. 64-channel cardiac computed tomography: intraobserver and interobserver variability (part 1): coronary angiography. *J Comput Assist Tomogr*. (2009) 33:161–8. doi: 10.1097/RCT.0B013E31817C423E

36. Kerl JM, Schoepf UJ, Bauer RW, Tekin T, Costello P, Vogl TJ, et al. 64-slice multidetector-row computed tomography in the diagnosis of coronary artery disease: interobserver agreement among radiologists with varied levels of experience on a per-patient and per-segment basis. *J Thorac Imaging*. (2012) 27:29–35. doi: 10.1097/RTI.0B013E3181F82805

37. Murphy ML, Galbraith JE, de Soyza N. The reliability of coronary angiogram interpretation: an angiographic-pathologic correlation with a comparison of radiographic views. *Am Heart J*. (1979) 97:578–84. doi: 10.1016/0002-8703(79)90184-4

38. Achenbach S, Ropers D, Holle J, Muschiol G, Daniel WC, Moshage W. In-plane coronary arterial motion velocity: measurement with electron-beam CT. *Radiology*. (2000) 216:457–63. doi: 10.1148/RADIOLOGY.216.2.R00AU19457

39. Leipsic J, Yang TH, Thompson A, Koo BK, John Mancini GB, Taylor C, et al. CT angiography (CTA) and diagnostic performance of noninvasive fractional flow reserve: results from the determination of fractional flow reserve by anatomic CTA (DeFACTO) study. *Am J Roentgenol*. (2014) 202:989–94. doi: 10.2214/AJR.13.11441

40. Tesche C, Otani K, De Cecco CN, Coenen A, De Geer J, Kruk M, et al. Influence of coronary calcium on diagnostic performance of machine learning CT-FFR: results from MACHINE registry. *JACC Cardiovasc Imaging*. (2020) 13:760–70. doi: 10.1016/J.JCMG.2019.06.027

41. Takagi H, Ishikawa Y, Orii M, Ota H, Niiyama M, Tanaka R, et al. Optimized interpretation of fractional flow reserve derived from computed tomography: comparison of three interpretation methods. *J Cardiovasc Comput Tomogr*. (2019) 13:134–41. doi: 10.1016/J.JCCT.2018.10.027

42. Cami E, Tagami T, Raff G, Fonte TA, Renard B, Gallagher MJ, et al. Assessment of lesion-specific ischemia using fractional flow reserve (FFR) profiles derived from coronary computed tomography angiography (FFRCT) and invasive pressure measurements (FFRINV): importance of the site of measurement and implications for patient referral for invasive coronary angiography and percutaneous coronary intervention. *J Cardiovasc Comput Tomogr*. (2018) 12:480–92. doi: 10.1016/J.JCCT.2018.09.003

43. Gohmann RF, Seitz P, Pawelka K, Majunke N, Schug A, Heiser L, et al. Clinical medicine combined coronary CT-angiography and TAVI planning: utility of CT-FFR in patients with morphologically ruled-out obstructive coronary artery disease. *J Clin Med*. (2022) 11:1331–44. doi: 10.3390/jcm11051331

44. Iwasaki K, Kusachi S. Coronary pressure measurement based decision making for percutaneous coronary intervention. *Curr Cardiol Rev*. (2009) 5:323. doi: 10.2174/157340309789317832

10.3389/fcvm.2023.1301619

Appendix

TABLE 1 Difference in CAD categorizations between observers.

Level of observation		*n*	MM (%)	95% CI (%)
Patient		214	17.3	12.8, 22.9
Vessel	RCA	115	20.9	14.4, 29.2
	LM	13	7.7	1.4, 33.3
	LAD	177	23.2	17.6, 29.9
	LCX	114	38.6	30.2, 47.8
Segment	1	59	23.7	14.7, 36.0
	2	59	20.3	12.0, 32.3
	3	42	28.6	17.2, 43.6
	4	18	5.6	1.0, 25.8
	16	8	25.0	7.1, 59.1
	5	13	7.7	1.4, 33.3
	6	56	25.0	15.5, 37.7
	7	20	45.0	25.8, 65.8
	8	123	28.5	21.2, 37.0
	9	42	19.0	10.0, 33.0
	10	53	41.5	29.3, 54.9
	17	22	31.8	16.4, 52.7
	11	62	40.3	29.0, 52.7
	12	50	40.0	27.6, 53.8
	13	33	36.4	22.2, 53.4
	14	12	33.3	13.8, 60.9
	15	1	0.0	0.0, 79.3
	18	0	–	–

Rate of recategorization on patient, vessel and segment level and corresponding 95% CI. CI, confidence interval; LAD, left anterior descending artery; LM, left main coronary artery; LCX, circumflex artery; MM, mismatched coronary artery disease categorization; RCA, right coronary artery.

frontiers | Frontiers in Cardiovascular Medicine

TYPE Original Research
PUBLISHED 05 January 2024
DOI 10.3389/fcvm.2023.1305526

Check for updates

OPEN ACCESS

EDITED BY
Hitomi Anzai,
Tohoku University, Japan

REVIEWED BY
Kenichiro Suwa,
Hamamatsu University School of Medicine, Japan
Mingzi Zhang,
Macquarie University, Australia

*CORRESPONDENCE
Tomohiro Otani
otani.tomohiro.es@osaka-u.ac.jp

RECEIVED 01 October 2023
ACCEPTED 15 December 2023
PUBLISHED 05 January 2024

CITATION
Yi W, Otani T, Endo S and Wada S (2024) Do blood flow patterns in the left atriums differ between left upper lobectomy and other lobectomies? A computational study. Front. Cardiovasc. Med. 10:1305526. doi: 10.3389/fcvm.2023.1305526

COPYRIGHT
© 2024 Yi, Otani, Endo and Wada. This is an open-access article distributed under the terms of the Creative Commons Attribution License (CC BY). The use, distribution or reproduction in other forums is permitted, provided the original author(s) and the copyright owner(s) are credited and that the original publication in this journal is cited, in accordance with accepted academic practice. No use, distribution or reproduction is permitted which does not comply with these terms.

Do blood flow patterns in the left atriums differ between left upper lobectomy and other lobectomies? A computational study

Wentao Yi[1], Tomohiro Otani[1]*, Shunsuke Endo[2] and Shigeo Wada[1]

[1]Department of Mechanical Science and Bioengineering, Graduate School of Engineering Science, Osaka University, Osaka, Japan, [2]Saitama Medical Center, Jichi Medical University, Saitama, Japan

Background: Left atrial (LA) hemodynamics after lung lobectomies with pulmonary vein (PV) resection is widely understood to be a risk factor for LA thrombosis. A recent magnetic resonance imaging study showed that left upper lobectomy (LUL) with left superior pulmonary vein resection tended to cause LA flow patterns distinct from those of other lobectomies, with flow disturbances seen near the PV stump. However, little is known about this flow pattern because of severe image resolution limitations. The present study compared flow patterns in the LA after LUL with the flow patterns of other lobectomies using computational simulations.
Methods: The computational simulations of LA blood flow were conducted on the basis of four-dimensional computed tomography images of four lung cancer patients prior to lobectomies. Four kinds of PV resection cases were constructed by cutting each one of the PVs from the LA of each patient. We performed a total of five cases (pre-resection case and four PV resection cases) in each patient and evaluated global flow patterns formed by the remaining PV inflow, especially in the upper LA region.
Results: LUL tended to enhance the remaining left inferior PV inflow, with impingements seen in the right PV inflows in the upper LA region near the PV stump. These flow alterations induced viscous dissipation and the LUL cases had the highest values compared to other PV resection cases, especially in the LV systole in three patients, and reached three to four times higher than those in pre-resection cases. However, in another patient, these tendencies were weaker when PV inflow was stronger from the right side than from the left side, and the degree of flow dissipation was lower than those in other PV resection cases.
Conclusion: These findings suggest marked variations in LA flow patterns among patients after lobectomies and highlights the importance of patient-specific assessment of LA hemodynamics after lobectomies.

KEYWORDS

left atrium, lobectomy, pulmonary vein, computational fluid dynamics, hemodynamics

1 Introduction

Left atrial (LA) thrombosis has received much attention as a cause of cerebral infarction. Although LA thrombosis is thought to occur in pathological conditions such as LA fibrillation (1), recent cohort studies have shown that lung lobectomy, which is a common surgical treatment for lung cancer patients (2), is a significant risk factor for

LA thrombosis even in patients with no prior history of cardiac disease (3–5). A lobectomy requires an associated pulmonary vein (PV) resection from the LA and thrombus formation in the PV stump, where the remaining PV resected, was reported for 3.6% of 193 patients (6). Several potential factors of thrombus formation have been proposed such as LA hemodynamic alteration (7–11), PV stump morphologies (7), and inflammatory responses (12). However, thrombus formation after lobectomy is rare (approximately 5% of LUL cases (5)), and the mechanism of the thrombosis in the PV stump therefore remains unclear.

Furthermore, several clinical studies reported that left upper lobectomy (LUL) with left superior PV (LSPV) resection has a relatively high risk of thrombus formation (5, 6, 13), while this causal mechanism is unknown. To clarify the characteristic differences of the LUL from viewpoints of LA hemodynamics, Umehara et al. (14) compared LA flow patterns among four types of lobectomies, i.e., LUL and left-lower, right-upper, and right-lower lobectomies regardless of the thrombus formation by four-dimensional flow magnetic resonance imaging (MRI). They reported that LUL likely caused flow disturbances around the LSPV stump, which was absent in almost all cases treated with the other types of lobectomies. However, these findings were based on flow pathlines derived from flow velocity fields on MRI scans with severely limited spatiotemporal resolution. These LA flow patterns were variable and complex, characterized by multiple intermixing PV inflows, and little is known about them given the limited MRI data.

To address this issue, computational fluid dynamics (CFD) simulation of LA hemodynamics is a promising approach to describe flow patterns after lobectomies and associated PV resections. We previously investigated the possible effects of LUL (15) and associated physiological changes (16) on LA hemodynamics, and found remarkable LA flow changes associated with left and right PV inflow impingement after LUL. Because the computational approach can represent lobectomies with PV resection virtually in each patient, CFD simulations of LA hemodynamics with virtual PV resection could reveal the distinctive LA flow patterns after LUL implied by MRI studies through comparison with those after other lobectomies.

This study investigated LA flow patterns after different types of lobectomies using four-dimensional computed tomography (4D-CT)-based computational simulations and analyzed distinctive flow patterns after LUL. Following CFD simulation of LA blood flow and virtual PV resections, as developed in our previous study (16), we compared LA blood flow patterns before and after PV resection in four patients.

2 Material and methods

This study conducted CFD simulations of LA hemodynamics using 4D-CT images of four lung cancer patients before lobectomy. They received an LUL at the Department of Thoracic and Cardiovascular Surgery at Jichi Medical University Hospital. Thrombus formation in the PV stump was not found for each patient after the LUL. CT images were acquired in previous studies (15, 16). The study was approved by the Institutional Review Board of Jichi Medical University.

2.1 Preprocessing

First, 4D-CT images of four lung cancer patients (participants 1–4) were obtained using a 128-slice multi-detector CT scanner (SOMATOM Definition Flash; Siemens, Berlin, Germany) at Jichi Medical University Hospital and reconstructed over 20 phases of the cardiac cycle from ventricular end-diastole. The cardiac length T in each participant was shown in Table 1.

LA surface shapes in each phase were reconstructed using Mimics software (version 23; Materialise, Inc., Yokohama, Japan), in which cuts were made in proximal parts of the PVs before the first bifurcation, where the PV cross section was orthogonal to the PV direction. Figure 1 shows a representative LA surface (a) and time courses of the LA and left ventricle (LV) volume in each participant (b). The PV cross-sectional area is shown in Table 1. In each patient, the cross-sectional areas of the left and right superior PVs (LSPV and RSPV, respectively) tended to be larger than those of the left and right inferior PVs (LIPV and RIPV, respectively), except for the LSPV in participant 4.

LA wall displacements in a cardiac cycle were estimated from non-rigid point registration (17, 18) and temporally interpolated by Fourier series expansion. Cylindrical tubes were attached to sections of the PVs and mitral valve (MV) to reduce the effects of artificially set boundary conditions on LA blood flow (19). Furthermore, the time courses of LV volume were interpolated using Fourier series expansion to compute the total flow rate through the MV in LV diastole.

2.1.1 Virtual PV resection

To compare LA blood flow patterns with different PV resections, each PV resection case was constructed for each subject, as shown in Figure 2. Each one of the PVs was cut and smoothly filling the incision to form a stump-like structure as in Yi et al. (16). Consequently, a total of five cases (one pre-cases and four PV-resection cases) was prepared in each participant.

2.2 Computational fluid dynamics simulation

In the CFD simulations, LA blood flow was treated as a prescribed moving-wall boundary problem using moving LA

TABLE 1 Participant information: cardiac length T (ms) and cross-sectional area (mm^2) of each pulmonary vein (PV) in each participant (left superior PV: LSPV, left inferior PV: LIPV, right superior PV: RSPV, right inferior PV: RIPV).

	Cardiac cycle (ms)	Cross-sectional area (mm^2)			
		LSPV	LIPV	RSPV	RIPV
Subject 1	870	211	97.2	194	212
Subject 2	920	271	225	271	145
Subject 3	1000	180	116	196	145
Subject 4	984	95.3	171	175	135

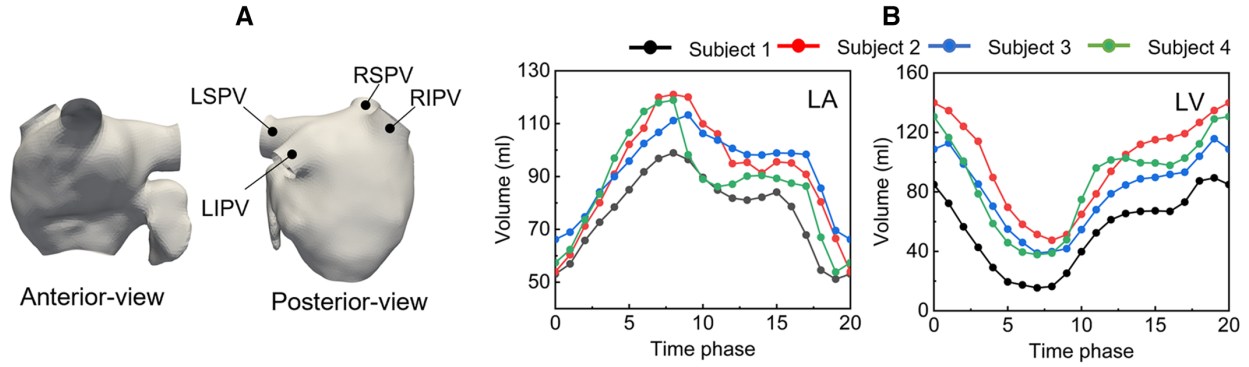

FIGURE 1
Representative left atrium surface (anterior and posterior views) of participant 1 at phase 9(a), and time courses of the left atrium and left ventricle volume (b).

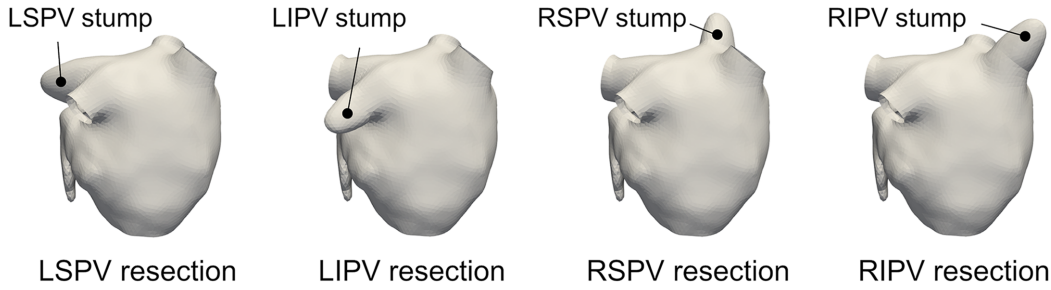

FIGURE 2
Representative left atrium surfaces with virtual pulmonary vein (PV) resections of the left-superior (LS), left-inferior (LI), right-superior (RS), and right-inferior (RI) PVs for participant 1.

surfaces. The simulations were performed using a Cartesian grid CFD solver developed in (15, 20). Blood was assumed to be an incompressible Newtonian fluid, and continuity and incompressible Navier-Stokes equations were adopted to yield the governing equation:

$$\nabla \cdot \mathbf{v} = 0, \tag{1}$$

$$\rho(\partial_t \mathbf{v} + \mathbf{v} \cdot \nabla \mathbf{v}) = -\nabla p + \eta \nabla^2 \mathbf{v}, \tag{2}$$

where $\mathbf{v}$ is the velocity vector, p is pressure, blood density $\rho = 1.05 \times 10^3$ kg/m^3, and dynamic viscosity $\eta = 3.5 \times 10^{-3}$ Pa·s. Governing equations are discretized using the finite difference method in conventional staggered grids, and flow velocities and pressure are updated in a step-by-step manner. For details of the computational schemes and spatiotemporal discretization, please see our previous work (15).

The boundary conditions are as follows. The no-slip boundary condition was assigned on the wall boundary using the boundary data immersion method (21). The MV was assumed to be a wall boundary when it was closed during LV systole, whereas a uniform transient velocity profile was set at the MV when the MV opened during LV diastole. The MV flow rate profile was determined by the time course of the LV volume change shown in Figure 1B. On each PV cross-section, we applied uniform pressure boundary conditions of pressure P_{PV}, expressed as $P_{PV} = P_0 + K_i Q_{PV}$, where P_0 is the baseline, K_i is the terminal resistance at each PV, and Q_{PV} is the flux through the PV cross section. We set $P_0 = 0$ Pa and K_i to be inversely proportional to the corresponding cross-sectional area of each PV, assuming that the velocity was the same for all PVs (22).

The computational domain was discretized as uniform Cartesian grids of $256 \times 256 \times 256$, where the grid size was 0.6 mm in each direction in accordance with a test of grid size dependencies conducted in our previous study (15). The time increment was chosen to ensure that the Courant–Friedrichs–Lewy number was less than 0.1. Each computational simulation was conducted over three cardiac cycles, and the Results section shows the solution in the third cycle unless otherwise noted.

2.3 Postprocessing

To clarify the global LA blood flow pattern in each PV resection case from a fluid mechanical sense, we adopted Lagrange-based flow descriptors which extract flow characteristics

from flow velocity fields. First, the flow pathline from $0T$ to $0.35T$ was depicted by mass-less tracers $\mathbf{x}_p$ set in each PV section before PV resection to confirm the PV inflow directions. Next, backward finite-time Lyapunov exponents (FTLEs) in the cross-sectional plane of the upper LA region were visualized in all cases to capture PV inflow before and after each PV resection. The backward FTLE can be understood as Lagrange coherent structure, which is locally the most strongly attracting material surface (i.e., flow boundaries) according to dynamical systems theory (23, 24), and thus is effective in quantifying complex LA flow topologies created by multiple PV inflows. The FTLEs were computed from the flow map $\phi_{t_0}^{t_0+\tau}: \mathbf{x}_p(t_0) \Rightarrow \mathbf{x}_p(t_0+\tau)$ with respect to mass-less tracers at initial time t_0 by solving the advection in the LA blood flow in finite time τ (23), given by

$$\mathrm{FTLE} = \frac{1}{|\tau|} \ln \left\| \frac{\partial \phi_{t_0}^{t_0+\tau}}{\partial \mathbf{x}} \right\|_2. \tag{3}$$

Here, We adopted $\tau = 50$ ms. For negative τ (<0), the FTLE ridges show directions of high flow stretching, known as attracting Lagrange coherent structure. Trajectories of mass-less tracers were computed by fourth-order Runge-Kutta method, and flow velocity fields were linearly interpolated in space and time in each grid.

Furthermore, global flow characteristics in the LA were evaluated on the basis of the flow kinetic energy and dissipation rate, given by

$$\text{Kinetic energy} = \int_{\Omega_f} \frac{1}{2} \rho(\mathbf{v} \cdot \mathbf{v}) d\Omega, \tag{4}$$

$$\text{Dissipation rate} = \int_{\Omega_f} 2\eta \mathbf{S} : \mathbf{S} d\Omega, \tag{5}$$

where Ω_f is the LA domain and $\mathbf{S}$ indicates the symmetric components of $\nabla \mathbf{v}$.

3 Results

3.1 Flow pathlines

Figure 3 shows representative flow pathlines of participant 2 before the lobectomies. LSPV inflow entered along the LA roof and LIPV inflows entered underneath the LSPV inflow. The inflows from the right PVs flowed directly into the inferior region of the LA, almost in parallel. These characteristics were also observed in other participants.

The flow pathlines in each virtual PV resection are shown in Figure 4. In LSPV resections, LIPV inflows entered directly, flowed toward the anterior LA wall, and impinged on the RSPV inflows. In RSPV resections, LSPV inflows also reached the right side of the LA and flowed downward. The changes in the remaining inflow patterns were relatively small in LIPV and RIPV resections.

3.2 Backward finite-time Lyapunov exponents

Figure 5 shows the backward FTLEs in the cross-sectional plane of the upper LA regions before PV resection, as well as each PV resection at end-systole ($t = 0.35T$) and early-diastole ($t = 0.55T$). Supplementary Video 1 shows time courses of FTLEs in all virtual PV resection cases over one cardiac cycle. Here, boundaries between PV inflows are shown in a high-FTLE region (attracting Lagrange coherent structure). In the LSPV resection, flow impingement was found between LIPV and RSPV inflows, and flow disturbances occurred near the LSPV stump. In the RSPV resection, the LSPV inflows reached the right side of the LA, while flow impingement was not found in the upper LA region and flow in the RSPV stump was isolated. In LIPV and RIPV resections, FTLE distributions generated by remaining PV inflows were almost the same as those in pre-resection cases.

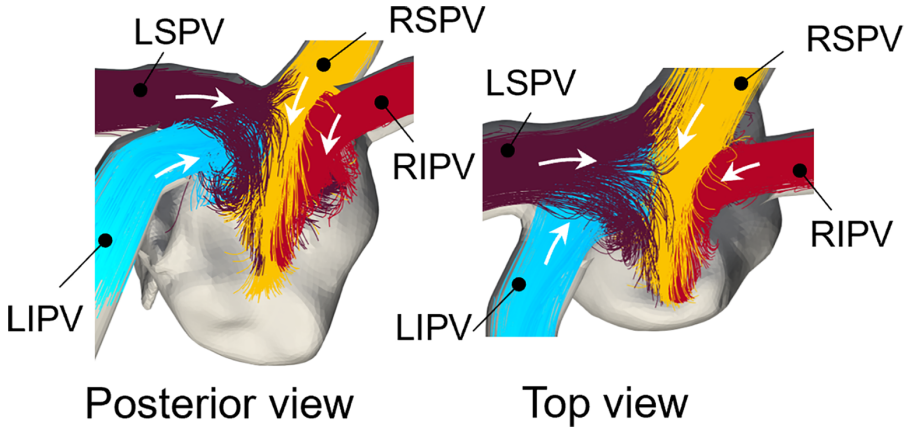

FIGURE 3
Representative pre-resection flow pathlines from $0T$ to $0.35T$ for participant 2 (LSPV: left superior pulmonary vein, LIPV: Left inferior pulmonary vein, RSPV: right superior pulmonary vein, RIPV: right inferior pulmonary vein). Colors of pathlines show each PV inflow and white arrows show the inflow direction from the pulmonary veins.

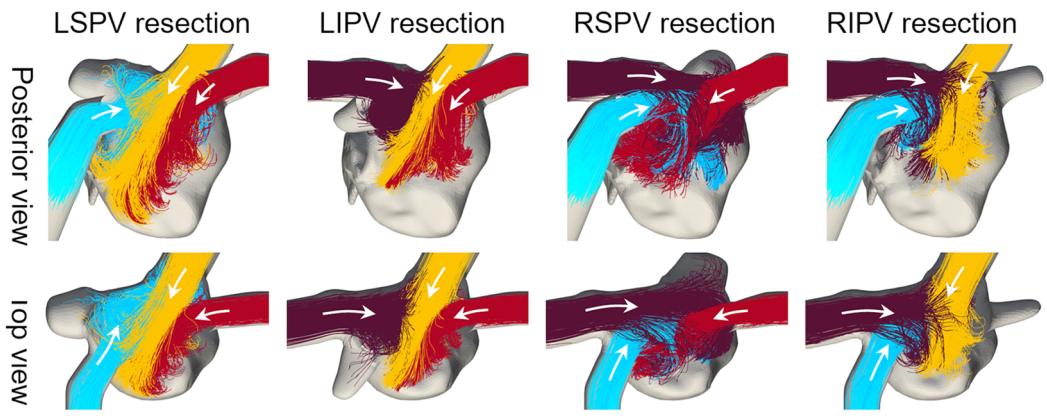

FIGURE 4
Same as Figure 3, but in cases with virtual PV resections.

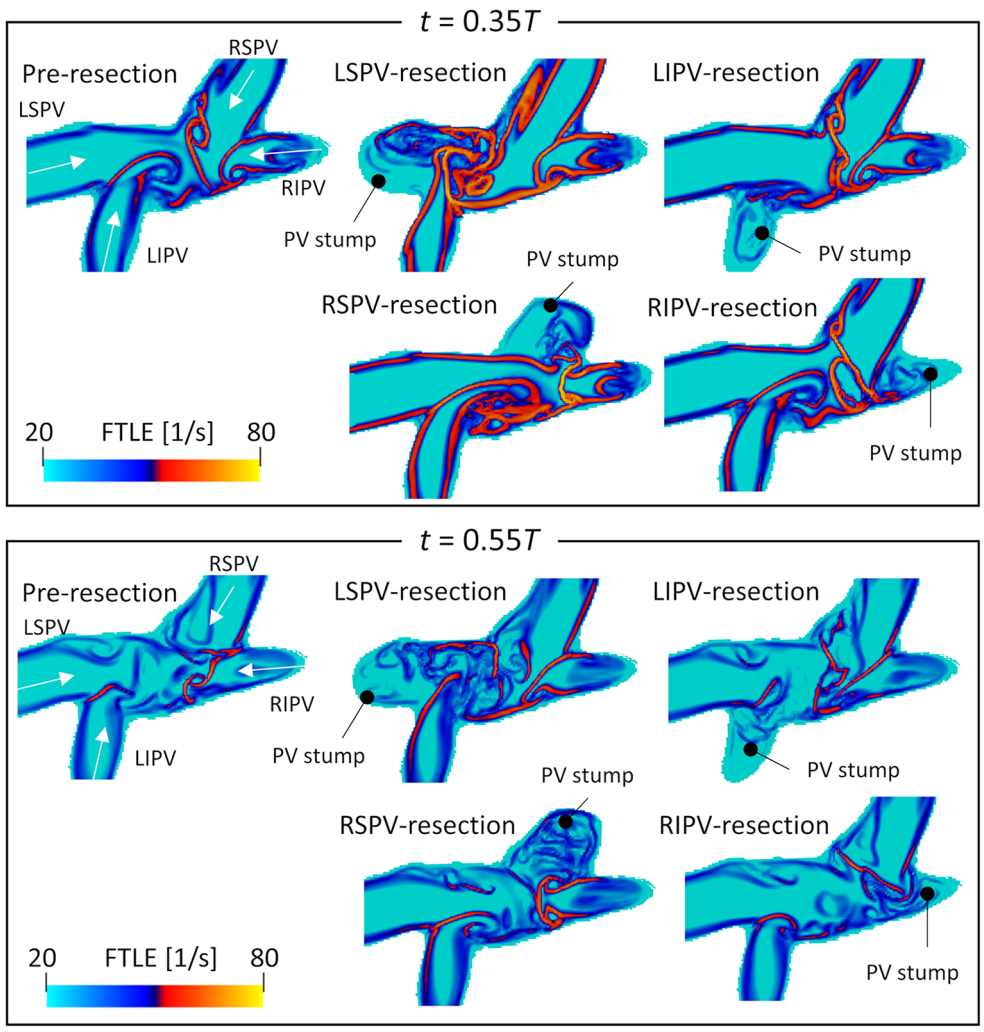

FIGURE 5
Spatial distribution of the backward finite-time Lyapunov exponent on the cross-sectional plane of the left atrial upper region, at $t = 0.35T$ (systole) and $t = 0.55T$ (diastole) in participant 2 before PV resection (LSPV, left superior pulmonary vein; LIPV, left inferior pulmonary vein; RSPV, right superior pulmonary vein; RIPV, right inferior pulmonary vein). Representative PV resection cases are also shown. These time courses are shown in a whole cardiac cycle in Supplementary Video 1.

Figure 6 shows the backward FTLE distribution in participant 4 at end-systole ($t = 0.35T$) and early-diastole ($t = 0.55T$). Both LSPV and LIPV resection caused flow disturbances in the center region, whereas the flow boundaries of the right PV inflows were almost the same as the pre-resection ones. Conversely, RSPV resection enhanced the RIPV inflows, which extended to the anterior side of the LA. Similarly, in the RIPV resection case, RSPV inflows entered the posterior side of the LA.

3.3 Global energetic states

Figure 7 shows time courses of the flow kinetic energy and dissipation rate in the LA before and after each PV resection in each participant. Overall, the kinetic energy and dissipation rate in a whole cardiac cycle showed similar trends in pre-resection and PV resection cases, while in PV resection cases they were relatively larger than the pre-resection ones in all participants. The kinetic energy had three local maximum peaks at mid-systole, early to mid-diastole, and late diastole. In participants 1–3, the kinetic energy increased moderately during the LV systole phase and reached at most 3 mJ in all participants, whereas those in the LSPV resection cases showed the highest values at systole peak compared to other PV resection cases (approximately two to three folds higher than those in pre-resection cases). Also, the dissipation rate in the LV systole phase was almost constant in pre-resection cases (at most 3 mJ/s), whereas those in the LSPV resection case had the highest values at the systolic peak and approached three to four folds higher than those in pre-resection case. On the contrary, the values for LSPV were lower than those for the other PV resections in participant 4, for whom RSPV showed the greatest flow dissipation during a cardiac cycle.

4 Discussion

The effect of LUL on LA hemodynamics has received much attention because of its association with LA thrombosis (5, 7). A recent MRI study pointed out the distinctive blood flow patterns in the LA after LUL compared with other lobectomies regardless of thrombus formation (14), but detailed flow characteristics remain elusive because of severe image resolution limitations. Therefore, this study conducted CFD simulations with virtual PV resections and analyzed the resulting LA blood flow patterns.

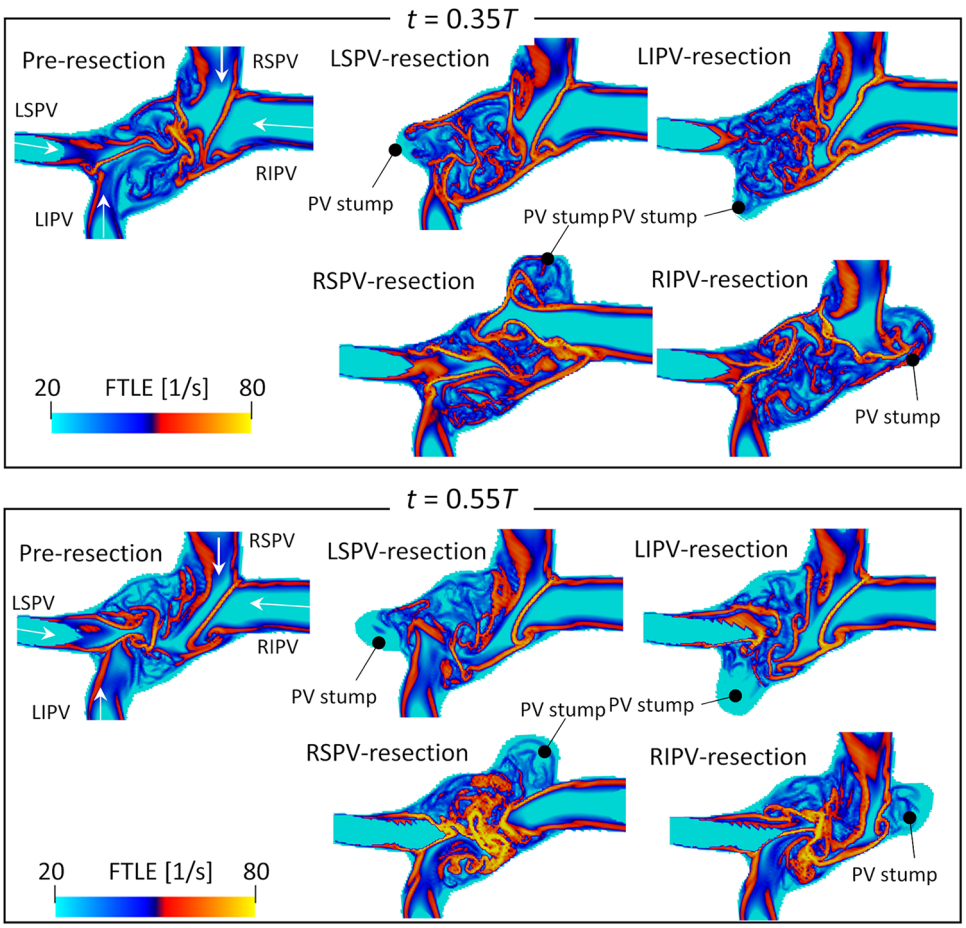

FIGURE 6
Same as Figure 5 but for participant 4.

10.3389/fcvm.2023.1305526

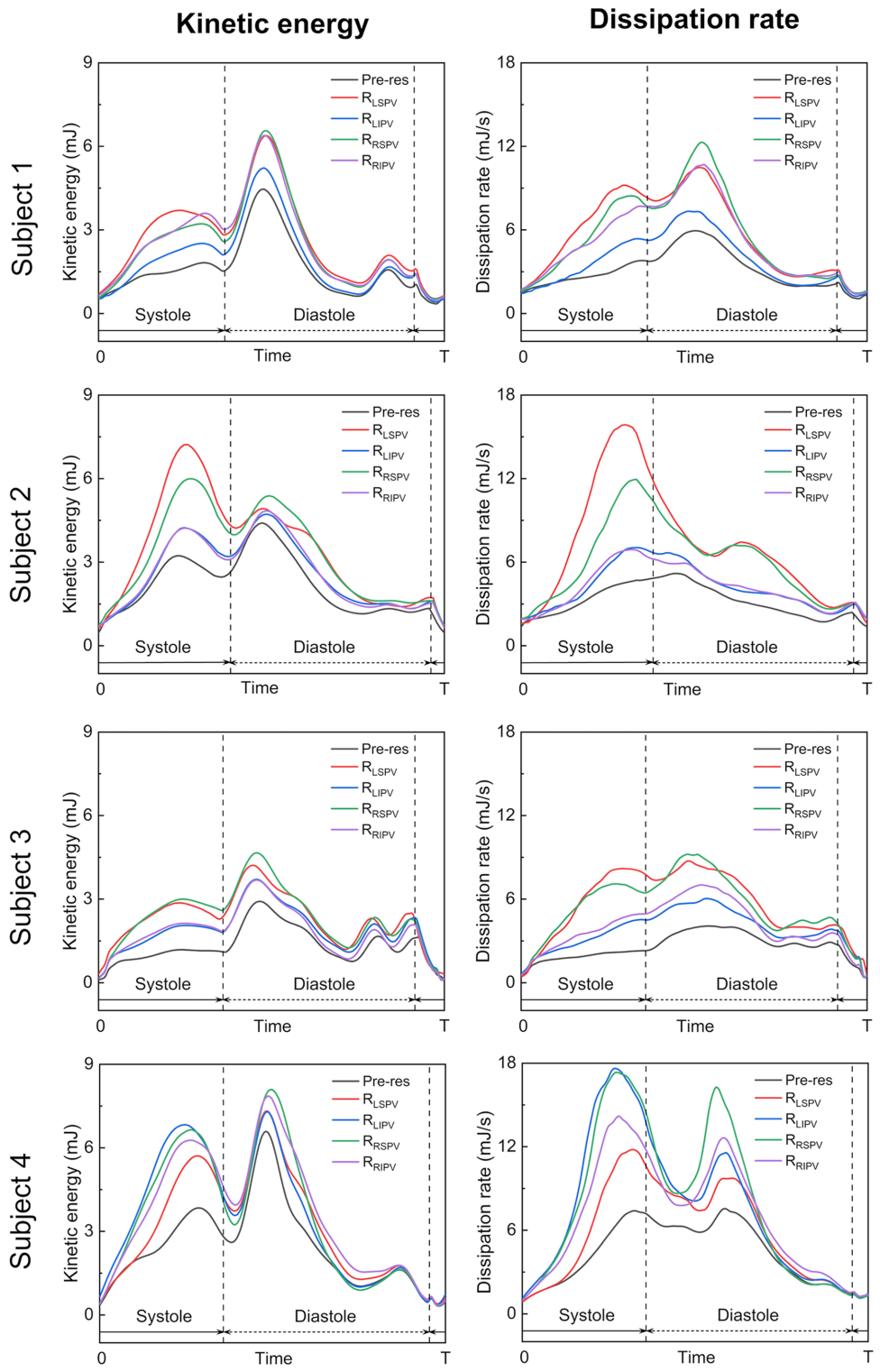

FIGURE 7
Time courses of the flow kinetic energy (left) and dissipation rate (right) in the left atrium over a whole cardiac cycle in the pre-resection case (Pre-res), left superior pulmonary vein (LSPV) resection case (RLSPV), left inferior pulmonary vein (LIPV) resection case (RLIPV), right superior pulmonary vein (RSPV) resection case (RRSPV), and right inferior pulmonary vein (RIPV) resection case (RRIPV), in each participant.

The blood flow pattern in the LA for each PV resection was visualized using Lagrange descriptors, especially in the upper region of the LA, and the global energetic states were calculated. Before PV resection, the left PV inflow was horizontal and flowed toward the right side of the LA without impingement, whereas both right PV inflows flowed downward in parallel

(Figure 3). This asymmetric flow pattern is well known, being shown by existing measurements (25, 26) and CFD simulations (27). As a representative case, in participant 2 in this study, LSPV resection increased LIPV inflow, and the LIPV reached the anterior LA wall with impingement of the right PV inflows causing flow disturbances around the LPSV stump (Figure 5). In contrast, the RSPV resection also enhanced the remaining LSPV inflow, while flow disturbances in the upper LA region were relatively weak, and the effects of LIPV and RIPV resections on the global LA flow patterns were small. These tendencies were also reflected in the global energetic states as relatively strong flow dissipation (Figure 7) in participants 1–3, and these findings are consistent with the clinical observation that LSPV resection tends to form distinctive flow patterns with flow disturbances occurring near the PV stump (14). Because these flow patterns may be induced by asymmetric LA flow patterns originating from anatomically complex LA geometries (25), the LA blood flow alteration after LUL noted above is likely typical in clinical datasets.

However, LA and PV geometries varied markedly among patients, and thus the resulting blood flow patterns also had large variations, as seen in participant 4 in this study. In this case, the LSPV cross-sectional area was the smallest among all PVs (Table 1), and the effects of LSPV resection were smallest on the global energetic state of the LA (Figure 7). In contrast, RSPV resection induced strong flow dissipation, which may have resulted from enhanced flow impingement between the left PV inflows and the remaining RIPV inflows caused by the RSPV resection (Figure 6). Although the LIPV tended to be smallest among all PVs, large patient-specific variations in PV morphologies have been documented (28). Given that PV location and flow rate balance have been considered as factors influencing LA blood flow even for the MV plane and LA appendage (29–31), patient-specific variations in PV morphologies and the remaining PV inflows are essential when considering patient-specific flow characteristics in the PV stump.

It should be noted that this study investigated global LA flow patterns after PV resections, and thus evaluated the flow kinetic energy and dissipation rate in a whole LA domain as indicators of global hemodynamic states. Because the same total flow rate through the LA was set in both pre and post-resection cases based on measurements in our previous studies (15, 16), a PV resection increased the inflow rate and associated flow velocity through the remaining PVs. Furthermore, this inflow enhancement tended to induce flow impingement with viscous dissipation (Figure 5). Therefore, we believe that the relatively high kinetic energy and dissipation rate in post PV resection (Figure 7) are reasonable from a fluid mechanical viewpoint.

This study had four main limitations. First, it aimed to clarify the distinctive LA blood flow patterns after LUL observed in clinical practice, and the association between LA flow patterns and PV stump thrombosis was beyond its scope. Although global LA flow patterns and its flow disturbances are considered one of the risk factors for thrombus formation in the PV stump (7, 9, 14), thrombus formation in PV stump is rare (approximately 5% (5)) depending on several influential factors not only the LA hemodynamics but also PV stump morphologies (7) and physiological factors such as inflammatory responses (12). In addition, due to shortages of patient datasets, four participants recruited in this study are not cases of PV stump thrombosis after LUL. Thus, systematic studies with large patient datasets are necessary to identify the essential factors in PV stump thrombosis. Second, lobectomies may cause physiological changes in the remaining PV inflow, as well as in LA and LV function, as discussed in our previous study (16). Thus, CFD simulation with virtual PV resection may over- or underestimate LA flow alteration after lobectomies. However, comparison of LA flow patterns among PV resections within the same participant is clinically infeasible, and computational modeling is a possible alternative to estimate the effects of each PV resection on LA hemodynamics. Third, this study assumed that the flow velocity was identical among PV inflows and did not consider patient-specific inflow rates. Flow rate balance among PVs is not only determined by the lung lobe volume (32) but is also influenced by body posture (33); therefore, it is difficult to identify even within a single patient. Furthermore, lobectomies lead to expansion of the remaining lung lobes to compensate for the resected lobe function (34). Lobectomies may also alter the inflow rate balance among remaining PV inflows, although to our knowledge no studies have examined PV inflow rate changes after lobectomies. Further clinical investigation of PV inflows would provide valuable insights into the mechanisms underlying the LA blood flow patterns associated with thrombosis. Fourth, quantification of the global LA blood flow patterns by possibly a single parameter is an interesting topic for clinical usage, while these issues include multi-scale turbulent flow dynamics and are still challenging, even in the turbulent research field, to our knowledge. As an alternative approach, we considered visualizing the flow topology from flow velocity fields and extracted the flow boundaries formed by multiple PV inflows. Such postprocessing is effective in interpreting characteristic behaviors of spatiotemporally varying velocity fields while limiting quantitative discussion for further analyses using large patient datasets. For this issue, a data science approach that can handle big data problems would be reasonable to quantify the complex blood flow patterns.

5 Conclusions

This study considered the distinctive LA blood flow patterns after LUL pointed out by recent MRI studies relative to those of lobectomies performed in other sites. We performed 4D-CT-based CFD simulations of LA blood flow without and with virtual PV resections, which modeled the effects of lung lobectomy, and compared the blood flow patterns, especially for the remaining PV inflows. LSPV resection tended to enhance LIPV inflow such that it reached the LA anterior wall, resulting in impingement of the right PV inflows in the upper LA region with relatively severe flow disturbances around the PV stump. However, LA flow patterns after PV resections showed large patient-specific variations because of the LA and PV geometries, and the relative effects of each PV resection on

the LA flow patterns differed among participants. These results suggest the marked patient-specific variations and highlights the importance of patient-specific assessment of the LA hemodynamics after lobectomies.

Data availability statement

The raw data supporting the conclusions of this article will be made available by the authors, without undue reservation.

Ethics statement

The studies involving humans were approved by the Institutional Review Board of Jichi Medical University. The studies were conducted in accordance with the local legislation and institutional requirements. The participants provided their written informed consent to participate in this study.

Author contributions

WY: Writing – original draft, Data curation, Formal Analysis, Investigation, Methodology, Visualization; TO: Writing – original draft, Conceptualization, Funding acquisition, Project administration, Software, Supervision; SE: Data curation, Funding acquisition, Writing – review & editing; SW: Conceptualization, Funding acquisition, Project administration, Supervision, Writing – review & editing.

Funding

The author(s) declare financial support was received for the research, authorship, and/or publication of this article.

This work was supported by the Japan Society for the Promotion of Science Grants-in-Aid for Scientific Research (No. 23K11830), the "Program for Promoting Researches on the Supercomputer Fugaku" (Project ID: hp220161 and hp230208) funded by the Ministry of Education, Culture, Sports, Science and Technology, and Multidisciplinary Research Laboratory System for Future Developments, Osaka University Graduate School of Engineering Science.

Acknowledgments

We thank Michael Irvine, PhD, from Edanz (https://jp.edanz.com/ac) for editing a draft of this manuscript.

Conflict of interest

The authors declare that the research was conducted in the absence of any commercial or financial relationships that could be construed as a potential conflict of interest.

Publisher's note

All claims expressed in this article are solely those of the authors and do not necessarily represent those of their affiliated organizations, or those of the publisher, the editors and the reviewers. Any product that may be evaluated in this article, or claim that may be made by its manufacturer, is not guaranteed or endorsed by the publisher.

Supplementary material

The Supplementary Material for this article can be found online at: https://www.frontiersin.org/articles/10.3389/fcvm.2023.1305526/full#supplementary-material

References

1. Wolf PA, Abbott RD, Kannel WB. Atrial fibrillation as an independent risk factor for stroke: the Framingham Study. *Stroke*. (1991) 22:983–8. doi: 10.1161/01.STR.22.8.983

2. Hartwig MG, D'Amico TA. Thoracoscopic lobectomy: the gold standard for early-stage lung cancer? *Ann Thorac Surg*. (2010) 89:S2098–101. doi: 10.1016/j.athoracsur.2010.02.102

3. Hattori A, Takamochi K, Kitamura Y, Matsunaga T, Suzuki K, Oh S, et al. Risk factor analysis of cerebral infarction, clinicopathological characteristics of left upper pulmonary vein stump thrombus after lobectomy. *Gen Thorac Cardiovasc Surg*. (2019) 67:247–53. doi: 10.1007/s11748-018-1017-8

4. Wankhede D, Grover S, Awendila L. Left upper lobectomy for lung cancer as a risk factor for cerebral infarction: a systematic review, meta-analysis. *Lung*. (2021) 199:535–47. doi: 10.1007/s00408-021-00480-4

5. Riddersholm S, Tayal B, Kragholm K, Andreasen JJ, Rasmussen BS, Søgaard P, et al. Incidence of stroke after pneumonectomy and lobectomy: a nationwide, register-based study. *Stroke*. (2019) 50:1052–9. doi: 10.1161/STROKEAHA.118.024496

6. Ohtaka K, Hida Y, Kaga K, Kato T, Muto J, Nakada-Kubota R, et al. Thrombosis in the pulmonary vein stump after left upper lobectomy as a possible cause of cerebral infarction. *Ann Thorac Surg*. (2013) 95:1924–8. doi: 10.1016/j.athoracsur.2013.03.005

7. Ohtaka K, Hida Y, Kaga K, Takahashi Y, Kawase H, Hayama S, et al. Left upper lobectomy can be a risk factor for thrombosis in the pulmonary vein stump. *J Cardiothorac Surg*. (2014) 9:1–5. doi: 10.1186/1749-8090-9-5

8. Ohtaka K, Takahashi Y, Uemura S, Shoji Y, Hayama S, Ichimura T, et al. Blood stasis may cause thrombosis in the left superior pulmonary vein stump after left upper lobectomy. *J Cardiothorac Surg*. (2014) 9:1–7. doi: 10.1186/s13019-014-0159-8

9. Matsumoto M, Takegahara K, Inoue T, Nakaza M, Sekine T, Usuda J. 4D flow MR imaging reveals a decrease of left atrial blood flow in a patient with cardioembolic cerebral infarction after pulmonary left upper lobectomy. *Magn Reson Med Sci*. (2020) 19:290–3. doi: 10.2463/mrms.ici.2019-0142

10. Nakaza M, Matsumoto M, Sekine T, Inoue T, Ando T, Ogawa M, et al. Dual-VENC 4D flow MRI can detect abnormal blood flow in the left atrium that potentially causes thrombosis formation after left upper lobectomy. *Magn Reson Med Sci*. (2022) 21:433–43. doi: 10.2463/mrms.mp.2020-0170

11. Sekine T, Nakaza M, Matsumoto M, Ando T. 4D flow MR imaging of the left atrium: what is non-physiological blood flow in the cardiac system? Basic concepts of 4D flow MRI assessment of left atrium (2022) 21:293–308. doi: 10.2463/mrms.rev.2021-0137

12. Usui G, Takayama Y, Hashimoto H, Katano T, Yanagiya M, Kusakabe M, et al. Cerebral embolism caused by thrombus in the pulmonary vein stump after left lower lobectomy: a case report, literature review. *Intern Med*. (2019) 58:1349–54. doi: 10.2169/internalmedicine.1962-18

13. Xie N, Meng X, Wu C, Lian Y, Wang C, Yu M, et al. Both left upper lobectomy, left pneumonectomy are risk factors for postoperative stroke. *Sci Rep*. (2019) 9:1–7. doi: 10.1038/s41598-019-46989-w

14. Umehara T, Takumi K, Ueda K, Tokunaga T, Harada-Takeda A, Suzuki S, et al. Four-dimensional flow magnetic resonance imaging study to explain high prevalence of pulmonary vein stump thrombus after left upper lobectomy. *J Thorac Dis*. (2020) 12:5542–51. doi: 10.21037/jtd-20-1606

15. Otani T, Yoshida T, Yi W, Endo S, Wada S. On the impact of the left upper lobectomy on the left atrial hemodynamics. *Front Physiol*. (2022) 13:830436. doi: 10.3389/fphys.2022.830436

16. Yi W, Otani T, Yoshida T, Endo S, Wada S. Computational study on hemodynamic effects of left superior pulmonary vein resection and associated physiological changes in the left atrium after left upper lobectomy. *Comput Methods Biomech Biomed Engin*. (2023):1–12. doi: 10.1080/10255842.2023.2178258

17. Myronenko A, Song X. Point set registration: coherent point drifts. *IEEE Trans Pattern Anal Mach Intell*. (2010) 32:2262–75. doi: 10.1109/TPAMI.2010.46

18. Otani T, Shiga M, Endo S, Wada S. Performance assessment of displacement-field estimation of the human left atrium from 4D-CT images using the coherent point drift algorithm. *Comput Biol Med*. (2019) 114:103454. doi: 10.1016/j.compbiomed.2019.103454

19. Otani T, Al-Issa A, Pourmorteza A, McVeigh ER, Wada S, Ashikaga H. A computational framework for personalized blood flow analysis in the human left atrium. *Ann Biomed Eng*. (2016) 44:3284–94. doi: 10.1007/s10439-016-1590-x

20. Otani T, Shindo T, Ii S, Hirata M, Wada S. Effect of local coil density on blood flow stagnation in densely coiled cerebral aneurysms: A computational study using a cartesian grid method. *J Biomech Eng*. (2018) 140:041013. doi: 10.1115/1.4039150

21. Weymouth GD, Yue DKP. Boundary data immersion method for cartesian-grid simulations of fluid-body interaction problems. *J Comput Phys*. (2011) 230:6233–47. doi: 10.1016/j.jcp.2011.04.022

22. García-Villalba M, Rossini L, Gonzalo A, Vigneault D, Martinez-Legazpi P, Durán E, et al. Demonstration of Patient-Specific simulations to assess left atrial appendage thrombogenesis risk. *Front Physiol*. (2021) 12:1–14. doi: 10.3389/fphys.2021.596596

23. Shadden SC. Lagrangian coherent structures. In: *Transport and mixing in laminar flows from microfluidics to oceanic currents*. Wiley Online Library (2011). p. 59–89. doi: 10.1002/9783527639748.ch3

24. Haller G. Lagrangian coherent structures. *Annu Rev Fluid Mech*. (2015) 47:137–62. doi: 10.1146/annurev-fluid-010313-141322

25. Kilner PJ, Yang GZ, Wilkest AJ, Mohladdlin RH, Firmin DN, Yacoub MH. Asymmetric redirection of flow through the heart. *Nature*. (2000) 404:759–61. doi: 10.1038/35008075

26. Fyrenius A, Wigström L, Ebbers T, Karlsson M, Engvall J, Bolger AF. Three dimensional flow in the human left atrium. *Heart*. (2001) 86:448–55. doi: 10.1136/heart.86.4.448

27. Vedula V, George R, Younes L, Mittal R. Hemodynamics in the left atrium and its effect on ventricular flow patterns. *J Biomech Eng*. (2015) 137:111003. doi: 10.1115/1.4031487

28. Elliott M. Pulmonary vein anatomy: atypical is typical. *J Cardiovasc Electrophysiol*. (2011) 22:8–9. doi: 10.1111/j.1540-8167.2010.01903.x

29. Dahl SK, Thomassen E, Hellevik LR, Skallerud B. Impact of pulmonary venous locations on the intra-atrial flow and the mitral valve plane velocity profile. *Cardiovasc Eng Technol*. (2012) 3:269–81. doi: 10.1007/s13239-012-0099-1

30. Durán E, García-Villalba M, Martinez-Legazpi P, Gonzalo A, McVeigh E, Kahn AM, et al. Pulmonary vein flow split effects in patient-specific simulations of left atrial flow. *Comput Biol Med*. (2023) 163:107128. doi: 10.1016/j.compbiomed.2023.107128

31. Lantz J, Gupta V, Henriksson L, Karlsson M, Persson A, Carlhäll CJ, et al. Impact of pulmonary venous inflow on cardiac flow simulations: comparison with in vivo 4D flow MRI. *Ann Biomed Eng*. (2019) 47:413–24. doi: 10.1007/s10439-018-02153-5

32. Cheng CP, Taur AS, Lee GS, Goris ML, Feinstein JA. Relative lung perfusion distribution in normal lung scans: observations and clinical implications. *Congenit Heart Dis*. (2006) 1:210–6. doi: 10.1111/j.1747-0803.2006.00037.x

33. Wieslander B, Ramos JG, Ax M, Petersson J, Ugander M. Supine, prone, right and left gravitational effects on human pulmonary circulation. *J Cardiovasc Magn Reson*. (2019) 21:1–15. doi: 10.1186/s12968-019-0577-9

34. Dai J, Xie D, Wang H, He W, Zhou Y, Hernández-Arenas LA, et al. Predictors of survival in lung torsion: a systematic review and pooled analysis. *J Thorac Cardiovasc Surg*. (2016) 152:737–745.e3. doi: 10.1016/j.jtcvs.2016.03.077

frontiers | Frontiers in Cardiovascular Medicine

TYPE Original Research
PUBLISHED 11 March 2024
DOI 10.3389/fcvm.2024.1383082

Check for updates

OPEN ACCESS

EDITED BY
Gaoyang Li,
Tohoku University, Japan

REVIEWED BY
Yang Liu,
Chinese PLA General Hospital, China
Zhenxia Mu,
Shandong Provincial Hospital Affiliated to Shandong First Medical University, China

*CORRESPONDENCE
Mengyao Duan
✉ duanmengyao0715@163.com

RECEIVED 06 February 2024
ACCEPTED 01 March 2024
PUBLISHED 11 March 2024

CITATION
Mao B, Zhao Z, Wei M, Liu X, Zhao R, Zhang W and Duan M (2024) Study on the related factors of TCM constitution and hemodynamics in patients with coronary heart disease.
Front. Cardiovasc. Med. 11:1383082.
doi: 10.3389/fcvm.2024.1383082

COPYRIGHT
© 2024 Mao, Zhao, Wei, Liu, Zhao, Zhang and Duan. This is an open-access article distributed under the terms of the Creative Commons Attribution License (CC BY). The use, distribution or reproduction in other forums is permitted, provided the original author(s) and the copyright owner(s) are credited and that the original publication in this journal is cited, in accordance with accepted academic practice. No use, distribution or reproduction is permitted which does not comply with these terms.

Study on the related factors of TCM constitution and hemodynamics in patients with coronary heart disease

Boyan Mao[1], Zhou Zhao[2], Minghui Wei[1], Xinzhu Liu[1], Ruoqi Zhao[3], Weipeng Zhang[4] and Mengyao Duan[5]*

[1]School of Life Sciences, Beijing University of Chinese Medicine, Beijing, China, [2]Cardiac Surgery Department, Peking University People's Hospital, Beijing, China, [3]School of Chinese Materia Medica, Beijing University of Chinese Medicine, Beijing, China, [4]Chengdu Techman Software Co. Ltd., Chengdu, China, [5]School of Traditional Chinese Medicine, Beijing University of Chinese Medicine, Beijing, China

Background: The concepts of "individualization" and "preventive treatment" should be incorporated into the precise diagnosis and treatment of coronary heart disease (CHD). Both hemodynamics and Chinese medicine constitution studies align with these two concepts.
Methods: This study utilized data from 81 patients with CHD, including 12 patients with balanced constitution (BC), 20 patients with blood stasis constitution (BSC), 17 patients with phlegm-dampness constitution (PDC), 15 patients with qi-deficiency constitution (QDC), and 17 patients with other constitutions. Clinical data provided information on the patients' blood property, heart function, degree of coronary stenosis, coronary hemodynamics, and so on. These parameters were compared between patients with balanced constitution vs. biased constitutions as well as between those with blood stasis constitution, phlegm-dampness constitution, and qi-deficiency constitution.
Results: Compared to biased constitution (BC), patients with balanced constitution exhibited lower total cholesterol (TC) levels and low-density lipoprotein (LDL) levels. Additionally, they had lighter stenosis degrees in the Left anterior descending branch (LAD) and Left circumflex branch (LCX) branches. The hemodynamic condition of the LAD and LCX was better for those with balanced constitution; however there was no difference in heart function. Among the groups categorized by blood stasis, phlegm dampness or qi deficiency constituions, patients classified under phlegm dampness had higher levels of LDL compared to those classified under blood stasis or qi deficiency, while patients classified under qi deficiency had higher levels of blood glucose compared to those classified under blood stasis or phlegm dampness. Hemodynamic environments also differed among the LAD and LCX for each group but there were no significant differences observed in heart function or degree of coronary stenosis among these three groups.
Conclusion: The balanced constitution demonstrates superior blood property, degree of coronary artery stenosis, and coronary hemodynamics compared to the biased constitution. Furthermore, among the three constitutions with CHD, variations in blood property and certain hemodynamic parameters are observed. These findings emphasize the significant clinical value of incorporating physical factors into the diagnosis and treatment of patients with CHD.

KEYWORDS

coronary artery, coronary heart disease, traditional Chinese medicine constitution, hemodynamics, modeling and simulation

1 Introduction

Coronary heart disease is a prevalent cardiovascular disorder (1, 2) caused by stenosis in the coronary artery that impedes blood perfusion. The primary cause of this stenosis is the development of atherosclerotic plaque (3). Atherosclerotic plaques form within the coronary artery and subsequently obstruct it, leading to inadequate blood supply to the distal end of the artery and resulting in symptoms such as angina pectoris. In order to achieve precise diagnosis and treatment for coronary heart disease, it is essential to adopt the concepts of "individualization" and "preventive treatment". The term "individualization" implies that even if patients exhibit similar examination results, their diagnosis and treatment decisions should still be tailored specifically for each individual. Similarly, "preventive treatment" emphasizes not only focusing on current coronary artery stenosis but also assessing future coronary blood flow transport capacity and preventing risk factors among potential patients with coronary heart disease. These two concepts are effectively implemented in hemodynamics theory and TCM constitution.

Hemodynamics is a scientific discipline that investigates the impact of blood flow and vascular physiology. Hemodynamic factors play a pivotal role in the onset and progression of coronary heart disease. Research has demonstrated that stable high wall shear stress (WSS) promotes the expression of endothelial cells' anti-atherogenic genes, whereas low WSS and high Oscillating shear index (OSI) facilitate the expression of atherogenic genes (4, 5). Analyzing the cardiovascular hemodynamic environment in patients enables an assessment of their risk for developing coronary heart disease, facilitating personalized prevention and treatment strategies for patients.

The constitution is a comprehensive and relatively stable trait of morphological structure, physiological function, and mental state that develops based on innate endowment and acquired factors. In traditional Chinese Medicine, the study of constitution characteristics, evolution rules, influencing factors, and classification standards aims to understand different constitutions starting from human beings. TCM has a complete theoretical and practical system for preventing, diagnosing, treating, rehabilitating, and preserving health in diseases. The balanced constitution is the most prevalent among the general population in China, comprising 32.14% according to epidemiological survey data conducted by academician Qi Wang across 9 provinces and cities with a sample size of 21,948 individuals. Meanwhile, the biased constitution accounts for 67.86%. Coronary heart disease (CHD) is a chronic disease with high incidence and risk where the concept of "arguing body to judge treatment" based on TCM constitution can significantly contribute to its diagnosis and treatment. Among the prevalent constitutional types observed in patients with CHD, the predominant three are blood stasis constitution, phlegm-dampness constitution, and qi-deficiency constitution, accounting for 20.96%, 18.46%, and 15.86% respectively (6). The TCM constitution is closely associated with the severity of coronary artery stenosis and the number of affected branches, as well as blood properties such as density, hemodynamic viscosity, and other cardiovascular characteristics.

Both hemodynamics and TCM constitution incorporate the principles of "personalized" and "preventive treatment" in the diagnosis and management of coronary heart disease. Simultaneously, they also examine CHD from a holistic perspective, considering patients' overall health status as well as local blood flow characteristics within the coronary artery. Consequently, this study aims to investigate the correlation between patients' constitution and hemodynamic factors associated with CHD, encompassing the relationship between constitution and blood properties, constitution and cardiac function, constitution and morphological structure of coronary arteries, as well as constitution and coronary hemodynamics.

2 Method

2.1 Patient data collection

The clinical patient data utilized in this study were obtained from the Heart Center of Peking University People's Hospital between 2021 and 2023. The following are the selection criteria for inclusion by our patients.

2.1.1 Inclusion and exclusion criteria of patients

Inclusion criteria:

① Age ≥18 and ≤90:
② Completed coronary CTA, echocardiography and blood routine examination in the hospital;
③ The informed consent shall be signed by the applicant or his/her immediate family member.
④ The TCM Constitution Classification and Judgment Scale should be filled in truthfully under the guidance of TCM doctors.

Exclusion criteria:

① Age <18 years or >90 years;
② Received coronary stent or coronary artery bypass graft surgery;
③ Unclear consciousness, can not express subjective symptoms and psychiatric patients;
④ Accompanied by more than one serious secondary progressive malignant tumor or other serious wasting disease.

Coronary CTA enables the acquisition of the number, stenosis rate, and stenosis length for each branch of the LAD, LCX, and right coronary artery (RCA). Additionally, it facilitates 3D reconstruction of the coronary artery to calculate hemodynamics for each vessel. Echocardiography was employed to measure ejection fraction (EF), left ventricular end-diastolic diameter (LVEDD), and left atrial diameter (LA). Blood tests were conducted to determine TC levels, LDL levels, and blood glucose levels.

TCM constitution identification was accomplished by guiding patients through completion of the *TCM Constitution Classification and Judgment Scale*. Patients answered all questions on a 5-point scale within this questionnaire. Original scores were calculated alongside transformation scores to evaluate each patient's constitution type. In cases where patients exhibited more than two biased constitution, their main constitution type

was identified based on higher transformation scores. A healthy constitution was defined as balanced while other constitutions were classified as biased constitution. Among patients with CHD, common constitution types included blood stasis constitution, phlegm-dampness constitution, and qi-deficiency constitution. This paper compares different constitutions in two aspects: firstly comparing balanced vs. biased constitution; secondly comparing blood stasis constitution against phlegm-dampness constitution and qi-deficiency constitution.

2.2 Construction of coronary hemodynamic model and data collection

2.2.1 3D coronary artery model construction

In this study, a 0D-3D coupled multi-scaled modeling method was utilized to construct a coronary hemodynamic model. The coronary artery CTA data were used for 3D reconstruction, and tetrahedral grids were employed for meshing. All grids passed sensitivity analysis. Then, the vessel properties and blood properties were set as rigid wall, the blood was set as incompressible viscous Newtonian fluid, the density of the blood was set as 1,050 kg/m^3, and the kinetic viscosity was set as 0.0035 Pa·s. The governing equation of blood flow is Navier-Stokes equation (N-S equation), and the flow is set to laminar flow.

2.2.2 Construction of coronary 0D-3D coupled multi-scaled model

In this study, the lumped parameter model (also known as 0D model) was used to provide boundary conditions for the 3D model, so it is necessary to design 0D model of different structures according to the parts connected by the inlet and outlet of the 3D model. The inlet of the 3D model was the heart, and its outlet included the distal of the aorta and its bifurcation vessels, as well as the distal of the coronary vessels. Therefore, the 0D model for this study consists of three modules: the heart module, the systemic circulation module and the coronary circulation module. The design structure of these three modules is shown in Figure 1.

For the heart module, its structure is shown in Part A of the figure. In order to provide a boundary condition for the aortic inlet of the 3D model, our heart model only contains the left heart part, and omits the right heart part. In the left heart, the blood enters the left ventricle through the left atrium and the mitral valve. The left ventricle pushes the blood out of the aorta and then the systemic circulation is completed. Ula in part A of the picture is a constant voltage source, representing the pressure in the left atrium, This is because the stress in the left atrium is small and does not fluctuate significantly with the cardiac cycle, so a constant voltage source can be used instead. The two diodes represent the mitral valve and the aortic valve from left to right respectively, which ensures the unidirectional conduction of the current; the resistance Rla and the inductance Lla represent the blood flow resistance and the blood flow inertia flowing through the mitral valve respectively; the resistance Rlv represents the blood flow resistance flowing through the aortic valve. $C(t)$ is a time-varying capacitance that reflects the periodic contraction and relaxation of the left ventricle over time, and its value is regulated by the pressure-volume relationship of the left ventricle.

For the systemic circulation module, it is shown in part B of the figure. The resistance R_p represents the resistance of arterial blood flow, the resistance R_d represents the sum of the resistance of the arterial end, the microcirculatory system and the venous system, and the capacitance C represents the elasticity of the arterial blood vessel.

For the coronary module, unlike other vessels, the coronary vessel reaches its peak blood flow during diastole. In order to simulate the special phenomenon of coronary artery, the lumped parameter model of coronary artery needs to consider the influence of myocardial contraction, and the general method is to add a pressure source synchronous with the ventricular pressure

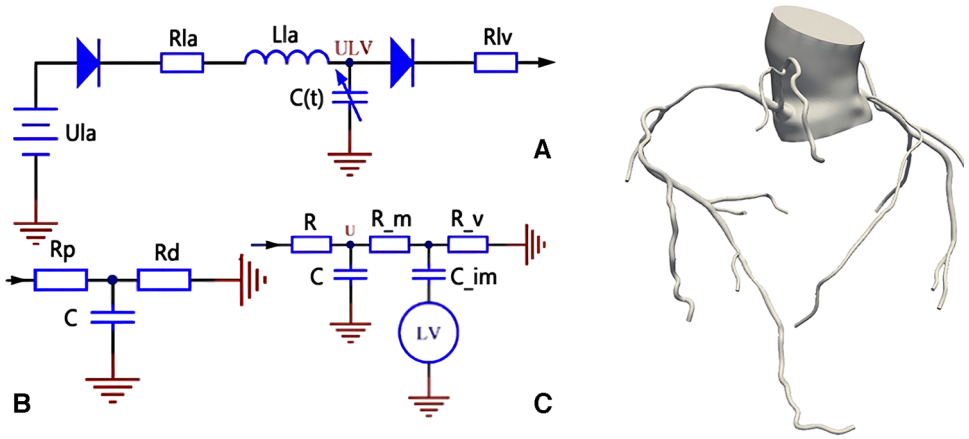

FIGURE 1
Coronary 0D-3D coupled multi-scaled model. (**A**) is the heart module, which provides boundary conditions for the aortic inlet of the model; (**B**) is the systemic circulation module, which provides boundary conditions for the aortic outlet of the model; and (**C**) is the coronary module, which provides boundary conditions for the coronary outlet of the model.

in the lumped parameter model. Part C in the figure is the structural diagram of the coronary lumped parameter model. The resistance R represents the coronary blood flow resistance, the resistance R_m represents the coronary microcirculation blood flow resistance, and the resistance R_v represents the venous blood flow resistance. Capacitor C represents the coronary artery. The capacitance C_im represents the vascular compliance of coronary microcirculation. The lower end of the capacitance C_im is connected with a voltage source which represents the extrusion of the myocardial motion to the coronary artery, and the change of the value follows the change of the pressure of the left ventricle.

After determining the structure of the lumped parameter model, the next task is to select the appropriate parameters for each component of the model. In this paper, the genetic algorithm is used to optimize the parameters, and the problem of matching the parameters of the components with the physiological data is solved with the patient's personalized physiological characteristics data as the target (9).

Using the data of systolic pressure, diastolic pressure, heart rate and cardiac output of normal people, the aortic pressure waveform and cardiac output waveform of normal people are fitted as two optimized target waveforms. Based on the research of Kim (8), the parameter values of the lumped parameter model are adjusted manually to the extent that the output waveform matches the target waveform, and the parameters at this time are used as the reference values of the subsequent personalized parameters. In this process, two important points should be noted: (1) the total coronary flow accounts for 4% of the cardiac output, and the left coronary flow and the right coronary flow account for 60% and 40% of the total coronary flow, respectively; (2) the blood flow of the coronary branches accounts for 2.7 power.

Then, the 3D model and 0D model were coupled with specific interface conditions and coupling algorithms, and the coronary 0D-3D coupled multi-scaled model was constructed as shown in Figure 1. The 0D model provides the flow conditions at the entrance and the pressure boundary conditions at the exit for the 3D model. After calculation, the 3D model is the return pressure at the entrance and the discharge at the exit of the 0D model. The specific construction process of 0D-3D coupled multi-scaled model can be referred to the previous research of our research group (9, 10–12).

2.2.3 Extraction of hemodynamic results

After constructing the multi-scaled model and completing the calculation, the hemodynamic results of the three main branches of the coronary artery were extracted, including WSS, wall shear stress gradient (WSSG), OSI and other parameters. At the same time, the 0D model was adjusted to make the afterload become 0.24 times of the resting state to simulate the maximum hyperemia state. The model was calculated under this state, and the FFR (fractional flow reserve) at the distal end of the three main coronary branches was extracted (13, 14).

2.3 Construction of coronary artery repair model

Traditional Chinese medicine constitution is good at analyzing the vulnerability and tendency of different people to diseases, which emphasizes "prevention before disease onset". The effect of hemodynamics on blood vessels can also be revealed through a certain period of time. In order to study the long-term development of coronary heart disease in patients with different constitutions, a coronary artery repair model was constructed based on a real coronary artery model, as shown in Figure 2.

In this study, the diameter of the anterior and posterior ends of the coronary artery stenosis was averaged as the reference diameter,

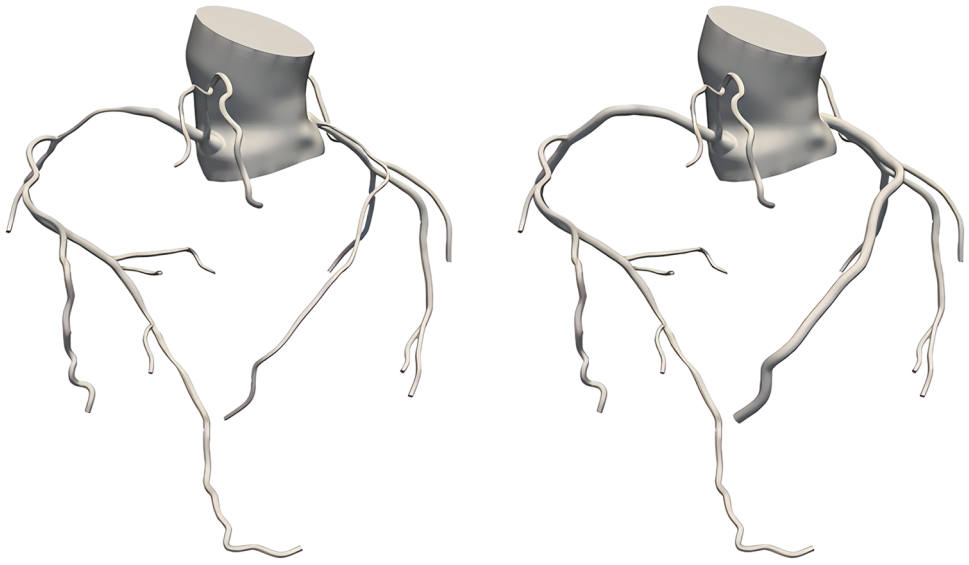

FIGURE 2
True coronary artery model (left), coronary artery repair model (right).

and then the coronary artery stenosis was repaired using virtual surgical software to make its diameter into the reference diameter, so that the coronary artery repair model without stenosis was obtained. The coronary artery repair model was used to simulate the state of patients when they were "normal", and to study whether there were differences in hemodynamics between patients with different constitutions when they were normal. The subsequent modeling methods and the extraction process of hemodynamic results of the coronary repair model were consistent with the real coronary model.

2.4 Statistical method

One-way analysis of variance (ANOVA) was utilized to compare the differences between two groups, namely balanced constitution and biased constitution, as well as three groups including blood stasis constitution, phlegm-dampness constitution, and qi-deficiency constitution. The statistical analysis was conducted using SPSS software. This method effectively enables us to explore the variations in mean values among different groups and subsequently verify our research hypothesis. Prior to conducting the analysis, normal distribution and homogeneity of variance were confirmed for all data. Results were expressed as means with standard deviations. *P*-value less than 0.05 indicated a significant difference between groups.

3 Results

3.1 Patient baseline data and constitution type

The data utilized in this study were obtained from the Heart Center of Peking University People's Hospital during the period from 2021 to 2023, encompassing a total of 81 patients. The baseline data and constitution classifications are presented in Table 1.

3.2 Comparison of blood properties and cardiac function in patients with different TCM constitutions

In this study, TC, LDL, blood glucose, left ventricular ejection fraction (LVEF), LVEDD, LA and other parameters were obtained according to blood examination and cardiac ultrasound examination of patients, and their comparison in different TCM constitution groups was as follows. For the grouping of balanced constitution and biased constitution, the results are shown in Table 2.

Table 2 demonstrates significant disparities in TC and LDL levels between patients with balanced and biased constitution. The balanced constitution group exhibited lower levels of both TC and LDL, whereas the biased constitution group displayed higher levels of both biomarkers. These differences were statistically significant. Furthermore, there was a discernible distinction in blood glucose levels between patients with balanced and biased constitution. However, this disparity did not meet the criteria for statistical significance. Notably, no significant variations were observed between the two groups regarding other cardiac function measures such as LVEF, LVEDD, and LA. For the groups of blood stasis, phlegm dampness, and qi deficiency, the results are shown in Table 3.

According to Table 3, significant differences were observed in LDL and blood glucose levels among patients with blood stasis constitution, phlegm-dampness, and qi-deficiency constitutions. Post hoc multiple comparisons revealed that the LDL level was significantly higher in patients with phlegm-dampness constitution compared to those with blood stasis constitution and qi-deficiency constitutions. Additionally, the blood glucose level was significantly higher in patients with qi-deficiency constitution compared to those with blood stasis constitution and phlegm-dampness constitutions. However, no significant differences were found in TC levels and various cardiac function indexes among the three constitutional types.

3.3 To compare the severity of coronary artery stenosis among patients with different traditional Chinese medicine constitutions

In this study, all patients were examined for the three main branches of the coronary artery. The degree of coronary artery stenosis was determined based on CTA data, which primarily included the maximum stenosis rate of each coronary artery, the corresponding length of stenosis at the maximum rate, and the FFR measurement at the distal end of each coronary artery. Table 4 presents the findings for both groups with a balanced constitution and biased constitution.

TABLE 1 Baseline data and constitution types of patients.

Number of patients	81
Height (cm)	167.3 ± 7.5
Age	62.9 ± 9.3
Weight (kg)	72.5 ± 14.1
Gender	Male 61/female 20
balanced quality	12
Blood stasis	20
Phlegm dampness	17
Qi-deficiency quality	15
Other constitution	17

TABLE 2 Comparison of blood properties and cardiac function between balanced and biased constitution.

	Balanced constitution	Biased constitution	*P*-value
TC (mmol/L)	3.258 ± 0.364	3.828 ± 0.888	<0.05
LDL (mmol/L)	1.903 ± 0.344	2.393 ± 0.660	<0.05
Blood glucose (mmol/L)	5.378 ± 0.930	6.483 ± 2.099	0.078
LVEF (%)	62.225 ± 13.231	63.812 ± 8.896	0.599
LVEDD (mm)	50.383 ± 7.938	47.712 ± 11.680	0.449
LA (mm)	39.442 ± 5.332	36.359 ± 8.450	0.227

TABLE 3 Comparison of blood property and cardiac function of blood stasis constitution, phlegm dampness constitution and qi-stagnation constitution qualities.

	blood stasis constitution	Phlegm dampness	Qi-deficiency	*P*-value
TC (mmol/L)	3.974 ± 0.766	4.191 ± 1.228	3.635 ± 0.574	0.228
LDL (mmol/L)	2.383 ± 0.619	2.825 ± 0.831	2.105 ± 0.483	<0.05
Blood glucose (mmol/L)	5.901 ± 1.412	6.355 ± 1.622	8.139 ± 3.263	<0.05
LVEF (%)	63.150 ± 7.797	65.159 ± 7.745	64.196 ± 11.302	0.792
LVEDD (mm)	45.380 ± 14.337	49.776 ± 4.201	44.000 ± 16.236	0.399
LA (mm)	35.375 ± 11.755	37.459 ± 5.302	33.940 ± 8.786	0.555

According to Table 4, there were statistically significant differences observed between patients with balanced and biased constitution in terms of the maximum rate of stenosis in LAD, as well as the FFR values for both LAD and LCX. Specifically, the maximum rate of stenosis in LAD was significantly higher in the biased constitution group compared to the balanced constitution group. Additionally, the FFR value for LAD was significantly lower in the biased constitution group than in the balanced constitution group. These findings suggest a higher likelihood of coronary stenosis occurring specifically within LAD among patients with a biased constitution. Similarly, LCX FFR values were significantly lower in the biased group compared to those with a balanced constitution, indicating a more severe degree of coronary stenosis within LCX among patients with a biased constitution.

The results for the groups with blood stasis constitution, phlegm dampness, and qi-deficiency constitution are presented in Table 5. It is evident that there were no statistically significant differences observed in the degree of stenosis among the three coronary arteries across these groups.

3.4 Comparison of coronary hemodynamics in patients with different TCM constitutions

The coronary 0D-3D coupled multi-scaled model was constructed using coronary CTA in this study, and the hemodynamic parameters WSS, WSSG, and OSI were extracted from LAD, LCX, and RCA after calculation. Based on the coronary artery repair model, the hemodynamic parameters in the "normal" state were calculated and extracted. Table 6 presents the results for grouping based on balanced constitution and biased constitution.

TABLE 4 Comparison of the degree of coronary artery stenosis between the balanced constitution and the biased constitution.

	Balanced constitution	Biased constitution	*P*-value
Maximum stenosis rate of LAD	0.579 ± 0.339	0.769 ± 0.192	<0.05
Length of LAD stenosis (cm)	2.960 ± 2.465	3.932 ± 2.369	0.196
LAD FFR	0.788 ± 0.184	0.487 ± 0.172	<0.05
LCX maximum stenosis rate	0.450 ± 0.342	0.609 ± 0.316	0.117
LCX stenosis length (cm)	2.538 ± 2.866	2.121 ± 1.937	0.525
LCX FFR	0.761 ± 0.167	0.628 ± 0.204	<0.05
Maximum RCA stenosis	0.621 ± 0.367	0.712 ± 0.278	0.319
RCA stenosis length (cm)	2.306 ± 2.711	4.104 ± 3.931	0.133
RCA FFR	0.688 ± 0.220	0.592 ± 0.214	0.157

TABLE 5 Comparison of the degree of coronary artery stenosis of blood stasis, phlegm dampness and qi deficiency.

	Blood stasis constitution	Phlegm dampness	Qi-deficiency	*P*-value
Maximum stenosis rate of LAD	0.755 ± 0.161	0.799 ± 0.206	0.75 ± 0.218	0.734
LAD stenosis length (cm)	4.087 ± 1.687	3.528 ± 1.759	4.42 ± 2.839	0.477
LAD FFR	0.437 ± 0.161	0.470 ± 0.173	0.52 ± 0.182	0.362
LCX maximum stenosis	0.595 ± 0.294	0.535 ± 0.333	0.68 ± 0.235	0.345
LCX stenosis length (cm)	2.102 ± 1.832	1.621 ± 1.357	2.54 ± 2.171	0.358
LCX FFR	0.562 ± 0.216	0.676 ± 0.204	0.64 ± 0.143	0.197
Maximum RCA stenosis	0.740 ± 0.233	0.668 ± 0.311	0.63 ± 0.318	0.544
RCA stenosis length (cm)	4.322 ± 3.977	2.528 ± 1.928	5.27 ± 5.728	0.162
RCA FFR	0.543 ± 0.221	0.656 ± 0.187	0.60 ± 0.240	0.290

In the real coronary model, significant differences in WSS and WSSG were observed between patients with a balanced constitution and those with a biased constitution, as presented in Table 6. The WSS and WSSG values were higher in the biased constitution group compared to the balanced constitution group, particularly in the LAD and LCX coronary branches. No significant differences were found for OSI among different coronary artery branches. However, no significant variations in hemodynamic parameters of each coronary artery were observed between the two groups in the coronary repair model.

Table 7 presents the results for the groups categorized by blood stasis, phlegm dampness, and qi-deficiency. In the realistic coronary model, significant differences were observed in WSS among the LAD branches across the three groups. Post hoc multiple comparisons revealed that the LAD-WSS of the blood stasis type was lower than that of both the phlegm dampness type and qi-deficiency type. Significant differences were also found in OSI among LCX branches within these three groups. According to *post hoc* multiple comparisons, the LCX-OSI of the qi deficiency type was lower compared to both blood stasis and phlegm dampness types. No significant differences were observed among these three groups for other hemodynamic parameters. However, in terms of coronary repair models, all hemodynamic parameters showed no significant variations between groups.

4 Discussion

4.1 TCM constitution and coronary heart disease

The TCM constitution theory classifies patients into nine fundamental constitution types:balanced constitution, qi-deficiency constitution, yin-deficiency constitution, yang-

TABLE 6 Comparison of coronary hemodynamics between balanced constitution and biased constitution.

		Balanced constitution	Biased constitution	*P*-value
True model of coronary artery	LAD-WSS (dyn/cm^2)	51.771 ± 27.801	70.627 ± 31.622	<0.05
	LAD-WSSG (dyn/cm^3)	208.616 ± 133.624	317.467 ± 157.940	<0.05
	LAD-OSI	0.0098 ± 0.0071	0.0101 ± 0.0154	0.945
	LCX-WSS (dyn/cm^2)	54.326 ± 34.009	80.509 ± 46.167	<0.05
	LCX-WSSG (dyn/cm^3)	246.186 ± 203.123	389.418 ± 247.637	<0.05
	LCX-OSI	0.0059 ± 0.0037	0.0073 ± 0.0081	0.574
	RCA-WSS (dyn/cm^2)	51.515 ± 29.091	67.563 ± 32.761	0.116
	RCA-WSSG (dyn/cm^3)	241.061 ± 163.609	316.871 ± 178.248	0.173
	RCA-OSI	0.0070 ± 0.0079	0.0075 ± 0.0085	0.831
Model of coronary artery repair	LAD-WSS (dyn/cm^2)	65.016 ± 26.717	64.634 ± 30.798	0.968
	LAD-WSSG (dyn/cm^3)	249.951 ± 102.668	246.670 ± 123.256	0.931
	LAD-OSI	0.0086 ± 0.0059	0.0091 ± 0.0090	0.839
	LCX-WSS (dyn/cm^2)	71.081 ± 47.490	71.427 ± 38.576	0.978
	LCX-WSSG (dyn/cm^3)	299.826 ± 194.996	316.860 ± 190.293	0.776
	LCX-OSI	0.0053 ± 0.0052	0.0071 ± 0.0076	0.412
	RCA-WSS (dyn/cm^2)	63.333 ± 30.792	64.396 ± 34.051	0.920
	RCA-WSSG (dyn/cm^3)	245.235 ± 118.169	257.592 ± 147.201	0.784
	RCA-OSI	0.0057 ± 0.0055	0.0061 ± 0.0089	0.893

deficiency constitution, phlegm-dampness constitution, blood stasis constitution, damp-heat constitution, qi-stagnation constitution, and inherited special constitution. Each constitutional type possesses distinct characteristics in terms of physical property, physiological traits, psychological features, pathological response states, and disease tendencies. The balanced constitution represents a state of optimal health. The remaining eight constitutions are referred to as biased constitution which impact the overall health status of patients as well as their susceptibility and predisposition to diseases. Among the general population in China, the most prevalent constitutional type is the balanced constitution accounting for 32.14%. Biased constitution account for 67.86%, with the top three being qi-deficiency Constitution, damp-heat constitution, and yang-deficiency constitution (6). Balanced and biased constitution serve as crucial classifications in constitutional studies representing healthy patients vs. those with compromised health conditions. Among the common constitution types of patients with CHD, the three most prevalent are blood-stasis constitution, phlegm-dampness constitution, and qi-deficiency constitution, accounting for 20.96%, 18.46%, and 15.86% respectively (6). Among these three CHD-prone constitutions, blood stasis showed the most severe degree of coronary artery stenosis and higher levels of blood lipids, making it more susceptible to hypertension. phlegm-dampness exhibited a relatively better heart function performance but also had a higher degree of coronary artery stenosis and elevated blood lipid levels, making it highly prone to hypertension. Qi-deficiency demonstrated a more serious degree of coronary artery stenosis along with higher blood glucose levels and poor vascular

TABLE 7 Comparison of coronary hemodynamics of blood stasis, phlegm dampness and qi deficiency.

		Blood stasis constitution	Phlegm dampness	Qi-deficiency	*P*-value
True model of coronary artery	LAD-WSS (dyn/cm^2)	54.765 ± 23.501	78.511 ± 30.647	81.439 ± 39.171	<0.05
	LAD-WSSG (dyn/cm^3)	259.22 ± 122.661	336.62 ± 164.750	365.2 ± 190.434	0.127
	LAD-OSI	0.0149 ± 0.0266	0.0086 ± 0.0055	0.0083 ± 0.0095	0.451
	LCX-WSS (dyn/cm^2)	78.922 ± 45.708	78.266 ± 53.599	90.421 ± 50.787	0.742
	LCX-WSSG (dyn/cm^3)	364.27 ± 210.795	378.05 ± 273.240	472.2 ± 317.341	0.457
	LCX-OSI	0.0103 ± 0.0085	0.0099 ± 0.0131	0.0040 ± 0.0029	< 0.05
	RCA-WSS (dyn/cm^2)	58.025 ± 34.508	68.218 ± 33.687	77.667 ± 35.127	0.254
	RCA-WSSG (dyn/cm^3)	262.35 ± 165.519	327.63 ± 176.788	361.3 ± 215.026	0.276
	RCA-OSI	0.0092 ± 0.0093	0.0073 ± 0.0067	0.0072 ± 0.0124	0.790
Model of coronary repair	LAD-WSS (dyn/cm^2)	50.240 ± 32.746	61.719 ± 31.486	72.978 ± 26.799	0.105
	LAD-WSSG (dyn/cm^3)	186.37 ± 129.582	230.45 ± 121.661	282.9 ± 104.689	0.073
	LAD-OSI	0.0112 ± 0.0134	0.0104 ± 0.0091	0.0073 ± 0.0041	0.504
	LCX-WSS (dyn/cm^2)	70.103 ± 49.109	65.529 ± 44.340	72.29 ± 29.021	0.899
	LCX-WSSG (dyn/cm^3)	306.344 ± 244.391	282.262 ± 203.807	331.107 ± 161.624	0.807
	LCX-OSI	0.0080 ± 0.0091	0.0102 ± 0.0100	0.0057 ± 0.0041	0.322
	RCA-WSS (dyn/cm^2)	54.870 ± 38.976	62.137 ± 35.038	71.825 ± 33.256	0.396
	RCA-WSSG (dyn/cm^3)	212.11 ± 159.639	258.18 ± 158.509	290.098 ± 152.239	0.344
	RCA-OSI	0.0101 ± 0.0152	0.0051 ± 0.0032	0.0041 ± 0.0029	0.150

compliance (15–18). Patients with other biased constitutions accounted for a small proportion among those with CHD, and their diagnostic characteristics for this condition were relatively weak; therefore, they were not included in this study.

Many scholars have conducted targeted and highly detailed studies on the correlation between TCM constitution and CHD. These research findings have laid a preliminary foundation for our team's work, enabling us to further contemplate the relationship between constitution and CHD, as well as conduct more in-depth research.

In terms of the relationship between TCM constitution and coronary artery morphology, numerous scholars have discovered significant variations in coronary artery morphology among patients with different constitutions suffering from CHD, including differences in the degree of stenosis and number of affected branches (15). Overall, biased constitutions exhibit greater degrees of coronary artery stenosis compared to balanced constitutions. The qi-deficiency constitution, blood-stasis constitution, phlegm-dampness constitution, and other CHD-prone constitutions demonstrate higher levels than other biased constitutions. Positive syndrome constitutions (blood-stasis constitution, phlegm-dampness constitution) surpass deficiency syndrome constitutions (qi-deficiency constitution, yang-deficiency constitution), with blood-stasis constitutional types exceeding phlegm-dampness constitutional types.

Regarding TCM constitution and blood properties, certain constituents such as total cholesterol, triglyceride, low-density lipoprotein cholesterol (LDL-C) are considered risk factors for increased blood viscosity and vascular blockage. Scholars have observed that specific constitutions can elevate blood lipids and glucose levels while inducing viscous blood consistency leading to circulatory obstruction, impaired hemodynamics, and subsequent vascular blockages (16–18). Generally speaking, Yin deficiency and qi-deficiency constitute primarily contribute to elevated blood glucose levels.

However, most researchers have solely focused on the association between constitution, blood properties, and coronary artery stenosis without conducting a multi-faceted comparison based on a batch of data. No scholars have explored the relationship between constitution and FFR, WSS, WSSG, OSI—parameters that can characterize the current or future blood transport function of the coronary artery. Our team believes that delving into this area of research may yield greater value. Therefore, we aim to further investigate the relationship between constitution and hemodynamics in TCM building upon previous scholarly research.

Introducing TCM constitution into the study of coronary hemodynamics holds significant importance. The constitutional theory of TCM serves as an essential basis for diagnosing and treating CHD within this field. Patients with different constitutions exhibit distinct manifestations of CHD requiring varying treatment methods. Approaching treatment from a constitutional perspective aligns with the concept of "preventive treatment for diseases" by focusing on preventing illness before it occurs or progresses while also preventing relapse after recovery. The combination of TCM constitution analysis with hemodynamic studies has demonstrated great value in diagnosing and treating patients with CHD.

4.2 Traditional Chinese medicine constitution and blood properties, heart function, coronary artery morphology and structure

The study revealed no disparity in cardiac function between patients with a balanced constitution and those with a biased constitution. However, significant variations were observed in blood property and the extent of coronary artery stenosis, potentially linked to the metabolic and physiological characteristics associated with each constitution type. The balanced constitution group exhibited lower levels of TC and LDL, both crucial risk factors for cardiovascular disease, suggesting better cardiovascular health. Conversely, patients with a biased constitution displayed higher levels of these measures, indicating an elevated risk for cardiovascular disease. Furthermore, although not statistically significant, the discrepancy in glucose levels between patients with a balanced or biased constitution is noteworthy due to hyperglycemia's association as another risk factor for cardiovascular disease. The degree of coronary artery stenosis serves as an essential indicator to assess the severity of cardiovascular disease. Significant disparities were found in the maximum LAD stenosis rate, LAD FFR, and LCX FFR between patients with balanced constitution compared to those with biased constitution; this suggests that the biased constitution group is more prone to developing coronary stenosis. This outcome may be attributed to risk factors such as dyslipidemia and inflammatory response prevalent among patients with a biased constitution.

For the grouping of blood stasis constitution, phlegm dampness and qi-deficiency constitutions, this study found that there were significant differences among the three constitutions in the levels of LDL and blood glucose, but no significant differences in TC and various cardiac function indexes were found among the three constitutions. Specifically, the LDL level of the phlegm-dampness constitution was significantly higher than that of the blood stasis constitution and the qi-deficiency constitution, and the blood glucose level of the qi-deficiency constitution was significantly higher than that of the blood stasis constitution and the phlegm-dampness constitution, which suggested that the phlegm-dampness constitution population faced the risk of hyperlipidemia, and the qi-deficiency constitution population faced the risk of hyperglycemia. There was no significant difference in heart function and degree of coronary artery stenosis among the three constitutions. This indicates that the differences among the three constitutions of CHD are only in the properties of blood, but there is no significant difference in the structure and function of the heart and coronary vessels.

4.3 Constitution of traditional Chinese medicine and coronary hemodynamics

For the groups with mild and biased constitution, significant differences were observed in WSS and WSSG, but not in OSI in the real coronary model. Specifically, WSS and WSSG were higher in the biased group compared to the mild group, particularly in the LAD and LCX coronary branches. This finding is consistent with a higher degree of stenosis observed in

patients with a biased constitution compared to those with a balanced constitution. Blood flow velocity increases at the site of stenosis, and as stenosis severity worsens, this increase becomes more pronounced, leading to an elevation in WSS within hemodynamics. The increase in WSS occurs locally at the site of stenosis followed by a rapid decrease in flow velocity reflected by WSSG, resulting in an overall increase of adverse hemodynamic factors that can contribute to further aggravation of atherosclerosis. In the coronary repair model, no differences were found between both groups regarding all hemodynamic parameters across all coronary branches. This indicates that there are no disparities concerning hemodynamics between patients with balanced constitution and those with biased constitution under "normal" conditions. Furthermore, it suggests that adverse hemodynamic environments are not solely generated due to inherent morphological structures associated with biased constitution themselves. From a purely hemodynamic perspective alone, patients with biased constitution do not exhibit a greater predisposition for developing coronary artery stenosis compared to those with balanced constitution. However, it should be noted that these findings do not take into account potential variations related to blood properties.

For the groups with blood stasis constitution, phlegm-dampness constitution, and qi-deficiency constitution in the realistic coronary model, this study observed that the WSS of the LAD branch in patients with blood stasis constitution was significantly lower compared to those with phlegm-dampness constitution and qi-deficiency constitution. Additionally, the WSSG was slightly smaller for patients with blood stasis constitution compared to the other two constitutions, approaching values similar to those of patients with a balanced constitution. These findings suggest that patients with blood stasis constitution exhibit a hemodynamic environment in their LAD branch comparable to that of patients with a balanced constitution. However, it should be noted that the OSI of the LCX branch in patients with qi-deficiency quality is lower than that of those with blood stasis and phlegm-dampness constitution. OSI is considered an unfavorable hemodynamic factor indicating better hemodynamic conditions for patients with qi-deficiency quality in their LCX branch. In contrast, no significant differences were observed among all groups regarding hemodynamic parameters across all coronary branches within the coronary artery repair model. This suggests that there are no variations in hemodynamics related to blood stasis, phlegm-dampness, and qi-deficiency under "normal" conditions.

4.4 Limitation

The present study has the following limitations: (1) The sample size selected for the study was insufficient, with data collected from only 81 eligible patients, resulting in small sample sizes for each constitution after grouping. Particularly for patients with a balanced constitution, the proportion of such patients among coronary heart disease patients is low and significantly differs from biased constitution data. (2) During hemodynamic modeling and simulation, only the personalized 3D model of the coronary artery was considered, while other conditions, especially blood properties based on different constitutions, were not taken into account. Current results indicate significant variations in blood properties between different constitutions–whether it be balanced constitution and partial constitution or blood stasis constitution, phlegm-dampness constitution, and qi-deficiency constitution. However, our model assumes uniform blood density and kinetic viscosity which may introduce certain deviations in hemodynamic outcomes.

5 Conclusion

Through this study, we investigated the association between balanced constitution and biased constitution, as well as the relationship among blood stasis constitution, phlegm-dampness constitution, and qi-deficiency constitution in terms of blood property, cardiac function, degree of coronary stenosis, and coronary hemodynamics. The findings of this study revealed that patients with a balanced constitution exhibited superior blood property compared to those with a biased constitution, along with reduced degree of coronary artery stenosis and improved coronary hemodynamics. Furthermore, variations in blood properties and certain hemodynamic parameters were observed among the three constitutions in patients with CHD. These results emphasize the significant clinical value of incorporating physical factors into the diagnosis and treatment of patients with coronary heart disease.

Data availability statement

The raw data supporting the conclusions of this article will be made available by the authors, without undue reservation.

Ethics statement

The studies involving humans were approved by the medical ethics committee of Beijing University of Chinese Medicine. The studies were conducted in accordance with the local legislation and institutional requirements. The participants provided their written informed consent to participate in this study.

Author contributions

BM: Conceptualization, Investigation, Writing – original draft. ZZ: Data curation, Formal Analysis, Writing – original draft. MW: Data curation, Formal Analysis, Writing – original draft. XL: Data curation, Methodology, Writing – review & editing. RZ: Investigation, Methodology, Writing – review & editing. WZ: Investigation, Methodology, Writing – review & editing. MD: Conceptualization, Supervision, Writing – original draft.

Funding

The authors declare that financial support was received for the research, authorship, and/or publication of this article.

This research is supported by National Natural Science Foundation of China (grant no. 12102064), the Ministry of Education industry-university cooperative education project (grant no. 220906291052940), China Postdoctoral Science Foundation (grant no. GZC20230323).

Conflict of interest

WZ was emplyed by Chengdu Techman Software Co., Ltd.

The remaining authors declare that the research was conducted in the absence of any commercial or financial relationships that could be construed as a potential conflict of interest.

The handling editor GL declared a past co-authorship with the authors BM, ZZ, MW, MD.

Publisher's note

All claims expressed in this article are solely those of the authors and do not necessarily represent those of their affiliated organizations, or those of the publisher, the editors and the reviewers. Any product that may be evaluated in this article, or claim that may be made by its manufacturer, is not guaranteed or endorsed by the publisher.

References

1. Bhatia SK. *Biomaterials for Clinical Applications*. Wilmington: Springer (2010).

2. Naghavi M, Wang H, Lozano R, Davis A, Liang X, Zhou M, et al. Global, regional, and national age-sex specific all-cause and cause-specific mortality for 240 causes of death, 1990–2013: a systematic analysis for the global burden of disease study 2013. *Lancet*. (2015) 385(9963):117–71. doi: 10.1016/S0140-6736(14)61682-2

3. De Rezende LF, Azeredo CM, Canella DS, Luiz OC, Levy RB, Eluf Neto J, et al. Coronary heart disease mortality, cardiovascular disease mortality and all-cause mortality attributable to dietary intake over 20 years in Brazil. *Int J Cardiol*. (2016) 217:64–8. doi: 10.1016/j.ijcard.2016.04.176

4. Berk B C. Atheroprotective signaling mechanisms activated by steady laminar flow in endothelial cells. *Circulation*. (2008) 117(8):1082–9. doi: 10.1161/CIRCULATIONAHA.107.720730

5. Taylor CA, Draney MT. Experimental and computational methods in cardiovascular fluid mechanics. *Fluid Mech*. (2004) 36(36):197–231. doi: 10.1146/annurev.fluid.36.050802.121944

6. Wang Q, Zhu Y. Epidemiological investigation of constitutional types of Chinese medicine in general population: base on 21,948 epidemiological investigation data of nine provinces in China. *Chin J Tradit Chin Med*. (2009) 24 (1):7–12.

7. Li B, Wang W, Mao B, Liu Y. A method to personalize the lumped parameter model of coronary artery. *Int J Comput Methods*. (2018) 15(1):1842004. doi: 10.1142/S0219876218420045

8. Kim HJ, Vignon-Clementel IE, Coogan JS, Figueroa CA, Jansen KE, Taylor CA. Patient-specific modeling of blood flow and pressure in human coronary arteries. *Ann Biomed Eng*. (2010) 38(10):3195–209. doi: 10.1007/s10439-010-0083-6

9. Li L, Liu Y, Zhao X, Mao B, Zhang H. Impact of competitive flow on hemodynamics of lima-lad grafting with different stenosis: a numerical study. *J Mech Med Biol*. (2017) 17(02):1750040. doi: 10.1142/S0219519417500403

10. Mao B, Wang W, Li B, Zhang X, Liu Y. Competitive flow effects of internal mammary artery bypass with different coronary stenosis lengths. *Int J Comput Methods*. (2019) 16(3):1842013. doi: 10.1142/S0219876218420136

11. Zhao X, Liu Y, Li L, Wang W, Xie J, Zhao Z. Hemodynamics of the string phenomenon in the internal thoracic artery grafted to the left anterior descending artery with moderate stenosis. *J Biomech*. (2016) 49(7):983–91. doi: 10.1016/j.jbiomech.2015.11.044

12. Mao B, Zhao Z, Li B, Feng Y, Feng Y, Liu Y. The comparison of venous sequential and normal graft patency based on hemodynamics. *J Mech Med Biol*. (2020) 20(2):1950080. doi: 10.1142/S0219519419500805

13. Taylor CA, Fonte TA, Min JK. Computational fluid dynamics applied to cardiac computed tomography for noninvasive quantification of fractional flow reserve: scientific basis. *J Am Coll Cardiol*. (2013) 61(22):2233–41. doi: 10.1016/j.jacc.2012.11.083

14. Li B, Mao B, Feng Y, Liu J, Zhao Z, Duan M, et al. The hemodynamic mechanism of FFR-guided coronary artery bypass grafting. *Front Physiol*. (2021) 12:503687. doi: 10.3389/fphys.2021.503687

15. Lingfang L, Yuxian C, Gaoye L, Hong L, Zhifang C. Comparison and analysis of degree of coronary artery disease in patients with coronary heart disease with different TCM constitutions. *General Nursing*. (2014) 12(16):1443–5.

16. Liming L, Sining L, Danlei W. The constitution distribution of angina pectoris patients in lingnan area. *Chin J Tradit Chin Med*. (2012) 53(15):1305–7.

17. Shujing S. *The Dinvestigation of Constitutional Types of Patient Swith Dislipiodiema and Study of the Mechanism of the Decoction of Reducing Turbidity and Regulating Fat in Regulating Plasma*. Guangzhou: Guangzhou University of Traditional Chinese Medicine (2015).

18. Han LB, Cui HX, Liu JF, Li XL, Wang LJ. Types of TCM constitutions and blood fat indexes in patients with type 2 diabetes combined with hyperlipidemia. *J Beijing Univ Chin Med*. (2011) 18(3):4–7.

frontiers | Frontiers in Cardiovascular Medicine

TYPE Original Research
PUBLISHED 25 March 2024
DOI 10.3389/fcvm.2024.1377765

Check for updates

OPEN ACCESS

EDITED BY
Aike Qiao,
Beijing University of Technology, China

REVIEWED BY
Bin Gao,
Beijing University of Technology, China
Guangyu Zhu,
Xi'an Jiaotong University, China
Zhaoming He,
Texas Tech University, United States

*CORRESPONDENCE
Shengzhang Wang
✉ szwang@fudan.edu.cn

RECEIVED 28 January 2024
ACCEPTED 11 March 2024
PUBLISHED 25 March 2024

CITATION
Chen T, Cheng X, Liu X, Zhang H and Wang S (2024) Study on the optimal elastic modulus of flexible blades for right heart assist device supporting patients with single-ventricle physiologies.
Front. Cardiovasc. Med. 11:1377765.
doi: 10.3389/fcvm.2024.1377765

COPYRIGHT
© 2024 Chen, Cheng, Liu, Zhang and Wang. This is an open-access article distributed under the terms of the Creative Commons Attribution License (CC BY). The use, distribution or reproduction in other forums is permitted, provided the original author(s) and the copyright owner(s) are credited and that the original publication in this journal is cited, in accordance with accepted academic practice. No use, distribution or reproduction is permitted which does not comply with these terms.

Study on the optimal elastic modulus of flexible blades for right heart assist device supporting patients with single-ventricle physiologies

Tong Chen[1], Xiaoming Cheng[2], Xudong Liu[3], Huifeng Zhang[4] and Shengzhang Wang[1,2]*

[1]Academy for Engineering and Technology, Fudan University, Shanghai, China, [2]Department of Aeronautics and Astronautics, Fudan University, Shanghai, China, [3]Shanghai Key Laboratory of Interventional Medical Devices and Equipment, Shanghai MicroPort Medical Group Co., Ltd, Shanghai, China, [4]Department of Cardiothoracic Surgery, Children's Hospital of Fudan University, Shanghai, China

Background: Patients with single-ventricle physiologies continue to experience insufficient circulatory power after undergoing palliative surgeries. This paper proposed a right heart assist device equipped with flexible blades to provide circulatory assistance for these patients. The optimal elastic modulus of the flexible blades was investigated through numerical simulation.
Methods: A one-way fluid-structure interaction (FSI) simulation was employed to study the deformation of flexible blades during rotation and its impact on device performance. The process began with a computational fluid dynamics (CFD) simulation to calculate the blood pressure rise and the pressure on the blades' surface. Subsequently, these pressure data were exported for finite element analysis (FEA) to compute the deformation of the blades. The fluid domain was then recreated based on the deformed blades' shape. Iterative CFD and FEA simulations were performed until both the blood pressure rise and the blades' shape stabilized. The blood pressure rise, hemolysis risk, and thrombosis risk corresponding to blades with different elastic moduli were exhaustively evaluated to determine the optimal elastic modulus.
Results: Except for the case at 8,000 rpm with a blade elastic modulus of 40 MPa, the pressure rise associated with flexible blades within the studied range (rotational speeds of 4,000 rpm and 8,000 rpm, elastic modulus between 10 MPa and 200 MPa) was lower than that of rigid blades. It was observed that the pressure rise corresponding to flexible blades increased as the elastic modulus increased. Additionally, no significant difference was found in the hemolysis risk and thrombus risk between flexible blades of various elastic moduli and rigid blades.
Conclusion: Except for one specific case, deformation of the flexible blades within the studied range led to a decrease in the impeller's functionality. Notably, rotational speed had a more significant impact on hemolysis risk and thrombus risk compared to blade deformation. After a comprehensive analysis of blade compressibility, blood pressure rise, hemolysis risk, and thrombus risk, the optimal elastic modulus for the flexible blades was determined to be between 40 MPa and 50 MPa.

KEYWORDS

single-ventricle physiology, right heart assist device, flexible blade, one-way fluid-structure interaction simulation, elastic modulus

1 Introduction

Congenital heart defects are the most prevalent type of birth defect, occurring in approximately 9 out of every 1,000 live births (1). Among these, 9%–12% are classified as single ventricle physiologies (2). Patients with single-ventricle physiologies often have atrial and ventricular septal defects, leading to the mixing of arterial and venous blood within the heart chambers. A portion of the venous blood enters the systemic circulation without being oxygenated, causing organ hypoxia. Typically, patients undergo three-stage palliative surgeries: the Norwood, Glenn, and Fontan procedures (3). After the Fontan procedure, patient's superior and inferior vena cava (SVC and IVC, respectively) are connected to the pulmonary artery (PA), forming a total cavopulmonary connection (TCPC) structure. This setup forces the single ventricle to pump blood through both systemic and pulmonary circulations in the absence of a functional right ventricle. Over time, this can result in high central venous pressure and low pulmonary artery pressure (known as Fontan failure) (4). Approximately 40% of patients eventually suffer from single ventricle pumping failure (5).

Assistive devices play a critical role in augmenting circulatory power for these patients. In 2010, Throckmorton et al. (6) introduced an axial blood pump into the IVC to aid blood flow to the lungs. However, as the outlet of the blood pump is oriented towards the SVC, the blood flow pressurized by the pump collides with the blood flow within the SVC. This collision leads to an increase in blood pressure inside the SVC and hinders blood return. Then in 2013, Throckmorton et al. (7) implanted axial blood pumps in both SVC and IVC to provide dual-lumen assistance. In 2014, Wang et al. (8) used a paired umbrella double-lumen cannula (Maquet Cardiovascular, Wayne, NJ) and extracorporeal blood pump CentriMag (Thoratec, Pleasanton, CA) for total cavopulmonary assist. Animal studies revealed that this setup effectively improved hemodynamics in failing Fontan sheep. Subsequently, in 2019, Wang et al. (9) combined a double-lumen cannula with a two-valve extracardiac conduit and CentriMag to achieve effective support. In 2016, Gandolfo et al. (10) designed a T-shaped mechanically assisted TCPC model using the Jarvik Child 2,000 axial pump (Jarvik Heart, New York, NY, USA), which showed promising results *in vivo*. Although these techniques can provide total cavopulmonary assist, they have drawbacks such as the need for multiple devices, limitations on patient activity due to extracorporeal blood pumps, and the necessity for vascular reconfiguration.

To address the issues mentioned above, this study proposed a novel right heart assist device, as shown in Figure 1. The main components of this device are made of flexible materials. During minimally invasive surgery, the device is in a contracted state with a smaller diameter. Once implanted in the human body, the device expands and begins to function. It is anticipated that the deformation of flexible components during operation will impact the device's performance. Consequently, ensuring rigidity in its expanded state while maintaining flexibility during folding poses the principal challenge in developing this device. The material selection for each component is crucial. This research focuses on a key component—the blades, investigating their optimal elastic modulus. A one-way FSI simulation was employed to study blades' deformation during rotation, and their impact on blood pressure increase, hemolysis risk, and thrombosis risk. The optimal elastic modulus is determined through a comprehensive analysis of these indicators.

2 Materials and methods

2.1 Flexible right heart assist device and computational models

Figure 1 shows the proposed right heart assist device, consisting of a protective stent, a bearing seat, a bearing, a shaft, an impeller, a constrictor ring, a motor, and cables. The protective stent is made of Nitinol. One end of the stent is fixed to the bearing seat, while the other end connects to the constrictor ring and can move axially. The impeller is fabricated from flexible materials such as polyurethane through an integrated molding process. It consists of two parts: the hub and the blades, with the base of the blades affixed to the surface of the hub. The hub's upper end is mounted on the shaft, and its lower end can move axially. The blades can adopt two configurations: curled and unfolded. When the assist device contracts, the lower end of the hub moves downward, and the blades curl. As the device expands, both the hub and the blades revert to their initial shape. The motor is powered by cables, and drives the rotation of the shaft and impeller. During surgery, the entire device is compressed within a delivery catheter and implanted into the TCPC via the femoral vein. Once released,

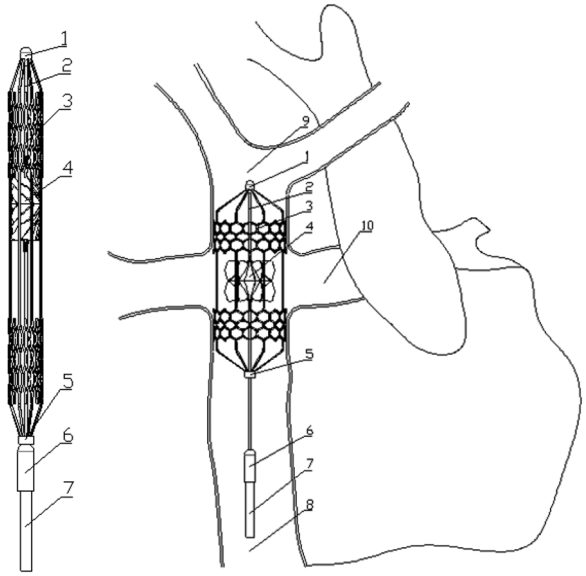

FIGURE 1
Contraction state and post-implantation state of the flexible right heart assist device. (1. bearing seat; 2. shaft; 3. protective stent; 4. impeller; 5. constrictor ring; 6. motor; 7. cable; 8. inferior vena cava; 9. superior vena cava; 10. pulmonary artery).

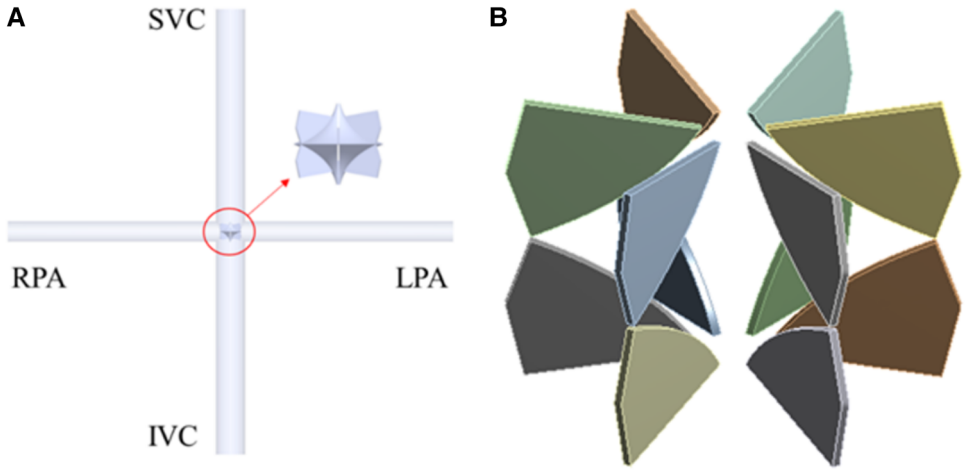

FIGURE 2
CFD and FEA simulation model. (A) Ideal TCPC structure; (B) blades of right heart assist device.

the protective stent expands to tightly fit against the inner walls of the vena cava, stabilizing the device. The rotating impeller aids in directing blood within the SVC and IVC into the PA. Additionally, the hub is uniquely designed in a spindle shape to prevent blood from colliding. The design goal of this assist device is to provide a pressure rise of 2–25 mmHg for the total systemic blood flow (3l /min 11) in Fontan patients when operating at 4,000–8,000 rpm (12).

This paper focuses on flexible blades, therefore adopts simplified computational models. The TCPC model is an ideal circular tube model derived from patient's data (13). According to the principle of equal area, the diameters of the SVC and IVC are set at 13 mm, while those of the LPA and RPA are set at 9 mm. In CFD simulation, only the impeller is retained. The base of the blades is fixed to the hub's surface to ensure the model's consistency with reality. The minimum and maximum diameters of the impeller are 0.4 mm and 10.9 mm respectively, the number of blades is 12, and the thickness of the blades is 0.2 mm. In FEA simulation, only the blades are retained. The deformation of the hub is ignored. The impeller and blade models presented in this paper are the optimized versions after structural optimization. Figure 2 illustrates the final computational models used in this study.

2.2 One-way FSI methodology, boundary conditions and solving settings

In this study, one-way FSI simulation was used to analyze the flexible blades' deformation and its effect on the device performance, as shown in Figure 3. First, ANSYS Fluent 2020R2 (Canonsburg, USA) was used to model the fluid dynamics in TCPC and obtain the blade surface pressure. Subsequently, these pressure data were utilized in ANSYS Structural 2020R2 (Canonsburg, USA) to compute blades' deformation. The deformation of the blades was quantitatively described by the

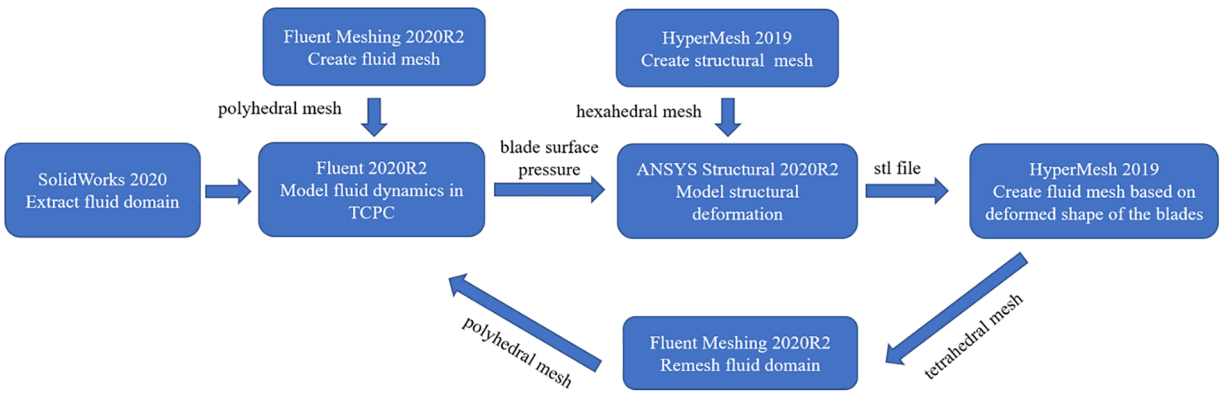

FIGURE 3
One-way FSI simulation process.

displacement of nodes on the blades. After the deformed shape of the blades was exported, the fluid domain was remeshed. Subsequently, the CFD simulation was performed again. The cycle was ended when the difference in blood pressure rise between two consecutive CFD simulations was less than 5%. Finally, the last CFD result was used to calculate the hemolysis risk and thrombus risk.

In CFD simulation, flow boundary conditions were defined at the SVC and IVC inlets, with flow rates of 1.2l /min and 1.8l /min respectively (11). The LPA and RPA outlets were set as pressure boundary conditions, with a pressure value of 1,750 Pa, corresponding to the average pulmonary artery pressure during a patient's cardiac cycle (13). Blood was modeled as a Newtonian fluid with a density of 1,060 kg/m^3 and a dynamic viscosity of 3.5 cP. This article analyzes the operation of the assist device at its lowest and highest rotational speeds. The flow domain is divided into rotating and stationary regions. The rotational speed of the rotating region is set at 4,000 rpm and 8,000 rpm. Furthermore, rotational boundary conditions are applied to the surfaces of the hub and blades, with the rotational speed settings matching those of the rotating region. The remaining surfaces are treated as stationary boundaries. Additionally, the SST k-ω model was used to simulate turbulent conditions, as this model can accurately resolve the flow fields both at the wall and in the bulk flow regime (12, 14, 15). The fluid domain was meshed as a polyhedral grid using Fluent Meshing 2020R2 (Canonsburg, USA). After grid independence study, the fluid mesh consisting of approximately 1.35 million elements was used for CFD simulation. Inflation layers were also used in the fluid meshes to achieve the SST k-ω turbulence model requirement (y + less than 2). A steady-state solver was employed, with the convergence criteria was set to a maximum residual of below the 1×10^{-4} threshold.

In FEA simulation, the blade material was set based on the polyurethane material properties. There is a wide variety of linear elastic polyurethanes, with elastic moduli ranging from 6.2 MPa to 27,600 MPa (16). A pre-simulation (a single round of one-way FSI) was conducted to narrow down the range of elastic moduli for the study, as shown in Figure 4. At 4,000 rpm and 8,000 rpm, the maximum deformation of the blades showed a consistent pattern. When the elastic modulus is within 50 MPa, the maximum deformation decreases rapidly as the elastic modulus increases. Between 50 MPa and 200 MPa, the decrease in maximum deformation is more gradual. Above 200 MPa, both the absolute value and the variation in maximum deformation are extremely small. Based on these results, the elastic moduli selected for the study were 10 MPa, 20 MPa, 30 MPa, 40 MPa, 50 MPa, 100 MPa, and 200 MPa. In the actual configuration, the base of the blades is fixed to the hub's surface, leading to the application of a fixed constraint at the base of the blades. The structural mesh of the blade, generated using HyperMesh (Altair, USA), is a hexahedral mesh and consists of two layers along the thickness direction. After the grid independence study, the structural mesh consisting of 36,096 elements was used for FEA simulation. A transient solver was employed, with a total computational duration

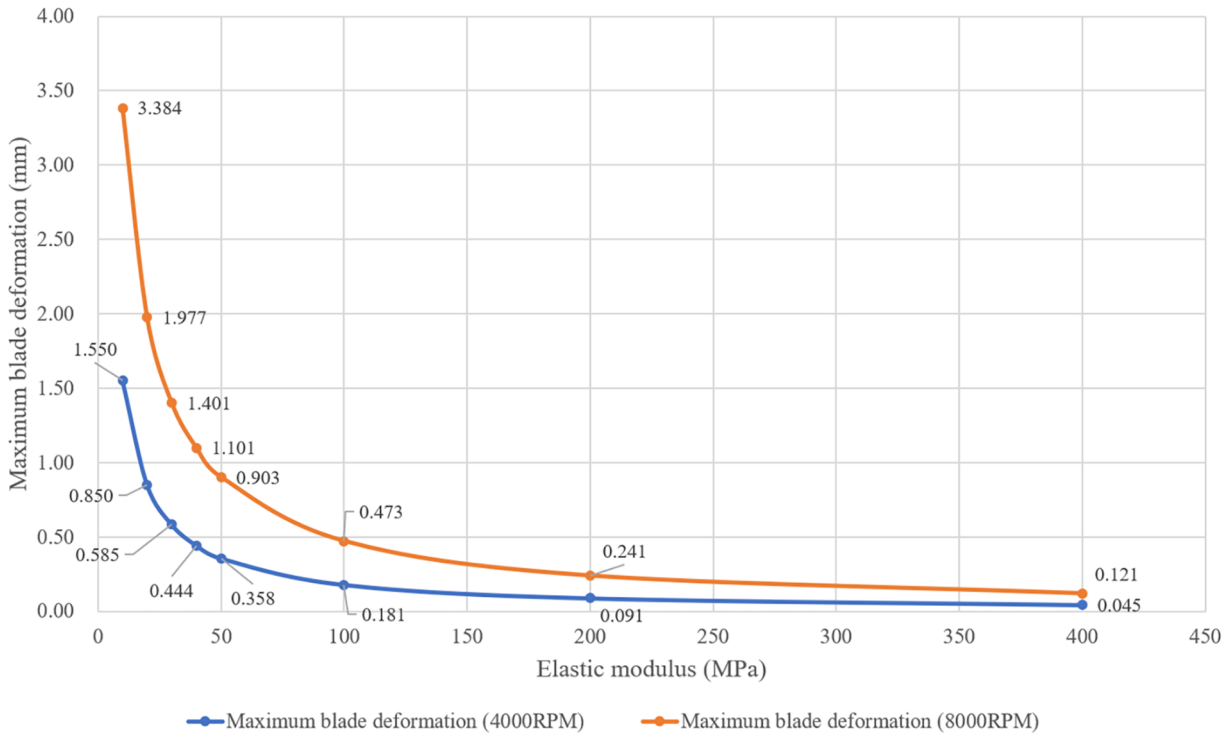

FIGURE 4
Maximum deformation of blades with different elastic moduli at rotational speeds of 4,000 rpm and 8,000 rpm. (These results were obtained from one round of one-way FSI simulation).

of 1.1 s and a time step of 0.001 s. The convergence criteria was set as changes of the maximum deformation, the minimum deformation, and the average deformation are all less than 1%.

2.3 Hemolysis risk assessment model

During the high-speed rotation of the impeller, red blood cells are destroyed due to shear forces, resulting in hemolysis. The hemolysis risk can be quantitatively evaluated using the Normalized index of hemolysis (NIH). Numerical simulations and hemolysis experiments employ different calculation methods to derive this index. In numerical simulation, NIH is commonly derived through a power law model, as detailed in Equations 1–3 (17–19).

$$\sigma = \left(\frac{1}{6}\sum(\sigma_{ii} - \sigma_{jj})^2 + \sum\sigma_{ij}^2\right)^{\frac{1}{2}} \tag{1}$$

$$D = \sum_{inlet}^{outlet} C \cdot \sigma^{\alpha} \cdot \Delta T^{\beta} \tag{2}$$

$$NIH = 0.00015 * D \tag{3}$$

where σ is the scalar stress, ΔT is the exposure time, and C, α, β are constants obtained from hemolysis experiments. Mitamura et al. (20) derived a set of parameters based on the experimental data from axial blood pumps: $C = 3.62 \times 10^{-5}$, $\alpha = 2.416$, $\beta = 0.785$. Heuser et al. (21) used experimental data from a Couette viscometer to fit another set of parameters: $C = 1.8 \times 10^{-6}$, $\alpha = 1.991$, $\beta = 0.765$. The working principle of the impeller in this paper differs considerably from that of the axial blood pump and Couette viscometer, and is closer to that of the centrifugal blood pump. Therefore, this paper uses experimental data of centrifugal blood pumps, provided by the U.S. Food and Drug Administration (FDA), to determine the parameters of the hemolysis risk assessment model (22).

In addition, Blackshear et al. (23) conducted a hemolysis experiment and proposed the relationship between shear stress experienced by red blood cells and their exposure time:

$$(\tau_{rbc}^2)(t) = C_1 \tag{4}$$

In the above equation C_1 is a constant of proportionality. The results of Blackshear et al. indicate that the hemolysis risk is proportional to the exposure time and the square of the shear stress. Combined with Equations 1–4, the final hemolysis risk assessment model used in this paper is as follows:

$$\sigma = \left(\frac{1}{6}\sum(\sigma_{ii} - \sigma_{jj})^2 + \sum\sigma_{ij}^2\right)^{\frac{1}{2}} \tag{5}$$

$$NIH = \sum_{inlet}^{outlet} A \cdot \sigma^{2B} \cdot \Delta T^{B} \tag{6}$$

In Equation 6, A represents the overall scaling factor, set at 2.7×10^{-10}. This value was derived by multiplying the scaling factor C, provided by Heuser (21), with the scaling factor of 0.00015 from Equation 3. The parameter B, set at 0.55, was determined from experimental data, as detailed in the Supplementary Document.

2.4 Thrombus risk assessment model

Thrombus formation is another common complication associated with rotary assist devices (24). It involves the generation, transport, and cascade reactions of numerous components. The adhesion and activation of platelets are critical steps in thrombus formation. Cell adhesion only occurs in areas where the wall shear strain rate ($\dot{\gamma}$) is lower than 100 /s (25). Therefore, the shear strain rate can be used to identify areas prone to thrombus growth (26). Its calculation method is shown in Equation 7. An accelerated thrombus formation model is utilized to quantitatively assess the thrombus risk (27). This model includes three convection-diffusion equations (Equations 8–10), describing the generation and transport of non-activated platelets (NP), activated platelets (AP), and adenosine diphosphate (ADP). The concentration of AP is ultimately used to represent the thrombus risk.

$$\dot{\gamma} = \left[2\left(\left(\frac{\partial u}{\partial x}\right)^2 + \left(\frac{\partial v}{\partial y}\right)^2 + \left(\frac{\partial w}{\partial z}\right)^2\right) + \left(\frac{\partial u}{\partial y} + \frac{\partial v}{\partial x}\right)^2 + \left(\frac{\partial u}{\partial z} + \frac{\partial w}{\partial x}\right)^2 + \left(\frac{\partial v}{\partial z} + \frac{\partial w}{\partial y}\right)^2\right]^{\frac{1}{2}} \tag{7}$$

$$\frac{\partial(\phi_a)}{\partial t} + (u \cdot \nabla)\phi_a = D_a\nabla^2\phi_a + \{[A_C(ADP)]\phi_n + [A_M(\phi_f, \tau)](\phi_a + \phi_n)\} \tag{8}$$

$$\frac{\partial(\phi_n)}{\partial t} + (u \cdot \nabla)\phi_n = D_n\nabla^2\phi_n - \{[A_C(ADP)]\phi_n + [A_M(\phi_f, \tau)](\phi_a + \phi_n)\} \tag{9}$$

$$\frac{\partial(ADP)}{\partial t} + (u \cdot \nabla)ADP = D_{ADP}\nabla^2 ADP + R_{ADP}\{[A_C(ADP)]\phi_n + [A_M(\phi_f, \tau)](\phi_a + \phi_n)\} \tag{10}$$

In the above equations, D_x is the respective diffusivity coefficient, A_M and A_C denotes mechanical activation and chemical activation, and R_{ADP} is the amount of ADP contained in a platelet. Platelet activation (change from NP to AP) occurs either with mechanical cues (Equation 11) or chemical cues (Equation 12).

$$A_M(\phi_f, \tau) = (1 - \phi_f)C_1^{\frac{1}{\beta_1}}\beta_1\phi_f^{\frac{\beta_1 - 1}{\beta_1}}\tau^{\frac{\alpha_1}{\beta_1}} \tag{11}$$

$$A_C(\mathrm{ADP}) = \begin{cases} \dfrac{\mathrm{ADP}}{\mathrm{ADP}_t \cdot t_{\mathrm{ADP}}}, & \mathrm{ADP} \geq \mathrm{ADP}_t \\ 0, & \mathrm{ADP} < \mathrm{ADP}_t \end{cases} \tag{12}$$

where ϕ_f is the ratio of the number of activated platelets to total platelets count, α_1, β_1 and C_1 are the power law model parameter,

ADP_t is the threshold for chemical platelet activation, t_{ADP} is the characteristic time of platelet activation, and τ is the shear stress calculated from Equations 13–15.

$$\tau = \frac{1}{\sqrt{3}}\sqrt{\sigma_{xx}^2 + \sigma_{yy}^2 + \sigma_{zz}^2 - \sigma_{xx}\sigma_{yy} - \sigma_{yy}\sigma_{zz} - \sigma_{xx}\sigma_{zz} + 3(\sigma_{xy}^2 + \sigma_{yz}^2 + \sigma_{xz}^2)} \tag{13}$$

$$\sigma_{ij} = \mu\left(\frac{\partial u_i}{\partial x_j} + \frac{\partial u_j}{\partial x_i}\right) - \rho\overline{u_i' u_j'} \tag{14}$$

$$-\rho\overline{u_i' u_j'} = \mu_t\left(\frac{\partial u_i}{\partial x_j} + \frac{\partial u_j}{\partial x_i}\right) - \frac{2}{3}\rho k\delta_{ij} \tag{15}$$

In the above equations μ is the dynamic viscosity, μ_t is the eddy viscosity, ρ is the fluid density, k is the turbulent kinetic energy, δ_{ij} is the Kronecker delta, u_i is the velocity component and u_i is the spatial component.

3 Results

3.1 Variation of blades' deformation and pressure rise during FSI simulation iterations

Figure 5; Table 1 illustrate the changes in blades' deformation and blood pressure rise during FSI simulation iterations. Figures 5A,C,D sequentially show the blades' deformation during three rounds of FSI simulation. It is evident that as the iterations progress, the solid body gradually aligns with the dashed frame. Additionally, the maximum deformation of the blades gradually decreases, indicating that the blade shape is stabilizing. According to Table 1, the pressure rises in both the SVC and IVC also tend to stabilize during the iteration process. The pressure rises of the last two iterations differing by less than 5%. These results validate that the one-way FSI simulation used in this paper can achieve a stable blade shape and the corresponding pressure rise.

Moreover, stress exists within the blade in the second and subsequent rounds of FSI simulation. Figures 5A,B were compared with each other to verify the accuracy of applied stress. Figure 5A shows the blade bending under surface pressure. Figure 5B depicts the blade returning to vertical shape after the removal of surface pressure, while stress is retained. The maximum deformations in Figures 5A,B are 1.55 mm and 1.505 mm, respectively. The difference is only 3%, indicating that the stress is sufficiently precise.

3.2 Blood pressure rise corresponding to blades with different elastic moduli at two rotational speeds

Figure 6 displays the blood pressure rise corresponding to flexible blades and rigid blades. DP-Total represents the total pressure rise, obtained by the weighted sum of DP-SVC and DP-IVC, based on the flow rates in SVC and IVC (DP-Total = DP-SVC × 0.4 + DP-IVC × 0.6). At a speed of 8,000 rpm, blades with an elastic modulus of 10 MPa deform excessively and lose their functionality entirely. Consequently, data related to this condition are not included in the analysis.

From Figure 6A, it can be observed that at 4,000 rpm, the pressure rises corresponding to flexible blades show an increasing trend. As the elastic modulus increases, DP-SVC, DP-IVC and DP-Total all gradually increase. The pressure rises corresponding to flexible blades with elastic moduli of 50 MPa, 100 MPa, and 200 MPa are relatively close to those of rigid blades. Figure 6B reveals that at 8,000 rpm, the pressure rises corresponding to flexible blades also trends upward. However, when the elastic modulus of the blades increases from 40 MPa to 50 MPa, the pressure rise decreases instead. The pressure rises corresponding to flexible blades with elastic moduli of 40 MPa, 50 MPa, 100 MPa, and 200 MPa are relatively close to those of rigid blades. Notably, the pressure rise corresponding to the 40 MPa elastic modulus flexible blade is higher than that of the rigid blades. Comprehensive analysis indicates that in most cases, blade deformation leads to a decrease in functionality. However, at the highest rotational speed, there are instances where blade deformation results in an increase in functionality.

3.3 Hemolysis risk corresponding to blades with different elastic moduli at two rotational speeds

Figure 7 shows the hemolysis risk associated with flexible blades and rigid blades. After completing the streamline number independence test, 1,100 streamlines were released at both the SVC and IVC inlets. The NIH values for each streamline were calculated and average values were used to represent the hemolysis risk in the blood flow of the SVC and IVC (NIH-SVC and NIH-IVC). The overall hemolysis risk (NIH-Total) was derived by the weighted sum of NIH-SVC and NIH-IVC (NIH-Total = NIH-SVC × 0.4 + NIH-IVC × 0.6). The results indicate that at both rotational speeds, the hemolysis risks associated with flexible and rigid blades are relatively similar. At 4,000 rpm, the NIH-Total for flexible blades ranges between 7.26×10^{-4} and 7.67×10^{-4} g/100 L, with a maximum difference of 5.6%. The NIH-Total for rigid blades is 7.03×10^{-4} g/100 L. Therefore, the difference in NIH-Total between flexible and rigid blades ranges from 3.3% to 9.1%. At 8,000 rpm, the NIH-Total for flexible blades ranges between 15.01×10^{-4} and 16.65×10^{-4} g/100 L, with a maximum difference of 10.9%. The NIH-Total for rigid blades is 15.48×10^{-4} g/100 L.As a result, the difference in NIH-Total between flexible and rigid blades ranges from 0.2% to 7.6%.

Under the same rotational speed, flexible blades with different elastic moduli have varying shapes, yet the corresponding hemolysis risks are similar. This suggests that the impact of rotational speed on hemolysis risk is greater than that of blade deformation. Moreover, literature data indicate that the NIH values for HeartMateII (Thoratec Inc., Pleasanto, California, USA) and CH-VAD (CH Biomedical, Inc., Suzhou, China) at medium speeds are 5.83×10^{-3} g/100 L and 1.35×10^{-3} g/100 L, respectively (28). The highest NIH-Total in this study is 1.665×10^{-3} g/100 L, falling between the NIH values of HeartMateII and

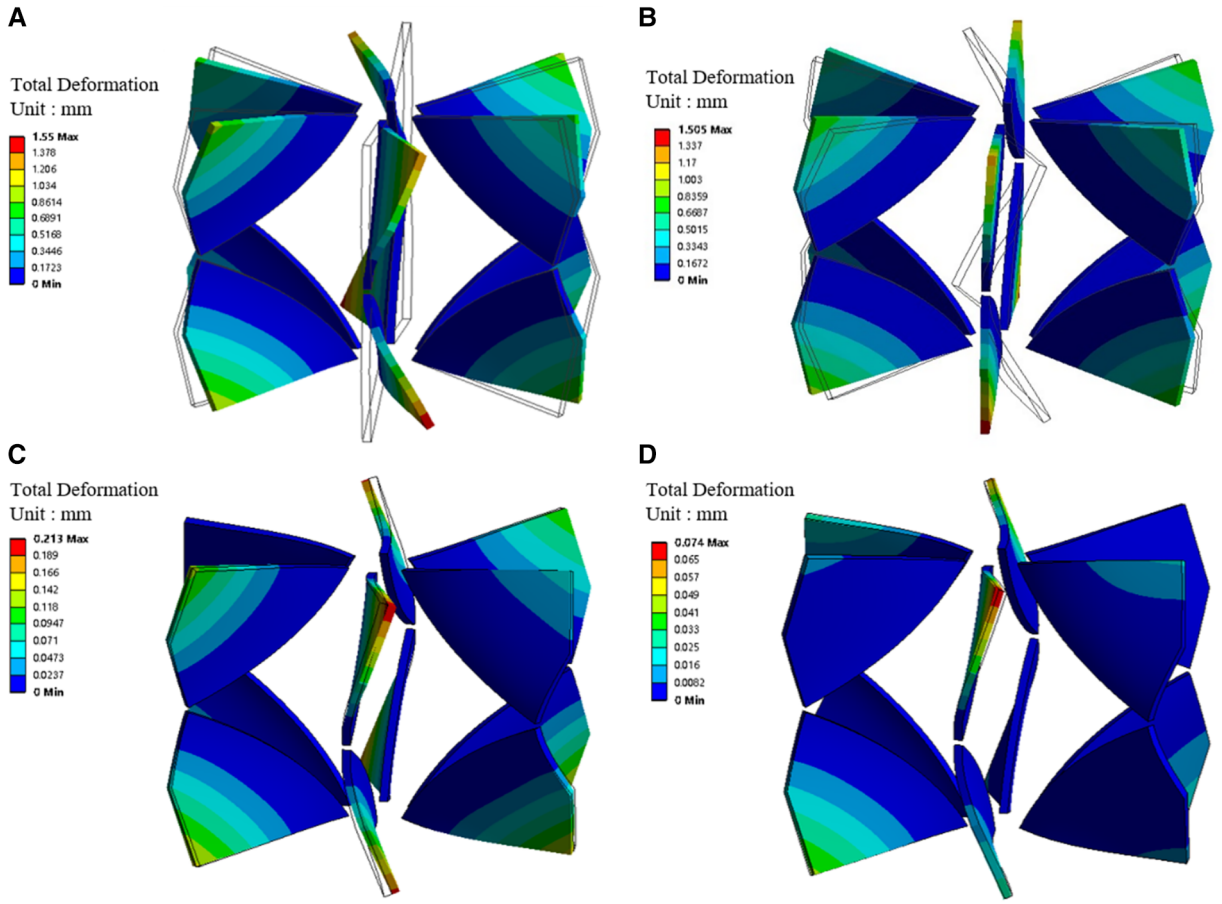

FIGURE 5
Blades' deformation during the one-way FSI simulation iterations. (**A**) Blades' deformation obtained from the first round of FSI; (**B**) Blades' deformation under stress; (**C**) Blade deformation obtained from the second round of FSI; (**D**) Blade deformation obtained from the third round of FSI. (Dotted frame represents the blade shape before deformation, solid body represents the blade shape after deformation).

CH-VAD. This result demonstrates that the assist device proposed in this paper is reliable in terms of hemolysis.

3.4 Thrombus risk corresponding to blades with different elastic moduli at two rotational speeds

Figure 8 presents the results of thrombus formation simulation, corresponding to a rotational speed of 4,000 rpm and a blade elastic modulus of 10 MPa. As mentioned earlier, the shear strain rate (SSR) is utilized to determine areas prone to thrombus growth. The concentration of AP is used for quantitatively assessing the thrombus risk. To enhance readability, the AP concentration is scaled and represented as the SAP index. This index has a minimum value of 0, corresponding to the initial AP concentration (25×10^{12} /m^3). Each unit increase indicates an increase of one millionth of the initial AP concentration. Figure 8A shows the distribution of wall SSR. It is observed that regions with SSR less than 100 /s are only present on the walls of the SVC, LPA and RPA. There are no low SSR areas on the blades' surfaces. Figure 8B, based on Figure 8A, displays grids where the SAP exceeds 23 in a dark red color. Detailed examination through close-up and cross-sectional views reveals that all four vessels exhibit wall grids with higher SAP. However, IVC lacks regions with low SSR, and the high SAP at the LPA and RPA outlets is due to the transport of AP. Only the wall of the SVC displays areas with both low SSR and high SAP, indicating that thrombus is more likely to form on the SVC wall. Figure 8C shows streamlines released from the IVC. Due to the larger flow volume in the IVC, a portion of the blood enters the SVC, leading to a collision within the SVC. This collision area has a

TABLE 1 Maximum blade deformation and blade pressure rise during three rounds of one-way FSI simulation.

	First round	Second round	Third round
Maximum blade deformation(mm)	1.551	0.213	0.074
DP-SVC (Pa)	439.14	465.94	443.36
DP-IVC (Pa)	313.45	345.36	350.05

DP-SVC indicates the blood pressure rise in the SVC, calculated as the pressure at the PA outlet minus the pressure at the SVC inlet. DP-IVC indicates the blood pressure rise in the IVC, calculated as the pressure at the PA outlet minus the pressure at the IVC inlet.

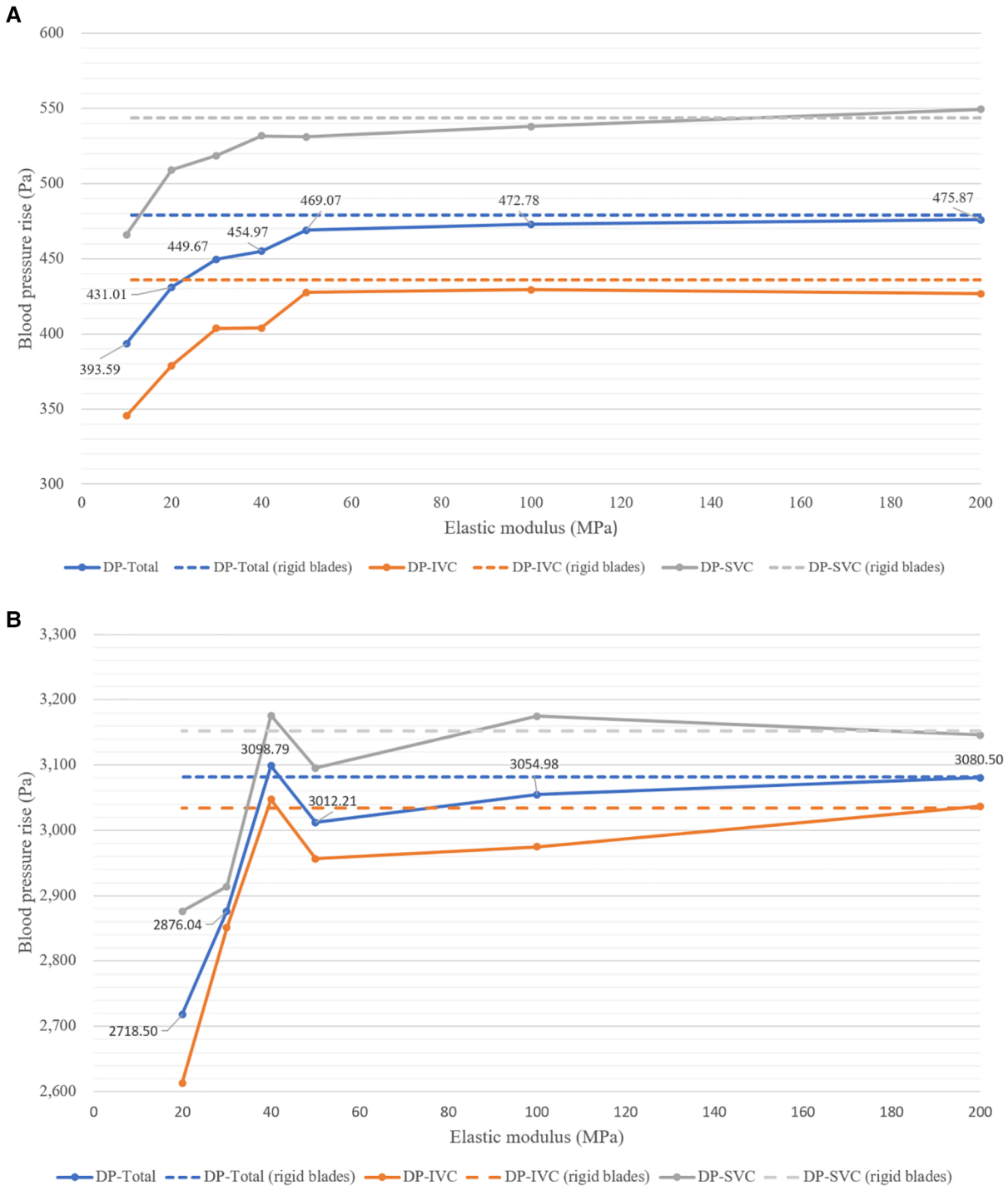

FIGURE 6
Blood pressure rise corresponding to blades with different elastic moduli at two rotational speeds. (A) At 4,000 rpm; (B) at 8,000 rpm.

low SSR, which facilitates the deposition of AP and thus the formation of thrombus. At both rotational speeds, the thrombus formation scenarios for different blades are similar to those depicted in Figure 8B. Thrombus are more likely to growth on the wall of SVC, hence separate illustrations are not provided.

A statistical analysis of the mean SAP values in the SVC for different blades provides the following insights: At 4,000 rpm, the mean SAP value for flexible blades with various elastic moduli ranges between 2.60 and 2.68, with a maximum difference of 3%. The mean SAP value for rigid blades is 2.60. As a result, the maximum difference in the thrombus risk between flexible and rigid blades is 3%. At 8,000 rpm, the mean SAP value for flexible blades with different elastic moduli ranges from 14.92 to 15.88, with a maximum

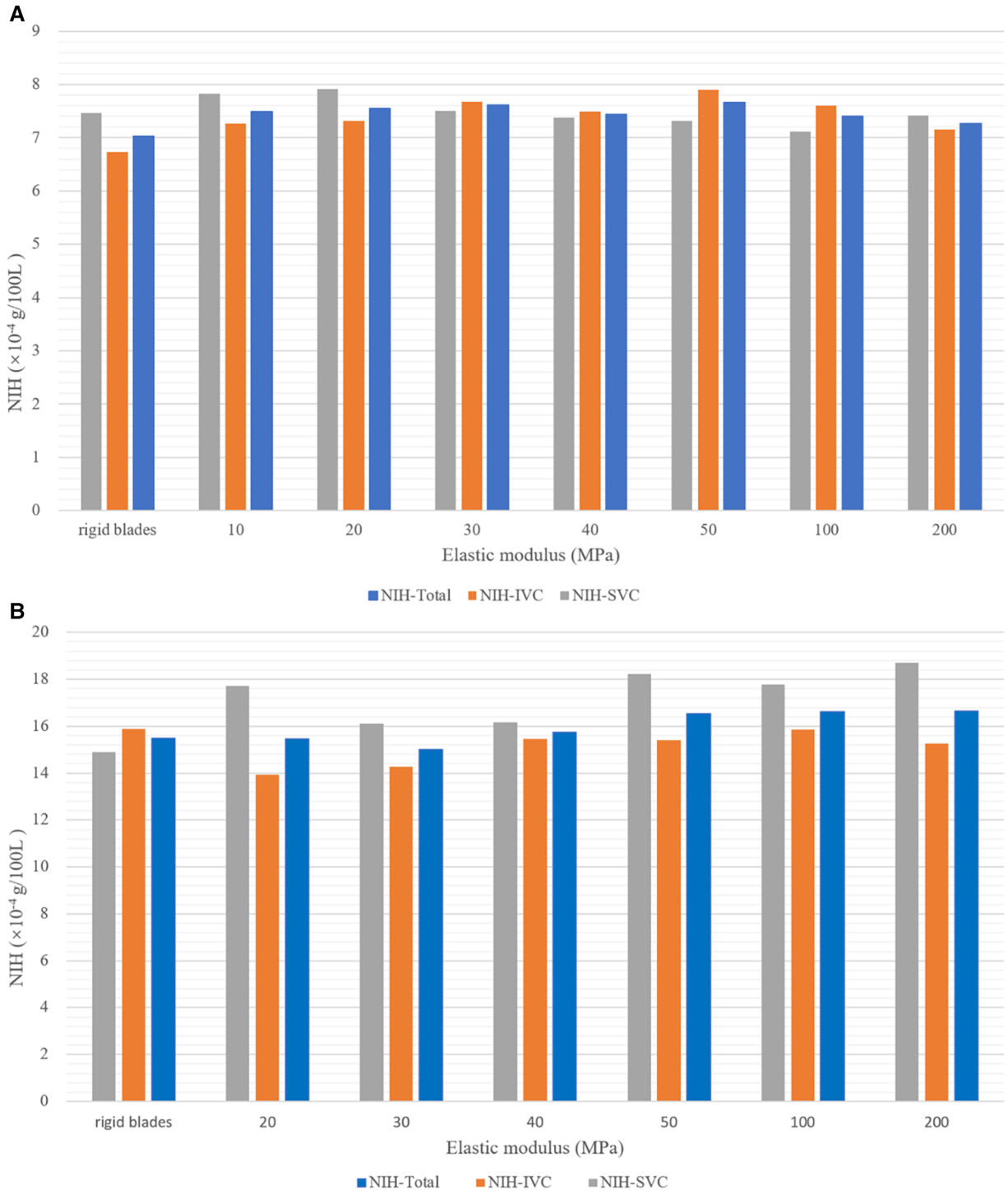

FIGURE 7
Hemolysis risk corresponding to blades with different elastic moduli at two rotational speeds. (A) At 4,000 rpm; (B) at 8,000 rpm.

difference of 6%. The mean SAP value for rigid blades is 15.24. Therefore, the maximum difference in thrombus risk between flexible and rigid blades is 4.2%. These results indicate that, in terms of thrombus formation, the impact of rotational speed is also much greater than that of blade deformation.

4 Discussion

The Fontan surgery successfully diverts venous blood into the lungs by constructing the TCPC structure. The issue of mixing between arterial and venous blood has been resolved. However, long-term reliance on a single ventricle to power both systemic

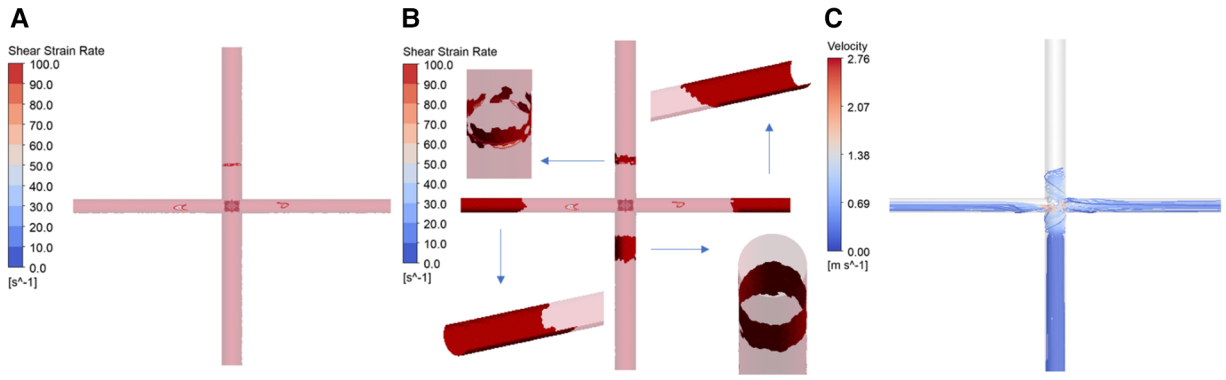

FIGURE 8
Simulation results of thrombus formation. (Corresponding to rotational speed of 4,000 rpm, blade elastic modulus of 10 MPa. (**A**) Distribution of wall shear strain rate; (**B**) thrombus distribution; (**C**) IVC streamline diagram).

and pulmonary circulations can lead to various complications, such as elevated central venous pressure, increased pre-load on the single ventricle, and insufficient pulmonary perfusion. Patients are at high risk of developing single ventricle heart failure. Numerous scholars have proposed a variety of solutions to provide additional power for the Fontan circulation. Based on the location of the assistive device, these solutions can be categorized into extracorporeal and intracorporeal assistance. Trusty et al. (29) used pulsatile blood pumps, conduits, and baffles to explore efficient extracorporeal assistance methods in an *in vitro* loop. Their findings revealed that without partitions, blood pumped out of the pump's outlet tube could be reabsorbed by the inlet tube, causing recirculation. Effective power assistance was only possible by completely separating the inlet and outlet tubes. Wang et al. (8, 9) used dual-lumen catheters and extracorporeal blood pumps for Fontan support. The successful assistance achieved was also due to the use of valves or umbrella-like membranes that separated the inlet and outlet of the dual-lumen catheters. Therefore, providing extracorporeal assistance to patients requires the addition of specific obstructions to the existing TCPC structure, increasing the number of devices and the complexity of surgery. Intracorporeal assistance methods are more convenient as they do not alter the existing TCPC structure. Among these, collapsible assist devices have a smaller size during implantation, leading to reduced invasiveness. After implantation, these devices expand, increasing in diameter. Compared to rigid devices of similar implantation size, collapsible devices operate at lower speeds to achieve the same pressure rise. Therefore, the temperature increase, mechanical wear, and blood damage during the operation of collapsible pumps are all lower (30).

In the field of ventricular assist devices, the folding mechanisms of flexible blades mainly include mechanical folding, material folding, and hybrid folding. Mechanical folding typically employs hinged structures (31–33), requiring locking components to ensure the blades' operational shape. However, the use of complex blood-immersed joint significantly increases thrombus risks. Material folding relies on the material's properties for folding, offering simpler structures (34–36). This approach requires the blades to exhibit two distinct states: one for elastic deformation into the stored position, and another to resist hydrodynamic forces during operation. The hybrid folding mechanism combines the advantages of the previous two methods. It involves designing unique structures for flexible blades to achieve structural anisotropy (37, 38). This mechanism allows the device to be both easily collapsible and capable of maintaining its operational shape. In the latter two folding mechanisms, the blade deformation and its impact on device performance are particularly crucial for product development. FSI simulation can rapidly explore relevant patterns, offering guidance for material selection and structural design.

For high-speed rotating devices, conducting two-way FSI simulation can yield results that are closer to reality. However, this method requires a significant amount of resources. At the early stage of research, employing one-way FSI simulation can also reveal certain patterns while substantially reducing resource consumption. The results demonstrate that the one-way FSI simulation described in this paper can accurately model the stable shape of flexible blades. This allows for the investigation of the impact of blade deformation on device performance, aiding in the determination of the optimal blade elastic modulus. It is important to note that one-way FSI simulation neglects the impact of blade deformation velocities and accelerations on the fluid, failing to capture transient flow fluctuations. This leads to some deviation in the calculations of blood pressure rise, hemolysis risk, and thrombus risk. However, these neglected fluctuations are primarily near the impeller, and their impact area is limited. As presented in the paper, blood pressure rise is largely determined by the rotational speed and blade morphology. Furthermore, the hemolysis risk and thrombus risk are mainly influenced by the rotational speed. Compared to these factors, the impact of flow fluctuations is relatively minor. Although one-way FSI simulation overlooks the influence of structural dynamics on the fluid, it still accurately depicts the impact of the main factors on performance indicators. This method can be further applied to the entire impeller to explore

the effect of hub deformation. For flexible left ventricular assist device, such as impella ECP (Abiomed, Danvers, MA), one-way FSI simulation is equally applicable.

This study has the following limitations: (1) It did not analyze the entire device, thus ignoring the impact of components other than the impeller on blood pressure rise, hemolysis risk, and thrombus risk; (2) Fluctuations in rotational speed caused by the operation of the brushless motor were not considered; (3) The one-way FSI simulation can't capture blades' status at each moment; (4) No experiments were conducted to verify the accuracy of the simulation results; (5) This study employs steady-state boundary conditions and an ideal TCPC model for research, neglecting the effects of blood pulsatility and real vascular geometry. The future research plans include: (1) Modeling and simulating the entire device; (2) Constructing an in-vitro experimental system, using a high-speed camera to capture the shape of flexible blades during rotation, and comparing it with the simulation results; (3) Conducting hydraulic experiments, particle image velocimetry (PIV) experiments, hemolysis experiments, and thrombosis experiments to verify the simulation results of pressure rise, velocity field, hemolysis risk, and thrombus risk; (4) Collecting data on rotational speeds during device operation and applying these varying speeds in FLUENT using a user-defined function (UDF); (5) Exploring two-way FSI simulation methods and using transient simulation to study the impact of blade flutter on the flow field; (6) Performing patient-specific studies using measured boundary conditions and real TCPC models.

5 Conclusion

This article proposed a right heart assist device equipped with flexible blades. A one-way FSI simulation was used to study the deformation of the flexible blades and its impact on the device's performance. The simulation results indicate that within the studied range (rotational speeds of 4,000 rpm and 8,000 rpm, elastic modulus between 10 MPa and 200 MPa), deformation of the flexible blades leads to a decrease in functionality. However, within a certain range of elastic modulus, the pressure rise associated with flexible blades is close to that of rigid blades. Additionally, compared to blade deformation, rotational speed has a more significant impact on the hemolysis risk and thrombus risk. After a comprehensive analysis of blade compressibility, blood pressure rise, hemolysis risk, and thrombus risk, the optimal elastic modulus for the flexible blades is determined to be between 40 MPa and 50 MPa.

Data availability statement

The original contributions presented in the study are included in the article/**Supplementary Material**, further inquiries can be directed to the corresponding author.

Ethics Statement

Ethical review and approval was not required for the study on human participants in accordance with the local legislation and institutional requirements. Written informed consent from the patients/participants was not required to participate in this study in accordance with the national legislation and the institutional requirements.

Author contributions

TC: Conceptualization, Formal Analysis, Investigation, Methodology, Software, Validation, Visualization, Writing – original draft, Writing – review & editing. XC: Conceptualization, Formal Analysis, Investigation, Methodology, Software, Validation, Writing – review & editing. XL: Methodology, Software, Writing – review & editing. HZ: Data curation, Resources, Writing – review & editing. SW: Conceptualization, Funding acquisition, Project administration, Supervision, Writing – review & editing, Resources.

Funding

The author(s) declare that financial support was received for the research, authorship, and/or publication of this article.

This research was funded by National Natural Science Foundation of China, grant number 32071310.

Conflict of interest

XL is employed by Shanghai Key Laboratory of Interventional Medical Devices and Equipment, Shanghai MicroPort Medical Group Co., Ltd, Shanghai, China.

The remaining authors declare that the research was conducted in the absence of any commercial or financial relationships that could be construed as a potential conflict of interest.

Publisher's note

All claims expressed in this article are solely those of the authors and do not necessarily represent those of their affiliated organizations, or those of the publisher, the editors and the reviewers. Any product that may be evaluated in this article, or claim that may be made by its manufacturer, is not guaranteed or endorsed by the publisher.

Supplementary material

The Supplementary Material for this article can be found online at: https://www.frontiersin.org/articles/10.3389/fcvm.2024.1377765/full#supplementary-material

References

1. Botto LD, Correa A, Erickson JD. Racial and temporal variations in the prevalence of heart defects. *Pediatrics*. (2001) 107(3):e32–32. doi: 10.1542/peds.107.3.e32

2. Pike NA, Evangelista LS, Doering LV, Griffin DK, Lewis AB, Child JS. Clinical profile of the adolescent/adult fontan survivor. *Congenit Heart Dis*. (2011) 6 (1):9–17. doi: 10.1111/j.1747-0803.2010.00475.x

3. Trusty PM, Slesnick TC, Wei ZA, Rossignac J, Kanter KR, Fogel MA, et al. Fontan surgical planning: previous accomplishments, current challenges, and future directions. *J Cardiovasc Transl*. (2018) 11:133–44. doi: 10.1007/s12265-018-9786-0

4. Khairy P, Fernandes SM, Mayer JE, Triedman JK, Walsh EP, Lock JE, et al. Long-term survival, modes of death, and predictors of mortality in patients with fontan surgery. *Circulation*. (2008) 117:85–92. doi: 10.1161/CIRCULATIONAHA.107.738559

5. Rodefeld MD, Frankel SH, Giridharan GA. Cavopulmonary assist: (em)powering the univentricular fontan circulation. *Semin Throac Cardiov*. (2011) 14:45–54. doi: 10.1053/j.pcsu.2011.01.015

6. Bhavsar SS, Moskowitz WB, Throckmorton AL. Interaction of an idealized cavopulmonary circulation with mechanical circulatory assist using an intravascular rotary blood pump. *Artif Organs*. (2010) 34:816–27. doi: 10.1111/j.1525-1594.2010.01080.x

7. Throckmorton AL, Lopez Isaza S, Moskowitz W. Dual-pump support in the inferior and superior vena cavae of a patient-specific fontan physiology. *Artif Organs*. (2013) 37:513–22. doi: 10.1111/aor.12039

8. Wang D, Gao G, Plunkett M, Zhao G, Topaz S, Ballard-Croft C, et al. A paired membrane umbrella double-lumen cannula ensures consistent cavopulmonary assistance in a fontan sheep model. *J Thorac Cardiovasc Surg*. (2014) 148:1041–7. doi: 10.1016/j.jtcvs.2014.04.051

9. Zhou C, Wang D, Condemi F, Zhao G, Topaz S, Ballard-Croft C, et al. Avalonelite double lumen cannula for total cavopulmonary assist in failing fontan sheep model with valved extracardiac conduit. *Asaio J*. (2019) 65:361–6. doi: 10.1097/MAT.0000000000000817

10. Gandolfo F, Brancaccio G, Donatiello S, Filippelli S, Perri G, Iannace E, et al. Mechanically assisted total cavopulmonary connection with an axial flow pump: computational and in vivo study. *Artif Organs*. (2016) 40:43–9. doi: 10.1111/aor.12641

11. Zhao ZX, Chen T, Liu XD, Wang SZ, Lu HY. Numerical investigation of an idealized total cavopulmonary connection physiology assisted by the axial blood pump with and without diffuser. *Comput Model Eng Sci*. (2020) 125(3):1173–84. doi: 10.32604/cmes.2020.013702

12. Hirschhorn M, Bisirri E, Stevens R, Throckmorton AL. Fluid-structure interaction analysis of a collapsible axial flow blood pump impeller and protective cage for fontan patients. *Artif Organs*. (2020) 44:E337–47. doi: 10.1111/aor.13685

13. Chen T, Liu X, Si B, Feng Y, Zhang H, Jia B, et al. Comparison between single-phase flow simulation and multiphase flow simulation of patient-specific total cavopulmonary connection structures assisted by a rotationally symmetric blood pump. *Symmetry (Basel)*. (2021) 13:912. doi: 10.3390/sym13050912

14. Jagani J, Mack E, Gong J, Untaroiu A. Effect of stent design parameters on hemodynamics and blood damage in a percutaneous cavopulmonary assist device. *ASME*. (2018) 51562:V002T11A007. doi: 10.1115/FEDSM2018-83210

15. Pei J, Meng F, Li Y, Yuan S, Chen J. Fluid–structure coupling analysis of deformation and stress in impeller of an axial-flow pump with two-way passage. *Adv Mech Eng*. (2016) 8:168781401664626. doi: 10.1177/1687814016646266

16. TPU. Unspecified (2024). Available online at: https://www.plasdata.com/ (accessed January 25, 2024).

17. Bludszuweit C. Three-dimensional numerical prediction of stress loading of blood particles in a centrifugal pump. *Artif Organs*. (1995) 19:590–6. doi: 10.1111/j.1525-1594.1995.tb02386.x

18. Giersiepen M, Wurzinger LJ, Opitz R, Reul H. Estimation of shear stress-related blood damage in heart valve prostheses–in vitro comparison of 25 aortic valves. *Int J Artif Organs*. (1990) 13:300–6. doi: 10.1177/039139889001300507

19. Throckmorton AL, Kishore RA. Design of a protective cage for an intravascular axial flow blood pump to mechanically assist the failing fontan. *Artif Organs*. (2009) 33:611–21. doi: 10.1111/j.1525-1594.2009.00779.x

20. Mitamura Y, Nakamura H, Sekine K, Kim DW, Youzu R, Kawada S, et al. Prediction of hemolysis in rotary blood pumps with computational fluid dynamics analysis. *J CongestHeart Fail Circ Supp*. (2001) 1(4):331–6. doi: 10.1201/B14731-35

21. Heuser G, Opitz R. A couette viscometer for short time shearing in blood. *Biorheology*. (1980) 17(1-2):17–24. doi: 10.3233/BIR-1980-171-205

22. Malinauskas RA, Hariharan P, Day SW, Herbertson LH, Buesen M, Steinseifer U, et al. FDA benchmark medical device flow models for CFD validation. *Asaio J*. (2017) 63:150–60. doi: 10.1097/MAT.0000000000000499

23. Blackshear PL, Dorman FD, Steinbach JH. Some mechanical effects that influence hemolysis. *ASAIO J*. (1965) 11(1):112–7. doi: 10.1097/00002480-196504000-00022

24. Copeland JG, Copeland H, Gustafson M, Mineburg N, Covington D, Smith RG, et al. Experience with more than 100 total artificial heart implants. *J Thorac Cardiovasc Surg*. (2012) 143:727–34. doi: 10.1016/j.jtcvs.2011.12.002

25. Goel MS, Diamond SL. Adhesion of normal erythrocytes at depressed venous shear rates to activated neutrophils, activated platelets, and fibrin polymerized from plasma. *Blood*. (2002) 100:3797–803. doi: 10.1182/blood-2002-03-0712

26. Menichini C, Xu XY. Mathematical modeling of thrombus formation in idealized models of aortic dissection: initial findings and potential applications. *J Math Biol*. (2016) 73:1205–26. doi: 10.1007/s00285-016-0986-4

27. Blum C, Groß-Hardt S, Steinseifer U, Neidlin M. An accelerated thrombosis model for computational fluid dynamics simulations in rotary blood pumps. *Cardiovasc Eng Techn*. (2022) 13:638–49. doi: 10.1007/s13239-021-00606-y

28. Berk ZBK, Zhang J, Chen Z, Tran D, Griffith BP, Wu Z. Evaluation of in vitro hemolysis and platelet activation of a newly developed maglev LVAD and two clinically used LVADs with human blood. *Artif Organs*. (2019) 43:870–9. doi: 10.1111/aor.13471

29. Trusty PM, Tree M, Vincent D, Naber JP, Maher K, Yoganathan AP, et al. In vitro examination of the VentriFlo true pulse pump for failing fontan support. *Artif Organs*. (2019) 43:181–8. doi: 10.1111/aor.13301

30. Hsu PL, McIntyre M, Kuetting M, Jack P, Christina E, Rudiger A, et al. Review of recent patents on foldable ventricular assist device. *Recent Patents Biomed Eng (Discontinued)*. (2012) 5(3):208–22. doi: 10.2174/1874764711205030208

31. Reitan Ö, Epple K. Catheter Pump for Circulatory Support. United States Patent US 20110034874 (2011).

32. Siess T. Foldable Intravascularly Inserted Blood Pump. United States Patent US 20080103591 (2008).

33. Röhn D. Radially Compressible and Expandable Rotor for a Fluid Pump. Would Intellectual Property Organization Patent WO 2011076439 (2011).

34. McBride MW, Mallison TM, Dillon GP, Campbell RL, Boger DA, Hambrie SA, et al. Expandable Impeller Pump. United States Patent US 7927068 (2011).

35. Schmitz-Rode T, Günther RW. Self-deploying Axial-flow Pump Introduced Intravascularly for Temporary Cardiac Support. United States Patent US 6533716 (2003).

36. Pfeffer JG, Schmitz-Rode T, Günther RW. Catheter Device. United States Patent US 20090093764 (2009).

37. Töllner T. Compressible and Expandable Blade for a Fluid Pump. Would Intellectual Property Organization Patent WO 2010149393 (2010).

38. Töllner T, Scheckel M. Radially Compressible and Expandable Rotor for a Pump Having an Impeller Blade. Would Intellectual Property Organization patent WO 2012007140 (2012).

frontiers | Frontiers in Cardiovascular Medicine

TYPE Original Research
PUBLISHED 17 April 2024
DOI 10.3389/fcvm.2024.1297218

Check for updates

OPEN ACCESS

EDITED BY
Gaoyang Li,
Tohoku University, Japan

REVIEWED BY
Jianfeng Wang,
Soochow University, China
Greta Ziubryte,
Lithuanian University of Health Sciences, Lithuania
Zhou Zhao,
Peking University People's Hospital, China

*CORRESPONDENCE
Qin Chen
ndcq@163.com
Yukun Luo
luoyukun@hotmail.com

RECEIVED 20 September 2023
ACCEPTED 22 March 2024
PUBLISHED 17 April 2024

CITATION
Chen L, Zhong J, Hong R, Chen Y, Li B, Wang L, Yan Y, Chen L, Chen Q and Luo Y (2024) Predictive value of the inconsistency between the residual and post-PCI QFR for prognosis in PCI patients.
Front. Cardiovasc. Med. 11:1297218.
doi: 10.3389/fcvm.2024.1297218

COPYRIGHT
© 2024 Chen, Zhong, Hong, Chen, Li, Wang, Yan, Chen, Chen and Luo. This is an open-access article distributed under the terms of the Creative Commons Attribution License (CC BY). The use, distribution or reproduction in other forums is permitted, provided the original author(s) and the copyright owner(s) are credited and that the original publication in this journal is cited, in accordance with accepted academic practice. No use, distribution or reproduction is permitted which does not comply with these terms.

Predictive value of the inconsistency between the residual and post-PCI QFR for prognosis in PCI patients

Lihua Chen[1,2,3,4], Jiaxin Zhong[1,2,3], Ruijin Hong[1,2,3], Yuxiang Chen[1,2,3], Beilei Li[1,2,3], Laicheng Wang[1,2,3], Yuanming Yan[1,2,3], Lianglong Chen[1,2,3], Qin Chen[1,2,3]* and Yukun Luo[1,2,3]*

[1]Department of Cardiology, Fujian Medical University Union Hospital, Fuzhou, Fujian, China, [2]Fujian Institute of Coronary Heart Disease, Fujian Medical University Union Hospital, Fuzhou, Fujian, China, [3]Fujian Heart Medical Center, Fujian Medical University Union Hospital, Fuzhou, Fujian, China, [4]Changle District People's Hospital Cardiovascular Department, Fuzhou, Fujian, China

Introduction: To investigate the prognostic value of the consistency between the residual quantitative flow ratio (QFR) and postpercutaneous coronary intervention (PCI) QFR in patients undergoing revascularization.
Methods: This was a single-center, retrospective, observational study. All enrolled patients were divided into five groups according to the ΔQFR (defined as the value of the post-PCI QFR minus the residual QFR): (1) Overanticipated group; (2) Slightly overanticipated group; (3) Consistent group; (4) Slightly underanticipated group; and (5) Underanticipated group. The primary outcome was the 5-year target vessel failure (TVF).
Results: A total of 1373 patients were included in the final analysis. The pre-PCI QFR and post-PCI QFR were significantly different among the five groups. TVF within 5 years occurred in 189 patients in all the groups. The incidence of TVF was significantly greater in the underanticipated group than in the consistent group ($P = 0.008$), whereas no significant differences were found when comparing the underanticipated group with the other three groups. Restricted cubic spline regression analysis showed that the risk of TVF was nonlinearly related to the ΔQFR. A multivariate Cox regression model revealed that a ΔQFR≤ −0.1 was an independent risk factor for TVF.
Conclusions: The consistency between the residual QFR and post-PCI QFR may be associated with the long-term prognosis of patients. Patients whose post-PCI QFR is significantly lower than the residual QFR may be at greater risk of TVF. An aggressive PCI strategy for lesions is anticipated to have less functional benefit and may not result in a better clinical outcome.

KEYWORDS

quantitative flow ratio, percutaneous coronary intervention, coronary artery disease, target vessel failure, prognostic value

Introduction

Percutaneous coronary intervention (PCI) is widely recognized in clinical practice to improve the symptoms and outcomes of patients with coronary artery disease (CAD) (1, 2). Despite the established benefits of PCI, certain patients who undergo successful PCI still experience adverse cardiovascular events (3). Conventional coronary angiography can provide information only on the contour of the culprit vessel and

may not account for physiological dysfunction, which explains the unanticipated adverse events in patients undergoing successful revascularization (4).

Physiological assessments are of increasing importance because of their ability to provide functional information about target vessels and to optimize treatment strategies (5, 6). Fractional flow reserve (FFR) is a widely accepted physiological assessment technique and is considered the gold standard in revascularization procedures (7, 8). Although the FFR provides significant functional information, it is still underutilized in clinical practice due to the prolonged procedure time and invasive use of guidewires (9, 10). The quantitative flow ratio (QFR) has emerged as an alternative approach for deriving physiological parameters, with the advantages of having equivalent diagnostic value and being faster and more convenient than the FFR (11, 12).

The residual QFR is an essential indicator derived from the QFR computation procedure and can simulate the anticipated QFR value after successful revascularization based on pre-PCI angiographic images (13). Previous studies have reported that the residual QFR significantly correlates with the post-PCI FFR, especially in patients with suboptimal PCI results (14). Based on the residual QFR, a cardiologist can identify the major lesion from a functional perspective, further optimizing the PCI strategy. The residual QFR-guided PCI strategy was superior to angiographic guidance in reducing the 2-year incidence of target vessel failure (TVF) (15, 16). However, research into the predictive value of the residual QFR for adverse events is limited, particularly in patients whose residual QFR does not match their post-PCI QFR. Therefore, the present study aimed to further investigate the prognostic value of the residual QFR by exploring the correlation between the ΔQFR (defined as the value of the post-PCI QFR minus the residual QFR) and clinical outcomes.

Materials and methods

Study design

The present research was a single-center, retrospective, observational study. Consecutive patients who underwent PCI were recruited from January 1, 2016, to December 31, 2017, at Fujian Medical University Union Hospital. The QFR of the enrolled patients were retrospectively assessed at the different time points of the PCI procedure, and the patients were further divided into five groups according to the ΔQFR: (1) Overanticipated group: $\Delta QFR \geq 0.1$; (2) Slightly overanticipated group: $0 < \Delta QFR < 0.1$; (3) Consistent group: $\Delta QFR = 0$; (4) Slightly underanticipated group: $-0.1 < \Delta QFR < 0$; and (5) Underanticipated group: $\Delta QFR \leq -0.1$. The primary purpose of this study was to test the prognostic value of the consistency between the residual QFR and post-PCI for cardiovascular adverse events. This study was approved by the Ethics Committee of Fujian Medical University Union Hospital (No. 2020KY098).

The study population consisted of adult patients who underwent successful PCI, including patients with stable or unstable angina pectoris, non-ST elevation myocardial infarction (NSTEMI), or ST elevation myocardial infarction (STEMI), over 7 days. All enrolled patients met the requirements for QFR computation, which suggests that in all patients, at least one lesion with a percent diameter stenosis (DS%) between 50% and 90% is present in a coronary artery with a reference vessel diameter of ≥2.5 mm according to visual assessment. Patients were excluded if they had any of the following criteria: (1) acute myocardial infarction (AMI) within 7 days, (2) lack of follow-up data, or (3) inability to perform QFR computation, including patients who only had one coronary artery lesion with >90% stenosis and a TIMI grade <3; the interrogated lesion involving the myocardial bridge; severe overlap in the stenosed segment or severe tortuosity of any interrogated vessel; or poor angiographic image quality.

PCI procedure and QFR computation

PCI was performed, and the stenting strategy was determined by an experienced cardiologist according to the ESC/EACTS guidelines at the time of enrollment (17). All patients received standard dual antiplatelet therapy for at least 12 months after successful revascularization. Rational medication was prescribed according to the clinical situation.

The QFR was computed using the AngioPlus system (Pulse Medical Imaging Technology Shanghai, China) according to standard operating procedures, which were performed by two independent investigators blinded to the clinical data. All coronary angiography images were transferred locally to the AngioPlus system. Angiographic images were recorded with an AngioPlus system at a rate of 15 frames/second. Two angiographic image runs, acquired at angles greater than or equal to 25 degrees, were transferred to the QFR system via the local network. Based on the reconstruction of the contoured vessels, the QFR value was computed using a contrast flow velocity model. The QCA information derived from the QFR analysis of the interrogated vessels consisted of the minimum lumen diameter (MLD), diameter stenosis percentage (DS%) and area stenosis percentage (AS%).

Data collection and clinical outcomes

The biochemical indices and examination results, including low-density lipoprotein cholesterol (LDL-C), fasting blood glucose, creatinine, N-terminal pro brain natriuretic peptide (NT-proBNP), troponin I, left ventricular ejection fraction (LVEF), and E/E′, were recorded. E/E′ is the ratio of the peak mitral early filling velocity (E) to the early diastolic mitral annular velocity (E′), as an indicator of diastolic cardiac function.

Target vessel failure (TVF) was defined as a combination of cardiogenic death, target vessel-related myocardial infarction and target vessel revascularization (TVR) (18). TVR was defined as a repeat PCI or surgical bypass of any segment of the target vessel,

including the target lesion (18). All patients were followed for 5 years and received optimal guideline-based medical therapy during follow-up.

Statistical analysis

Continuous variables are expressed as the mean ± standard deviation (SD) or median [interquartile range (IQR)]. Categorical variables are expressed as numbers (percentages). Continuous variables were compared by ANOVA or the Kruskal–Wallis test, and categorical variables were compared by chi-squared analysis. The association between the ΔQFR and 5-year TVF in the five groups was estimated by the Kaplan–Meier method and compared by the log-rank test. Restricted cubic spline regression analysis was used to assess the association between the ΔQFR and the hazard ratio (HR) for TVF. A 2-sided P value < 0.05 was considered to indicate statistical significance. All analyses were performed with R software version 4.1.1 (R Foundation for Statistical Computing, Vienna, Austria) and SPSS version 26 (IBM, Inc., New York, NY, USA).

Results

Study population

Between January 1, 2016, and December 31, 2017, 1,986 patients who underwent PCI were screened for enrollment; 268 patients were excluded due to meeting the clinical exclusion criteria, and 345 patients were excluded due to meeting the angiographic exclusion criteria. The remaining 1,373 patients were included in the final analysis. According to the ΔQFR, all enrolled patients were further divided into five groups: (1) the overanticipated group: ΔQFR ≥ 0.1, $n = 105$; (2) the slightly overanticipated group: $0 < \Delta QFR < 0.1$, $n = 536$; (3) the consistent group: ΔQFR = 0, $n = 257$; (4) the slightly underanticipated group: $-0.1 < \Delta QFR < 0$, $n = 390$; and (5) the underanticipated group: ΔQFR ≤ −0.1, $n = 85$. (Figure 1).

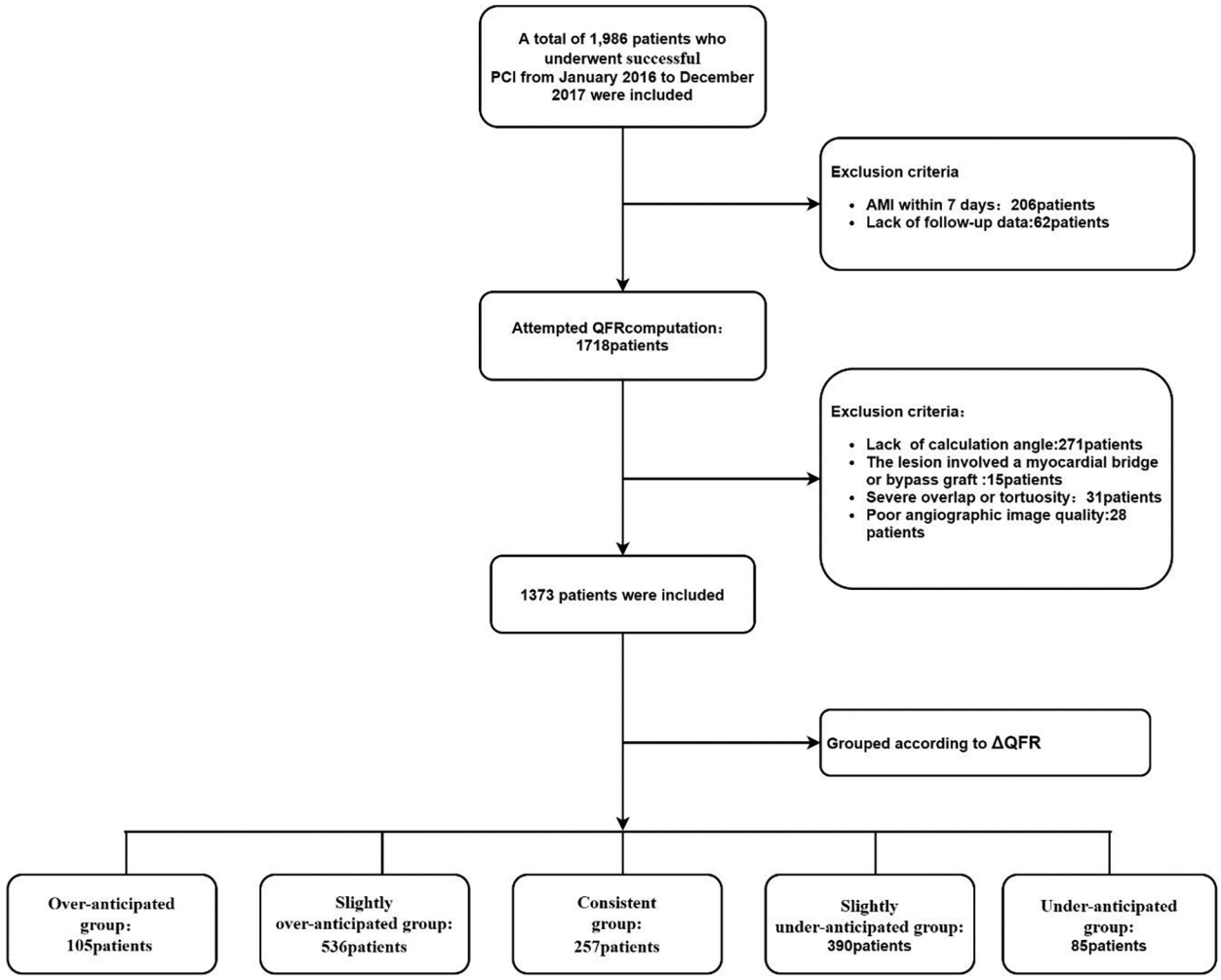

FIGURE 1
Study flowchart. PCI, percutaneous coronary intervention; STEMI, ST-segment elevation myocardial infarction; QFR, quantitative flow ratio; ΔQFR = post-PCI QFR—residual QFR.

Clinical baseline characteristics

The baseline characteristics are shown in Table 1. No significant differences were found between the groups with regard to age, sex, smoking status, hypertension, diabetes, previous MI, previous PCI, type of coronary artery disease, or post-PCI medication. Patients in the five groups had similar pre-PCI results for troponin I, LDL-C, NT-proBNP, blood glucose, serum creatinine, LVEF and E/E′.

QCA and QFR analysis

The results of the QCA and QFR analyses are summarized in Tables 2, 3. In terms of target vessel locations, the consistent group had a greater proportion of LCX (22.6%) and a lower proportion of LAD (47.5%). Compared with those in the consistent group, the patients in the overanticipated group had longer stents (43.42 ± 17.47 vs. 31.41 ± 14.12, $P < 0.001$), more stents (1.65 ± 0.62 vs. 1.23 ± 0.45, $P < 0.001$), and similar stent diameters (3.03 ± 0.42 vs. 3.11 ± 0.44, $P = 0.056$).

There was a significant difference in the pre-PCI QFR among the five groups ($P < 0.001$), with lower pre-PCI QFRs in the overanticipated group and underanticipated group. Significant differences in the post-PCI QFR were found in the five groups, of which the underanticipated group had a significantly worse post-PCI QFR than the other groups. No significant differences in DS%, AS% or MLD were found among the five groups at pre-PCI, whereas a difference was found for the post-PCI between the groups.

Clinical outcomes

A five-year follow-up was completed for all eligible patients, with a median follow-up of 61 months. Comparisons of the clinical outcomes between the 5 groups are shown in Table 4. TVF occurred within 5 years in 189 patients in all the groups; 14 patients were in the overanticipated group, 66 patients were in the slightly overanticipated group, 30 patients were in the consistent group, 60 patients were in the slightly underanticipated group, and 19 patients were in the underanticipated group. The consistent group had the lowest incidence of TVF, and the underanticipated group had the highest risk of TVF. Supplementary Table S1 compares the difference in the incidence of TVF between the consistent group

TABLE 1 Baseline characteristics.

	Total ($N = 1,373$)	Overanticipated group ($N = 105$)	Slightly overanticipated group ($N = 536$)	Consistent group ($N = 257$)	Slightly underanticipated group ($N = 390$)	Underanticipated group ($N = 85$)	P value
Age (years)	65.05 ± 10.43	66.38 ± 11.26	65.04 ± 10.65	64.68 ± 10.16	64.67 ± 10.08	66.31 ± 10.16	0.438
Male, *n* (%)	1,057 (77.0)	82 (77.0)	408 (76.1)	193 (75.1)	309 (79.2)	65 (76.5)	0.747
Hypertension, *n*(%)	925 (67.4)	77 (73.3)	353 (65.9)	169 (65.8)	270 (69.2)	56 (65.9)	0.515
Diabetes, *n* (%)	472 (34.4)	41 (39.0)	179 (33.4)	80 (31.1)	137 (35.1)	35 (41.2)	0.369
Previous MI, *n* (%)	109 (7.9)	5 (4.8)	37 (6.9)	27 (10.5)	33 (8.5)	7 (8.2)	0.318
Previous PCI, *n* (%)	177 (12.9)	14 (13.3)	68 (12.7)	30 (11.7)	52 (13.3)	13 (15.3)	0.927
Smoking history, *n* (%)	722 (52.6)	52 (49.5)	283 (52.8)	130 (50.6)	213 (54.6)	44 (51.8)	0.829
Type of coronary artery disease							0.679
Unstable angina, *n* (%)	782 (57.0)	58 (55.2)	303 (56.5)	158 (61.5)	222 (56.9)	41 (48.2)	
Stable angina, *n* (%)	142 (10.3)	11 (10.5)	58 (10.8)	27 (10.5)	38 (9.7)	8 (9.4)	
NSTEMI, *n* (%)	251 (18.3)	23 (21.9)	100 (18.7)	37 (14.4)	69 (17.7)	22 (25.9)	
STEMI (≥7 days), *n* (%)	198 (14.4)	13 (12.4)	75 (14.0)	35 (13.6)	61 (15.6)	14 (16.5)	
Medications at discharge							
Antiplatelet agent, *n* (%)	1,371 (99.9)	105 (100.0)	536 (100.0)	256 (99.6)	389 (99.7)	85 (100.0)	0.656
Statin, *n* (%)	1,348 (98.2)	103 (98.2)	529 (98.7)	248 (96.5)	385 (98.7)	83 (97.6)	0.229
ACEI/ARB, *n*(%)	929 (67.7)	71 (67.6)	369 (68.8)	176 (68.5)	258 (66.2)	55 (64.7)	0.884
Troponin I(ug/L)	4.15 ± 10.90	2.44 ± 7.04	3.70 ± 10.01	4.39 ± 11.49	5.01 ± 12.18	4.10 ± 11.84	0.669
NT-proBNP (pg/ml)	191.5 (62.0,792.3)	347.5 (110.5,1,123.0)	185.0 (58.0,700.0)	160.0 (53.0,675.0)	198.0 (67.0,845.8)	220.0 (58.5,873.3)	0.758
Glucose (mmol/L)	6.34 ± 2.46	6.32 ± 2.10	6.46 ± 2.69	6.06 ± 2.18	6.33 ± 2.39	6.43 ± 2.46	0.313
Creatinine (umol/L)	86.65 ± 56.11	91.93 ± 31.65	87.95 ± 66.60	81.76 ± 45.55	86.84 ± 56.18	85.88 ± 29.23	0.530
LDL-C (mmol/L)	2.84 ± 1.03	2.89 ± 1.09	2.84 ± 1.04	2.86 ± 1.04	2.79 ± 1.02	2.89 ± 0.97	0.835
LVEF (%)	60.21 ± 11.37	60.09 ± 13.37	60.87 ± 10.66	60.75 ± 11.48	59.35 ± 11.46	58.29 ± 12.09	0.146
E/E′	13.63 ± 5.70	14.53 ± 6.32	13.45 ± 5.55	13.60 ± 6.01	13.67 ± 5.62	13.66 ± 5.33	0.563

The values are presented as the mean ± standard deviation, median (interquartile range) or *n* (%).
NSTEMI, Non-ST elevation myocardial infarction; STEMI, ST-segment elevation myocardial infarction; MI, myocardial infarction; PCI, percutaneous coronary intervention; ACEI, angiotensin-converting-enzyme inhibitor; ARB, angiotensin II receptor blocker; NT-proBNP, N-terminal pro-B type natriuretic peptide; LDL-C, low-density lipoprotein cholesterol; LVEF, left ventricular ejection fraction; E/E′, ratio of early diastolic mitral flow velocity to early diastolic mitral ring motion velocity.

TABLE 2 The results of the QCA and QFR analysis.

	Total ($N = 1,373$)	Overanticipated group ($N = 105$)	Slightly overanticipated group ($N = 536$)	Consistent group ($N = 257$)	Slightly underanticipated group ($N = 390$)	Underanticipated group ($N = 85$)	*P* value
Target vessel							0.015
LAD, *n* (%)	794	69 (65.7)[b]	319 (59.5)[b]	122 (47.5)[a]	232 (59.5)[b]	52 (61.2)[a]	
LCX, *n* (%)	223	15 (14.3)[a,b]	75 (14.0)[b]	58 (22.6)[a]	64 (16.4)[a,b]	11 (12.9)[a,b]	
RCA, *n* (%)	356	21 (20.0)[a]	142 (26.5)[a]	77 (30.0)[a]	94 (24.1)[a]	22 (25.9)[a]	
Pre-PCI							
DS (%)	57.51 ± 12.09	56.61 ± 11.52	56.88 ± 12.52	57.94 ± 12.50	58.13 ± 11.89	58.36 ± 9.36	0.433
AS (%)	77.44 ± 11.83	76.58 ± 10.96	76.91 ± 11.75	76.61 ± 11.83	78.51 ± 12.49	79.51 ± 9.83	0.069
MLD (mm)	1.15 ± 0.59	1.10 ± 0.39	1.13 ± 0.43	1.15 ± 0.47	1.19 ± 0.85	1.17 ± 0.47	0.535
QFR	0.68 ± 0.18	0.59 ± 0.13	0.70 ± 0.16	0.73 ± 0.16	0.65 ± 0.19	0.56 ± 0.20	<0.001
Residual QFR	0.96 ± 0.05	0.84 ± 0.04	0.95 ± 0.04	0.99 ± 0.03	0.97 ± 0.03	0.96 ± 0.06	<0.001
Post-PCI							
DS (%)	25.70 ± 10.74	23.63 ± 8.75	21.83 ± 8.35	20.44 ± 8.21	31.26 ± 8.84	43.10 ± 11.88	<0.001
AS (%)	38.38 ± 16.37	33.70 ± 13.53	32.44 ± 14.13	29.68 ± 13.74	47.90 ± 11.04	64.28 ± 12.44	<0.001
MLD (mm)	2.02 ± 0.54	1.97 ± 0.40	2.09 ± 0.50	2.20 ± 0.51	1.90 ± 0.55	1.58 ± 0.57	<0.001
QFR	0.96 ± 0.06	0.98 ± 0.03	0.98 ± 0.03	0.99 ± 0.03	0.94 ± 0.04	0.79 ± 0.10	<0.001

The values are presented as the mean ± standard deviation (*n*%).
PCI, percutaneous coronary intervention; LAD, left anterior descending coronary artery; LCX, left circumflex coronary artery; RCA, right coronary artery; AS, area stenosis; DS, diameter stenosis; MLD, minimal lumen diameter; QFR, quantitative flow ratio.
Each letter represents a subset of the group based on the difference level between residual QFR and post-PCI QFR, the same letter means no significant, with no significant difference between groups at $p = 0.05$ level.

TABLE 3 Parameters related to the stent.

	Overanticipated group ($N = 105$)	Slightly overanticipated group ($N = 536$)	Consistent group ($N = 257$)	Slightly underanticipated group ($N = 390$)	Underanticipated group ($N = 85$)	*P* value
Stent diameter(mm)	3.03 ± 0.42	3.03 ± 0.41	3.11 ± 0.44	3.03 ± 0.41	2.96 ± 0.41	0.023
Stent length(mm)	43.42 ± 17.47	32.86 ± 17.25	31.41 ± 14.12	30.80 ± 13.66	29.09 ± 15.70	<0.001
Number of stents	1.65 ± 0.62	1.32 ± 0.55	1.23 ± 0.45	1.25 ± 0.47	1.31 ± 0.49	<0.001

The values are presented as the mean ± standard deviation [*n* (%)].

and the other groups. Supplementary Table S2 shows shows that TVF is independent of target vessel distribution. The incidence of TVF was significantly greater in the underanticipated group than in the consistent group ($P = 0.008$), whereas no significant differences were found when comparing the underanticipated group with the other three groups.

The Kaplan-Meier method was used to further confirm the difference in the incidence of TVF among the five groups (Figures 2, 3). There was a significant difference in the risk of 5-year TVF among the five groups (log-rank $P = 0.039$). The incidence of TVF was lower in the consistent group than in the underanticipated group (HR = 0.068, 95% CI = 0.51–0.90, $P = 0.008$), while no significant differences were found between the consistent group and the remaining three groups.

Restricted cubic spline regression analysis was used to analyze and visualize the association between ΔQFR and TVF (Figure 4). As the ΔQFR increased, the hazard ratio of TVF first decreased and then gradually increased.

TABLE 4 Clinical outcomes at the 5-year follow-up.

	Overanticipated group ($N = 105$)	Slightly overanticipated group ($N = 536$)	Consistent group ($N = 257$)	Slightly underanticipated group ($N = 390$)	Underanticipated group ($N = 85$)	*P* value
TVF, *n* (%)	14 (13.3)[a,b]	66 (12.3)[b]	30 (11.3)[b]	60 (15.4)[a,b]	19 (22.4)[a]	0.076
Cardiovascular death, *n* (%)	6 (5.7)	30 (5.6)	14 (5.4)	25 (6.4)	3 (3.5)	0.885
MI, *n* (%)	1 (1.0)	11 (2.1)	2 (0.8)	5 (1.3)	3 (3.5)	0.363
TVR, *n* (%)	7 (6.7)[a,b]	32 (6.0)[a]	15 (5.8)[a]	33 (8.5)[a,b]	13(15.3)[b]	0.025

The values are presented as *n* (%).
PCI, percutaneous coronary intervention; TVF, target vessel failure. MI, myocardial infarction; TVR, target vessel revascularization.
Each letter represents a subset of the group based on the difference level between residual QFR and post-PCI QFR, the same letter means no significant, with no significant difference between groups at $p = 0.05$ level.

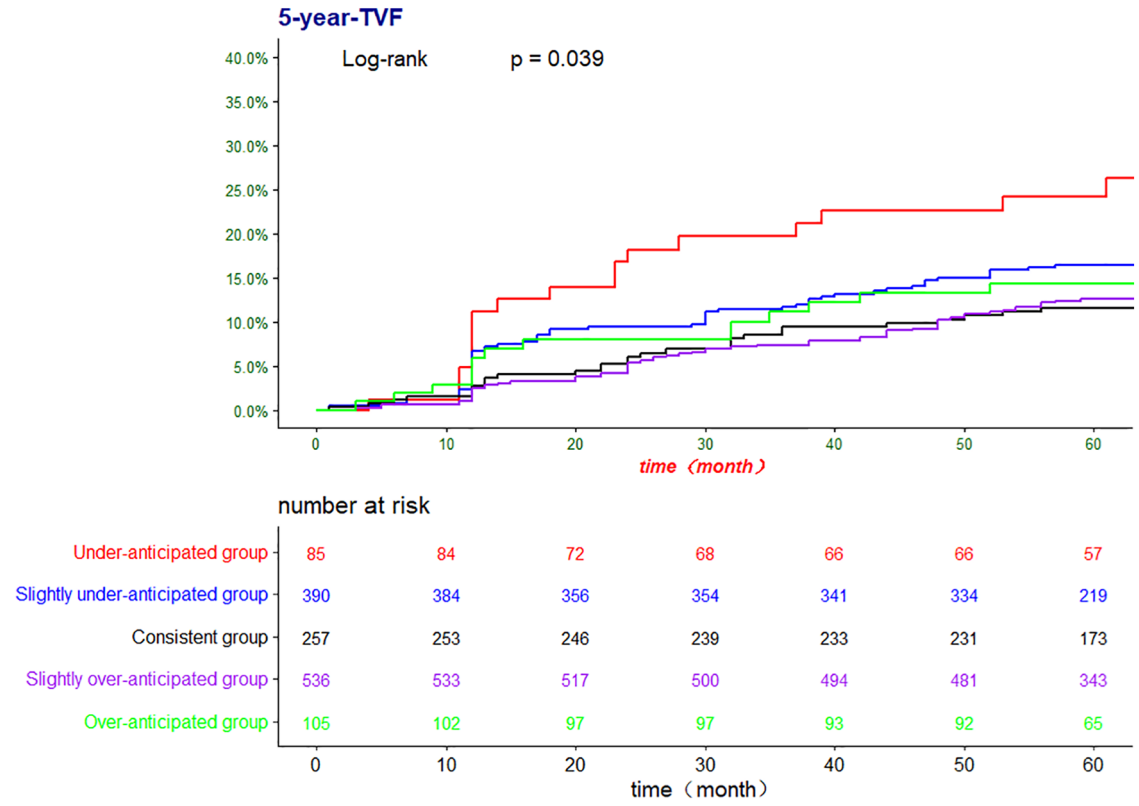

FIGURE 2
The Kaplan-Meier analysis for TVF according to ΔQFR. TVF, target vessel failure; QFR, quantitative flow ratio; ΔQFR = post-PCI QFR—residual QFR.

Predictive performance of the ΔQFR for 5-year TVF

Univariate analysis and multivariate Cox regression analysis were performed to evaluate the predictive performance of the ΔQFR for the 5-year TVF (Table 5). After screening via univariate Cox regression ($P < 0.05$), ΔQFR ≤ −0.1, age, previous MI, hypertension, diabetes, creatinine, and LVEF were included in the multivariate analysis. The multivariate analysis revealed that a ΔQFR ≤ −0.1, old age, previous MI, and diabetes were independent risk factors for TVF, and a high LVEF was an independent protective factor.

Discussion

The present study was the first to evaluate the prognostic value of the consistency between the residual QFR and post-PCI QFR in TVF. The main findings are as follows: (1) The incidence of TVF in the consistent group was significantly lower than that in the underanticipated group, whereas it was similar to that in the overanticipated group, suggesting that the consistency between the residual QFR and post-PCI QFR is associated with the long-term prognosis of patients. (2) This study provides a new perspective on the residual QFR to further explore the potential of the QFR in clinical practice.

Despite successful revascularization, some patients with CAD still experience symptoms of angina pectoris or recurrent cardiovascular adverse events (19, 20). Previous studies suggest that plaque burden rather than stenosis is one of the main predictors of cardiovascular adverse events (21), which may partly explain the uncertain association between the degree of luminal stenosis and the severity of myocardial ischemia. Previous landmark studies have demonstrated the instrumental value of the QFR in guiding the PCI procedure and further improving the clinical prognosis (10–12). The residual QFR is a predicted QFR value based on coronary angiographic imaging that simulates successful stent implantation in the culprit lesion, correlates well with the post-PCI FFR and QFR, and predicts the occurrence of adverse events after revascularization (13, 14, 16, 22). A retrospective analysis of the PANDA III trial showed that the predicted clinical outcome of residual QFR-guided PCI was superior to that of angio-guided PCI (15, 23). In addition, the ability of the residual QFR to distinguish functional stenosis was confirmed (16). Compared with the post-PCI QFR, the residual QFR can predict post-PCI coronary function in advance and provide anticipated post-PCI vascular information on the culprit lesion segment, further delaying revascularization in lesions with

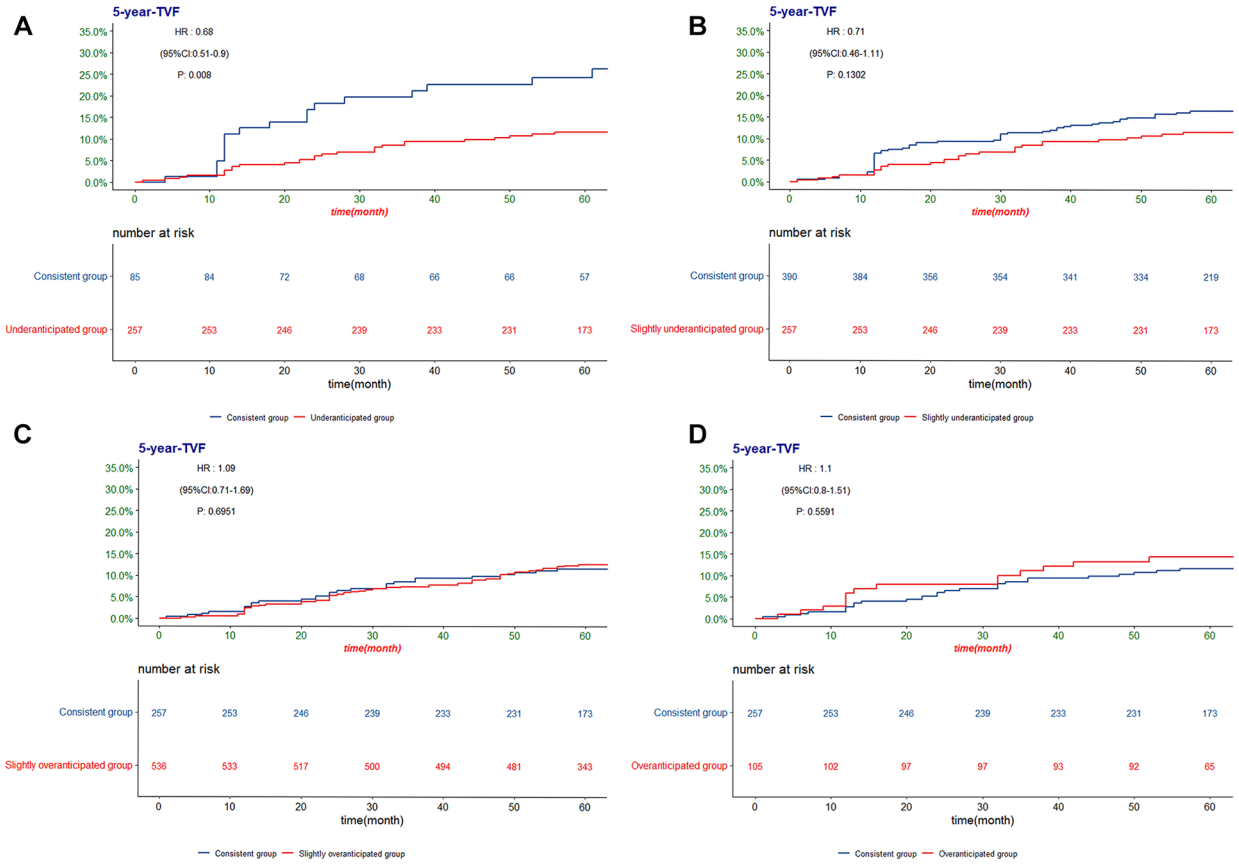

FIGURE 3
The Kaplan-Meier analysis of TVF according to the difference between post-PCI QFR and residual QFR for the (A) consistent group and underanticipated group; (B) consistent group and slightly underanticipated group; (C) consistent group and slightly overanticipated group; (D) consistent group and overanticipated group. TVF, target vessel failure; QFR, quantitative flow ratio.

anticipated insignificant functional benefit. The number and length of stents that are assigned to be implanted in the coronary arteries can be reduced by knowing the stenoses with relatively high treatment benefits and the coronary lesions with potentially low treatment benefits in the index PCI.

In our study, the post-PCI QFR was significantly lower than the residual QFR in the underanticipated group, with a greater incidence of TVF than in the consistent group (22.4% vs. 11.3%, $P = 0.003$). A multivariate Cox regression model revealed that a $\Delta QFR \leq -0.1$ (OR: 1.673, 95% CI: 1.039–2.698 $P = 0.034$) was an independent risk factor for TVF, which indicates the potential for consistency between the residual QFR and post-PCI QFR to predict adverse events; namely, a QFR significantly lower than the residual QFR is prone to be associated with TVF after successful revascularization. Accumulating evidence suggests that a poor physiological outcome may be indicative of stent malapposition, an uncovered stent, a stent under expansion, or incomplete postdialation (24). The residual QFR was calculated as the maximum QFR outside the stent segment of the entire vessel, which may lead to an inadequate assessment of stent malapposition or under expansion. A suboptimal stenting strategy may increase in-stent restenosis and endothelial hyperplasia (25), further increasing the incidence of repeat revascularization, which may explain the high incidence of TVF in the underanticipated group. The stent diameter in the underanticipated group in this study was smaller (2.96 ± 0.41 vs. 3.11 ± 0.44, $P = 0.004$) than that in the consistent group, supporting the previous hypothesis. A low residual QFR suggests that the target vessel may have a limited or diffuse lesion that the operator is unaware of or that the benefit of intervention for this coronary lesion is low, and this information may help to modify the PCI strategy (14). In addition, compared with the consistent group, the overanticipated group had a greater mean number of stents implanted (1.65 ± 0.62 vs. 1.23 ± 0.45, $P < 0.001$) and a longer total stent length (43.42 ± 17.47 vs. 30.80 ± 13.66, $P < 0.001$), which may have contributed to the greater post-PCI QFR than residual QFR in the overanticipated group. According to the RCS regression analysis, the risk of VTVF was nonlinearly related to the ΔQFR and had a V-shape. Although patients in the underanticipated group had a higher risk of TVF, the incidence of TVF was not reduced in the overanticipated

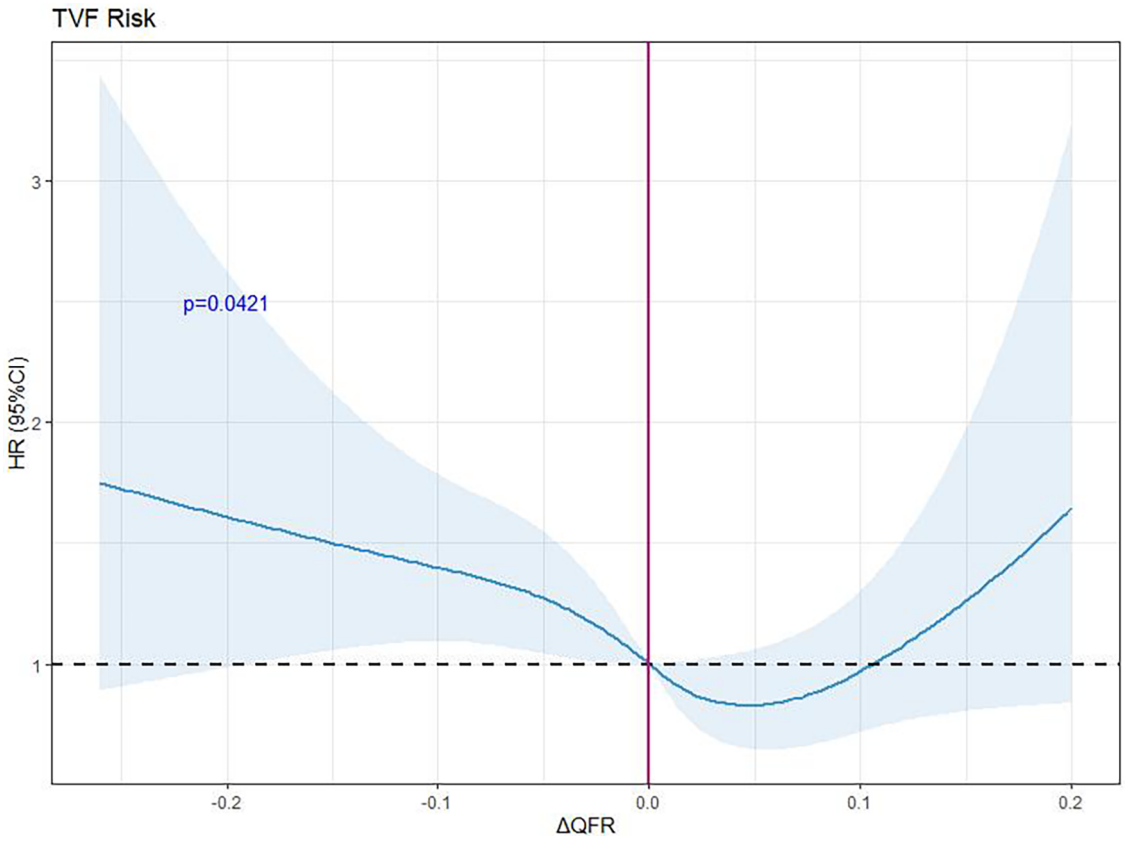

FIGURE 4
Hazard ratios for the TVF based on restricted cubic spline. The purple line represents the reference hazard ratio, and the blue area represents the 95% confidence interval. RCS, restricted cubic spline; HR, hazard ratio; ΔQFR, postoperative QFR minus preoperative residual QFR.

patients. This may indicate that a more aggressive PCI strategy leads to a higher post-PCI QFR but prolongs the operation time, and too many stents may increase stent-related risks. Furthermore, the post-PCI QFR was significantly greater than the residual QFR in the overanticipated group, while the incidence of TVF was not lower than that in the consistent group (13.3% vs. 11.3%, $P = 0.559$), which confirms the ability of the residual QFR to discriminate less functionally beneficial coronary lesions and indicates that aggressive treatment does not reduce the incidence of adverse events in such lesions.

This study has several limitations. First, the current study was a single-center, retrospective, observational study. These findings need to be further validated by prospective, multicenter studies. Second, some patients were excluded due to the lack of optimal

TABLE 5 Univariate and multivariate Cox regression analyses of factors influencing the TVF.

	Univariable		Multivariable	
	OR (95% CI)	*P* value	OR (95% CI)	*P* value
Age	1.023 (1.009–1.038)	0.001	1.019 (1.005–1.034)	0.014
Male	0.987 (0.704–1.383)	0.940		
Smoking history	1.027 (0.771–1.368)	0.856		
Previous MI	2.518 (1.712–3.701)	<0.001	1.689 (1.119–2.550)	0.013
Hypertension	1.398 (1.009–1.936)	0.044	1.246 (0.884–1.754)	0.209
Diabetes	2.216 (1.664–2.951)	<0.001	1.842 (1.366–2.484)	<0.001
ΔQFR ≤ −0.1	1.874 (1.166–3.012)	0.009	1.673 (1.039–2.698)	0.034
Troponin I	0.995 (0.973–1.017)	0.632		
LDL-C	0.916 (0.793–1.059)	0.233		
LVEF	0.968 (0.958–0.979)	<0.001	0.975 (0.964–0.986)	<0.001

ΔQFR = post-PCI QFR minus residual QFR.
PCI, percutaneous coronary intervention; TVF, target vessel failure; MI, myocardial infarction; LDL-C, low-density lipoprotein cholesterol; LVEF, left ventricular ejection fraction; QFR, quantitative flow ratio.

angiographic images for QFR analysis, which led to selection bias. In addition, the residual QFR is a novel index that provides vascular information for PCI treatment, but the accuracy and feasibility of a treatment strategy based on the residual QFR need to be further confirmed.

Conclusions

The consistency between the residual QFR and post-PCI QFR may be associated with the long-term prognosis of patients. Patients whose post-PCI QFR is significantly lower than the residual QFR may be at greater risk of TVF. An aggressive PCI strategy for lesions anticipated to have less functional benefit may not result in a better clinical outcome.

Data availability statement

The raw data supporting the conclusions of this article will be made available by the authors, without undue reservation.

Ethics statement

The studies involving humans were approved by the Ethics Committee of Union Hospital, Fujian Medical University. The studies were conducted in accordance with the local legislation and institutional requirements. The human samples used in this study were acquired from primarily isolated as part of your previous study for which ethical approval was obtained. Written informed consent for participation was not required from the participants or the participants' legal guardians/next of kin in accordance with the national legislation and institutional requirements. Written informed consent was obtained from the individual(s) for the publication of any potentially identifiable images or data included in this article.

Author contributions

LC: Writing – original draft, Writing – review & editing. JZ: Writing – original draft, Writing – review & editing. RH: Writing – original draft, Writing – review & editing. YC: Writing – original draft, Writing – review & editing. BL: Writing – review & editing, Data curation, Visualization. LW: Writing – original draft, Writing – review & editing. YY: Writing – original draft, Writing – review & editing. LC: Writing – review & editing. QC: Writing – original draft, Writing – review & editing. YL: Writing – original draft, Writing – review & editing.

Funding

The author(s) declare financial support was received for the research, authorship, and/or publication of this article.

This work was supported by Joint Funds for Fujian Provincial Health Technology Project (2021GGBO04); Fujian Provincial Health Technology Project (2022CXBO05). The Innovation of Science and Technology, Fujian province (Grant number: 2020Y9098).

Conflict of interest

The authors declare that the research was conducted in the absence of any commercial or financial relationships that could be construed as a potential conflict of interest.

Publisher's note

All claims expressed in this article are solely those of the authors and do not necessarily represent those of their affiliated organizations, or those of the publisher, the editors and the reviewers. Any product that may be evaluated in this article, or claim that may be made by its manufacturer, is not guaranteed or endorsed by the publisher.

Supplementary material

The Supplementary Material for this article can be found online at: https://www.frontiersin.org/articles/10.3389/fcvm.2024.1297218/full#supplementary-material

References

1. El-Hayek GE, Gershlick AH, Hong MK, Casso Dominguez A, Banning A, Afshar AE, et al. Meta-analysis of randomized controlled trials comparing multivessel versus culprit-only revascularization for patients with ST-segment elevation myocardial infarction and multivessel disease undergoing primary percutaneous coronary intervention. *Am J Cardiol*. (2015) 115:1481–6. doi: 10.1016/j.amjcard.2015.02.046

2. Sethi A, Bahekar A, Bhuriya R, Singh S, Ahmed A, Khosla S. Complete versus culprit only revascularization in acute ST elevation myocardial infarction: a meta-analysis. *Cathet Cardiovasc Intervent*. (2011) 77:163–70. doi: 10.1002/ccd.22647

3. Al-Lamee R, Thompson D, Dehbi H-M, Sen S, Tang K, Davies J, et al. Percutaneous coronary intervention in stable angina (ORBITA): a double-blind, randomised controlled trial. *Lancet*. (2018) 391:31–40. doi: 10.1016/S0140-6736(17)32714-9

4. Sugiyama T, Kanno Y, Hamaya R, Kanaji Y, Hoshino M, Murai T, et al. Determinants of visual-functional mismatches as assessed by coronary angiography and quantitative flow ratio. *Cathet Cardio Intervent*. (2021) 98:1047–56. doi: 10.1002/ccd.29388

5. Toth G, Hamilos M, Pyxaras S, Mangiacapra F, Nelis O, De Vroey F, et al. Evolving concepts of angiogram: fractional flow reserve discordances in 4000 coronary stenoses. *Eur Heart J*. (2014) 35:2831–8. doi: 10.1093/eurheartj/ehu094

6. De Maria GL, Garcia-Garcia HM, Scarsini R, Hideo-Kajita A, Gonzalo López N, Leone AM, et al. Novel indices of coronary physiology: do we need alternatives to fractional flow reserve? *Circ: Cardiovasc Intervent*. (2020) 13:e008487. doi: 10.1161/CIRCINTERVENTIONS.119.008487

7. Tonino PAL, Siebert U, Manoharan G, Maccarthy PA. Fractional flow reserve versus angiography for guiding percutaneous coronary intervention. *N Engl J Med*. (2009) 12.

8. Neumann F-J, Sousa-Uva M, Ahlsson A, Alfonso F, Banning AP, Benedetto U, et al. 2018 ESC/EACTS guidelines on myocardial revascularization. *Eur Heart J*. (2019) 40:87–165. doi: 10.1093/eurheartj/ehy394

9. Xaplanteris P, Fournier S, Pijls NHJ, Fearon WF, Barbato E, Tonino PAL, et al. Five-year outcomes with PCI guided by fractional flow reserve. *N Engl J Med*. (2018) 379:250–9. doi: 10.1056/NEJMoa1803538

10. Tu S, Westra J, Yang J, von Birgelen C, Ferrara A, Pellicano M, et al. Diagnostic accuracy of fast computational approaches to derive fractional flow reserve from diagnostic coronary angiography. *JACC Cardiovasc Interv*. (2016) 9:2024–35. doi: 10.1016/j.jcin.2016.07.013

11. Westra J, Andersen BK, Campo G, Matsuo H, Koltowski L, Eftekhari A, et al. Diagnostic performance of in-procedure angiography-derived quantitative flow reserve compared to pressure-derived fractional flow reserve: the FAVOR II Europe-Japan study. *J Am Heart Assoc*. (2018) 7. doi: 10.1161/JAHA.118.009603

12. Xu B, Tu S, Song L, Jin Z, Yu B, Fu G, et al. Angiographic quantitative flow ratio-guided coronary intervention (FAVOR III China): a multicentre, randomised, sham-controlled trial. *Lancet*. (2021) 398:2149–59. doi: 10.1016/S0140-6736(21)02248-0

13. Rubimbura V, Guillon B, Fournier S, Amabile N, Chi Pan C, Combaret N, et al. Quantitative flow ratio virtual stenting and post stenting correlations to post stenting fractional flow reserve measurements from the DOCTORS (does optical coherence tomography optimize results of stenting) study population. *Catheter Cardiovasc Interv*. (2020) 96:1145–53. doi: 10.1002/ccd.28615

14. van Diemen PA, de Winter RW, Schumacher SP, Bom MJ, Driessen RS, Everaars H, et al. Residual quantitative flow ratio to estimate post-percutaneous coronary intervention fractional flow reserve. *J Interv Cardiol*. (2021) 2021:1–11. doi: 10.1155/2021/4339451

15. Zhang R, Xu B, Dou K, Guan C, Zhao Y, Wang X, et al. Post-PCI outcomes predicted by pre-intervention simulation of residual quantitative flow ratio using augmented reality. *Int J Cardiol*. (2022) 352:33–9. doi: 10.1016/j.ijcard.2022.01.054

16. Guan S, Gan Q, Han W, Zhai X, Wang M, Chen Y, et al. Feasibility of quantitative flow ratio virtual stenting for guidance of serial coronary lesions intervention. *J Am Heart Assoc*. (2022) 11:e025663. doi: 10.1161/JAHA.122.025663

17. Authors/Task Force members; Windecker S, Kolh P, Alfonso F, Collet JP, Cremer J, Falk V, et al. 2014 ESC/EACTS guidelines on myocardial revascularization: the task force on myocardial revascularization of the European society of cardiology (ESC) and the European association for cardio-thoracic surgery (EACTS) developed with the special contribution of the European association of percutaneous cardiovascular interventions (EAPCI). *Eur Heart J*. (2014) 35:2541–619. doi: 10.1093/eurheartj/ehu278

18. Garcia-Garcia HM, McFadden EP, Farb A, Mehran R, Stone GW, Spertus J, et al. Standardized end point definitions for coronary intervention trials: the academic research consortium-2 consensus document. *Circulation*. (2018) 137:2635–50. doi: 10.1161/CIRCULATIONAHA.117.029289

19. Cohen DJ, Mohr FW. Quality of life after PCI with drug-eluting stents or coronary-artery bypass surgery. *N Engl J Med*. (2011) 364:1016–26. doi: 10.1056/NEJMoa1001508

20. Stone GW, Ellis SG, Gori T, Metzger DC, Stein B, Erickson M, et al. Blinded outcomes and angina assessment of coronary bioresorbable scaffolds: 30-day and 1-year results from the ABSORB IV randomised trial. *Lancet*. (2018) 392:1530–40. doi: 10.1016/S0140-6736(18)32283-9

21. Mortensen MB, Dzaye O, Steffensen FH, Bøtker HE, Jensen JM, Rønnow Sand NP, et al. Impact of plaque burden versus stenosis on ischemic events in patients with coronary atherosclerosis. *J Am Coll Cardiol*. (2020) 76:2803–13. doi: 10.1016/j.jacc.2020.10.021

22. Li Z, Zhan J, Han J, Fu G, Jin C. Comparison of diagnostic accuracy of immediate angiography derived residual quantitative flow ratio after bioresorbable scaffold and drug eluting stent implantation. *Rev Cardiovasc Med*. (2022) 23:059. doi: 10.31083/j.rcm2302059

23. Xu B, Gao R, Yang Y, Cao X, Qin L, Li Y, et al. Biodegradable polymer-based sirolimus-eluting stents with differing elution and absorption kinetics. *J Am Coll Cardiol*. (2016) 67:2249–58. doi: 10.1016/j.jacc.2016.03.475

24. Wolfrum M, De Maria GL, Benenati S, Langrish J, Lucking AJ, Channon KM, et al. What are the causes of a suboptimal FFR after coronary stent deployment? Insights from a consecutive series using OCT imaging. *EuroIntervention*. (2018) 14: e1324–31. doi: 10.4244/EIJ-D-18-00071

25. Song H-G, Kang S-J, Ahn J-M, Kim W-J, Lee J-Y, Park D-W, et al. Intravascular ultrasound assessment of optimal stent area to prevent in-stent restenosis after zotarolimus-, everolimus-, and sirolimus-eluting stent implantation: IVUS optimization of stent area. *Cathet Cardiovasc Intervent*. (2014) 83:873–8. doi: 10.1002/ccd.24560

frontiers | Frontiers in Cardiovascular Medicine

TYPE Original Research
PUBLISHED 25 April 2024
DOI 10.3389/fcvm.2024.1395257

Check for updates

OPEN ACCESS

EDITED BY
Gaoyang Li,
Tohoku University, Japan

REVIEWED BY
Xiaochang Leng,
ArteryFlow Technology Co., Ltd, China
Abhinav Grover,
Medical College of Wisconsin, United States

*CORRESPONDENCE
Dalin Tang
dtang@wpi.edu
Haibo Jia
jhb101180@163.com

RECEIVED 03 March 2024
ACCEPTED 11 April 2024
PUBLISHED 25 April 2024

CITATION
Huang M, Maehara A, Tang D, Zhu J, Wang L, Lv R, Zhu Y, Zhang X, Zhao C, Jia H and Mintz GS (2024) Impact of residual stress on coronary plaque stress/strain calculations using optical coherence tomography image-based multi-layer models. Front. Cardiovasc. Med. 11:1395257. doi: 10.3389/fcvm.2024.1395257

COPYRIGHT
© 2024 Huang, Maehara, Tang, Zhu, Wang, Lv, Zhu, Zhang, Zhao, Jia and Mintz. This is an open-access article distributed under the terms of the Creative Commons Attribution License (CC BY). The use, distribution or reproduction in other forums is permitted, provided the original author(s) and the copyright owner(s) are credited and that the original publication in this journal is cited, in accordance with accepted academic practice. No use, distribution or reproduction is permitted which does not comply with these terms.

Impact of residual stress on coronary plaque stress/strain calculations using optical coherence tomography image-based multi-layer models

Mengde Huang[1], Akiko Maehara[2], Dalin Tang[1,3]*, Jian Zhu[4], Liang Wang[1], Rui Lv[5], Yanwen Zhu[1], Xiaoguo Zhang[4], Chen Zhao[6], Haibo Jia[6]* and Gary S. Mintz[2]

[1]School of Biological Science and Medical Engineering, Southeast University, Nanjing, China, [2]The Cardiovascular Research Foundation, Columbia University, New York, NY, United States, [3]Mathematical Sciences Department, Worcester Polytechnic Institute, Worcester, MA, United States, [4]Department of Cardiology, Zhongda Hospital, Southeast University, Nanjing, China, [5]Department of Cardiac Surgery, Shandong Second Provincial General Hospital, Jinan, China, [6]Department of Cardiology, The Second Affiliated Hospital of Harbin Medical University, Harbin, China

Introduction: Mechanical stress and strain conditions play an important role in atherosclerosis plaque progression, remodeling and potential rupture and may be used in plaque vulnerability assessment for better clinical diagnosis and treatment decisions. Single layer plaque models without residual stress have been widely used due to unavailability of multi-layer image segmentation method and residual stress data. However, vessel layered structure and residual stress have large impact on stress/strain calculations and should be included in the models.
Methods: In this study, intravascular optical coherence tomography (OCT) data of coronary plaques from 10 patients were acquired and segmented to obtain the three-layer vessel structure using an in-house automatic segmentation algorithm. Multi- and single-layer 3D thin-slice biomechanical plaque models with and without residual stress were constructed to assess the impact of residual stress on stress/strain calculations.
Results: Our results showed that residual stress led to a more uniform stress distribution across the vessel wall, with considerable plaque stress/strain decrease on inner wall and increase on vessel out-wall. Multi-layer model with residual stress inclusion reduced inner wall maximum and mean plaque stresses by 38.57% and 59.70%, and increased out-wall maximum and mean plaque stresses by 572.84% and 432.03%.
Conclusion: These findings demonstrated the importance of multi-layer modeling with residual stress for more accurate plaque stress/strain calculations, which will have great impact in plaque cap stress calculation and plaque rupture risk assessment. Further large-scale studies are needed to validate our findings.

KEYWORDS
residual stress, opening angle, coronary plaque, multi-layer artery model, plaque stress

1 Introduction

Mechanical stress/strain conditions play an important role in atherosclerosis plaque progression, remodeling and potential rupture (1–6). Accurate models serve as the basis for plaque stress/strain calculations and the subsequent prediction of plaque progression and

rupture. While it is well known that arteries have three-layer structure and residual stress (7, 8), single-layer models without residual stress were used in most current publications due to lack of available multi-layer image and residual stress data. With unprecedented optical coherence tomography (OCT) resolution (5–15 μm), we introduced a multi-layer OCT image segmentation method and multi-layer plaque models recently to demonstrate the impact of multi-layer structure on plaque stress/strain conditions (9, 10). In this paper, OCT-based multi-layer coronary plaque models with and without residual stress inclusion were constructed and compared with single-layer models to investigate the influence of model residual stress inclusion on plaque stress/strain calculations.

Residual stress, defined as the stress remaining in an *ex vivo* vessel ring under no-load condition, was initially observed by Fung and his colleagues (7, 11). When the vessel ring is cut open radially, the inherent residual stress causes the ring to spring open, forming a sector with a specific opening angle. Following this discovery, Holzapfel et al. revealed a diverse range of opening angles across different layers by experiments, with the media layer's angle may exceeding 180 degrees (12, 13).

Residual stress inclusion in vessel models may have considerable impact on vessel stress and strain distributions. Vito and Delfino et al. reported that incorporating residual stress led to a more uniform circumferential stress distribution in arterial models (8, 14). Ohayon et al. found that peak strain in coronary artery models is significantly overestimated when residual stress is not considered (15). Wang et al. demonstrated that residual stress led to reduced lumen and increased out-wall stress (16). Pierce et al. observed the impact of residual stress on the deformation and stress distribution within arterial tissue in abdominal aortic aneurysms models (17).

In this paper, patient-specific multi-layer and single thin-slice models with and without residual stress inclusion for coronary plaques were constructed using a three-step modelling procedure based on segmented OCT image data. Stress/strain results from vessel inner- and out-wall were extracted for comparison analysis. Patient variations of model differences were also observed.

2 Materials and methods

2.1 Data acquisition and multi-layer segmentation

Intravascular optical coherence tomography (OCT) coronary plaque data sets from 10 patients (8 male; 2 female) were used in this study. Of the 10 patients, 4 existing de-identified OCT data sets were obtained from Cardiovascular Research Foundation (CRF, New York, New York); 4 OCT data sets were acquired from Southeast University Affiliated Zhongda Hospital using protocol approved by Southeast University Zhongda Hospital Institutional Review Board (approval code 2019ZDKYSB046) with informed consent obtained. 2 existing de-identified OCT data sets were obtained from The Second Affiliated Hospital of Harbin Medical University. OCT images were acquired with ILUMIEN OPTIS System and Dragonfly JP Imaging Catheter (St. Jude Medical, Westford, Massachusetts). Patient demographic information is given in Table 1.

TABLE 1 Patient demographic data and clinical information.

Patient	Age	Sex	Vessel segment	BP (mmHg)	Comorbidities
P1	70	M	RCA	155/84	HT
P2	66	M	LCX	150/89	DM
P3	61	M	LCX	128/78	HT DM HL
P4	72	M	LCX	143/80	HT DM HL
P5	56	M	LAD	115/64	HT HL
P6	55	M	LAD	130/90	HT
P7	65	M	LAD	124/84	N/A
P8	50	F	LAD	175/92	HT HL
P9	43	M	LAD	132/90	HL
P10	59	F	LAD	121/71	HT HL

BP, blood pressure; RCA, right coronary artery; LCX, left circumflex artery; LAD, left anterior descending artery; HT, hypertension; DM, diabetes mellitus; HL, hyperlipoproteinemia.

It is well-known that arteries have a three-layer structure: intima, media, and adventitia. While most publications used single-layer models, multi-layer models are desirable for more realistic modeling of the artery and more accurate plaque stress/strain calculations. For this purpose, multi-layer automatic segmentation of OCT images was performed to get vessel layer structures using a MATLAB-based method (MATLAB R2021a, MathWorks, USA) previously introduced by Huang et al. (9). Figure 1 presents a flow chart of this segmentation process alongside a sample slice illustrating the three layers segmented from the OCT image. Figure 2 provided more details for the repair process. The OCT image was segmented by our automatic segmentation program which processes OCT images in polar coordinate system. We first applied edge detection algorithms, specifically a modified Canny method, to segment the visible portions (Figures 2A–C). Subsequently, cubic spline surface fitting was employed to fit the surface function $r = r(z, \theta)$ to get the locations of missing portions (Figures 2D–F). For accuracy validation, the automated segmentation results were compared with manual segmentations and good agreement were found. The plaque samples used in this study were mostly of circular shape which made the interpolation easier. The segmented slices with contours for the intima, media, and adventitia layers were then employed for model construction.

2.2 Multi-layer models with residual stress inclusion and layer-specific material properties

Plaque stress/strain conditions play an important role in plaque progression, remodeling and potential rupture. Accurate models are the base for reliable and precise stress/strain calculations. We recently introduced an OCT multi-layer segmentation method and OCT-based multi-layer plaque models (10). In this paper, we are adding residual stress to multi-layer models for further improvement. For comparison purpose, single-layer models with and without residual stress inclusion were also constructed to show differences for both single-layer and multi-layer models. The following four models were constructed for each patient: (a) multi-layer model without residual stress; (b) single-layer model without

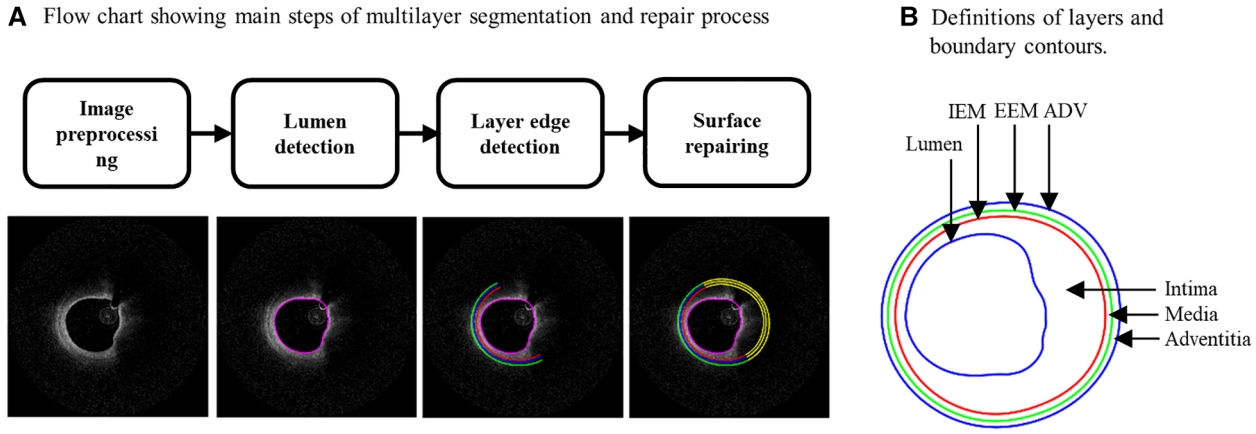

FIGURE 1
(A) Flow chart showing main steps of an in-house automatic multi-layer segmentation and repair process; (B) a sample slice showing segmented three layer contours. IEM, Internal elastic membrane; EEM, External elastic membrane; ADV, adventitia-periadventitia interface.

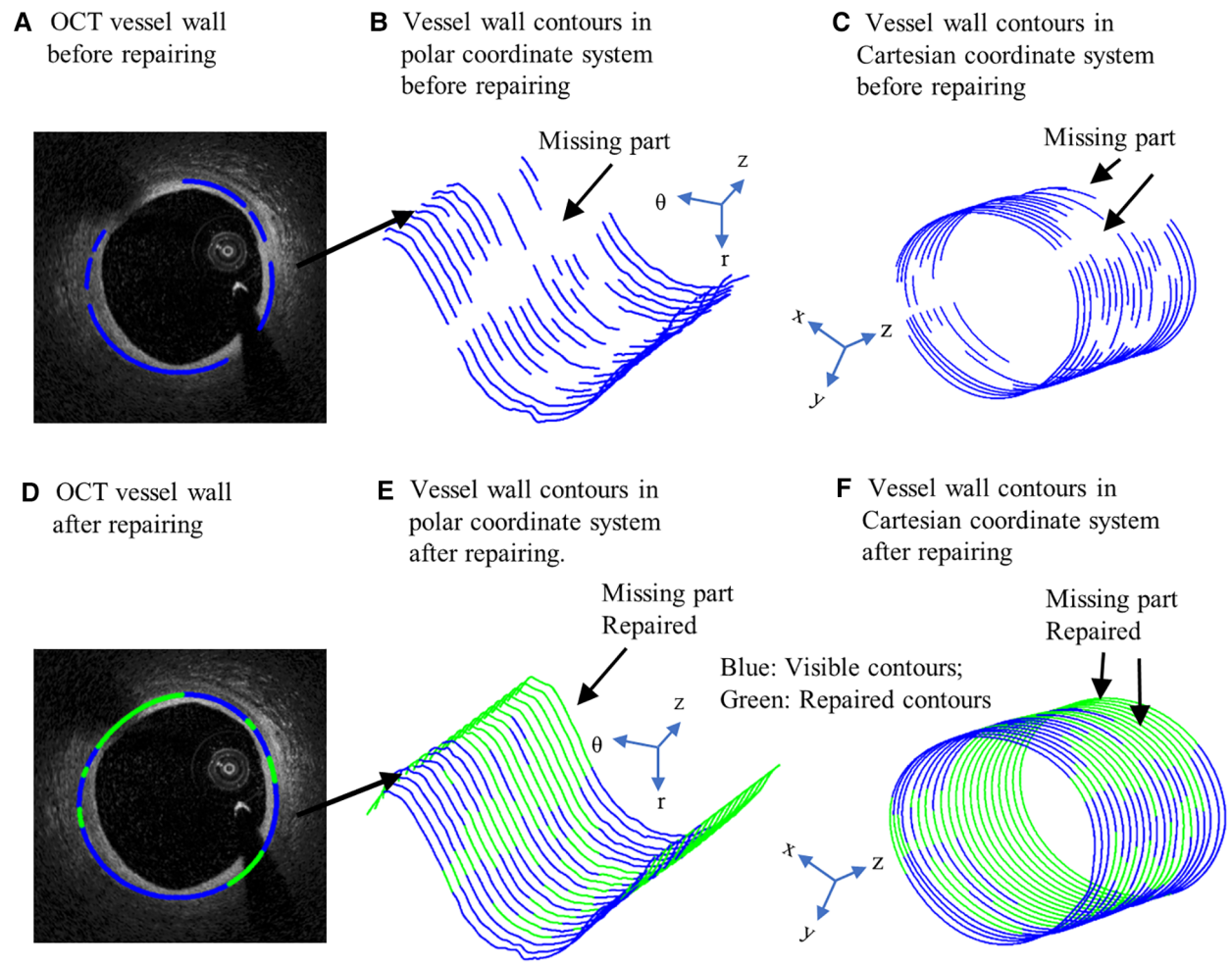

FIGURE 2
Schematic of OCT image repairing. (A) OCT vessel wall before repairing. (B) Vessel wall contours in polar coordinate system before repairing. (C) Vessel wall contours in Cartesian coordinate system before repairing. (D) OCT vessel wall after repairing. (E) Vessel wall contours in polar coordinate system after repairing. (F) Vessel wall contours in Cartesian coordinate system after repairing. Blue contours: Visible contours; Green contours: Repaired contours for missing parts.

residual stress; (c) multi-layer model with residual stress inclusion; and (d) single-layer model with residual stress inclusion. Our novel multi-layer model with residual stress inclusion added layer structure and residual stress to the other three models (one or both) and should provide more realistic representation of the physical artery/plaque among the four models. Details for material properties and residual modeling process are given below.

2.2.1 Layer-specific material models and material parameters

Vessel material properties for the three layers (and the single-layer) were assumed to be hyperelastic, anisotropic, nearly incompressible, and homogeneous, while plaque components like lipid and calcifications were considered isotropic. The modified Mooney–Rivlin material models were used for the layers using parameter values from available literature (18, 19). The modified Mooney-Rivlin material models were used because that were available on ADINA (Adina R & D, Watertown, MA, USA) which was used to solve our finite element models. We did model comparisons for Mooney-Rivlin model, Fung-type model and Choi-Vito model using biaxial testing data (4 coronary and 5 carotid plaque samples) and the modified Mooney-Rivlin material models provided better fitting accuracies (19). The strain energy functions are represented by Equations 1 and 2 given below.

$$W_{iso} = c_1(I_1 - 3) + c_2(I_2 - 3) + D_1[exp(D_2(I_1 - 3)) - 1] \quad (1)$$

$$W_{aniso} = W_{iso} + \frac{K_1}{K_2}\{exp[K_2(I_4 - 1)^2] - 1\} \quad (2)$$

where $I_1 = \sum(C_{ii})$, $I_2 = \frac{1}{2}[I_1^2 - C_{ij}C_{ij}]$, I_1 and I_2 denote the first and second invariants of right Cauchy–Green deformation tensor $C = [C_{ij}] = F^TF$, $F = [F_{ij}] = [\partial x_i/\partial a_j]$;$(x_i)$ is current position; (a_j) s original position; $I_4 = \lambda_\theta^2 cos^2\varphi + \lambda_z^2 \sin^2\varphi$, where λ_θ, λ_z, are the principal stretches associated with circumferential and axial direction and ϕ is the angle between the fiber reinforcement and the circumferential direction in individual layers. c_1, c_2, D_1, D_2, K_1 and K_2 are material parameters. Parameter values for the vessel layers and plaque components used in our models are (10, 18): Intima: $c_1 = -169.23$ kPa, $c_2 = 177.40$ kPa, $D_1 = 2.4$ kPa, $D_2 = 13$, $K_1 = 32$ kPa, $K_2 = 36$; Media: $c_1 = -67.25$ kPa, $c_2 = 35.01$ kPa, $D_1 = 17$ kPa, $D_2 = 2$, $K_1 = 7$ kPa, $K_2 = 4$, $\phi = 24.9°$; Adventitia; $c_1 = -94.44$ kPa, $c_2 = 102.42$ kPa, $D_1 = 0.8$ kPa, $D_2 = 10$, $K_1 = 10$ kPa, $K_2 = 40$, $\phi = 75.3°$; lipid core: $c_1 = 0.5$ kPa, $c_2 = 0$ kPa, $D_1 = 0.5$ kPa, $D_2 = 1.5$; calcification: $c_1 = 920$ kPa, $c_2 = 0$ kPa, $D_1 = 360$ kPa, and $D_2 = 2.0$. For single-layer models, intima parameter values were used for the entire vessel wall. Figure 3 depicts the stress–stretch curves of three layers derived from the modified Mooney–Rivlin material models.

2.2.2 Multi-layer 3D thin-slice model with residual stress inclusion

In vivo OCT image data were obtained when the blood vessel was under pressure and axially stretched. So the vessel image data should be shrunk circumferentially (radially) and axially to obtain its no-load state. The no-load geometry needs to be cut open to release the residual stress to obtain its stress-free state (11). To construct accurate coronary plaque models, it is

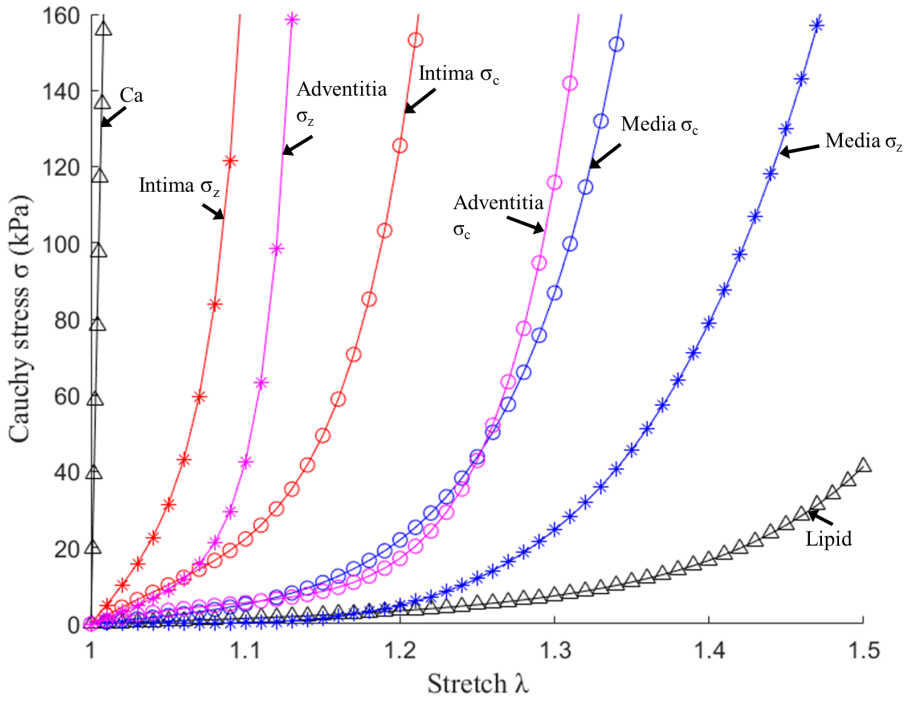

FIGURE 3
Stress–stretch curves of three layers and plaque components derived from the mooney-rivlin models and used in finite element modelling. σ_c, circumferential stress; σ_z, axial stress (10).

imperative to initiate from zero-stress state, which is a condition not readily extractable from medical image. To obtain vessel zero-stress state from its *in vivo* state, the vessel was shrunk circumferentially (radially) and axially to achieve a zero-load state first. A 5% axial pre-shrink and the circumferential pre-shrink process were used to get vessel no-load state (16). The circumferential shrinkage rate was set as 5% initially and adjusted by an iterative procedure until the pressurized slice under diastolic pressure matched the *in vivo* OCT slice (tolerance <0.1%). Subsequently, the zero-load geometry was cut open to release the residual stress to obtain its zero-stress state. The opening-up process adhered to two fundamental assumptions: (1) vessel wall volume was conserved and (2) the circumference of the middle line of the vessel wall remained unchanged. The opening angle of the vessel sector was postulated to be 120°, which was derived from the average of eight human coronary artery samples (19). Figure 4 illustrates the vessel's transition from zero-load to zero-stress state. The zero-stress geometry (cut-open slice) was then used as the starting geometry for model construction.

2.3 Three-step model solution procedure

Three-dimensional (3D) thin-slice models were constructed for 10 OCT slices from 10 patients using multi-layer segmented data obtained from our programs. Four types of models (multi-layer with and without residual stress, single-layer with and without residual stress) were constructed for each patient, resulting in 40 thin-slice models in total. The 3D thin-slice model was made by adding a 0.5 mm thickness to each slice to better approximate full 3D models, yet maintaining the low construction cost about the same as that of 2D models. A three-step modeling procedure was used in the modeling process starting from zero-stress state to recover the vessel *in vivo* state: (a) wrap the zero-stress vessel slice to its no-load geometry (note now the closed vessel slice carries residual stress/strain as desired). The wrapping process is accomplished by applying prescribed displacement to the two cut-openings of the opened vessel slice and bringing them to come together (contact); (b) stretch the vessel axially to its length *in vivo*; and (c) pressurize the vessel to recover *in vivo* geometry (16). Finite element mesh was generated using a commercial finite-element package ADINA 9.6 (Adina R & D, Watertown, MA, USA). Given the complex morphologies of plaques, a "volume-fitting" technique was employed to divide the 3-D plaque, intima, media and adventitia domains into many small "volumes" to curve-fit the irregular vessel geometry with plaque component inclusions (20). This technique was crucial for achieving convergent plaque finite element models. Mesh analysis was performed by decreasing mesh size by 10% (in each dimension) incrementally until solution differences were less than 2%. The optimized mesh was then chosen for our simulations. The thin-slice models were solved following our established procedures (21). Because stress/strain are tensors, maximum principal stress and maximum principal strain (called stress and strain from here on, respectively) were chosen as their scale representatives for stress/strain comparisons.

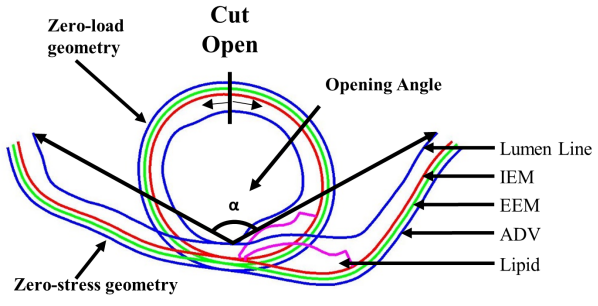

FIGURE 4
Vessel zero-load and zero-stress geometries with three-layer structure and opening angle.

2.4 Data extraction and analysis

After the models were solved, stress and strain values from 100 data points for each slice at plaque inner wall (called plaque stress/strain for simplicity) and out-wall (out-wall stress/strain) were extracted to compare results and investigate the impact of residual stress on plaque stress/strain calculations. The ratios (percentage) of maximum and mean stress/strain values between models with and without residual stress were calculated to investigate the impact of residual stress inclusion on stress/strain calculations. Since plaque slices often have irregular and nonuniform wall thickness, a four-quarter method was introduced to connect lumen points and out-wall points to avoid data distortion by thicker plaques (22). Figure 5 gives an illustration of the four-quarter method and the three layers of the vessel: intima, media and adventitia. The boundary between

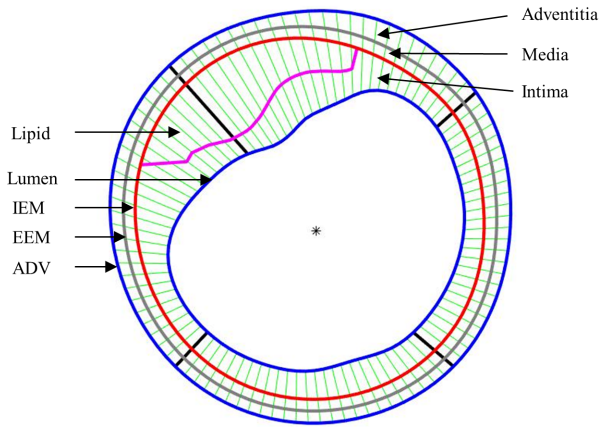

FIGURE 5
Schematic plot demonstrating the piecewise equal-step method to select 100 points for data extraction.

intima and media is called internal elastic membrane (IEM). The boundary between media and adventitia is called external elastic membrane (EEM). The boundary between adventitia and other peripheral tissues is called adventia-periadventitia interface (ADV).

3 Results

The following comparisons of plaque stress/strain values from multi-layer models (M-Model) and single-layer models (S-Model) with and without residual stress inclusion were made to investigate the impact of residual stress on plaque stress/strain conditions: (a) plaque stress/strain values on inner wall from multi-layer models with and without residual stress; (b) plaque stress/strain values on inner wall from single-layer models with and without residual stress; (c) plaque stress/strain values on out-wall from multi-layer models with and without residual stress; (d) plaque stress/strain values on out-wall from single-layer models with and without residual stress.

Stress/strain results from our novel multi-layer models with residual stress should be the most accurate among the 4 models compared, while single-layer model comparison results are also of interest since single-layer models are used in most publications. Plaque research has been focused on inner wall plaque stress/strain conditions. However, results from outer walls were reported since they were all important factors in plaque progression and remodeling process (8).

3.1 Multi-layer model with residual stress inclusion reduced inner wall maximum and mean plaque stresses by 38.57% and 59.70%

Table 2 gave maximum and mean plaque stress values on vessel inner wall from multi-layer and single-layer models and comparisons for models with and without residual stress for the 10 patients studied. From multi-layer models with residual stress inclusion, the inner wall maximum and mean plaque stress values (averaged over 10 patients) were 148.53 kPa and 50.68 kPa respectively, which were 38.57% and 59.70% lower than the values from corresponding models without residual stress. From single-layer models with residual stress, the inner wall maximum and mean plaque stress values were 59.14 kPa and 6.89 kPa, which were 61.46% and 94.72% lower than the values from corresponding models without residual stress. The influence of residual stress on plaque stress exhibited large patient variations for both multi-layer and single-layer models. It is evident that residual stress has large impact on plaque stress calculations.

3.2 Multi-layer model maximum and mean plaque strains on vessel inner wall were reduced by 31.96% and 52.84% with residual stress inclusion

Similar to Table 2, Table 3 gave maximum and mean plaque strain values on vessel inner wall and comparisons from

TABLE 2 Inner wall maximum and mean plaque stress comparisons between models with and without residual stress.

Plaque	Maximum plaque stress (kPa)				Mean plaque stress (kPa)			
	M-Model with residual stress	M-Model no residual stress	S-Model with residual stress	S-Model no residual stress	M-Model with residual stress	M-Model no residual stress	S-Model with residual stress	S-Model no residual stress
P1	124.74	238.71	57.96	146.95	42.89	109.61	1.29	70.81
	52.26%	100.00%	39.44%	100.00%	39.13%	100.00%	1.83%	100.00%
P2	60.54	126.87	6.34	65.94	26.52	71.94	−3.85	47.59
	47.72%	100.00%	9.62%	100.00%	36.87%	100.00%	−8.09%	100.00%
P3	176.22	195.62	72.97	143.34	33.19	99.16	−11.56	65.54
	90.08%	100.00%	50.91%	100.00%	33.47%	100.00%	−17.65%	100.00%
P4	178.66	346.11	29.35	214.84	58.69	159.02	3.29	85.64
	51.62%	100.00%	13.66%	100.00%	36.91%	100.00%	3.84%	100.00%
P5	101.76	249.30	67.26	129.92	37.29	120.55	4.02	79.93
	40.82%	100.00%	51.77%	100.00%	30.93%	100.00%	5.03%	100.00%
P6	293.74	260.33	96.29	141.88	111.33	138.60	37.03	94.36
	112.83%	100.00%	67.87%	100.00%	80.33%	100.00%	39.24%	100.00%
P7	289.90	388.15	158.10	204.86	107.47	203.26	34.75	124.70
	74.69%	100.00%	77.17%	100.00%	52.87%	100.00%	27.87%	100.00%
P8	109.26	334.76	49.61	209.43	44.93	99.93	11.85	71.71
	32.64%	100.00%	23.69%	100.00%	44.96%	100.00%	16.53%	100.00%
P9	47.06	124.67	45.79	103.49	−0.54	38.72	−3.25	34.47
	37.75%	100.00%	44.24%	100.00%	−1.40%	100.00%	−9.44%	100.00%
P10	103.46	140.02	7.80	111.01	45.06	92.10	−4.69	73.13
	73.88%	100.00%	7.03%	100.00%	48.92%	100.00%	−6.41%	100.00%
Mean ± STD	148.53 ± 86.35	240.45 ± 94.72	59.14 ± 44.74	147.16 ± 49.37	50.68 ± 34.62	113.29 ± 45.94	6.89 ± 16.52	74.79 ± 24.71
Mean ± STD (%)	61.43% ± 25.77%	100.00%	38.54% ± 24.46%	100.00%	40.30% ± 20.42%	100.00%	5.28% ± 17.83%	100.00%

M-Model, multi-layer model; S-Model, single-layer model.

10.3389/fcvm.2024.1395257

TABLE 3 Inner wall maximum and mean plaque strain comparisons between models with and without residual stress.

Plaque	Maximum plaque strain				Mean plaque strain			
	M-Model with residual stress	M-Model no residual stress	S-Model with residual stress	S-Model no residual stress	M-Model with residual stress	M-Model no residual stress	S-Model with residual stress	S-Model no residual stress
P1	0.194	0.308	0.130	0.282	0.062	0.161	0.024	0.140
	63.00%	100.00%	46.06%	100.00%	38.40%	100.00%	17.29%	100.00%
P2	0.097	0.256	0.094	0.242	0.032	0.137	0.029	0.119
	38.06%	100.00%	39.02%	100.00%	23.02%	100.00%	24.14%	100.00%
P3	0.155	0.214	0.186	0.177	0.069	0.119	0.061	0.099
	72.44%	100.00%	105.39%	100.00%	57.77%	100.00%	62.21%	100.00%
P4	0.141	0.353	0.108	0.284	0.079	0.146	0.052	0.112
	39.85%	100.00%	37.98%	100.00%	54.10%	100.00%	46.85%	100.00%
P5	0.204	0.197	0.164	0.170	0.066	0.128	0.059	0.106
	103.89%	100.00%	96.49%	100.00%	51.71%	100.00%	55.30%	100.00%
P6	0.199	0.287	0.149	0.269	0.090	0.144	0.061	0.123
	69.40%	100.00%	55.38%	100.00%	62.41%	100.00%	49.85%	100.00%
P7	0.203	0.217	0.171	0.197	0.102	0.158	0.067	0.130
	93.39%	100.00%	86.81%	100.00%	64.87%	100.00%	51.23%	100.00%
P8	0.118	0.180	0.074	0.155	0.064	0.117	0.053	0.100
	65.60%	100.00%	47.63%	100.00%	54.53%	100.00%	52.33%	100.00%
P9	0.148	0.189	0.214	0.184	0.034	0.109	0.067	0.105
	78.58%	100.00%	116.52%	100.00%	31.20%	100.00%	64.11%	100.00%
P10	0.125	0.222	0.054	0.207	0.053	0.156	0.014	0.144
	56.20%	100.00%	25.99%	100.00%	33.63%	100.00%	9.86%	100.00%
Mean ± STD	0.158 ± 0.039	0.242 ± 0.057	0.134 ± 0.052	0.217 ± 0.049	0.065 ± 0.022	0.137 ± 0.019	0.049 ± 0.019	0.118 ± 0.016
Mean ± STD (%)	68.04% ± 20.88%	100.00%	65.73% ± 32.36%	100.00%	47.16% ± 14.45%	100.00%	43.32% ± 19.13%	100.00%

M-Model, multi-layer model; S-Model, single-layer model.

multi-layer and single-layer models with and without residual stress inclusion. From multi-layer models with residual stress inclusion, the inner wall maximum and mean plaque strain values (average for 10 patients) were 0.158 and 0.065 respectively, which were 31.96% and 52.84% lower than the values from corresponding models without residual stress. From single-layer models with residual stress, the inner wall maximum and mean plaque strain values were 0.134 and 0.049, which were 34.27% and 56.68% lower than the values from corresponding models without residual stress. Overall, plaque strain comparison results and patient variations were similar to plaque stress behaviors.

To demonstrate model differences more clearly, Figure 6 gave plaque stress/strain distribution plots from the four models using a sample slice. Figures 6B–E showed stress and strain plots from multi-layer models while Figures 6F–I showed single-layer model stress/strain plots. Models with residual stress inclusion had lower maximum stress/strain values on inner wall and higher maximum stress/strain values on out-wall compared to models without residual stress.

3.3 Out-wall maximum and mean out-wall stresses increased by 572.84% and 432.03% for multi-layer models with residual stress inclusion

Plaque stress and strain on vessel out-wall play an important role in vessel remodeling process (8). Table 4 gave maximum and mean out-wall stress values from multi-layer and single-layer models and comparisons for models with and without residual stress for the 10 patients studied. From multi-layer models with residual stress, the maximum and mean out-wall stress values were 211.15 kPa and 97.03 kPa, which were 572.84% and 432.03% higher than the values from corresponding models without residual stress. From single-layer models with residual stress, the maximum and mean out-wall stress values were 400.28 kPa and 194.55 kPa, which were 770.93% and 591.31% higher than the values from corresponding models without residual stress.

3.4 Multi-layer models with residual stress inclusion increased maximum and mean out-wall strain by 240.21% and 299.79% respectively

Table 5 gave maximum and mean out-wall strain values from multi-layer and single-layer models and comparisons for models with and without residual stress for the 10 patients studied. From multi-layer models with residual stress inclusion, the maximum and mean out-wall strain values were 0.369 and 0.225, which were 240.21% and 299.79% higher than those from corresponding models without residual stress. From single-layer models with residual stress inclusion, the maximum and mean out-wall strain values were 0.265 and 0.164, 235.51% and 264.88% higher than those from corresponding models without residual stress, respectively.

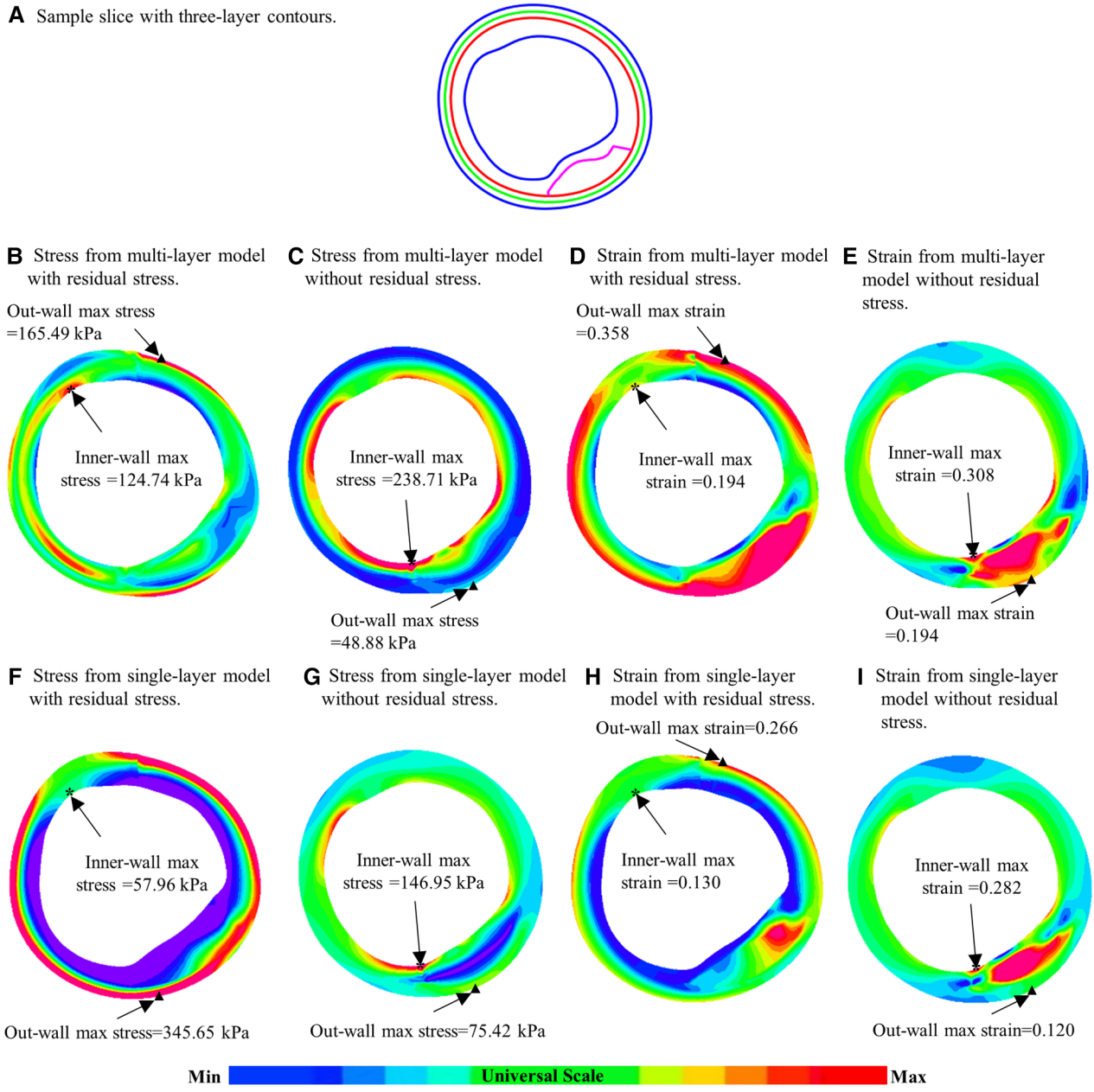

FIGURE 6
Comparison of plaque stress/strain distributions of four models using a sample slice. (A) A sample slice with three-layer contours. (B–E) Stress plots from multi-layer models with and without residual stress inclusion; (F–I) Stress from single-layer models with and without residual stress inclusion. *: Maximum stress/strain on inner wall; ▲: maximum stress/strain on out-wall.

4 Discussion

4.1 The impact of residual stress inclusion on stress/strain calculations

The importance of plaque stress/strain calculations for vulnerable plaque progression and rupture risk assessment is well recognized. To our knowledge, this paper should be a first report for impact of residual stress on plaque stress/strain calculations using patient-specific multi-layer models based on segmented 3-layer OCT data. Our findings revealed that residual stress inclusion reduced inner wall maximum and mean plaque stresses by 38.57% and 59.70% and increased out-wall maximum and mean plaque stresses by 572.84% and 432.03%. Using multi-layer model with residual stress inclusion as the base, the multi-layer model without residual stress inclusion over-estimated inner wall maximum and mean stress by 61.8% and 123.5%, respectively. The single-layer model situation is even more scary: the single layer model without residual stress inclusion over-estimated inner wall maximum and mean stress by 148.8% and 985.5% (using values from single layer model with residual stress), respectively. The incorporation of residual stress significantly impacts stress and

10.3389/fcvm.2024.1395257

TABLE 4 Out-wall maximum and mean out-wall stress comparisons between models with and without residual stress.

Plaque	Maximum out-wall stress (kPa)				Mean out-wall stress (kPa)			
	M-Model with residual stress	M-Model no residual stress	S-Model with residual stress	S-Model no residual stress	M-Model with residual stress	M-Model no residual stress	S-Model with residual stress	S-Model no residual stress
P1	165.49	48.88	345.65	75.42	89.30	24.85	185.90	41.01
	338.56%	100.00%	458.33%	100.00%	359.34%	100.00%	453.29%	100.00%
P2	209.17	24.49	305.38	36.51	99.72	16.79	183.28	24.90
	854.16%	100.00%	836.33%	100.00%	594.04%	100.00%	736.21%	100.00%
P3	246.51	25.66	358.05	42.23	96.99	16.58	163.43	25.38
	960.49%	100.00%	847.82%	100.00%	584.91%	100.00%	643.83%	100.00%
P4	231.92	46.17	271.38	72.96	102.69	29.81	149.97	48.19
	502.30%	100.00%	371.95%	100.00%	344.51%	100.00%	311.21%	100.00%
P5	114.51	35.07	516.57	64.67	60.00	20.68	220.26	35.55
	326.54%	100.00%	798.82%	100.00%	290.13%	100.00%	619.59%	100.00%
P6	199.11	44.76	294.56	80.32	84.22	22.83	154.52	38.71
	444.89%	100.00%	366.73%	100.00%	368.89%	100.00%	399.20%	100.00%
P7	233.05	46.68	364.80	90.51	91.82	29.16	168.47	53.02
	499.21%	100.00%	403.04%	100.00%	314.89%	100.00%	317.76%	100.00%
P8	164.42	32.12	265.36	57.63	80.48	19.80	146.60	32.70
	511.84%	100.00%	460.45%	100.00%	406.48%	100.00%	448.32%	100.00%
P9	391.54	24.99	780.87	28.08	153.02	10.90	327.86	15.32
	1,567.07%	100.00%	2,781.11%	100.00%	1,403.62%	100.00%	2,140.55%	100.00%
P10	155.81	21.54	500.19	36.12	112.05	17.15	245.26	29.09
	723.35%	100.00%	1,384.68%	100.00%	653.45%	100.00%	843.18%	100.00%
Mean ± STD	211.15 ± 75.66	35.04 ± 10.73	400.28 ± 159.65	58.45 ± 21.63	97.03 ± 24.26	20.85 ± 5.94	194.55 ± 56.51	34.39 ± 11.39
Mean ± STD (%)	672.84% ± 378.09%	100.00%	870.93% ± 743.90%	100.00%	532.03% ± 332.34%	100.00%	691.31% ± 539.32%	100.00%

M-Model, multi-layer model; S-Model, single-layer model.

TABLE 5 Out-wall maximum and mean out-wall strain comparisons between models with and without residual stress.

Plaque	Maximum out-wall strain				Mean out-wall strain			
	M-Model with residual stress	M-Model no residual stress	S-Model with residual stress	S-Model no residual stress	M-Model with residual stress	M-Model no residual stress	S-Model with residual stress	S-Model no residual stress
P1	0.358	0.194	0.266	0.120	0.246	0.087	0.176	0.072
	185.02%	100.00%	221.29%	100.00%	284.02%	100.00%	244.89%	100.00%
P2	0.389	0.099	0.275	0.078	0.248	0.049	0.189	0.039
	394.26%	100.00%	353.28%	100.00%	501.91%	100.00%	479.25%	100.00%
P3	0.396	0.073	0.258	0.059	0.227	0.055	0.161	0.051
	545.80%	100.00%	439.17%	100.00%	411.36%	100.00%	312.73%	100.00%
P4	0.397	0.148	0.279	0.083	0.238	0.082	0.151	0.058
	267.60%	100.00%	334.96%	100.00%	288.94%	100.00%	260.47%	100.00%
P5	0.435	0.097	0.303	0.081	0.171	0.065	0.114	0.056
	450.40%	100.00%	374.63%	100.00%	262.11%	100.00%	205.59%	100.00%
P6	0.326	0.130	0.229	0.099	0.200	0.070	0.154	0.061
	250.78%	100.00%	231.07%	100.00%	286.78%	100.00%	251.55%	100.00%
P7	0.306	0.141	0.218	0.109	0.205	0.086	0.152	0.067
	216.83%	100.00%	200.96%	100.00%	237.90%	100.00%	227.53%	100.00%
P8	0.307	0.098	0.213	0.073	0.194	0.062	0.146	0.055
	313.53%	100.00%	293.67%	100.00%	313.06%	100.00%	266.24%	100.00%
P9	0.451	0.110	0.371	0.065	0.245	0.026	0.209	0.020
	409.14%	100.00%	572.17%	100.00%	943.74%	100.00%	1,038.05%	100.00%
P10	0.326	0.088	0.244	0.073	0.271	0.058	0.193	0.053
	368.79%	100.00%	333.85%	100.00%	468.03%	100.00%	362.55%	100.00%
Mean ± STD	0.369 ± 0.052	0.118 ± 0.036	0.265 ± 0.047	0.084 ± 0.020	0.225 ± 0.031	0.064 ± 0.019	0.164 ± 0.028	0.053 ± 0.015
Mean ± STD (%)	340.21% ± 113.62%	100.00%	335.51% ± 111.76%	100.00%	399.79% ± 211.41%	100.00%	364.88% ± 249.68%	100.00%

M-Model, multi-layer model; S-Model, single-layer model.

strain calculations, which has great potential for enhancing the prediction accuracy of plaque progression and vulnerability. Furthermore, it might provide doctors with better patient screening strategies, enabling the timely application of appropriate interventions or conservative therapies. This will optimize the process of patient management, diagnosis, and treatment of cardiovascular diseases, ultimately aiming to improve patient outcomes in cardiovascular healthcare. There is also a well-accepted threshold stress value 300 kPa for plaques with high vulnerability (23, 24). When interpreting model results, the associated model assumptions should be taken into consideration.

Multi-layer model residual stress inclusion also increased out-wall maximum and mean plaque stresses by 572.84% and 432.03%. That led to a more uniform distribution of stress within the vessel wall (see Figure 5), which is consistent with the principle that the human body would regulate vessel stress to be uniform to achieve optimal functionality (8, 11). Essentially, residual stress introduced compressive circumferential stress in the intima and circumferential "stretch" in the adventitia. Interestingly, negative mean plaque stress values at inner wall location were observed in 1 multi-layer model and 4 single-layer models with residual stress inclusion in our study.

4.2 Comparison of multi-layer and single layer models with residual stress inclusion

Multi-layer models exhibited more uniform stress distributions compared to single-layer models. In multi-layer models with residual stress, the average mean stresses of 10 plaques at inner and out-wall locations were 50.68 kPa and 97.03 kPa, respectively. While from single-layer models with residual stress, the inner wall and out-wall stress values were 6.89 kPa and 194.55 kPa. Multi-layer models with and without residual stress inclusion had mean inner wall stresses 50.68 kPa and 113.29 kPa (averaged over 10 patients), respectively, compared to 6.89 kPa and 74.79 kPa from single-layer models. For out-wall mean stress values, multi-layer models with and without residual stress inclusion had 97.03 kPa and 20.85 kPa, compared to 194.55 kPa and 34.39 kPa from single-layer models. Stress differences from single-layer models with and without residual stress inclusion had much greater differences. Layer-specific material properties are the cause of these large differences.

4.3 Potential clinical benefits of multi-layer models with residual stress inclusion

Multi-layer models with residual stress inclusion could lead to more accurate plaque stress and strain calculations which could have a wide range of clinical applications including plaque vulnerability assessment, prediction of plaque progression and vulnerability change through diverse biomechanical indicators, as well as exploring the correlation between mechanical conditions and the incidence of future major adverse cardiovascular events. Plaque cap stress (which is on inner layer of the vessel) is well-recognized risk factor for possible plaque rupture.

Table 2 gave maximum and mean plaque stress values on vessel inner wall from multi-layer and single-layer models and comparisons for models with and without residual stress for the 10 patients studied. From multi-layer models with residual stress inclusion, the inner wall maximum and mean plaque stress values (averaged over 10 patients) were 148.53 kPa and 50.68 kPa respectively, which were 38.57% and 59.70% lower than the values from corresponding models without residual stress. From single-layer models with residual stress, the inner wall maximum and mean plaque stress values were 59.14 kPa and 6.89 kPa, which were 61.46% and 94.72% lower than the values from corresponding models without residual stress. The average of the inner-layer maximum stress of the 10 patients from the multi-layer models with residual stress inclusion was 148.53 ± 86.35 kPa while the value from the multilayer models without residual stress was 240.45 ± 94.72, a 61.8% over-estimate. Another potential use of the multi-layer models with residual stress was for artery remodeling which could be closed related to vessel out-wall stress/strain conditions. The average of the outer-layer maximum stress of the 10 patients from the multi-layer models with residual stress inclusion was 211.15 ± 75.66 kPa, while the value from the multilayer models without residual stress was 35.04 ± 10.73 kPa, only 16.6% of the value from models with residual stress. Those results suggest that residual stress inclusion would have considerable impact for vulnerable plaque and artery remodeling investigations.

While we demonstrated the considerable impact of residual stress on stress/strain calculations and subsequent clinical applications, it should be noted that clinical acceptance and implementation remain to be big challenges. Our small data size is a serious limitation. Large scale studies are needed to get solid validation of our initial results and then final clinical acceptance. Another challenge is model construction cost. The open-close process in the construction of models with residual stress was done manually which was very labor intensive. Automation of the modeling process is a must for potential clinical implementations.

4.4 The use of 3D thin-slice models vs. full 3D models

3D thin-slice models were used in this study with two major reasons: (a) 3D thin-slice model could provide better approximation than what 2D model would since it did have slice thickness and axial pre-shrink-stretch was performed to take axial residual stress into consideration; (b) model construction time for 3D thin-slice model was only slightly more than 2D models, but much less compared to full 3D models. The ultimate goal of computational modeling and vulnerable plaque research is to implement the modeling and mechanical analysis for possible clinical applications and providing stress/strain conditions to aid vulnerable plaque detection, cardiovascular disease diagnosis, management and possible prevention of drastic events such as heart attack and/or stroke. 3D models are too far away from actual implementation due to their labor cost. 3D thin-slice models could be a compromise in between: reasonable accuracy and labor cost which makes practical implementation possible. Wang Q et al. provided multi-patient

model comparisons and reported that the errors from 3D thin-slice models were around 10% compared to full 3D models (25). That was encouraging.

4.5 Limitations and future directions

We would like to acknowledge some limitations of our study: (a) Small patient size is a severe limitation. This is a pilot study to investigate the impact of residual stress on stress/strain calculations using a small patient size. Model construction with multilayers and residual stress inclusion is very time consuming due to the manual open-close process. Larger-scale studies are needed to further validate the impact of residual stress, and to explore its impact across various patient groups, in terms of age, sex, different plaque types and comorbidities, etc. This will enable a more comprehensive understanding of residual stress's role in plaque dynamics; (b) 3D thin-slice models were used to reduce labor cost. Techniques should be developed to construct full 3D models with residual stress inclusion to improve accuracy of stress/strain calculations, but also keeping labor cost at acceptable level; (c) Due to lack of available vessel residual stress data and material properties, an average opening angle and material parameter values from the literature were utilized in this study. It should be noted that it is not possible to obtain patient-specific opening angle from live patients. It is also challenging to obtain patient-specific multi-layer vessel material parameters.

5 Conclusion

In this study, multi-layer and single-layer coronary plaque models with and without residual stress inclusion were constructed for 10 patients based on automatically segmented three-layer OCT images to quantify the impact of residual stress on stress/strain calculations. Our results showed that residual stress plays a critical role in the stress distribution of vessel tissues, and led to reduced inner wall plaque stress and increased out-wall stress. Larger scale studies are needed to further improve model accuracy and validate our findings.

Data availability statement

The original contributions presented in the study and data supporting the conclusions are included in the article. Further inquiries can be directed to the corresponding author Dalin Tang, dtang@wpi.edu.

Ethics statement

The studies involving humans were approved by Southeast University Zhongda Hospital Institutional Review Board (approval code 2019ZDKYSB046). The studies were conducted in accordance with the local legislation and institutional requirements. Written informed consent for participation was not required from the participants or the participants' legal guardians/next of kin in accordance with the national legislation and institutional requirements.

Author contributions

MH: Conceptualization, Formal Analysis, Methodology, Writing – original draft, Writing – review & editing. AM: Data curation, Writing – review & editing. DT: Conceptualization, Methodology, Project administration, Writing – original draft, Writing – review & editing, Funding acquisition. JZ: Data curation, Project administration, Writing – review & editing. LW: Conceptualization, Formal Analysis, Methodology, Writing – review & editing. RL: Data curation, Writing – review & editing. YZ: Data curation, Writing – review & editing. XZ: Data curation, Formal Analysis, Writing – review & editing. CZ: Data curation, Writing – review & editing. HJ: Data curation, Writing – review & editing. GM: Data curation, Writing – review & editing.

Funding

The author(s) declare that financial support was received for the research, authorship, and/or publication of this article.

This research was funded by the National Sciences Foundation of China grant 11972117 and the Jiangsu Province Science and Technology Agency under grant number BE2016785.

Conflict of interest

The authors declare that the research was conducted in the absence of any commercial or financial relationships that could be construed as a potential conflict of interest.

The author(s) declared that they were an editorial board member of Frontiers, at the time of submission. This had no impact on the peer review process and the final decision.

Publisher's note

All claims expressed in this article are solely those of the authors and do not necessarily represent those of their affiliated organizations, or those of the publisher, the editors and the reviewers. Any product that may be evaluated in this article, or claim that may be made by its manufacturer, is not guaranteed or endorsed by the publisher.

References

1. Ku DN, Giddens DP, Zarins CK, Glagov S. Pulsatile flow and atherosclerosis in the human carotid bifurcation. Positive correlation between plaque location and low oscillating shear stress. *Arteriosclerosis*. (1985) 5:293–302. doi: 10.1161/01.atv.5.3.293

2. Bluestein D, Alemu Y, Avrahami I, Gharib M, Dumont K, Ricotta JJ, et al. Influence of microcalcifications on vulnerable plaque mechanics using FSI modeling. *J Biomech*. (2008) 41(5):1111–8. doi: 10.1016/j.jbiomech.2007.11.029

3. Samady H, Eshtehardi P, Mcdaniel MC, Suo J, Dhawan SS, Maynard C, et al. Coronary artery wall shear stress is associated with progression and transformation of atherosclerotic plaque and arterial remodeling in patients with coronary artery disease. *Circulation*. (2011) 124(7):779–88. doi: 10.1161/CIRCULATIONAHA.111.021824

4. Tang D, Teng Z, Canton G, Yang C, Ferguson M, Huang X, et al. Sites of rupture in human atherosclerotic carotid plaques are associated with high structural stresses: an in vivo MRI-based 3D fluid-structure interaction study. *Stroke*. (2009) 40 (10):3258–63. doi: 10.1161/STROKEAHA.109.558676

5. Wentzel JJ, Corti R, Fayad ZA, Wisdom P, Macaluso F, Winkelman MO, et al. Does shear stress modulate both plaque progression and regression in the thoracic aorta? Human study using serial magnetic resonance imaging. *J Am Coll Cardiol*. (2005) 45(6):846–54. doi: 10.1016/j.jacc.2004.12.026

6. Costopoulos C, Maehara A, Huang Y, Brown AJ, Gillard JH, Teng Z, et al. Heterogeneity of plaque structural stress is increased in plaques leading to mace: insights from the prospect study. *JACC Cardiovasc Imaging*. (2020) 13(5):1206–18. doi: 10.1016/j.jcmg.2019.05.024

7. Fung YC, Liu SQ. Strain distribution in small blood vessels with zero-stress state taken into consideration. *Am J Physiol*. (1992) 262(2 Pt 2):H544–52. doi: 10.1152/ajpheart.1992.262.2.H544

8. Rachev A, Taylor WR, Vito RP. Calculation of the outcomes of remodeling of arteries subjected to sustained hypertension using a 3D two-layered model. *Ann Biomed Eng*. (2013) 41(7):1539–53. doi: 10.1007/s10439-012-0727-9

9. Huang M, Maehara A, Tang D, Zhu J, Wang L, Lv R, et al. Human coronary plaque optical coherence tomography image repairing, multilayer segmentation and impact on plaque stress/strain calculations. *J Funct Biomater*. (2022) 13(4):213–26. doi: 10.3390/jfb13040213

10. Huang M, Maehara A, Tang D, Zhu J, Wang L, Lv R, et al. Comparison of multilayer and single-layer coronary plaque models on stress/strain calculations based on optical coherence tomography images. *Front Physiol*. (2023) 14:1251401. doi: 10.3389/fphys.2023.1251401

11. Fung YC. *A First Course in Continuum Mechanics*. Englewood Cliffs: New Jersey: Prentice Hall (1994).

12. Holzapfel GA, Sommer G, Auer M, Regitnig P, Ogden RW. Layer-specific 3D residual deformations of human aortas with non-atherosclerotic intimal thickening. *Ann Biomed Eng*. (2007) 35(4):530–45. doi: 10.1007/s10439-006-9252-z

13. Holzapfel GA, Ogden RW. Modelling the layer-specific three-dimensional residual stresses in arteries, with an application to the human aorta. *J R Soc Interface*. (2010) 7(46):787–99. doi: 10.1098/rsif.2009.0357

14. Delfino A, Stergiopulos N, Moore JE, Meister JJ. Residual strain effects on the stress field in a thick wall finite element model of the human carotid bifurcation. *J Biomech*. (1997) 30(8):777–86. doi: 10.1016/S0021-9290(97)00025-0

15. Ohayon J, Dubreuil O, Tracqui P, Le Floc'h S, Rioufol G, Chalabreysse L, et al. Influence of residual stress/strain on the biomechanical stability of vulnerable coronary plaques: potential impact for evaluating the risk of plaque rupture. *Am J Physiol Heart Circ Physiol*. (2007) 293(3):H1987–96. doi: 10.1152/ajpheart.00018.2007

16. Wang L, Zhu J, Samady H, Monoly D, Zheng J, Guo X, et al. Effects of residual stress, axial stretch, and circumferential shrinkage on coronary plaque stress and strain calculations: a modeling study using IVUS-based near-idealized geometries. *J Biomech Eng*. (2017) 139(1):014501. doi: 10.1115/1.4034867

17. Pierce DM, Fastl TE, Rodriguez-Vila B, Verbrugghe P, Fourneau I, Maleux G, et al. A method for incorporating three-dimensional residual stretches/stresses into patient-specific finite element simulations of arteries. *J Mech Behav Biomed Mater*. (2015) 47:147–64. doi: 10.1016/j.jmbbm.2015.03.024

18. Holzapfel GA, Sommer G, Gasser CT, Regitnig P. Determination of layer-specific mechanical properties of human coronary arteries with nonatherosclerotic intimal thickening and related constitutive modeling. *Am J Physiol Heart Circ Physiol*. (2005) 289(5):H2048–58. doi: 10.1152/ajpheart.00934.2004

19. Kural MH, Cai M, Tang D, Gwyther T, Zheng J, Billiar KL, et al. Planar biaxial characterization of diseased human coronary and carotid arteries for computational modeling. *J Biomech*. (2012) 45(5):790–8. doi: 10.1016/j.jbiomech.2011.11.019

20. Yang C, Bach RG, Zheng J, Naqa IE, Woodard PK, Teng Z, et al. In vivo IVUS-based 3-D fluid-structure interaction models with cyclic bending and anisotropic vessel properties for human atherosclerotic coronary plaque mechanical analysis. *IEEE Trans Biomed Eng*. (2009) 56(10):2420–8. doi: 10.1109/TBME.2009.2025658

21. Lv R, Maehara A, Matsumura M, Wang L, Zhang C, Huang M, et al. Using optical coherence tomography and intravascular ultrasound imaging to quantify coronary plaque cap stress/strain and progression: a follow-up study using 3D thin-layer models. *Front Bioeng Biotechnol*. (2021) 9:713525. doi: 10.3389/fbioe.2021.713525

22. Wang Q, Tang D, Wang L, Canton G, Wu Z, Hatsukami TS, et al. Combining morphological and biomechanical factors for optimal carotid plaque progression prediction: an MRI-based follow-up study using 3D thin-layer models. *Int J Cardiol*. (2019) 293:266–71. doi: 10.1016/j.ijcard.2019.07.005

23. Finet G, Ohayon J, Rioufol G. Biomechanical interaction between cap thickness, lipid core composition and blood pressure in vulnerable coronary plaque: impact on stability or instability. *Coron Artery Dis*. (2004) 15(1):13–20. doi: 10.1097/00019501-200402000-00003

24. Cardoso L, Weinbaum S. Changing views of the biomechanics of vulnerable plaque rupture, a review. *Ann Biomed Eng*. (2014) 42(2):415–31. doi: 10.1007/s10439-013-0855-x

25. Wang Q, Tang D, Wang L, Meahara A, Molony D, Samady H, et al. Multi-patient study for coronary vulnerable plaque model comparisons: 2D/3D and fluid–structure interaction simulations. *Biomech Model Mechanobiol*. (2021) 20 (4):1383–97. doi: 10.1007/s10237-021-01450-8

frontiers | Frontiers in Cardiovascular Medicine

TYPE Original Research
PUBLISHED 20 May 2024
DOI 10.3389/fcvm.2024.1388648

Check for updates

OPEN ACCESS

EDITED BY
Gaoyang Li,
Tohoku University, Japan

REVIEWED BY
Jing Tang,
Harbin Medical University, China
Xinya Xie,
The First Affiliated Hospital of Xi'an Jiaotong University, China

*CORRESPONDENCE
Erqing Li
✉ leq821128@163.com
Hui Fan
✉ 240731187@qq.com
Qiang Liu
✉ 723799507@qq.com

†These authors have contributed equally to this work and share co-first authorship

RECEIVED 20 February 2024
ACCEPTED 06 May 2024
PUBLISHED 20 May 2024

CITATION
Mao Y, Shi Y, Qiao W, Zhang Z, Yang W, Liu H, Li E, Fan H and Liu Q (2024) Symptom clusters and unplanned hospital readmission in Chinese patients with acute myocardial infarction on admission.
Front. Cardiovasc. Med. 11:1388648.
doi: 10.3389/fcvm.2024.1388648

COPYRIGHT
© 2024 Mao, Shi, Qiao, Zhang, Yang, Liu, Li, Fan and Liu. This is an open-access article distributed under the terms of the Creative Commons Attribution License (CC BY). The use, distribution or reproduction in other forums is permitted, provided the original author(s) and the copyright owner(s) are credited and that the original publication in this journal is cited, in accordance with accepted academic practice. No use, distribution or reproduction is permitted which does not comply with these terms.

Symptom clusters and unplanned hospital readmission in Chinese patients with acute myocardial infarction on admission

Yijun Mao[1†], Yuqiong Shi[1†], Wenfang Qiao[1†], Zhuo Zhang[1], Wei Yang[1], Haili Liu[1], Erqing Li[1*], Hui Fan[2*] and Qiang Liu[3*]

[1]Department of Cardiology, Xianyang Central Hospital, Shaanxi, China, [2]Department of Nursing, Xianyang Central Hospital, Shaanxi, China, [3]Department of Orthopedic, Xianyang Central Hospital, Shaanxi, China

Backgroud: Acute myocardial infarction (AMI) has a high morbidity rate, high mortality rate, high readmission rate, high health care costs, and a high symptomatic, psychological, and economic burden on patients. Patients with AMI usually present with multiple symptoms simultaneously, which are manifested as symptom clusters. Symptom clusters have a profound impact on the quality of survival and clinical outcomes of AMI patients.
Objective: The purpose of this study was to analyze unplanned hospital readmissions among cluster groups within a 1-year follow-up period, as well as to identify clusters of acute symptoms and the characteristics associated with them that appeared in patients with AMI.
Methods: Between October 2021 and October 2022, 261 AMI patients in China were individually questioned for symptoms using a structured questionnaire. Mplus 8.3 software was used to conduct latent class analysis in order to find symptom clusters. Univariate analysis is used to examine characteristics associated with each cluster, and multinomial logistic regression is used to analyze a cluster membership as an independent predictor of hospital readmission after 1-year.
Results: Three unique clusters were found among the 11 acute symptoms: the typical chest symptom cluster (64.4%), the multiple symptom cluster (29.5%), and the atypical symptom cluster (6.1%). The cluster of atypical symptoms was more likely to have anemia and the worse values of Killip class compared with other clusters. The results of multiple logistic regression indicated that, in comparison to the typical chest cluster, the atypical symptom cluster substantially predicted a greater probability of 1-year hospital readmission (odd ratio 8.303, 95% confidence interval 2.550–27.031, $P < 0.001$).
Conclusion: Out of the 11 acute symptoms, we have found three clusters: the typical chest symptom, multiple symptom, and atypical symptom clusters. Compared to patients in the other two clusters, those in the atypical symptom cluster—which included anemia and a large percentage of Killip class patients—had worse clinical indicators at hospital readmission during the duration of the 1-year follow-up. Both anemia and high Killip classification suggest that the patient's clinical presentation is poor and therefore the prognosis is worse. Intensive treatment should be considered for anemia and high level of Killip class patients with atypical presentation. Clinicians should focus on patients with atypical symptom clusters, enhance early recognition of symptoms, and develop targeted symptom management strategies to alleviate their discomfort in order to improve symptomatic outcomes.

KEYWORDS

acute myocardial infarction, symptom cluster, cross-section studies, latent class analysis, unplanned hospital readmission

1 Introduction

The American Heart Association (AHA) predicts that about 13 million people worldwide will suffer from cardiovascular disease in 2035, with coronary heart disease (CHD) being the leading cause of death among people with cardiovascular disease (1, 2). The task of preventing and controlling coronary heart disease in China is equally burdensome, and the Report on Cardiovascular Health and Disease in China 2022 points out that the incidence rate of coronary heart disease is rising year by year, and the number of people suffering from coronary heart disease in China has already reached 1.13 million, and the mortality rate of coronary heart disease has reached 0.12%. Since 2005, the mortality rate of coronary heart disease has been rising rapidly and tends to be younger. It can be seen that strengthening the prevention and treatment of coronary heart disease is a key measure to improve the management system of cardiovascular diseases in China (1, 3, 4).

Patients with acute myocardial infarction (AMI) usually present with a variety of symptoms at the onset of the disease, mainly chest pain/chest discomfort, sweating, dyspnea, nausea/vomiting, etc., and present in the form of symptom clusters (5–8). Each patient experiences an average of 3.6–4.75 symptoms in the previous studies (9, 10). Symptom clusters can be defined as two or more concurrently occurring symptoms that interact with each other (11–14). The symptoms of AMI are varied, and multiple symptoms often coexist, creating a negative symptom cluster synergy between symptoms. Compared with single symptoms, symptom clusters can increase the burden of disease in AMI patients, decrease their adherence to treatment, and have a serious negative impact on their quality of life and health status (15–17). The results of related studies have shown that symptom clusters in AMI patients can have a serious impact on functional status, readmission rates for cardiovascular events, and all-cause mortality (18). Symptom clusters consisting of multiple symptoms have a more profound impact on the clinical outcome of patients with AMI than a single symptom (19).

At this stage, the management of symptom clusters in patients with AMI has only progressed to the stage of symptom cluster identification, and more research is needed on the development of symptom cluster management strategies and the evaluation of outcomes (14).

AMI is an aggressive and rapidly progressive condition, and percutaneous coronary intervention (PCI) is the key to its successful treatment and the most common approach for coronary revascularization. Total number of coronary heart disease interventions in China reached 1.16 million in 2021, with 1.48 stents placed per capita in coronary heart disease patients. Reperfusion therapy has a time window requirement, with a 10% increase in patient morbidity and mortality for every 1 h of delay, making early recognition of AMI symptoms and prompt medical attention critical. Problems with the prognosis of PCI also arise; in-stent restenosis, cardiac rupture, and chest pain may cause repeated, multiple admissions to the hospital, which brings a serious economic and psychological burden to patients. It showed nearly 20% of patients were readmitted for cardiovascular events within 1 year of PCI in the previous study (20). Thus unplanned readmission in the early post-procedure period after PCI is considered to be a costly and common adverse outcome (20, 21).

In the United States, readmissions occur in one-fifth of PCI patients each year and account for 33% of the total cost of readmissions, amounting to $26 billion, with a low quality of life and a high economic burden, with 75% of these readmissions considered avoidable. However, there are few studies on the prognostic impact of symptom clusters in AMI patients, and few studies on the impact of symptom clusters on unplanned readmission in AMI patients have been reported. Therefore, the aim of this study was to explore the potential categories of symptom clusters in AMI patients and the effect of potential categories on readmission within 1 year after PCI using latent class analysis, with the aim of helping medical staff to be more targeted in symptom management and providing evidence support and theoretical basis.

2 Materials and methods

2.1 Study setting and population

This study is a cross-sectional survey study. Convenience sampling method was used to extract patients readmitted for treatment of acute myocardial infarction in the Department of Cardiology of Xianyang City Central Hospital from October 2021 to October 2022 for the study. Inclusion criteria were: (1) patients who survived and those with a final diagnosis of ST-elevation myocardial infraction (STEMI) or Non-ST-elevation myocardial infraction (NSTEMI) who underwent PCI, (2) age 18 years or older, (3) understanding of spoken Chinese, and (4) those who consented to take part in the study. Exclusion criteria were: (1) combination of major organic lesions; (2) new postoperative complications such as myocardial infarction and cerebral infarction.

In this study, the sample size calculation formula was $n = Z^2_{\alpha/2}(1-P)P/\delta^2$, setting the test level $\alpha = 0.05(Z_{\alpha/2} = 1.96)$, with a permissible margin of error $\delta = 0.05$, and based on the results of a similar study in the literature (20), the maximum incidence of re-admission of patients with AMI was 17%, which means that $P = 0.17$, and calculating the sample size $n = 1.96^2 \times (1-0.17) \times 0.17 \div 0.05^2 = 216$ cases, considering the 20% non-response rate, 259 cases were needed for the sample size. A total of 270 patients met the criteria, 9 were dropped due to the long follow-up period and we were unable to contact them. A total of 261 patients were included in this study, with a average age of 62.8 ± 11.2 years (range 34–89), and the rest of the general information, is shown in Table 1.

2.2 Ethics statement

The study protocol was approved by the Ethical Research Board of the affiliated institution (IRB No. 2023-64). Patients

TABLE 1 Baseline clinical characteristic.

Variables	Classification	$N = 261$	%
Age (years)	34–60	109	41.8
	61–89	152	58.2
Final diagnosis	ST-elevation myocardial infraction	178	68.2
	Non-ST-elevation myocardial infraction	83	31.8
Gender	Female	42	16.1
Marital status	Divorced/widowed/never married	2	0.8
Occupation status	Unemployed/retired	38	14.6
Risk factors[a]	Hypertension	120	46.0
	Diabetes mellitus	47	18.0
	Dyslipidemia	48	18.4
	Current smoking	135	51.7
	Obesity = body mass index>28 kg/m^2	24	9.2

[a]Answers were duplicated.

who consented to take part in the study signed an informed consent. Patient readmission information was obtained by telephone interview during follow-up period.

2.3 Questionnaire and data collection

2.3.1 Patients characteristics

The questionnaire of patients characteristics was developed by the researcher and consisted of 3 parts, (1) sociodemographic characteristic: gender, age, working status, marital status, and mode of payment for medical care; (2) disease-related information: risk factors, diagnosis, comorbid conditions, cardiac function class, Killip class, type of coronary artery lesion, history of hemodialysis and total hospital stay and (3) clinical outcome information: readmission within 1 year.

2.3.2 AMI symptoms

For this study, Illness Perception Questiormaire Revised (IPQ-R) was selected to collect patients symptoms. The IPQ-R is a targeted assessment tool for assessing the multisymptomatic nature of AMI and was developed by Moss Morris in a revision of the IPQ developed by Weinman et al. There are 11 symptoms, including: (1) chest pain, (2) chest discomfortable, (3) radiating pain, (4) dyspnea, (5) palpitation, (6) nausea/vomiting, (7) sweating, (8) weakness/fatigue, (9) dizziness, (10) syncope, (11) throat tighting sensation. Cronbach's α coefficient for internal consistency was 0.66–0.92 in the previous studies (22–25).

2.3.3 Hospital readmission

Unplanned readmission is defined as any unpredictable readmission that occurs after discharge for an activity that is not performed within the normal plan, excluding planned readmissions (e.g., follow-up review, secondary surgery, etc.) (26). Retain contact information and verify contact information for patients and their families during their hospitalization. We obtained readmission information through telephone interviews with patients by asking about the date and reason for readmission in the past 1 year. Hospital readmission was defined as a return or visit to the hospital due to AMI related complications or AMI recurrence, deterioration within 12 months after hospital discharge for AMI. Readmission excluded planned readmissions, such as elective surgery, regular hospital admissions for treatment, review, etc. and unrelated to the reason for the last hospitalization.

The purpose and requirements of the study were explained to the patients who met the criteria by two investigators who were uniformly trained, and the questionnaire was administered within 3 days of the patient's admission after obtaining informed consent. Uniform training was given to the investigators to ensure that they conducted one-on-one on-site surveys using uniform instructions; when data were collected face-to-face, they were filled in by the research subjects themselves; for older patients, they could be filled in on behalf of the research subjects by asking them one by one; if there were any questions during the filling in process, the researchers provided timely explanations, the questionnaires were distributed and collected on the spot, and on-site verification was carried out instantly. If there is any omission or obvious error, the research subjects are reminded to make up or correct in time; the questionnaire number is entered in time, and the confidentiality of the information is done. Each patients was collected information about the symptoms, risk factors, and chronic diseases related to the acute phase of acute myocardial infarction. Disease-related information was collected by reviewing the medical record system. Data for clinical outcome including hospital readmission was also obtained.

2.4 Statistical analysis

Latent class analysis (LCA) was used for analyzing the coded symptoms, and the evaluation indexes were as follows. (1) Information criteria: Akaike Information Criterion (AIC), Bayesian Information Criterion (BIC) and adjusted Bayesian Information Criterion (aBIC). Smaller values of such information criteria indicate better model fit. (2) Entropy index: indicates the degree of classification accuracy, the value range is 0–1, the closer to 1 indicates that the classification is more accurate. (3) Likelihood ratio metrics: Lo-Mendell-Rubin (LMR) and Bootstrapped likelihood ratio test (BLRT), significant LMR, BLRT values indicate that a model with K categories outperforms a model with K-1 categories (27, 28).

The collected data were analyzed using SPSS Statistic v.24. Univariate analysis was used to compare differences in the characteristics of samples of patients with different symptom clusters. Multiple logistic regression analysis was used to identify the effect of symptom clusters on readmission after adjusting for patients' baseline characteristics. The statistic significance level(α) was set at 0.05.

3 Results

3.1 Three sets of symptoms were identified by latent cluster analysis

Patients were included in the potential category model, and a total of 5 models were fitted. In model 3, AIC and aBIC were the

smallest, the *P*-value of BLRT test was <0.05, and the entropy was >0.7. Based on the clinical experience, model 3 was chosen to categorize the patients into 3 categories, as shown in Table 2.

3.2 Significant differences in the number and composition of the symptom in 3 cluster groups

Cluster 1 had the highest number of participants ($n = 168$, 64.4%), followed by Cluster 2 ($n = 77$, 29.5%) and Cluster 3 ($n = 16$, 6.1%).On average, patients reported 2.9 ± 1.2 symptoms. There was a significant difference in the number of symptoms among the 3 clusters ($P < 0.001$); with the highest number of symptoms in cluster 3 (5.0 ± 2.9) and the lowest number of symptoms in cluster 1 (2.6 ± 1.2). As for the distribution of symptoms in each cluster, excluding nausae or vomiting, sweating and syncope, the remaining symptoms (chest pain, chest discomfortable, pain or discomfortable in other parts, shortness of breath, palpitation, weakness or fatigue [all $P < 0.001$]; dizziness [$P = 0.014$]; throat tightening sensation [$P = 0.036$) showed significant differences between clusters. Most common was chest pain (83.9%), followed by sweating (73.2%). Less frequently reported symptoms were syncope (7.3%), palpitation (2.7%), and throat tightening sensation (1.9%) (Table 3).

In cluster 1, the frequency of chest pain was the highest at 100%, followed by sweating (75.0%) and nausea or vomiting (25.6%). In cluster 2, chest discomfortable at 98.7%, followed by shortness of breath (77.9%) and sweating (68.8%). Many atypical symptoms were present in Cluster 3, including radiating pain (75.0%), weakness or fatigue (56.3%), palpitation (37.5%) and dizziness (25.9%). The clusters have been called "classic symptoms" (cluster 1), "multiple symptoms" (cluster 2), and "atypical symptoms" (cluster 3), taking into account the number of symptoms, frequency, and distribution (Figure 1).

3.3 Patients of cluster 3 are more likely to have anemia and be with high value of killip class

In terms of comorbidities, the results of the univariate analysis in this study showed that there were differences in anemia ($P = 0.016$) among patients with different potential categories of AMI symptom clusters, and the patients of atypical symptom cluster were more likely to have anemia.

For disease factors, the results of the univariate analysis in this study showed that there were differences in Killip classes ($P = 0.003$) in patients with different potential categories of AMI symptom clusters, and the patients of atypical symptom clusters were more likely to have higher value for Killip classes, which has severe heart failure (Table 4).

3.4 Patients in cluster 3 anticipated a noticeably higher risk of 1-year readmission

During the follow-up period, a total of 55 (21.1%) patients had readmissions, including 23 (8.8%) planned readmissions, 4 (1.5%) unrelated disease readmissions, and 28 (10.7%) unplanned readmissions.

TABLE 2 Model fit results of LCA for symptom cluster in acute myocardial patients ($n = 261$).

Models	AIC	BIC	aBIC	Entropy	*P*		Number of patients in each category
					LMR-LRT	BLRT	
1	2,217.636	2,256.846	2,221.971	—	—	—	—
2	2,080.710	2,162.694	2,089.774	1.000	<0.001	<0.001	79/182
3	2,063.825	2,188.583	2,077.618	0.882	0.141	<0.001	168/77/16
4	2,066.800	2,234.332	2,085.323	0.800	0.387	0.158	48/5/80/128
5	2,069.524	2,279.831	2,092.776	0.839	0.148	0.500	158/19/13/10/61

TABLE 3 Comparison of frequency of presenting symptoms by cluster group ($n = 261$).

	Total	Cluster 1 ($n = 168$)	Cluster 2 ($n = 77$)	Cluster 3 ($n = 16$)	F/χ^2	*P*
No of total symptom (mean ± SD)	2.9 ± 1.2	2.6 ± 1.2	3.1 ± 1.1	5.0 ± 2.9	13.559	<0.001
Chest pain	219 (83.9)	168 (100.0)	44 (57.1)	7 (43.8)	99.475	<0.001
Chest discomfortable	79 (30.3)	0	76 (98.7)	3 (18.8)	285.615	<0.001
Radiating pain	57 (21.8)	37 (22.0)	8 (10.4)	12 (75.0)	27.035	<0.001
Dyspnea	92 (35.2)	25 (14.9)	60 (77.9)	7 (43.8)	92.476	<0.001
Palpitation	7 (2.7)	1 (6.0)	0	6 (37.5)	29.406	<0.001
Nausea/vomiting	67 (25.7)	43 (25.6)	16 (20.8)	8 (50.0)	5.499	0.059
Sweating	191 (73.2)	126 (75.0)	53 (68.8)	12 (75.0)	1.086	0.616
Weakness/fatigue	13 (5.0)	1 (6.0)	3 (3.9)	9 (56.3)	43.377	<0.001
Dizziness	19 (7.3)	8 (4.8)	7 (9.1)	4 (25.9)	7.819	0.014
Syncope	9 (3.4)	6 (3.6)	3 (3.9)	0	0.183	1.000
Throat tighting sensation	5 (1.9)	2 (1.2)	1 (1.3)	2 (12.5)	6.230	0.036

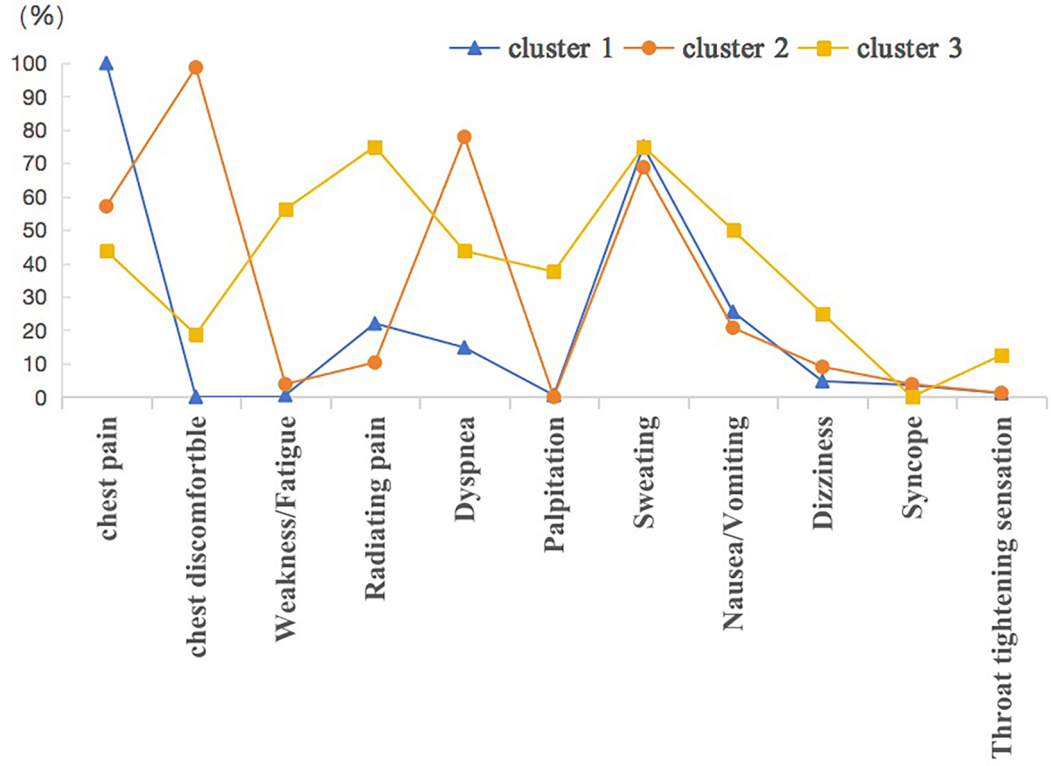

FIGURE 1
Symptom distribution by clustered groups.

A total of 28 patients readmitted during the course of the follow-up period. The hospital readmission proved to be significantly varied by cluster, using bivariate analysis ($P = 0.001$) (Table 5). Multinomial logistic regression analysis demonstrated that when patients characteristic were adjusted for, compared to patients in Cluster 1, patients in Cluster 3 anticipated a noticeably higher risk of 1-year readmission (odd ratio 8.303, 95% confidence interval 2.550–27.031, $P < 0.001$) (Table 6).

4 Discussion

This study identified symptom clusters in patients with AMI, explored the relationship between symptom clusters and patient-related variables, and examined into the impact of symptom clusters on hospital readmission in order to develop intervention strategies to lower the risk of readmission in Chinese patients with AMI. Using the latent class analysis, three symptom clusters were identified: typical chest symptom cluster (chest pain, sweating, nausea/vomiting), multiple symptom cluster(chest discomfortable, shortness of breath, sweating) and atypical symptom cluster(radiating pain, weakness/fatigue, palpitation, dizziness). Previous studies have categorized symptoms into four to five clusters (9, 19), with differences in this classification based on factors such as the target population, inclusion criteria, number of symptoms evaluated, and methods of clustering (29).

Hwang et al. (18) used latent class cluster analysis to extract three clusters were: typical chest pain (chest pain/discomfortable, cold sweat, shortness of breath, nause/vomiting, weakness/fatigue/dizziness), multiple symptoms (chest pain/discomfortable, left shoulder/arm pain, cold sweat, right shoulder/arm pain, nausea/vomiting), atypical symptom (shortness of breath, weakness/fatigue/dizziness, indigestion/abdominal pain, cold sweat, nausea/vomiting).

The results of the two studies were basically the same, but the composition of the symptoms within the clusters was not exactly the same, and the reasons for this were analyzed which were related to the inconsistency of the symptoms collected. This study used the IPQ-R with 11 symptom entries, Huwang et al. (18) analyzed 14 symptom entries and the composition of the entries was inconsistent.

Kim et al. (16) used cluster analysis to extract three symptom clusters, namely classic MI, stress symptoms, and multiple symptoms. In comparison to the present study, both of them yielded the same number of symptom clusters, although they took different statistical methods.

McSweeney et al. (30) used cluster analysis on 1,270 female patients, which includes 37 acute MI symptoms, to extract a total of 3 symptom clusters, (1) old, silent asymptomatic group, (2) diverse, mildly symptomatic group, and (3) younger, minority, multiple distressing symptom group.

In comparison to the present study, the number of symptom clusters derived from the two were the same despite different

TABLE 4 Relationships between cluster membership and sample characteristics ($n = 261$).

Variables	Cluster 1	Cluster 2	Cluster 3	P
	168 (64.4%)	77 (29.5)	16 (6.1)	
Age (years)				
(mean ± SD)	62.5 ± 11.1	63.3 ± 11.1	63.3 ± 12.5	0.879
<60	68	27	6	0.718
≥60	100	50	10	
Gender, *n* (%)				
Male	145 (86.3)	59 (76.6)	15 (93.8)	0.105
Female	23 (13.7)	18 (23.4)	1 (6.2)	
Occupation, *n* (%)				
Employed	146 (86.9)	65 (84.4)	12 (75.0)	0.368
Unemployed/retired	22 (13.1)	12 (15.6)	4 (25.0)	
Marital status, *n* (%)				
Married	167 (99.4)	76 (98.7)	16 (100.0)	0.587
Divorced/widowed/ never married, *n* (%)	1 (0.6)	1 (1.3)	0	
Insurance type, *n* (%)				
Insurance	165 (98.2)	77 (100.0)	15 (93.8)	0.205
Self-paying	3 (1.8)	0	1 (6.2)	
Smoking, *n* (%)				
None	63 (37.5)	36 (46.8)	4 (25.0)	0.376
Current	91 (54.2)	34 (44.2)	10 (62.5)	
Former	14 (8.3)	7 (9.1)	2 (12.5)	
Hypertension, *n* (%)	82 (48.8)	34 (44.2)	4 (25.0)	0.176
Dyslipidemia, *n* (%)	29 (17.3)	17 (22.1)	2 (12.5)	0.594
Diabetes mellitus, *n* (%)	27 (16.1)	16 (20.8)	4 (25.0)	0.435
Obesity (body mass index>28 kg/m^2), *n* (%)	15 (8.9)	9 (11.7)	0	0.419
Diagnosis STEMI, *n* (%)	114 (67.9)	51 (66.2)	13 (81.3)	0.496
NSTEMI, *n* (%)	54 (32.1)	26 (33.8)	3 (18.7)	
New onset heart failure in hospital, *n* (%)	8 (4.8)	3 (3.9)	0	1.000
History of revascularization, *n* (%)	5 (3.0)	2 (2.6)	2 (12.5)	0.171
Combidity, *n* (%)				
Coronary heart disease	9 (5.4)	3 (3.9)	3 (18.8)	0.097
Atrial fibrillation	10 (6.0)	1 (1.3)	2 (12.5)	0.084
Chronic heart failure	0	1 (1.3)	0	0.356
Cerebrovascular disease	15 (8.9)	8 (10.4)	1 (6.3)	0.934
Peripheral arterial disease	1 (0.6)	0	0	1.000
COPD	1 (0.6)	2 (2.6)	1 (6.3)	0.075
Chronic kidney disease	1 (0.6)	0	1 (6.3)	0.119
Anemia	7 (4.2)	4 (5.2)	4 (25.0)	0.016
Thyroid dysfunction	6 (3.6)	1 (1.3)	2 (12.5)	0.123
Malignancy	0	0	1 (6.3)	0.061
Numbers of symptoms, *n* (%)	2.6 ± 1.2	3.1 ± 1.1	5.0 ± 2.9	<0.001
Killip class≥Ⅱ, *n* (%)	42 (25.0)	30 (39.0)	9 (56.3)	0.003
Types of coronary artery disease, *n* (%)				
Single-vessel disease	26 (15.5)	7 (9.1)	2 (12.5)	0.434
Multi-vessel disease	142 (84.5)	70 (90.9)	14 (87.5)	
Total hospital stay (days)	7.0 ± 2.3	7.6 ± 2.7	7.9 ± 2.7	0.07

STEMI:ST-elevation myocardial infraction,NSTEMI:Non-ST-elevation myocardial infraction.

TABLE 5 Hospital readmission at 1-year follow-up by symptom clusters.

	Cluster 1 ($n = 168$)	Cluster 2 ($n = 77$)	Cluster 3 ($n = 16$)	P
Readmission				
0	155 (92.3)	69 (89.6)	9 (56.3)	0.001
≥1	13 (7.7)	8 (10.4)	7 (43.7)	

TABLE 6 Multinomial logistic regression analysis:factors related to each cluster.

Variables	B	SE	OR	P	95% CI	
					Lower	Upper
Cluster 2 vs. Cluster 1	0.206	0.490	1.228	0.675	0.470	3.209
Cluster 3 vs. Cluster 1	2.117	0.602	8.303	<0.001	2.550	27.031

statistical methods, but the number of symptoms comprising the clusters was greater in the study by McSweeney et al. (30) than in the present study. The reason for this is that the questionnaire used by McSweeney et al. had 37 symptom entries, which is more than the 11 entries in the present study.

In cluster 1 (typical chest symptom cluster), chest pain and sweating were predominant. This is similar to the "older/silent asymptomatic" reported by McSweeney et al. (30) and to the "classic symptoms" in the study by Lindgren et al. (31). The cluster 1 is characterized by a high incidence of typical chest symptoms in the previous studies (16, 30, 32, 33).

In cluster 2 (multiple symptom cluster), chest discomfortable and dyspnea were predominant. Cluster 2 in our study is similar to the "heavy symptom burden", and "chest pain", "shortness of breath" and "sweating" were the main components in the study by Devon et al. (34). Cluster 2 was characterized by a high prevalence of each symptom, including chest symptoms and other symptoms.

In cluster 3 (atypical symptom cluster), radiating pain, sweating and weakness/fatigue were predominant. The characteristics of cluster 3 are in part similar to the "weary symptom" reported by Rosenfeld et al. (33). Cluster 3 was characterized by a wide variety of symptoms but no representative symptoms with a high incidence, and a low incidence or absence of chest symptoms. Cluster 3 can lead to delays in seeking medical care due to the lack of typical chest pain symptoms and the inability of patients to recognize AMI symptoms in a timely manner or failing to attribute them to cardiac disease (35–37).

In this study, we found that in terms of the prevalence of symptoms, the presence of 8 of the 11 symptoms on the symptom assessment form was greater than 20% in patients with AMI at the time of admission, with the prevalence of chest pain, sweating, dyspnea, discomfort in the chest, nausea/vomiting, and radiating pain in descending order of prevalence, among which the prevalence of chest pain and cold sweating was greater than 50%.

This is similar to the findings of Kim et al. Kim found that the top 6 symptoms in terms of symptom prevalence in a survey of STEMI patients at the time of hospital admission were chest pain, sweating, dyspnea, nausea or vomiting, weakness radiating pain and dizziness. The results of Kim's study are almost included in terms of symptom composition, but the difference is that the symptoms of weakness and dizziness were ranked more

highly in Kim's study. The reason for this analysis is related to the fact that the AMI patients investigated in this study included NSTEMI patients, whereas the Kim investigations were all STEMI patients, and when compared to the two, the STEMI patients had large myocardial infarctions and were more prone to arrhythmias, and therefore had weakness and dizziness as their main manifestations.

Because of the existence of insufficient tissue perfusion in STEMI patients, the body is in a state of ischemia and hypoxia, so they show a state of weakness/dizziness, while NSTEMI patients have a lower incidence of weakness/dizziness than STEMI patients due to the longer duration of the lesion and the prolonged presence of ischemia and hypoxia, which is somewhat tolerated by the body.

In terms of comorbidities, the results in this study showed that there were differences in anemia among patients with different latent classes of AMI symptom clusters, and that patients with anemia are more likely to fall into the atypical symptom cluster. Anemia is a common comorbidity of AMI (38). Anemia exacerbates coronary artery ischemia, reduces oxygen-carrying capacity and myocardial oxygen consumption, and patients with anemia have a low hemoglobin concentration and a decreased ability of red blood cells to transport oxygen, which further aggravates the originally damaged myocardial ischemia and hypoxia, deforms cardiomyocytes, and receives a severe impact on cardiac systolic and diastolic function. The symptoms of weakness or fatigue and dizziness in the atypical symptom cluster may be related to anemia.

The atypical symptom cluster had considerably higher Killip class levels. Patients with higher Killip classification have more severe heart failure and poor clinical performance, and it has been shown that high Killip classification is an independent predictor of mortality in STEMI and NSTEMI in previous study (39). One explanation for this seems to be that patients with atypical symptom clusters have atypical symptoms, which are more likely to be delayed or misdiagnosed, resulting in more severe heart failure and thus affecting the prognosis. This study shows that atypical symptom clusters are predictors of whether readmission occurs in AMI patients.

Atypical symptom cluster related with significantly higher risk of readmission than typical chest symptom cluster and multiple symptom cluster. The findings of Hwang et al. (40) found that patients with the presence of atypical symptom clusters had the highest incidence of major adverse cardiovascular events (MACE) within 12 months. Hwang et al. (18) showed that the risk of death within 1 year in patients with the presence of atypical symptom clusters was 3.3 times. The results of related studies suggest that atypical symptom clusters in AMI patients can seriously affect the all-cause mortality of patients (11). The above findings suggest that atypical symptom cluster is an significant predictor of poor clinical outcomes in AMI patients, which may be related to the lack of typical chest pain symptoms, affecting patients' recognition of the disease and leading to delayed access to medical care, which in turn leads to a poor prognosis (11, 31, 41). Therefore, patients with atypical symptoms on admission should not only be treated properly during hospitalization, but also should not be neglected in post-discharge follow-up.

Patients with atypical symptom clusters are more likely to experience delayed consultation or be misdiagnosed than those with typical symptom clusters. Early recognition, diagnosis, and treatment of the disease facilitates accelerated recovery and shortens the duration of painful symptom, thereby improving symptom experience. Thus, providing patients with awareness and coping skills of AMI symptoms and symptom clusters is conducive to symptom relief. David et al. (42) combined health education and skill development, and through the implementation of health education and skill development interventions for females hospitalized for ACS, instructed the patients in symptom monitoring and analysis, recognition of symptom patterns and adoption of appropriate coping. The effectiveness of this intervention was confirmed. This shows that health education and skill development interventions can improve the ability to recognize and respond to the symptoms and symptom clusters of female patients with ACS, so that the patients can receive effective diagnosis and treatment.

Traditional Chinese medicine (TCM) has been applied as a symptom-relieving intervention for symptom management in patients with ACS and has been shown to be effective. It has been shown that auricular point pressure beans in combination with acupoint has a relieving effect on symptom clusters related to chest pain in patients with ACS (43). In the future, we can link up with the Traditional Chinese medicine to explore its long-term effect on symptom clusters.

Coronary artery disease is relatively costly to treat, may require long-term medication, and carries a high healthcare burden for patients. Therefore, the application value of the results of this study in clinical care is to screen high-risk readmission patients, and in the future, pre-discharge and post-discharge interventions can be developed for high-risk readmission patients, including medication use, self-management, follow-up, and monitoring of patients' disease progression, in order to enhance the quality of life of the patients, to further reduce the rate of in-admission, to reduce the burden of medical care for readmission, and to provide a follow-up continuity of care and a rehabilitation program ideas.

4.1 Limitations and suggestion

First, although the sample size is more than sufficient to meet the needs of the study, only one hospital was selected, and the hospital under investigation was a national cardiovascular hospital. The diagnosis and service level of the hospital is high, and the cooperation of the investigated patients is high, which has certain special characteristics, and the sample still lacks sufficient representativeness despite the fact that the investigated hospital's consultation area radiates the northwest region of China. There is a problem of readmission rate bias, patients may have other choices of medical treatment, which may underestimate the readmission rate. It is suggested that future studies should expand the sample size, select AMI patients from different levels of

hospitals in different regions, and consider conducting relevant international cooperative studies to compare the differences in symptom clusters of AMI patients from different countries and ethnic groups, in order to discover the pattern of change of symptom clusters, and to help clinical nurses guide patients to manage their symptoms in a more scientific way.

Secondly, the follow-up period was only 1 year after the patients were discharged from the hospital, and future studies may explore the symptom clusters at different time points after discharge to clarify the trajectory changes of the symptom clusters, which may suggest that we adopt different diagnostic and therapeutic measures according to the different phases, in order to improve the prognosis of the patients and enhance the quality of survival.

Another limitation is that follow-up visits are conducted by telephone, which has limitations in obtaining information about the patient, mainly because of the subjectivity of the patient's answers. In the future, consideration will be given to incorporating cell phone software in the form of self-assessment of the patient under permissible conditions, or using remote monitoring equipment to objectively and dynamically understand the patient's condition. In the future, remote network technology can also be combined with symptom management strategies to dynamically monitor patients' symptoms in real time and analyze subgroups of symptom clusters to help clinical caregivers identify high-risk patients and provide targeted guidance.

Finally, latent class analysis is only a method of extracting symptom clusters, and future research can use cluster analysis, exploratory factor, symptom cluster subgroup analysis, and compare the above methods, which is more in line with the patient's actual situation, with a view to helping clinical caregivers to accurately grasp the patient's symptom characteristics, so as to implement targeted care measures.

5 Conclusions

We used latent class analysis to identify three potential categories of AMI patients, which were typical chest symptom clusters, atypical symptom clusters, and multiple symptom clusters. Clinical data were collected on a total of 261 patients, of whom 28 patients experienced unplanned readmission within 1 year, a readmission rate of 10.7%. Anemia and Killip's classification were the most important factors influencing the potential categories of symptom clusters of the patients, and the patients with atypical symptom clusters were at higher risk of readmission within 1 year than the patients with other symptom clusters. Healthcare providers can pay more attention to patients with atypical symptom clusters, combining patients' symptoms with clusters for efficient and precise symptom management to improve patients' health outcomes. We recommended that future longitudinal studies explore the symptom clusters at different time points and clarify the trajectory of the symptom clusters, in order to guide the healthcare providers to adopt different diagnostic and therapeutic measures according to the different stages to improve the prognosis of the patients.

Data availability statement

The original contributions presented in the study are included in the article/Supplementary Material, further inquiries can be directed to the corresponding authors.

Ethics statement

The studies involving humans were approved by Medical Ethics Committee of Xianyang Central Hospital. The studies were conducted in accordance with the local legislation and institutional requirements. The participants provided their written informed consent to participate in this study. Written informed consent was obtained from the individual(s) for the publication of any potentially identifiable images or data included in this article.

Author contributions

YM: Conceptualization, Funding acquisition, Investigation, Methodology, Validation, Writing – original draft. YS: Investigation, Methodology, Writing – original draft. WQ: Investigation, Methodology, Writing – original draft. ZZ: Investigation, Methodology, Writing – original draft. WY: Investigation, Methodology, Writing – original draft. HL: Investigation, Methodology, Writing – original draft. EL: Conceptualization, Funding acquisition, Supervision, Validation, Writing – original draft. HF: Conceptualization, Resources, Validation, Writing – review & editing. QL: Funding acquisition, Resources, Supervision, Validation, Writing – review & editing.

Funding

The author(s) declare financial support was received for the research, authorship, and/or publication of this article.

This study was sponsored by research fund from Science and Technology Bureau of Xianyang, 2023 (L2023-ZDYF-SF-055).

Acknowledgments

I would like to appreciate the support of my friend, Dr. Yuting Guo of Kyoto University, who provided valuable discussions to my research.

Conflict of interest

The authors declare that the research was conducted in the absence of any commercial or financial relationships that could be construed as a potential conflict of interest.

Publisher's note

All claims expressed in this article are solely those of the authors and do not necessarily represent those of their affiliated organizations, or those of the publisher, the editors and the reviewers. Any product that may be evaluated in this article, or claim that may be made by its manufacturer, is not guaranteed or endorsed by the publisher.

References

1. Tsao CW, Aday AW, Almarzooq ZI, Anderson CAM, Arora P, Avery CL, et al. Heart disease and stroke statistics-2023 update: a report from the American Heart Association. *Circulation*. (2023) 147(8):e93–e621. doi: 10.1161/CIR.0000000000001123

2. Ding X, Zhang Y, Li J, Mao B, Guo Y, Li G. A feasibility study of multi-mode intelligent fusion medical data transmission technology of industrial internet of things combined with medical internet of things. *IoT*. (2023) 21:100689. doi: 10.1016/j.iot.2023.100689

3. Ades PA. Cardiac rehabilitation and secondary prevention of coronary heart disease. *N Engl J Med*. (2001) 345(12):892–902. doi: 10.1056/NEJMra001529

4. Zhang X, Mao B, Che Y, Kang J, Luo M, Qiao A, et al. Physics-informed neural networks (PINNs) for 4D hemodynamics prediction: an investigation of optimal framework based on vascular morphology. *Comput Biol Med*. (2023) 164:107287. doi: 10.1016/j.compbiomed.2023.107287

5. Dodd MJ, Miaskowski C, Paul SM. Symptom clusters and their effect on the functional status of patients with cancer. *Oncol Nurs Forum*. (2001) 28(3):465–70.

6. Kim HJ, McGuire DB, Tulman L, Barsevick AM. Symptom clusters: concept analysis and clinical implications for cancer nursing. *Cancer Nurs*. (2005) 28 (4):270–82. doi: 10.1097/00002820-200507000-00005

7. Aktas A. Cancer symptom clusters: current concepts and controversies. *Curr Opin Support Palliat Care*. (2013) 7(1):38–44. doi: 10.1097/SPC.0b013e32835def5b

8. Li G, Wang H, Zhang M, Tupin S, Qiao A, Liu Y, et al. Prediction of 3D cardiovascular hemodynamics before and after coronary artery bypass surgery via deep learning. *Commun Biol*. (2021) 4(1):99. doi: 10.1038/s42003-020-01638-1

9. Gao Y, Zhang HJ. The effect of symptoms on prehospital delay time in patients with acute myocardial infarction. *J Int Med Res*. (2013) 41(5):1724–31. doi: 10.1177/0300060513488511

10. Horne R, James D, Petric K, Weinman J, Vincent R. Patients' interpretation of symptoms as a cause of delay in reaching hospital during acute myocardial infarction. *Heart*. (2000) 83(4):388–93. doi: 10.1136/heart.83.4.388

11. Riegel B, Hanlon AL, McKinley S, Moser DK, Meischke H, Doering LV, et al. Differences in mortality in acute coronary syndrome symptom clusters. *Am Heart J*. (2010) 159(3):392–8. doi: 10.1016/j.ahj.2010.01.003

12. Barsevick AM, Whitmer K, Nail LM, Beck SL, Dudley WN. Symptom cluster research: conceptual, design, measurement, and analysis issues. *J Pain Symptom Manage*. (2006) 31(1):85–95. doi: 10.1016/j.jpainsymman.2005.05.015

13. Dodd M, Janson S, Facione N, Faucett J, Froelicher ES, Humphreys J, et al. Advancing the science of symptom management. *J Adv Nurs*. (2001) 33(5):668–76. doi: 10.1046/j.1365-2648.2001.01697.x

14. Miaskowski C, Dodd M, Lee K. Symptom clusters: the new frontier in symptom management research. *J Natl Cancer Inst Monogr*. (2004) 32:17–21. doi: 10.1093/jncimonographs/lgh023

15. Birnbach B, Höpner J, Mikolajczyk R. Cardiac symptom attribution and knowledge of the symptoms of acute myocardial infarction: a systematic review. *BMC Cardiovasc Disord*. (2020) 20(1):445. doi: 10.1186/s12872-020-01714-8

16. Kim HS, Eun SJ, Hwang JY, Lee KS, Cho SI. Symptom clusters and treatment time delay in Korean patients with ST-elevation myocardial infarction on admission. *Medicine (Baltimore)*. (2018) 97(19):e0689. doi: 10.1097/MD.0000000000010689

17. Li G, Song X, Wang H, Liu S, Ji J, Guo Y, et al. Prediction of cerebral aneurysm hemodynamics with porous-medium models of flow-diverting stents via deep learning. *Front Physiol*. (2021) 12:733444. doi: 10.3389/fphys.2021.733444

18. Hwang SY, Ahn YG, Jeong MH. Atypical symptom cluster predicts a higher mortality in patients with first-time acute myocardial infarction. *Korean Circ J*. (2012) 42(1):16–22. doi: 10.4070/kcj.2012.42.1.16

19. Yu DS, Li PW, Chong SO. Symptom cluster among patients with advanced heart failure: a review of its manifestations and impacts on health outcomes. *Curr Opin Support Palliat Care*. (2018) 12(1):16–24. doi: 10.1097/SPC.0000000000000316

20. Oliveira L, Costa I, Silva D, Silva J, Barreto-Filho J, Almeida-Santos M, et al. Readmission of patients with acute coronary syndrome and determinants. *Arq Bras Cardiol*. (2019) 113(1):42–9. doi: 10.5935/abc.20190104

21. Kwok CS, Chatterjee S, Bagur R, Sharma K, Alraies MC, Fischman D, et al. Multiple unplanned readmissions after discharge for an admission with percutaneous coronary intervention. *Catheter Cardiovasc Interv*. (2021) 97 (3):395–408. doi: 10.1002/ccd.28797

22. Sir Ö, Özakgül A. Evaluation of the perception of illness and quality of life in patients with acute myocardial infarction. *Turk Kardiyol Dern Ars*. (2022) 50 (3):209–16. doi: 10.5543/tkda.2022.21048

23. Yu Y, Wu AMS, Wing YK, Chan JWY, Lau MMC, Lau JTF. Validation of the revised illness perception questionnaire of obstructive sleep apnea among elderly Chinese in the general population. *Sleep Breath*. (2023) 27(1):337–44. doi: 10.1007/s11325-022-02598-y

24. Villalobos-Galvis FH, Mafla AC, Burbano-Trujillo WF, Sanchez-Figueroa AA. Psychometric properties of the revised illness perception questionnaire for oral health. *Caries Res*. (2017) 51(3):244–54. doi: 10.1159/000468993

25. Rivera E, Levoy K, Clark-Cutaia MN, Schrauben S, Townsend RR, Rahman M, et al. Content validity assessment of the revised illness perception questionnaire in CKD using qualitative methods. *Int J Environ Res Public Health*. (2022) 19 (14):8654. doi: 10.3390/ijerph19148654

26. Wasfy JH, Zigler CM, Choirat C, Wang Y, Dominici F, Yeh RW. Readmission rates after passage of the hospital readmissions reduction program: a pre-post analysis. *Ann Intern Med*. (2017) 166(5):324–31. doi: 10.7326/M16-0185

27. Yang Q, Zhao A, Lee C, Wang X, Vorderstrasse A, Wolever RQ. Latent profile/class analysis identifying differentiated intervention effects. *Nurs Res*. (2022) 71 (5):394–403. doi: 10.1097/NNR.0000000000000597

28. MacLean E, Dendukuri N. Latent class analysis and the need for clear reporting of methods. *Clin Infect Dis*. (2021) 73(7):e2285–6. doi: 10.1093/cid/ciaa1131

29. DeVon HA, Vuckovic K, Ryan CJ, Barnason S, Zerwic JJ, Pozehl B, et al. Systematic review of symptom clusters in cardiovascular disease. *Eur J Cardiovasc Nurs*. (2017) 16(1):6–17. doi: 10.1177/1474515116642594

30. McSweeney JC, Cleves MA, Zhao W, Lefler LL, Yang S. Cluster analysis of women's prodromal and acute myocardial infarction symptoms by race and other characteristics. *J Cardiovasc Nurs*. (2010) 25(4):311–22. doi: 10.1097/JCN.0b013e3181cfba15

31. Lindgren TG, Fukuoka Y, Rankin SH, Cooper BA, Carroll D, Munn YL. Cluster analysis of elderly cardiac patients' prehospital symptomatology. *Nurs Res*. (2008) 57 (1):14–23. doi: 10.1097/01.NNR.0000280654.50642.1a

32. Ryan CJ, DeVon HA, Horne R, King KB, Milner K, Moser DK, et al. Symptom clusters in acute myocardial infarction: a secondary data analysis. *Nurs Res*. (2007) 56 (2):72–81. doi: 10.1097/01.NNR.0000263968.01254.d6

33. Rosenfeld AG, Knight EP, Steffen A, Burke L, Daya M, DeVon HA. Symptom clusters in patients presenting to the emergency department with possible acute coronary syndrome differ by sex, age, and discharge diagnosis. *Heart Lung*. (2015) 44(5):368–75. doi: 10.1016/j.hrtlng.2015.05.008

34. DeVon HA, Ryan CJ, Rankin SH, Cooper BA. Classifying subgroups of patients with symptoms of acute coronary syndromes: a cluster analysis. *Res Nurs Health*. (2010) 33(5):386–97. doi: 10.1002/nur.20395

35. Farshidi H, Rahimi S, Abdi A, Salehi S, Madani A. Factors associated with Pre-hospital delay in patients with acute myocardial infarction. *Iran Red Crescent Med J*. (2013) 15(4):312–6. doi: 10.5812/ircmj.2367

36. Thuresson M, Jarlöv MB, Lindahl B, Svensson L, Zedigh C, Herlitz J. Thoughts, actions, and factors associated with prehospital delay in patients with acute coronary syndrome. *Heart Lung*. (2007) 36(6):398–409. doi: 10.1016/j.hrtlng.2007.02.001

37. Moser DK, Kimble LP, Alberts MJ, Alonzo A, Croft JB, Dracup K, et al. Reducing delay in seeking treatment by patients with acute coronary syndrome and stroke: a scientific statement from the American heart association council on cardiovascular nursing and stroke council. *J Cardiovasc Nurs*. (2007) 22(4):326–43. doi: 10.1097/01.JCN.0000278963.28619.4a

38. Salisbury AC, Alexander KP, Reid KJ, Masoudi FA, Rathore SS, Wang TY, et al. Incidence, correlates, and outcomes of acute, hospital-acquired anemia in patients with acute myocardial infarction. *Circ Cardiovasc Qual Outcomes*. (2010) 3 (4):337–46. doi: 10.1161/CIRCOUTCOMES.110.957050

39. El-Menyar A, Zubaid M, AlMahmeed W, Sulaiman K, AlNabti A, Singh R, et al. Killip classification in patients with acute coronary syndrome: insight from a multicenter registry. *Am J Emerg Med*. (2012) 30(1):97–103. doi: 10.1016/j.ajem.2010.10.011

40. Hwang SY, Kim J. Cluster dyads of risk factors and symptoms are associated with major adverse cardiac events in patients with acute myocardial infarction. *Int J Nurs Pract*. (2015) 21(2):166–74. doi: 10.1111/ijn.12241

41. Canto JG, Shlipak MG, Rogers WJ, Malmgren JA, Frederick PD, Lambrew CT, et al. Prevalence, clinical characteristics, and mortality among patients with myocardial infarction presenting without chest pain. *JAMA*. (2000) 283(24):3223–9. doi: 10.1001/jama.283.24.3223

42. Davis LL, McCoy TP. An educational and skill-building intervention to improve symptom recognition and interpretation in women with acute coronary syndrome: a pilot study. *Dimens Crit Care Nurs*. (2019) 38(1):29–37. doi: 10.1097/DCC.0000000000000329

43. Yu H, Hong M, Zhang M, Cao J, Chen R, Du T. The application of auricular point pressing beans combined with acupoint application in acute coronary syndrome. *Chin Med Mod Dist Educ China*. (2023) 21(08):133–5. doi: 10.3969/j.issn.1672-2779.2023.08.050

frontiers | Frontiers in Cardiovascular Medicine

TYPE Original Research
PUBLISHED 05 July 2024
DOI 10.3389/fcvm.2024.1426888

Check for updates

OPEN ACCESS

EDITED BY
Gaoyang Li,
Tohoku University, Japan

REVIEWED BY
Na Wu,
China Medical University, China
Zhengwu Sun,
Dalian Municipal Central Hospital, China

*CORRESPONDENCE
Atilla Orhan
atillaorhan@gmail.com

RECEIVED 02 May 2024
ACCEPTED 18 June 2024
PUBLISHED 05 July 2024

CITATION
Orhan A, Akbayrak H, Çiçek ÖF, Harmankaya İ and Vatansev H (2024) A user-friendly machine learning approach for cardiac structures assessment.
Front. Cardiovasc. Med. 11:1426888.
doi: 10.3389/fcvm.2024.1426888

COPYRIGHT
© 2024 Orhan, Akbayrak, Çiçek, Harmankaya and Vatansev. This is an open-access article distributed under the terms of the Creative Commons Attribution License (CC BY). The use, distribution or reproduction in other forums is permitted, provided the original author(s) and the copyright owner(s) are credited and that the original publication in this journal is cited, in accordance with accepted academic practice. No use, distribution or reproduction is permitted which does not comply with these terms.

A user-friendly machine learning approach for cardiac structures assessment

Atilla Orhan[1]*, Hakan Akbayrak[1], Ömer Faruk Çiçek[1], İsmail Harmankaya[2] and Hüsamettin Vatansev[3]

[1]Department of Cardiovascular Surgery, Faculty of Medicine, Selcuk University, Konya, Türkiye, [2]Department of Pathology, Faculty of Medicine, Selcuk University, Konya, Türkiye, [3]Department of Biochemistry, Faculty of Medicine, Selcuk University, Konya, Türkiye

Background: Machine learning is increasingly being used to diagnose and treat various diseases, including cardiovascular diseases. Automatic image analysis can expedite tissue analysis and save time. However, using machine learning is limited among researchers due to the requirement of technical expertise. By offering extensible features through plugins and scripts, machine-learning platforms make these techniques more accessible to researchers with limited programming knowledge. The misuse of anabolic-androgenic steroids is prevalent, particularly among athletes and bodybuilders, and there is strong evidence of their detrimental effects on ventricular myocardial capillaries and muscle cells. However, most studies rely on qualitative data, which can lead to bias and limited reliability. We present a user-friendly approach using machine learning algorithms to measure the effects of exercise and anabolic-androgenic steroids on cardiac ventricular capillaries and myocytes in an experimental animal model.

Method: Male Wistar rats were divided into four groups ($n = 28$): control, exercise-only, anabolic-androgenic steroid-alone, and exercise with anabolic-androgenic steroid. Histopathological analysis of heart tissue was conducted, with images processed and analyzed using the Trainable Weka Segmentation plugin in Fiji software. Machine learning classifiers were trained to segment capillary and myocyte nuclei structures, enabling quantitative morphological measurements.

Results: Exercise significantly increased capillary density compared to other groups. However, in the exercise + anabolic-androgenic steroid group, steroid use counteracted this effect. Anabolic-androgenic steroid alone did not significantly impact capillary density compared to the control group. Additionally, the exercise group had a significantly shorter intercapillary distance than all other groups. Again, using steroids in the exercise + anabolic-androgenic steroid group diminished this positive effect.

Conclusion: Despite limited programming skills, researchers can use artificial intelligence techniques to investigate the adverse effects of anabolic steroids on the heart's vascular network and muscle cells. By employing accessible tools like machine learning algorithms and image processing software, histopathological images of capillary and myocyte structures in heart tissues can be analyzed.

KEYWORDS

anabolic-androgenic steroid, artificial intelligence, cardiac capillaries, image segmentation, machine learning, myocardial hypertrophy, myocardial hypertrophy in athletes

1 Introduction

Artificial intelligence (AI) and machine learning (ML) techniques are increasingly used in medicine to improve the diagnosis and treatment of various diseases, including cardiovascular diseases (1). Automated techniques can make tissue analysis faster and more efficient, reducing the need for manual labor and saving time (2).

However, ML algorithms in medicine are new, and many researchers interested in using AI technologies may need more computer literacy or technical expertise. This is where image analysis platforms, such as ImageJ and Fiji, can be helpful (3, 4). These open-source software programs are easily extendable with plugins, scripts, pipelines, or workflows, allowing researchers with limited computing experience to develop and use ML algorithms.

Anabolic-androgenic steroids (AAS) have a wide range of clinically recognized uses. They are commonly used in heart transplant procedures to aid in the recovery process. AAS are also utilized in the treatment of osteoporosis to help increase bone density and reduce the risk of fractures. In addition, they are prescribed for individuals with chronic obstructive pulmonary disease to help improve muscle mass and strength. One of the most common indications for AAS therapy in men is hypogonadism, a condition where the body doesn't produce enough testosterone. AAS are also used in the treatment of catabolic states and cachexia, which are characterized by muscle wasting and weight loss. Furthermore, they may be prescribed as part of corticosteroid therapy to counteract the catabolic effects of long-term corticosteroid use. In addition to these uses, AAS have been employed in the treatment of depression, growth stimulation in male adolescence, prophylaxis of hereditary angioedema, and liver disease. They have also been used in the context of female-to-male transsexualism to promote the development of male secondary sexual characteristics. Furthermore, AAS have been investigated for their potential therapeutic effects in conditions such as multiple sclerosis, hypoplastic anemia, sexual dysfunction, and osteoporosis (5, 6). Anabolic-androgenic steroid (AAS) abuse is common among athletes and bodybuilders. There is strong evidence that co-administration of AAS with exercise can have negative effects on ventricular myocardial capillaries (7). However, most studies on this topic have relied on qualitative results and have a high margin of bias (2, 4). This highlights the importance of utilizing quantitative analyses to demonstrate the negative effects of AAS on the heart. AI and ML can be valuable tools in investigating these effects.

In this paper, we present a simple and user-friendly approach using ML algorithms to measure the effects of exercise and AAS on cardiac ventricular capillaries and myocytes in an animal model. This approach includes measuring the morphological features of capillary and myocyte structures from images obtained from the rats using the Trainable Weka Segmentation (TWS) plugin from Fiji (8). ML and TWS techniques, successfully utilized in analyzing various tissue structures, can also be effectively employed in the segmentation and morphological analysis of heart tissue structures such as capillaries and myocytes (9). Furthermore, we argue that even researchers without extensive programming and computer science knowledge can utilize artificial intelligence techniques to investigate the potentially detrimental effects of AAS on heart capillaries and myocytes in their studies.

2 Material and method

2.1 Ethical issues

This study followed "Experimental Animal Ethical Care" protocols approved by our University's Ethics Committee (27.04.2018-2018-15). The research center provided Male Wistar rats, kept in plastic cages at a temperature of 23 ± 2°C, 50% ± 10% relative humidity, and a 12-h day/night cycle while having *ad libitum* access to food and water. All rats used were male, and gender didn't affect the analysis.

2.2 Study design

The present study randomly divided Wistar-Albino male rats ($n = 28$) into four groups. Group I served as the control group and comprised sedentary animals without treatment with AAS. Group II consisted of animals that underwent an exercise protocol but did not receive AAS treatment. Group III included sedentary animals treated with AAS, while Group IV consisted of animals that underwent an exercise protocol and received AAS treatment. Following procedures, the animals were sacrificed by cervical dislocation under general anesthesia (Ketamine HCl 75 mg/kg and Xylazine 5 mg/kg).

2.3 Exercise procedure

For the exercise, an 8-lane treadmill specially designed for rats was used. At the beginning of the study, animals were placed in a 5-day acclimation period. Then, rats in exercise-related groups were given 45 min of exercise at 25 m/min 5 days a week for 6 weeks, as in the literature (10).

2.4 Anabolic androgenic steroid administration

We used Trenbolone enanthate as an AAS (Trenbolone E200, Pharma Generics). Trenbolone was administered intraperitoneally to groups III and IV rats, diluted in 100 ml peanut oil at a 10 mg/kg dose for different durations as in literature (10). The rats' body weights were measured at the start of the study and at the same time each week for the next 6 weeks, and dose adjustments were made for Trenbolone administration.

2.5 Histopathological procedure

After the animals had been euthanized, the rats' hearts were removed and fixed with a 10% formaldehyde solution, then

embedded in paraffin blocks. Sections of 4 µm thickness were prepared from paraffin blocks with a microtome (Leica Microsystems EG 1130, Wetzlar, Germany). Samples were immunocytochemically stained with CD31 (monoclonal rat, JC70A; Dako, Glostrup; Denmark) using the automated Ventana BenchMark XT instrument. Finally, digital images were obtained at 100× magnification with a light microscope (Carl Zeiss Axio Imager D1, Carl Zeiss Microscopy, LLC, USA).

2.6 Image processing

All tissue sample images were resized to 1,167 × 874 pixels and standardized. A calibration scale was also inserted (Figure 1).

2.7 Machine learning and TWS training steps

This study developed an ML classifier using the TWS plugin v3.2.34 in ImageJ v2.1.0, included in the Fiji distribution. The TWS is an open-source toolkit that utilizes the Waikato Information Analysis Environment (WEKA) for ML and data mining. The default ML method in TWS is Fast Random Forest, which is implemented in the classifier. Two segmentation classes were defined: Capillary cells and Background, with all other artifacts and non-capillary cell images included in the Background class. The number of trees (numTrees) was set to 200 to optimize performance. The optimum settings were chosen based on the balance between image size, segmentation performance, and processing time.

The default features used were Gaussian blur, Hessian, Membrane projection, Sobel filter, Difference of Gaussians, membrane thickness = 1, membrane patch size = 19, minimum sigma = 1.0, maximum sigma = 16.0 and Fast Random Forest values: maxDepth = 0, numFeatures = 2, numTrees = 200. The classifier was trained using randomly selected image samples from each study group until the classification performance was maximized. In both the Fiji software and WEKA segmentation toolkits, the primary criterion for determining optimal settings and achieving near-perfect segmentation was the compatibility between the original image and the segmented image. The training process was considered complete only after obtaining approval from the consulted pathologist at every training stage. Training took four hours on a standard laptop computer (MacBook Pro 13-inch, 2017, Intel Core i5 @ 2.3 GHz, two cores, 8GB RAM).

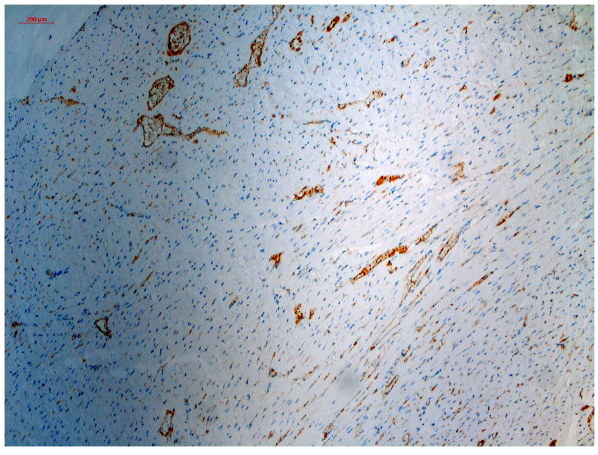

FIGURE 1
Histopathological specimen, immunohistochemically stained with CD-31 and digitalized and standardized at ×100 magnification with a light microscope.

After training, the classifiers and data files were saved and applied to all study samples. The segmented images were then refined with post-processing macro workflows and made suitable for morphological measurements (Table 1). Finally, morphological data were obtained from these refined images and saved in a data file for statistical processing.

The ML process was performed by creating two separate model files in the TWS. In the TWS plugin, the capillary structures were stained brown in the original image were labeled as Capillary, and everything else as Background (Figure 1). Classifier labels and sample images were trained by an experienced histopathologist and saved to the Capillary.model file and data to the Capillary_Data.arff file. Similarly, the myocyte nuclei stained dark blue in the original image (Figure 1) were labeled as the Nuclei, and everything else as the Background nuclei, and the model was recorded in the Nuclei.model file and the data in the Nuclei.arff file.

Subsequently, the TWS plugin was employed to apply the trained model files to additional samples sequentially, leading to their segmentation according to the procedure outlined in Table 1, Figure 2. This yielded classified and segmented images of capillaries and myocytes, as demonstrated in Figure 3. Finally, post-processing macro steps were applied to the segmented images to obtain digital morphological data, which were saved in a data file.

2.8 Statistical analysis

Data analysis was done with SPSS v22.0.0. A power analysis determined the sample size. Results show mean values and standard error of the mean. Statistical significance was $p < 0.05$. One-way ANOVA compared groups, with multiple group comparisons using Bonferroni *post hoc* test.

3 Results

3.1 Classification performance metrics

The automatic segmentation for capillary and myocyte nuclei detection showed high accuracy, with correctly classified instances for capillaries at 99.8223% and nuclei at 99.3464%. The performance of the TWS classifier was tested on both capillary and myocyte nuclei. A value of 1.0 in all performance measures indicates perfect classification. The precision value for the capillary model, the rate of over-prediction in capillary pixels,

TABLE 1 Step-by-step ML algorithm with trainable WEKA segmentation.

Spatial calibration
Open a study image with a calibration scale. Select the line selection tool to draw a straight line on the calibration scale. Go to menu analyze & set scale Enter the value on the calibration scale into the known distance field (The value in the study is 200 µm in all samples.) Set the units of the measurement (µm, mm or whatever) Check the "Global" option. Click OK. Finally, the spatial calibration settings are completed
Training a classification model
Select the workspace or whole space from the image Run the trainable Weka segmentation tool in Fiji (TWS plugin must be installed.) Rename classes (capillary and background) from settings. Select some capillaries with the freehand selection tool and add those traces to the capillary class. Select some background without capillary with freehand selection tool and add those traces to background class Click the "Train classifier" button and wait 2–3 min. After training, check if it works well. If it does not work well, add more traces and fix mistakes. Train again and redo previous steps if needed. Save classifier to a.model file Save data file to a.arff file //**The above steps must be repeated for myocyte nuclei.**
Applying classifier to another image
Open Image to apply RunTrainable Weka Segmentation Load Classifier >Select (your).model file Load Data File >Select (your).arff file Create Results
Post-Processing Macro Steps for the Classified Image

// **Selecting "Classified image" and 8 bit image conversion**
selectWindow("Classified image");
run("8-bit");
//**Thresholding procedure**
setThreshold(0, 120);
setOption("BlackBackground", true);
run("Threshold…");
//**Binarization and segmentation**
run("Make Binary");
run("Dilate");
run("Watershed");
//**Morphological analysis of target class (Capillary, Myocyte or whatever)**
run("Analyze Particles…", " show=Masks display exclude summarize");
//**Calculation of intercapillary distances (Nearest Neighbor Distances Calculation (NND)
plugin must be installed.**
//**Click Analyze -> Set Measurements, Make sure "Centroid" is checked.**
run("Nnd ")

was 0.974. The recall value for the capillary model, the rate of under-prediction in capillary pixels, was 0.954. The accuracy of the TWS classifier for the capillary model, as measured by the F-score, was 0.964 (Table 2).

Similarly, the precision value for the nucleus model, the rate of over-prediction in nuclei pixels, was 0.976. The recall value for the nucleus model, the rate of under-prediction in nuclei pixels, was 0.828. The accuracy of the TWS classifier for the nucleus model, as measured by the F-score, was 0.896 (Table 2).

The Precision/Recall trade-off was 1.02 for capillary pixels and 1.18 for nuclei pixels, and ROC curves were 0.999 for capillary pixels and 0.997 for nuclei pixels (Figure 4).

Overall, the performance of both models was close to perfect, with the capillary model outperforming the nucleus model.

3.2 Experimental results

The Results are shown in Table 3. The study investigated the effects of exercise, AAS administration, and their combination on heart tissue in rats. The ML was used to analyze heart tissue histopathological samples and measure capillary density, intercapillary distance (ICD), myocyte nuclei density, and internuclear distance (IND).

The study's results demonstrated the successful application of AI and ML in histopathological analysis. The ML algorithm could accurately segment and classify capillary and myocyte nuclei structures in the histopathological samples, enabling precise morphological measurements.

Accordingly, there was a significant difference between the groups in heart weight ($p = 0.02$). In addition, the data showed that exercise alone (Group II) significantly increased capillary density compared to the control (Group I) and the groups treated with AAS alone (Group III) or in combination with exercise (exercise + AAS) (Group IV) ($p < 0.05$). This indicates that exercise positively affects capillary density in heart tissue.

In contrast, the administration of AAS alone (Group III) did not significantly affect capillary density compared to the control group (Group I) ($p > 0.05$). However, in group IV, the administration of AAS attenuated the positive effect of exercise on capillary density. This suggests that AAS may hinder the beneficial effects of exercise on capillary density.

Furthermore, the ICD of the exercise group (Group II) was significantly shorter than in all other groups ($p < 0.05$). This indicates that exercise positively affects the spacing of capillaries in heart tissue. This trend was not observed in Group III and Group IV.

The data also showed no significant difference in the number of myocyte nuclei or IND among the groups ($p > 0.05$). This suggests that exercise, AAS administration, and their combination do not significantly affect these parameters in heart tissue.

All results showed that exercise benefits heart tissue, and AAS suppresses these effects. The study also demonstrated the potential of AI and ML for high accuracy in histopathological analysis.

4 Discussion

In this study, we used artificial intelligence and machine learning techniques to analyze the effects of the AAS and exercise on the heart in an animal model. Our results showed that exercise positively affected the heart in Group II compared to Group I. In contrast, the AAS (Group III) had negative effects, while AAS reduced the positive effects of exercise in Group IV. These findings align with previous research showing that AAS abuse can lead to structural and functional changes in the heart, including hypertrophy and fibrosis. On the other hand, exercise can improve cardiovascular health (6, 7).

The effects of the AAS and exercise on morphological parameters such as capillary and myocyte nuclei number and density, the ICD, and the IND in the myocardium at the

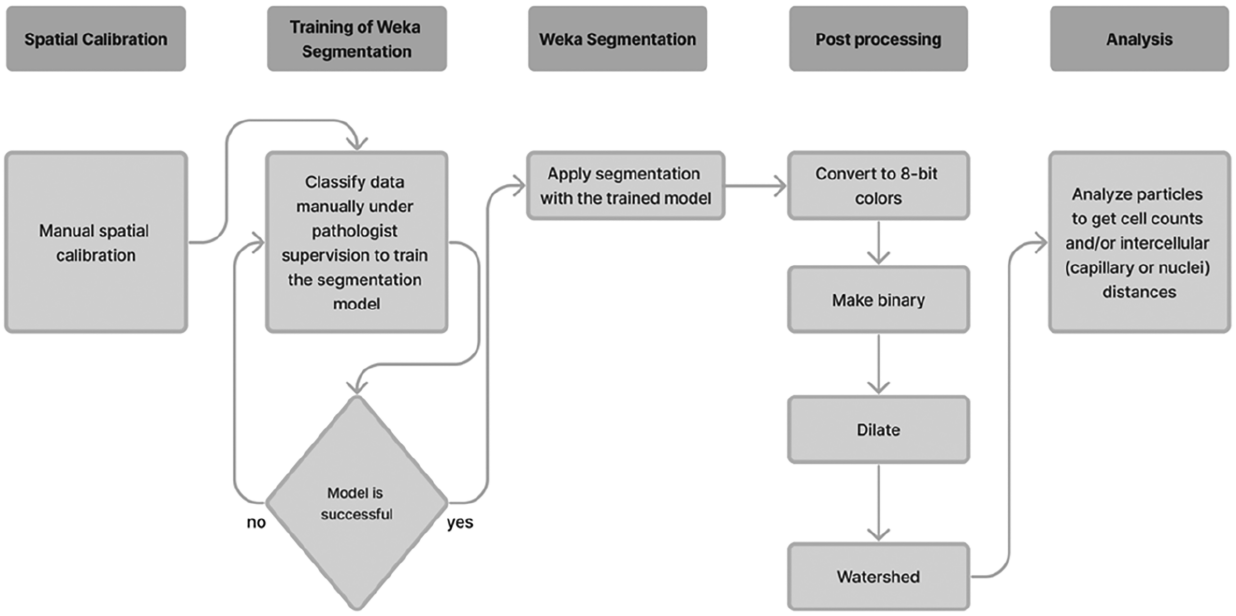

FIGURE 2
Detailed workflow for ML algorithm using trainable WEKA segmentation.

histopathological level are still being determined by manual methods. These methods are prone to bias and do not provide a quantitative result. Additionally, analyzing large numbers of images is time-consuming and laborious for researchers (1, 11, 12).

Our research presents an automated approach for measuring the effects of medical treatments using ML algorithms. ML techniques are increasingly used in the medical field, particularly in the analysis and automation of histopathological images. Various studies have shown that they result in more objective outcomes (2, 4, 8, 9, 13–18).

This study proposes a simple and efficient approach for capillary segmentation using basic image processing techniques. The proposed method was evaluated on a dataset of rat capillary cell images, and it produced favorable results. Moreover, the technique exhibited robustness and dependability, even in challenging situations where manual segmentation was unfeasible or subject to subjective errors. Finally, quantitative assessment of the proposed method included F-score, precision/recall trade-off, and ROC curves, which were nearly optimal.

This study has the advantage that the proposed method requires minimal user intervention and can provide reliable results even under adverse viewing conditions. Therefore, the study suggests it is possible to measure capillary morphological measurements accurately and sensitively using ML and the proposed technique.

The AAS has various clinically recognized uses, including in heart transplant procedures, treatment of osteoporosis, chronic obstructive pulmonary disease, and in individuals infected with HIV. Hypogonadism is the most common indication for AAS therapy in men. The other clinical applications of AAS include the treatment of catabolic states and cachexia, corticosteroid therapy, depression, growth stimulation in male adolescence, prophylaxis of hereditary angioedema, liver disease, female-to-male transsexualism, multiple sclerosis, hypoplastic anemia, sexual dysfunction, and osteoporosis (5, 6). This treatment is sometimes combined with an exercise conditioning regimen (6, 7). Furthermore, these drugs are also used for experimental purposes in individuals who exercise (7). Additionally, some competitive athletes and individuals participating in various forms of physical exercise misuse AAS (7). However, the use of AAS can have negative impacts on cardiovascular health, such as disrupting lipid and lipoprotein metabolism (6, 7), increasing peripheral vascular resistance, and augmenting atherosclerosis, leading to abnormal blood, thrombosis, impaired coronary flow and perfusion, overstimulation of the sympathetic nerves of the heart, ultrastructural damage to heart muscle cells, direct toxic effects in heart muscle cell cultures and cardiovascular complications in athletes (6, 7). AAS use can cause cardiovascular complications, often due to illegal use (6).

During exercise, the heart needs more oxygen. Capillary beds help the heart get enough oxygen. AAS can disrupt capillarization in skeletal muscle during exercise. Not much is known about the effect of AAS on the heart's microvasculature (6). In various studies, intense exercise has not resulted in cardiac hypertrophy, despite an initial increase in heart weight observed during the first weeks of training (6). However, other studies have reported that the heart does exhibit hypertrophy in response to various forms of exercise (6). Some research has also suggested that AAS use can lead to hypertrophy (19). However, most studies on this topic need more in-depth qualitative analysis and numerical data. Additionally, the hypertrophic effects of AAS use on heart muscle cells

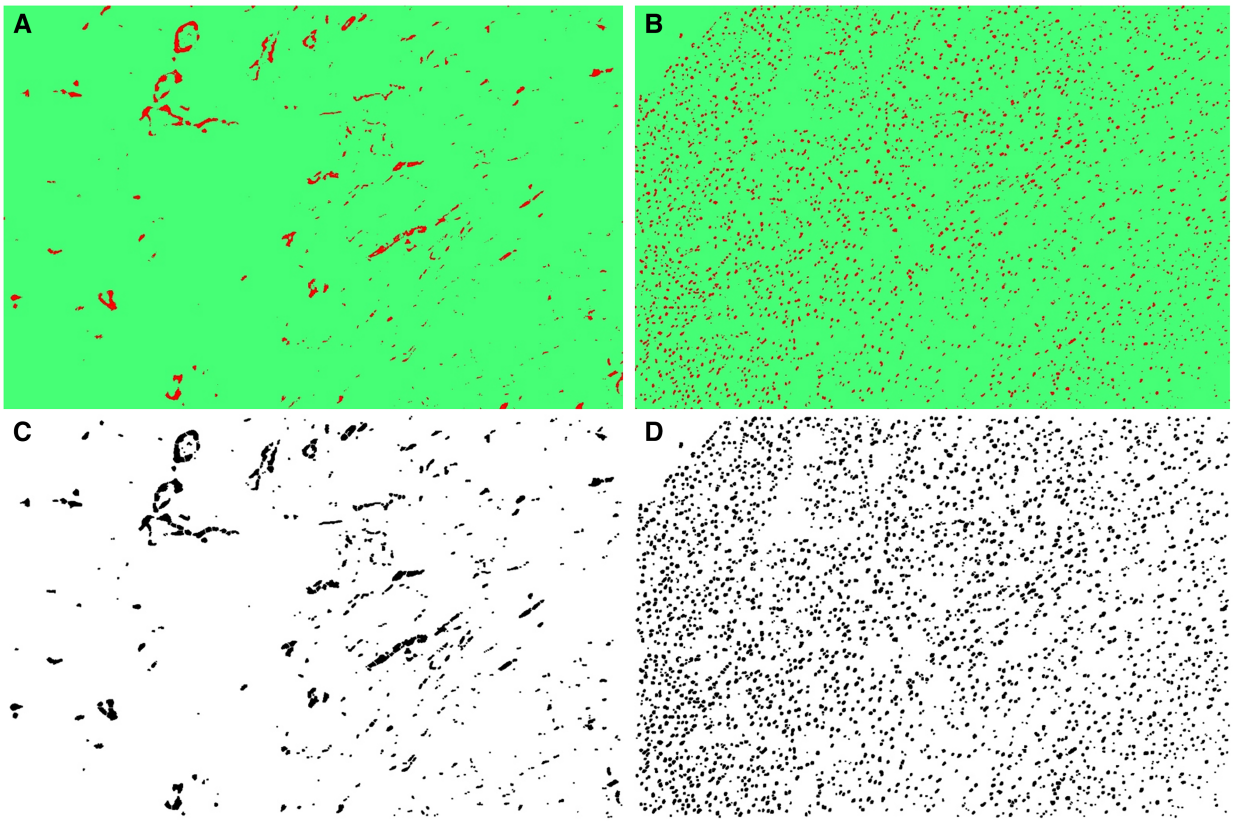

FIGURE 3
(A) The classified capillary images after the training of TWS, (B) the classified myocyte nuclei images after the exercise of TWS, (C) segmented capillary images obtained after running macro for post-processing, (D) segmented myocyte nuclei images obtained after running macro for post-processing.

TABLE 2 Trainable WEKA[a] segmentation performance summary for capillary and myocyte nuclei classes.

	Capillary	Myocyte nuclei
Correctly classified instances	62,371 (99.8223%)	49,397 (99.3464%)
Kappa statistic	0.9629	0.8924
Mean absolute error	0.0059	0.0172
Root mean squared error	0.0421	0.0736
Relative absolute error	12.1332%	26.2749%
Root relative squared error	27.0889%	40.6526%
Total number of instances	62,482	49,722

Confusion matrix for capillary and myocyte nuclei classes

	True class			True class	
Predicted class	Capillary	Background	Predicted class	Myocyte nuclei	Background_N
	1,480 (TP[a])	71 (FP[a])		1,397 (TP)	291 (FP)
	40 (FN[a])	60,891 (TN[a])		34 (FN)	48,000 (TN)

Detailed accuracy by capillary and myocyte nuclei classes

TP rate	FP rate	Precision	Recall	F-score	MCC	ROC area	PRC area	Class
0.954	0.001	0.974	0.954	0.964	0.963	1.000	0.992	Capillary
0.999	0.046	0.999	0.999	0.999	0.963	1.000	1.000	Background
0.998	0.045	0.998	0.998	0.998	0.963	1.000	1.000	Weighted avg.
0.828	0.001	0.976	0.828	0.896	0.896	0.998	0.977	Myocyte nuclei
0.999	0.172	0.994	0.999	0.997	0.896	0.998	1.000	Background nuclei
0.993	0.167	0.993	0.993	0.993	0.896	0.998	0.999	Weighted avg.

[a]WEKA, Waikato information analysis environment; TP, true positive; TN, true negative; FP, false positive; FN, false negative.

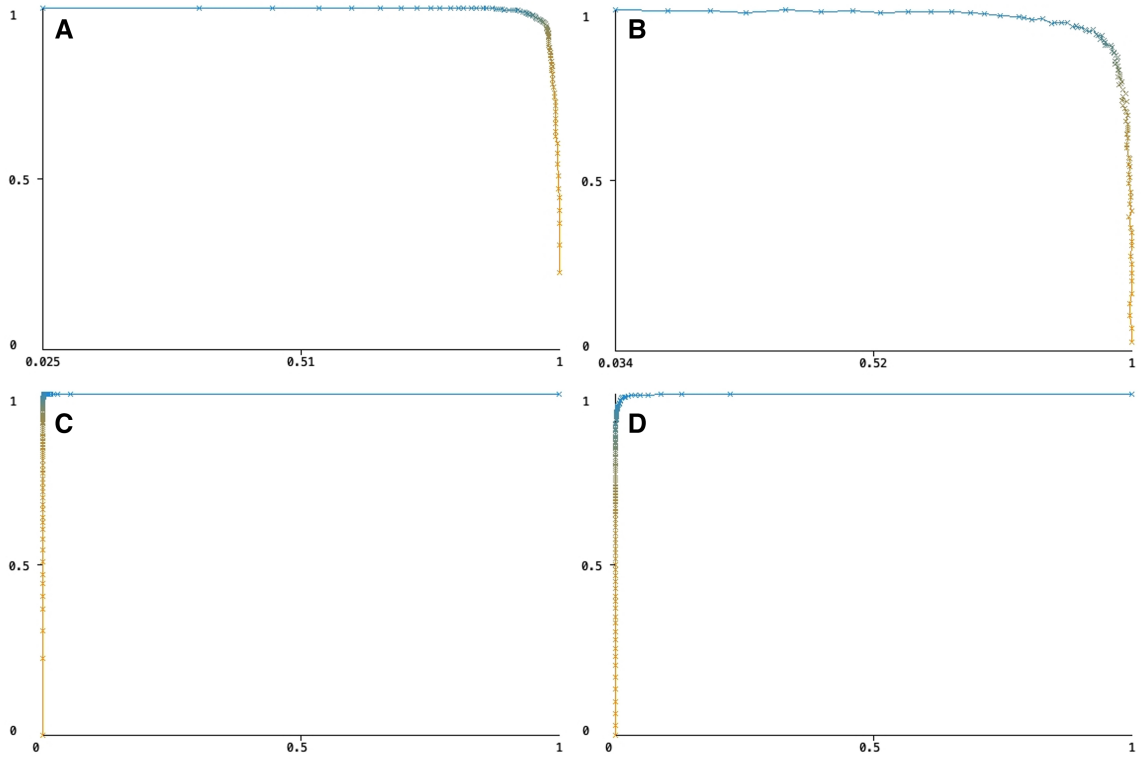

FIGURE 4
(A) The precision/recall trade-off for capillary pixels, (B) the precision/recall trade-off for myocyte nuclei pixels, (C) the ROC curve for capillary pixels, (D) the ROC curve for myocyte nuclei pixels.

and capillaries under training conditions have yet to be fully quantified.

Increased capillary number and density in the myocardium are well-established adaptations in response to physical exercise (6, 7). Studies have shown that increased capillary number and density increase the capillary-to-fiber ratio, ultimately decreasing oxygen diffusion distance (20). In our study, exercise positively affected the capillary number and density, while using AAS had a negative impact. In Group IV, AAS negated the positive effects of exercise on the capillary number and density.

The ICD and the IND are morphological measurements that provide valuable information about ventricular hypertrophy (21). To determine the ICD, we measured the distance between the centers of two neighboring capillary cells according to the Euclidean principle. This measurement was conducted using the Nearest-Neighbor Distances (NND) plug-in in Fiji (22), post-segmentation procedure, as part of a morphological analysis. Similarly, the IND was also calculated by determining the distance between the centers of two neighboring myocyte nuclei. These measurements increase due to the diameter of myocardial fibrils when there is ventricular hypertrophy (6, 7, 21). The ICD was significantly shorter in Group II compared to Group I ($p = 0.01$). This finding is consistent with previous studies. Like our findings, Tagarakis et al. (6, 7) argue that using AAS increases the ICD, which indicates ventricular hypertrophy. They found that the ICD did not cause a significant change in the AAS in the short-term study groups but did cause considerable prolongation in the long-term study groups.

We found the IND between groups to be insignificant, contrary to expectations. The limited sample size and short experimental time can explain this unexpected result at the IND. Also, studies show that regular exercise causes physiological changes in the ICD and the IND and does not cause pathological ventricular hypertrophy (6, 7).

One possible explanation for the harmful effects of AAS on the heart is that they alter the levels of hormones and growth factors in the body, leading to hypertrophy and fibrosis (23). On the other hand, exercise has been shown to improve cardiovascular health by increasing blood flow and promoting the growth of new blood vessels (24). However, our results suggest that combining AAS and exercise may harm the heart. This may be due to an imbalance in the hormones and growth factors that regulate cardiac function. These findings are consistent with previous studies, which have shown that co-administration of AAS and exercise can lead to increased oxidative stress and inflammation in the heart (19).

In our study, the heart and body weight of the rats were measured to evaluate the degree of hypertrophy. The ratio of heart weight to body weight (Wh/Wb) was calculated.

10.3389/fcvm.2024.1426888

TABLE 3 Results of the study on the effects of different treatment groups.

	Group I ($n = 7$)	Group II ($n = 7$)	Group III ($n = 7$)	Group IV ($n = 7$)	p-value
	Mean ± SEM	Mean ± SEM	Mean ± SEM	Mean ± SEM	
Height rat body (cm)	39.4 ± 0.5	38.2 ± 0.7	38.2 ± 0.8	38.4 ± 0.5	0.54
Wh (g)	1.15 ± 0.07	1.12 ± 0.05	0.99 ± 0.04	0.96 ± 0.03	0.02*
Wb (g)	295.1 ± 12.7	273.4 ± 9.2	275.1 ± 21.4	268.3 ± 8.7	0.39
Wh/Wb	0.004 ± 0.005	0.004 ± 0.0001	0.004 ± 0.0001	0.004 ± 0.0001	0.05
Capillary count	478.7 ± 39.6	895 ± 89.9	717.9 ± 83.1	921.3 ± 97	0.005*
Myocyte nuclei count	3,655.3 ± 326.2	4,001.3 ± 187.1	3,396.6 ± 194.4	3,499.1 ± 222.7	0.14
Intercapillary distance	55.9 ± 1.9	44.9 ± 1.5	48.9 ± 2.7	45.3 ± 1.6	0.01*
Internuclear distance	30.1 ± 1	29.3 ± 0.46	30.9 ± 0.64	30.3 ± 0.69	0.31
Results that constitute a statistically significant difference between study groups					
	Group		Group		p-value
Capillary count	I		II		0.006*
			III		0.18
			IV		0.004*
	II		III		0.42
			IV		1
	III		IV		0.31
Intercapillary distance	I		II		0.004*
			III		0.09
			IV		0.005*
	II		III		0.49
			IV		1
	III		IV		0.59

The groups are designated as I (Control), II (Exercise), III (Anabolic-androgenic steroid), and IV (Exercise + Anabolic-androgenic steroid). Wh, represents the weight of the rat heart; Wb, represents the weight of the rat body and Wh/Wb, is the ratio between them.
*The p-value indicates the statistical significance of the differences between groups.

Previous animal studies have suggested that the concomitant application of AAS and exercise training can increase heart weight (6, 25). Our statistical analysis revealed a significant difference in heart weight between the experimental and control groups ($p = 0.02$), with Group IV showing a higher heart weight. However, no significant difference was found in the Wh/Wb ratios between the groups. We attribute the lack of difference in the ratio to the limited sample size. Sample size limitation may not be sufficient to detect subtle changes in this ratio.

5 Limitations

A few limitations to our study should be considered when interpreting the results. First, we used a relatively small sample size, which may have limited our ability to detect significant differences between the groups due to the ethical committee decision. Second, our study was conducted in an animal model, which may not fully capture the complexity of human cardiovascular physiology. Indeed, this study is an animal study. We believe that further human-based research is necessary to evaluate the clinical applicability of its results. Finally, we only analyzed a few morphological features of the heart tissue, and there may be other changes that we did not measure that could be affected by AAS and exercise.

6 Conclusion

The study offers significant contributions to understanding the impact of AAS and exercise on cardiac health. It elucidates that exercise exerts beneficial effects on the heart, whereas the use of AAS and the concurrent administration of AAS and exercise can lead to unfavorable outcomes. These findings are noteworthy for athletes and bodybuilders contemplating using AAS to enhance performance. Furthermore, our study highlights the utility of ML algorithms in facilitating the automated analysis of heart tissue images, showcasing its potential for broader application to diverse diseases and tissue types. However, additional research is necessary to validate and expand our findings.

Data availability statement

The raw data supporting the conclusions of this article will be made available by the authors, without undue reservation.

Ethics statement

The animal study was approved by Selcuk University Experimental Animal Ethics Committee. The study was conducted in accordance with the local legislation and institutional requirements.

Author contributions

AO: Conceptualization, Data curation, Formal Analysis, Funding acquisition, Investigation, Methodology, Project administration, Resources, Software, Supervision, Validation, Visualization, Writing – original draft, Writing – review & editing. HA: Writing – original draft, Writing – review & editing, Conceptualization, Visualization. ÖFÇ: Data curation, Formal Analysis, Methodology, Validation, Visualization, Writing – review & editing. İH: Data curation, Formal Analysis, Investigation, Methodology, Writing – original draft, Writing – review & editing. HV: Writing – original draft, Writing – review & editing, Conceptualization, Visualization.

Funding

The author(s) declare that no financial support was received for the research, authorship, and/or publication of this article.

Acknowledgments

The authors would like to express their gratitude to Mr. Ahmet Safa Orhan and Mr. Halil Salih Orhan for their technical support, and Dr. Rahime Orhan, Dr. İlhan Çiftçi and Dr. Sefa Lök for their scientific contribution.

Conflict of interest

The authors declare that the research was conducted in the absence of any commercial or financial relationships that could be construed as a potential conflict of interest.

Publisher's note

All claims expressed in this article are solely those of the authors and do not necessarily represent those of their affiliated organizations, or those of the publisher, the editors and the reviewers. Any product that may be evaluated in this article, or claim that may be made by its manufacturer, is not guaranteed or endorsed by the publisher.

References

1. Ali O, Abdelbaki W, Shrestha A, Elbasi E, Alryalat MAA, Dwivedi YK. A systematic literature review of artificial intelligence in the healthcare sector: benefits, challenges, methodologies, and functionalities. *J Innov Knowl.* (2023) 8(1):100333. doi: 10.1016/j.jik.2023.100333

2. Deter HS, Dies M, Cameron CC, Butzin NC, Buceta J. A cell segmentation/tracking tool based on machine learning. *Methods Mol Biol.* (2019) 2040:399–422. doi: 10.1007/978-1-4939-9686-5_19

3. Schneider CA, Rasband WS, Eliceiri KW. NIH image to imageJ: 25 years of image analysis. *Nat Methods.* (2012) 9(7):671–5. doi: 10.1038/nmeth.2089

4. Schindelin J, Arganda-Carreras I, Frise E, Kaynig V, Longair M, Pietzsch T, et al. Fiji: an open-source platform for biological-image analysis. *Nat Methods*. (2012) 9 (7):676–82. doi: 10.1038/nmeth.2019

5. Basaria S, Wahlstrom JT, Dobs AS. Anabolic-androgenic steroid therapy in the treatment of chronic diseases. *J Clin Endocrinol Metab*. (2001) 86(11):5108–17. doi: 10.1210/jcem.86.11.7983

6. Tagarakis CV, Bloch W, Hartmann G, Hollmann W, Addicks K. Anabolic steroids impair the exercise-induced growth of the cardiac capillary bed. *Int J Sports Med*. (2000) 21(6):412–8. doi: 10.1055/s-2000-3835

7. Tagarakis CV, Bloch W, Hartmann G, Hollmann W, Addicks K. Testosterone-propionate impairs the response of the cardiac capillary bed to exercise. *Med Sci Sports Exerc*. (2000) 32(5):946–53. doi: 10.1097/00005768-200005000-00011

8. Arganda-Carreras I, Kaynig V, Rueden C, Eliceiri KW, Schindelin J, Cardona A, et al. Trainable Weka segmentation: a machine learning tool for microscopy pixel classification. *Bioinformatics*. (2017) 33(15):2424–6. doi: 10.1093/bioinformatics/btx180

9. Ikeda T, Okano S, Hashimoto N, Kimura K, Kudo K, Tsutsumi R, et al. Histomorphological investigation of intrahepatic connective tissue for surgical anatomy based on modern computer imaging analysis. *J Hepatobiliary Pancreat Sci*. (2021) 28(1):76–85. doi: 10.1002/jhbp.753

10. Ali S, Sefa L. The effects of trenbolone supplementation on the extremity bones in running rats. *Turk J Sport Exerc*. (2019) 21(2):366–71. doi: 10.1016/j.compbiomed.2018.10.016

11. Subudhi A, Acharya UR, Dash M, Jena S, Sabut S. Automated approach for detection of ischemic stroke using Delaunay triangulation in brain MRI images. *Comput Biol Med*. (2018) 103:116–29. doi: 10.1016/j.compbiomed.2018.10.016

12. Lormand C, Zellmer GF, Nemeth K, Kilgour G, Mead S, Palmer AS, et al. Weka trainable segmentation plugin in ImageJ: a semi-automatic tool applied to crystal size distributions of microlites in volcanic rocks. *Microsc Microanal*. (2018) 24(6):667–75. doi: 10.1017/S1431927618015428

13. Caetano Dos Santos FL, Michalek IM, Laurila K, Kaukinen K, Hyttinen J, Lindfors K. Automatic classification of IgA endomysial antibody test for celiac disease: a new method deploying machine learning. *Sci Rep*. (2019) 9(1):9217. doi: 10.1038/s41598-019-45679-x

14. Cui M, Zhang DY. Artificial intelligence and computational pathology. *Lab Invest*. (2021) 101(4):412–22. doi: 10.1038/s41374-020-00514-0

15. Mbiki S, McClendon J, Alexander-Bryant A, Gilmore J. Classifying changes in LN-18 glial cell morphology: a supervised machine learning approach to analyzing cell microscopy data via FIJI and WEKA. *Med Biol Eng Comput*. (2020) 58 (7):1419–30. doi: 10.1007/s11517-020-02177-x

16. Moran-Sanchez J, Santisteban-Espejo A, Martin-Piedra MA, Perez-Requena J, Garcia-Rojo M. Translational applications of artificial intelligence and machine learning for diagnostic pathology in lymphoid neoplasms: a comprehensive and evolutive analysis. *Biomolecules*. (2021) 11(6):793. doi: 10.3390/biom11060793

17. Opstad IS, Godtliebsen G, Ahluwalia BS, Myrmel T, Agarwal K, Birgisdottir AB. Mitochondrial dynamics and quantification of mitochondria-derived vesicles in cardiomyoblasts using structured illumination microscopy. *J Biophotonics*. (2022) 15 (2):e202100305. doi: 10.1002/jbio.202100305

18. Salum P, Güven O, Aydemir LY, Erbay Z. Microscopy-assisted digital image analysis with trainable Weka segmentation (TWS) for emulsion droplet size determination. *Coatings*. (2022) 12(3):364. doi: 10.3390/coatings12030364

19. Lusetti M, Licata M, Silingardi E, Reggiani Bonetti L, Palmiere C. Pathological changes in anabolic androgenic steroid users. *J Forensic Leg Med*. (2015) 33:101–4. doi: 10.1016/j.jflm.2015.04.014

20. Pereira F, de Moraes R, Tibirica E, Nobrega AC. Interval and continuous exercise training produce similar increases in skeletal muscle and left ventricle microvascular density in rats. *Biomed Res Int*. (2013) 2013:752817. doi: 10.1155/2013/752817

21. Henquell L, Odoroff C, Honig C. Intercapillary distance and capillary reserve in hypertrophied rat hearts beating in situ. *Circ Res*. (1977) 41(3):400–8. doi: 10.1161/01.res.41.3.400

22. Zhang KY, Tuffy C, Mertz JL, Quillen S, Wechsler L, Quigley HA, et al. Role of the internal limiting membrane in structural engraftment and topographic spacing of transplanted human stem cell-derived retinal ganglion cells. *Stem Cell Reports*. (2021) 16(1):149–67. doi: 10.1016/j.stemcr.2020.12.001

23. de Souza ÉLP, Dias RL, Rios RS, Vieira TM, Damião B, Rossi WC, et al. Effects of supraphysiological doses of steroids on the left ventricle of sedentary mice: morphometric analysis. *J Morphol Sci*. (2019) 36(02):091–6. doi: 10.1055/s-0039-1681109

24. Hydock DS, Lien CY, Schneider CM, Hayward R. Effects of voluntary wheel running on cardiac function and myosin heavy chain in chemically gonadectomized rats. *Am J Physiol Heart Circ Physiol*. (2007) 293(6):H3254–64. doi: 10.1152/ajpheart.00801.2007

25. Goncalves L, de Souza RR, Maifrino LB, Caperuto EC, Carbone PO, Rodrigues B, et al. Resistance exercise and testosterone treatment alters the proportion of numerical density of capillaries of the left ventricle of aging Wistar rats. *Aging Male*. (2014) 17(4):243–7. doi: 10.3109/13685538.2014.919252

frontiers | Frontiers in Cardiovascular Medicine

TYPE Original Research
PUBLISHED 05 August 2024
DOI 10.3389/fcvm.2024.1358601

Check for updates

OPEN ACCESS

EDITED BY
Aike Qiao,
Beijing University of Technology, China

REVIEWED BY
Fuyou Liang,
Shanghai Jiao Tong University, China
Caglar Ozturk,
Massachusetts Institute of Technology, United States

*CORRESPONDENCE
Omid Amili
✉ omid.amili@utoledo.edu

RECEIVED 20 December 2023
ACCEPTED 25 June 2024
PUBLISHED 05 August 2024

CITATION
Mansouri H, Kemerli M, MacIver R and Amili O (2024) Development of idealized human aortic models for *in vitro* and *in silico* hemodynamic studies.
Front. Cardiovasc. Med. 11:1358601.
doi: 10.3389/fcvm.2024.1358601

COPYRIGHT
© 2024 Mansouri, Kemerli, MacIver and Amili. This is an open-access article distributed under the terms of the Creative Commons Attribution License (CC BY). The use, distribution or reproduction in other forums is permitted, provided the original author(s) and the copyright owner(s) are credited and that the original publication in this journal is cited, in accordance with accepted academic practice. No use, distribution or reproduction is permitted which does not comply with these terms.

Development of idealized human aortic models for *in vitro* and *in silico* hemodynamic studies

Hamid Mansouri[1], Muaz Kemerli[1,2], Robroy MacIver[3] and Omid Amili[1]*

[1]Department of Mechanical, Industrial, and Manufacturing Engineering, University of Toledo, Toledo, OH, United States, [2]Department of Mechanical Engineering, Sakarya University, Sakarya, Turkey, [3]Children's Heart Clinic, Children's Hospitals and Clinics of Minnesota, Minneapolis, MN, United States

Background: The aorta, a central component of the cardiovascular system, plays a pivotal role in ensuring blood circulation. Despite its importance, there is a notable lack of idealized models for experimental and computational studies.
Objective: This study aims to develop computer-aided design (CAD) models for the idealized human aorta, intended for studying hemodynamics or solid mechanics in both *in vitro* and *in silico* settings.
Methods: Various parameters were extracted from comprehensive literature sources to evaluate major anatomical characteristics of the aorta in healthy adults, including variations in aortic arch branches and corresponding dimensions. The idealized models were generated based on averages weighted by the cohort size of each study for several morphological parameters collected and compiled from image-based or cadaveric studies, as well as data from four recruited subjects. The models were used for hemodynamics assessment using particle image velocimetry (PIV) measurements and computational fluid dynamics (CFD) simulations.
Results: Two CAD models for the idealized human aorta were developed, focusing on the healthy population. The CFD simulations, which align closely with the PIV measurements, capture the main global flow features and wall shear stress patterns observed in patient-specific cases, demonstrating the capabilities of the designed models.
Conclusions: The collected statistical data on the aorta and the two idealized aorta models, covering prevalent arch variants known as Normal and Bovine types, are shown to be useful for examining the hemodynamics of the aorta. They also hold promise for applications in designing medical devices where anatomical statistics are needed.

KEYWORDS

aorta, idealized model, CAD model, *in vitro*, *in silico*, PIV, CFD

1 Introduction

The aorta plays a vital role in the circulatory system as the largest arterial vessel, responsible for distributing oxygenated blood from the heart to the rest of the body (1). The hemodynamics (blood flow behavior) within the aorta may be strongly influenced by its geometric configuration (2). As such, for certain interventions or for the development of a personalized treatment plan, a 3D patient-specific reconstruction of the aorta (or part of the aorta) may be needed. However, to develop a generalizable understanding of the complex fundamental fluid mechanics in the aorta, aortic valve, and many other aspects of hemodynamics in both healthy and diseased cases, realistic

but idealized models of the aorta or a related site are useful. Idealized models can facilitate the study of hemodynamics, offering insights applicable to broader populations, unlike patient-specific models. Additionally, idealized models are used for the development of computational and experimental methods and benchmarking data. This includes *in vitro* (experimental) studies such as particle image/tracking velocimetry (PIV/PTV), four-dimensional flow magnetic resonance imaging (4D-Flow MRI), and *in silico* (numerical) studies such as computational fluid dynamics (CFD), and more recently direct numerical simulation (DNS) of complex flow phenomena in the aorta or close sites. For example, in studying the local hemodynamics of the aortic valve, additional parameters such as ascending aorta diameter, sinus dimensions, annulus diameter, sinotubular junction height, coronary arteries diameters, and other dimensions of the aorta are required, highlighting the need for anatomical statistics. Examples of studies with idealized aortic geometries include (3–10).

Additionally, conducting comparative analyses in patient-specific geometries is often difficult due to the unique characteristics and distinct flow dynamics associated with each individual geometry (11). To address this common issue, one approach is to introduce an idealized model having the common features of the patient-specific anatomies, but yet generalizable to a large population. Such an idealized model can serve as a reference base case for both *in vitro* and *in silico* studies of the aorta and facilitating the design of medical devices. By employing such a model, it becomes possible to gain insight into the main characteristics of aortic blood flow and enhance our understanding of the dynamics of the circulatory system.

Furthermore, using an ideal model simplifies the complex manufacturing process of phantoms for physical experiments. The traditional fabrication method for *in vitro* hemodynamics involves manufacturing a phantom using clear silicon resin molding, e.g., (12). Another approach, made possible by recent advances in additive manufacturing methods, is 3D printing phantoms using a transparent material for optical imaging, e.g., (13), or using an opaque (or transparent) material for magnetic imaging, e.g., (14, 15). Additionally, a combination of 3D-printing and silicon modeling has been attempted recently (16). Overall, idealized models are easier to fabricate in both approaches due to their generally simpler geometry and superior surface smoothness. The smooth walls in generalized models potentially improve the imaging quality and minimize the light distortion and refraction in PIV/PTV experiments compared to segmented models. In numerical studies, due to the simplified model structure, grid generation becomes easier, resulting in improved mesh quality and solution convergence. Furthermore, idealized models can be easily modified digitally using various open-source or commercial CAD platforms since they are based on mathematical formulations as opposed to unstructured triangulated surfaces in patient-specific models that are based on biomedical imaging modalities.

We have examined the literature to determine the availability of any idealized models of the aorta. We noticed such models are very scarce, and among those available, the focus is on specific clinical conditions such as aortic dissection (17–19), ascending aortic aneurysm (20), and abdominal aortic aneurysm (21). Certain other studies had focused on specific sections of the aorta such as the abdominal aorta (22). Furthermore, the vast majority of these models tend to be an extremely simplified reconstruction of patient-specific cases, often adopting a straight tube, e.g., (6), or a basic U-bend tube configuration, e.g., (23), that neglects important anatomical factors such as curvatures and varying diameters of the thoracic aorta. For example, the model in the study by Vasava et al. (24) is based on a single patient data of Shahcheraghi et al. (25). Finally, to the best of the authors' knowledge, none of the above studies shared an open-access CAD model or formulated a 3D geometry for use in aortic studies, whether experimentally or computationally, with the exception of the study by Liang et al. (20). In their study, they constructed a statistical shape model for the aortic curvature in patients with ascending aortic aneurysm, neglecting the branching vessels. In light of these limitations, the present study aims to address this gap by incorporating a comprehensive representation of reviewed anatomical features of healthy subjects into useful CAD models.

The anatomy of a healthy aorta has diverse applications, including the investigation of hemodynamics and thrombi transport within the aorta. For instance, it aids in the cardiogenic embolic stroke risk assessment, stroke location prediction, and understanding of stroke etiology and arterial embolism (26, 27). Additionally, they are utilized in the context of venous-arterial extracorporeal membrane oxygenation (VA-ECMO) for acute cardiogenic shock patients (28), and in benchmarking numerical studies in cardiovascular settings for boundary conditions (29), as well as exploring the effect of blood rheology modeling in aorta (30). Moreover, investigations focusing on the aorta from a solid mechanics perspective, which involve determining stress distribution in the aortic wall through finite element modeling (FEM) or utilizing deep learning (31, 32), as well as fluid–structure interaction (FSI) simulations (33, 34), also draw advantages from studies involving healthy populations. Importantly, there has been a growing focus on studying hemodynamics in the aorta of heart failure patients implanted with a left ventricular assist device (LVAD), most commonly a continuous-flow pump. The complex hemodynamics is of interest from several perspectives, including understanding altered hemodynamics, transport of small and large inertial thrombi, aortic insufficiency prevention, and optimizing the cannula graft angle and position (4, 35–39). The shape and dimensions of the aorta in such LVAD patients involve a healthy aorta without any abnormalities.

The main objective of this study is to develop idealized aortic models for the general population, intended for use in experimental or numerical investigations of the hemodynamics or solid mechanics of the aorta. The utilization of the models contributes to an enhanced comprehension of cardiovascular hemodynamics and holds the potential for improving the quality of life for patients in clinical settings. The idealized models presented in this study are developed by considering various geometrical parameters of the aorta as documented in the existing literature. These parameters are extracted from publications that utilized diverse imaging techniques such as

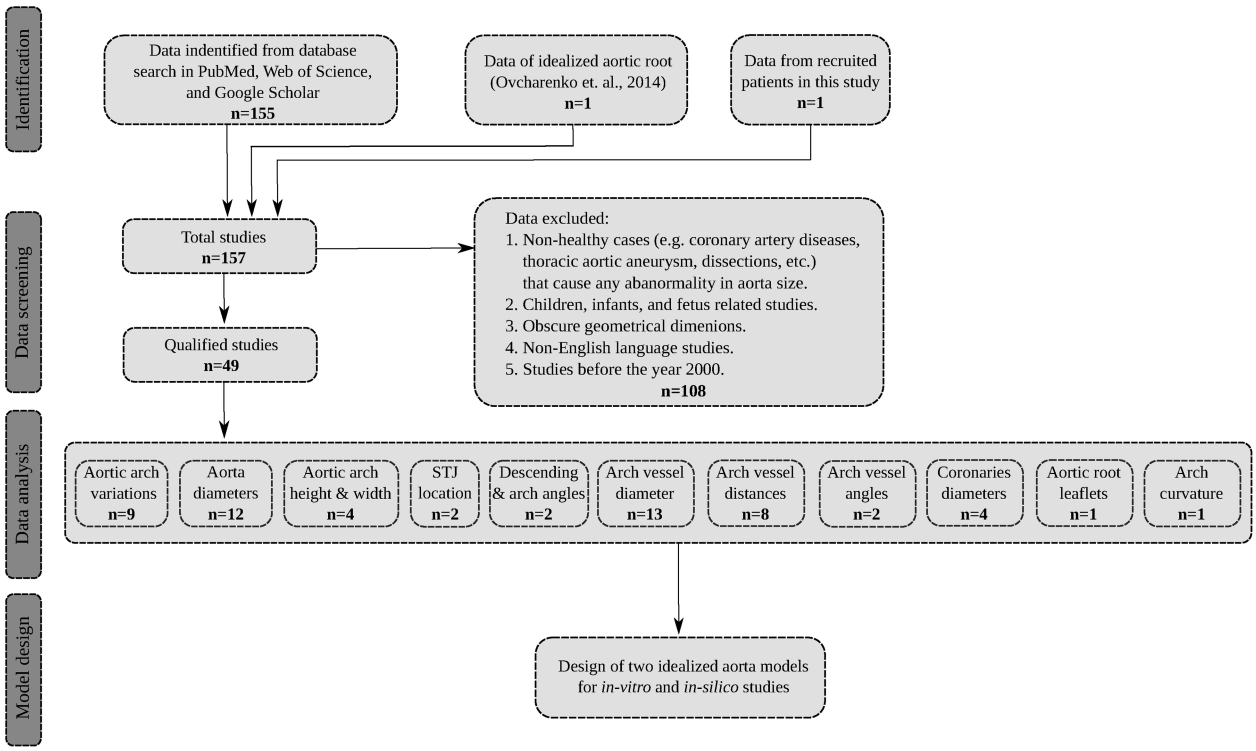

FIGURE 1
The flowchart of the search process, data extraction, and model development. The total number of qualified studies is $n = 49$. Note that in the data analysis step, certain studies have reported more than one dimension of interest.

computed tomography (CT), magnetic resonance imaging (MRI), cardiovascular magnetic resonance imaging (CMR), echocardiography, computed tomography angiography (CTA), quantitative coronary angiography (QCA), or are based on cadaveric studies. The dimensions collected from these sources encompass a broad range of population samples, spanning from 17 to 89 years old, with a specific focus on healthy adults. The study is structured to provide details on the search workflow, data compilation, and model development. It is followed by an experimental and computational assessment of the hemodynamics within the models, as well as discussion and conclusions.

2 Materials and methods

2.1 Study selection and data extraction

To identify relevant studies pertaining to aortic morphology, a critical search was conducted across prominent scientific databases, including PubMed, Web of Science, and Google Scholar. The search strategy aimed to encompass a comprehensive range of literature by utilizing appropriate keywords that included: “aortic arch morphology”, “thoracic aorta size”, “aortic arch geometry”, “arch vessel size”, “arch vessel distance/spacing”, “arch curvature”, “aortic root”, “coronary artery size”, and “arch vessel angle”. This extensive set of keywords ensured a thorough exploration of the literature landscape. The search was primarily focused on literature published from the year 2000 to 2023, providing an up-to-date perspective on aorta morphology studies.

Initially, a total of 156 articles were identified through this screening. Subsequently, after reviewing the title, abstract, and the patient cohort, 108 articles were excluded from the study due to their focus on aortic size abnormalities in non-healthy patient populations such as coronary artery diseases, or thoracic ascending or abdominal aortic aneurysms and dissections. Additionally, articles that reported aortic dimensions in infants and children under the age of 16 were also excluded since such sizes can statistically differ from the adult population as suggested by Barmparas et al. (40) and Food et al. (41). Only studies that examined the aortic morphology in young, middle-aged, and elderly populations were considered. This included subjects spanning from 17 to 89 years old, and encompassed original research articles, review articles, and case reports, all of which were based on clinical imaging modalities or cadaveric investigations. Furthermore, non-English language studies were excluded from the final selection. The qualified studies were then categorized based on the various geometrical parameters of the thoracic aorta as reported in the following sections. By utilizing the average values of the identified parameters, weighted by the cohort size, two distinct aorta models were generated within a computer-aided design (CAD) environment. A flowchart showing the search, data collection and analysis is shown in Figure 1.

2.2 Data from recruited patients

In addition to the compiled data from the above search, anatomical dimensions of four patients recruited for a hemodynamics study by the authors were used to construct the aortic lumen models. High-resolution CT scan data of the patients were acquired after the institutional review board (IRB) approval, and were segmented using 3D Slicer® software, an open-source platform sponsored by the National Institutes of Health (NIH). Different dimensions were then extracted from the 3D models as reported in tables in Section 3 as well as a summary in Table 10.

2.3 Experimental study

To assess the hemodynamic performance of the idealized models developed in Section 4, we performed planar refractive-index-matched particle image velocimetry (PIV) measurements in a left ventricular assist device (LVAD) setting. Our choice has been inspired by the significance of hemodynamics within the aorta in LVAD patients as addressed in Section 1. We digitally grafted the device cannula, with a diameter of 16 mm, into the ascending aorta at a clinically common location and angle, and added a 0.6 mm wall thickness to the lumen, along with incorporating inflow and outflow fittings. The models were then 3D printed using stereolithography with Somos® WaterShed XC 11122 at 50 µm layers. Water was used as the working fluid, and the assessment of optical distortion showed sub-pixel accuracy attributed to the model's thin wall thickness and smooth surface. To account for the viscosity difference between water and blood, we imposed inflow conditions corresponding to Reynolds numbers of approximately 1,757 and 3,163 (based on the inflow bulk velocity and the cannula diameter) as if the flow were blood stream at 5 LPM and 9 LPM, respectively. The steady-state inflow was distributed to different branches following the approach and rates described by Amili et al. (36), which utilized duplex ultrasound data.

The model was placed in a flow loop where its flow rate, pressure, and temperature were fully regulated and monitored. The flow was seeded with fluorescent green polyethylene beads and was illuminated using a light sheet generated by a continuous-wave laser at 405 nm. The light sheet with a thickness of approximately 2 mm was positioned at the symmetry plane of the inflow cannula, cutting through the model. This illumination was complemented by four DC LED lights at 415 nm. The seeded flow was then imaged using a Phantom T1340 high-speed camera in conjunction with a Zeiss lens at an f-number of 4.0, focused at the center plane of the light sheet. A sequence of 10,000 images was recorded at 200 Hz and 400 Hz for the low and high flow rates, respectively. For particle peak detection, a least-squares Gaussian fit (3×3 points) was employed. The interrogation window with the final pass size of 48×48 pixels with 75% overlap was used for the FFT-based cross-correlation.

2.4 Numerical study

A computational fluid dynamics (CFD) study of the hemodynamics was conducted within the idealized aorta models experimentally studied in Subsection 2.3, as well as the four patient-specific cases in Subsection 2.2. ANSYS Fluent steady-state k-ω based turbulent CFD solver was used with a tetrahedron mesh ranging from approximately 13 to 19 million elements, depending on the case. Inflation mesh layers were also defined at the lumen boundaries to better capture the near-wall gradients. The properties of blood were set to a dynamic viscosity of 0.004 Pa.s and a density of 1,060 kg/m^3. An extension pipe with a length of 15 inlet diameter was added at the cannula inlet to ensure a fully developed inflow.

The inflow boundary condition was defined as the inlet velocity with a uniform bulk velocity corresponding to flow rates of 5 LPM and 9 LPM, matching the Reynolds numbers of Subsection 2.3. A uniform inflow turbulent intensity was applied at the inlet to match the bulk flow at the experimental conditions. The exit of the descending aorta was defined as a zero-pressure outlet, and the remaining vessels were described as mass flow rate outlets corresponding to the flow distribution of the experimental conditions. Second-order schemes were used for the spatial discretization, and the flow field was initialized with the hybrid initialization method in ANSYS Fluent solver. Simulations were performed at the Ohio Supercomputer Center (OSC), commonly at a node with 28 cores and 128 GB of memory.

3 Geometrical parameters of aorta

Dimensions of the aorta have long been utilized in the medical domain to facilitate the diagnosis and treatment of diverse cardiovascular conditions such as atherosclerosis or dilation (42, 43). However, such investigations have primarily focused on examining the general variability of geometric parameters across a broad population, rather than establishing a simplified and representative geometric model that accurately captures the complexity of the human aorta. In order to ensure broader applicability of proposed idealized models, the initial step involved identifying different types of aortic arches and presenting the statistical findings on the most prevalent arch variants. Subsequently, critical geometric parameters were precisely defined for the aorta and were subjected to a thorough analysis across a substantial population.

3.1 Variations of aortic arch branches

The anatomy of the aortic arch in humans exhibits diverse branching patterns that can vary significantly among individuals (44) and thus would lead to distinct hemodynamic characteristics. Understanding the variations in the type of aortic arch branches is essential for proposing a generalized ideal model to better represent the population. In the literature, three major types of aortic arches have been identified: Type I (also known as the Normal type), Type

TABLE 1 Prevalence of different aortic arch branch types.

Authors	Cohort size (age [years])	Method	Normal type (Type I) [%]	Bovine type (Type II) [%]	Isolated type (Type III) [%]
Nelson and Sparks (45)	$N = 193$[a]	Cadaver	94.3	1.03	3.1
Nayak et al. (46)	$N = 62$ (45–79)	CT	91.4	4.8	1.6
Natsis et al. (47)	$M = 447$, $F = 186$ (19–79)	DSA	83	15	0.79
Jakanani and Adair (48)	$N = 643$	CT	74	20	6
Celikyay et al. (44)	$N = 1{,}136$	CT	74.7	21.1	2.9
Dumfarth et al. (49)	$N = 361$	MSCTA	78.12	11.36	2.22
Huapaya et al. (50)	$N = 556$	CT	66.5	24.6	6.3
Popieluszko et al. (51)	$N = 23{,}882$[b]	Review	80.9	13.6	2.8
Recruited patients	$N = 4$ (72.75 $\pm$ 9.32)	CT	75	25	0
Weighted average			80.31	14.18	2.89

CT, computed tomography; DSA, digital subtraction angiography; MSCTA, multi slice CT spiral angiography; F, female; M, male.
[a]Among the male population.
[b]A systematic review of 51 different articles.

II (the Bovine type), and Type III (the Isolated type). The distribution of these three variants is presented in Table 1.

The Normal type is the most prevalent configuration at which the aortic arch gives rise to three major branches: the brachiocephalic artery (BA), left common carotid artery (LCA), and left subclavian artery (LSA). This type of aortic arch is present in approximately 80% of the general population. The Bovine type constitutes the second category where the BA and LCA arteries arise from a common trunk, while the LSA artery branches out from the aortic arch. This configuration comprises approximately 14% of the population. The Isolated type is characterized by the presence of four branches and is significantly less common with approximately 3% of the population. It is followed by several other uncommon variants of the aortic arch vessel configurations. The rare variants documented in the literature all combined cover almost 3% of the population. Therefore, our study primarily focuses on developing idealized models based on the first two variants.

3.2 Thoracic aorta dimensions

It is widely recognized that the dimensions of the thoracic aorta are influenced by various factors including gender, age, and body size (52). Despite variations, it is feasible to establish a general range with a reasonable standard deviation (53). This is owing to the fact that the increase in the thoracic aorta over 5 decades of aging is only 7 mm (54), and gender only puts on a 2 mm difference, corresponding to an approximate 7.5% increase in the aortic arch diameter, and this difference between genders decreases with age (55).

We have reviewed the normal ranges of these dimensions and their variations in different populations as well as the measuring methods. By examining the variations of thoracic aortic dimensions towards clinical and research contexts, we have obtained the weighted average values of each section of the thoracic aorta presented in Table 2. We have focused on the five key dimensions which are the diameters of the aortic root, ascending aorta, aortic arch, proximal descending aorta, and mid-descending aorta. The diameters of the ascending aorta, aortic arch, and mid-descending aorta denoted as D_1, D_2, and D_3, respectively, are used for the developed idealized models as shown in Figure 2. These three dimensions suffice for a good representation of the aorta and are practical for CAD modeling of an idealized model since the aortic root diameter is very similar to the diameter of the ascending part, and the diameters of the mid-descending and proximal descending parts are also very similar to each other. The two parameters that are not considered in the idealized model development are reported in Table 2 for potential clinical use.

3.3 Height, width, and curvature of aortic arch

The morphology of the aortic arch typically exhibits a gradual curvature as it ascends from the aortic root and descends towards the descending aorta. The length and curvature of the aortic arch may vary among subjects and with age (54). To quantify these differences, it is common to measure the height (H) and width (W) of the aortic arch at a parasagittal plane. Additionally, the height-to-width ratio (H/W) serves as an important marker for identifying the elongation of the aorta. These parameters are applicable to both types of the aortic arch addressed in Subsection 3.1 and are illustrated in Figure 2. In addition to the height and width of the aortic arch, when viewing the aortic arch from a transverse (axial) plane, the arch slightly bends from the ascending side towards the descending side which is marked as R in Figure 2. Note that studies reporting this curvature dimension are very scarce; therefore we have used our recruited patients' data as reported in Table 3.

3.4 Distance from sinotubular junction (STJ) to start of the aortic arch

This dimension starts from the end of the leaflets up to the point where the ascending aorta starts to bend and is shown by L in Figure 2. There is also an absolute lack of reporting of this

TABLE 2 Thoracic aorta dimensions.[a]

Authors	Cohort size (age [years])	Method	Aortic root [cm]	Ascending part D_1 [cm]	Aortic arch D_2 [cm]	Proximal descending [cm]	Mid-descending D_3 [cm]
Hager et al. (53)	$M = 46$, $F = 24$ (17–89)	Helical CT	$M = 3.04$, $F = 2.88$	$M = 3.20$, $F = 2.90$	$M = 2.85$, $F = 2.63$	$M = 2.55$, $F = 2.32$	$M = 2.51$, $F = 2.27$
Wolak et al. (56)	$N = 4{,}039$ (55 ± 10.2)	CT	NA	3.3	NA	2.4	NA
Biaggi et al. (42)	$M = 815$, $F = 984$ (20–80)	TTE	$M = 3.40$, $F = 3.10$	$M = 3.20$, $F = 3.00$	NA	NA	NA
Evangelista et al. (57)	$N = 187$	Echo	2.90	2.90	2.90	2.50	2.50
Redheuil et al. (54)	$M = 45$, $F = 55$ (20–70)	MRI	NA	$M = 3.10$, $F = 3.00$	NA	$M = 2.40$, $F = 2.20$	$M = 2.25$, $F = 2.10$
Craiem et al. (58)	$N = 51$ (34–88)	CTA	NA	2.98	2.61	2.27	2.27
Davis et al. (59)	$M = 208$, $F = 239$ (19–70)	CMR	$M = 2.5$, $F = 2.2$	$M = 2.7$, $F = 2.6$	NA	$M = 2.1$, $F = 1.9$	NA
Vizzardi et al. (60)	$M = 495$, $F = 507$	Echo	$M = 2.63$, $F = 2.40$	$M = 2.59$, $F = 3.39$	$M = 2.59$, $F = 2.44$	NA	NA
Guo et al. (61)[b]	$M = 42$, $F = 14$ (58.2 ± 17.9)	CTA	NA	3.20	2.73	2.54	2.47
Craiem et al. (62)	$N = 200$ (58 ± 9)	CT	NA	3	2.6	2.3	2.3
Zubair et al. (63)	$N = 116$ (77.4 ± 10)	CT	3.08	3.52	3.05	2.60	2.63
Recruited patients	$N = 4$ (72.75 ± 9.32)	CT	3.05	3.2	2.7	2.7	2.4
Weighted average			2.9	3.2	2.6	2.4	2.5

CMR, cardiac magnetic resonance; MRI, magnetic resonance imaging; Echo, echocardiography; TTE, transthoracic echocardiography; CT, computed tomography; CTA, computed tomography angiography; F, female; M, male.
[a]Data has been reported based on the mean values and has the standard deviation range of 5-17% with respect to the mean.
[b]Chinese population.

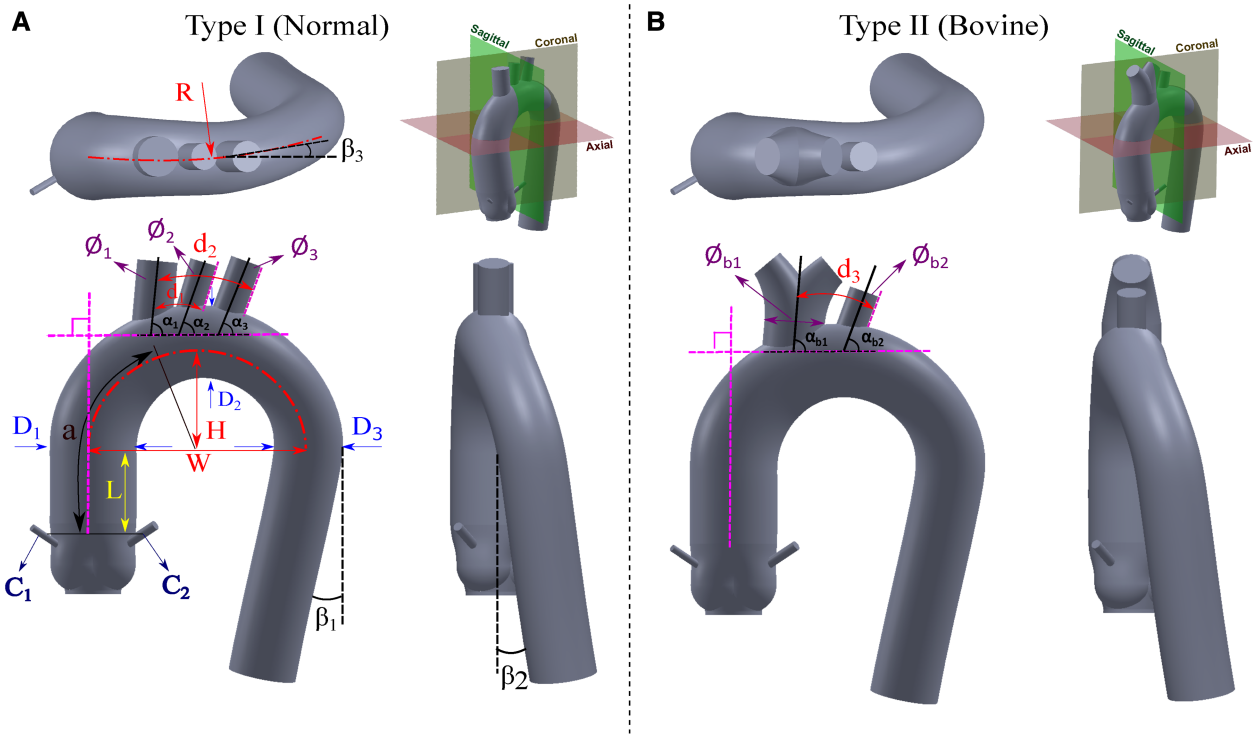

FIGURE 2
Proposed idealized models for the (A) Normal type (Type I), and (B) Bovine type (Type II).

TABLE 3 Height, width, and curvature of aortic arch.[a]

Authors	Cohort size (age [years])	Method	H [cm]	W [cm]	H/W	R [cm]
Redheuil et al. (54)	$M = 45$, $F = 55$ (20–70)	MRI	3.83	6.87	0.56	NA
Craiem et al. (62)	$N = 51$ (34–88)	CTA	4.2	8.3	0.51	NA
Alhafez et al. (64)	$N = 120$ (BAV), $N = 234$ (TAV)	CT	4.1	8.2	0.5	NA
Recruited patients	$N = 4$ (72.75 $\pm$ 9.32)	CT	4.0	8.6	0.47	12.2
Weighted average			4.06	7.95	0.51	12.2

BAV, bicuspid aortic valve; TAV, tricuspid aortic valve; F, female; M, male.
[a]Data has been reported based on the mean values and has the standard deviation range of 12-16% with respect to the mean.

dimension in the literature. Therefore, for the construction of both the Normal and Bovine idealized aortic models, we rely on our recruited patients' data and the study by Vasava et al. (24) as summarized in Table 4.

3.5 Angles of descending aorta and aortic arch

The aortic arch has certain angles with respect to different axes that form the overall complex shape of the thoracic aorta. These angles are the two angles of rotation in descending aorta (β_1 and β_2) and one angle for aortic arch rotation in a transverse plane (β_3) as all shown in Figure 2. The angle β_1 of the descending aorta is measured in reference to a line tangent to the circumference of the mid-descending aorta. In addition, the descending aorta twists toward the posterior side with the angle of β_2. Moreover, when the thoracic arch traverses through the descending aorta, it deviates with an angle toward the posterior side denoted as β_3. Unfortunately, very limited data is available for these dimensions in the literature. To estimate the angle β_1, we rely on our recruited patients and the study by Vasava et al. (24). For the angles β_2 and β_3, we also extracted the data from our patients. All these three angles are shown in Table 5.

TABLE 4 Distance from sinotubular junction to the beginning of the aortic arch.

Authors	Cohort size (age [years)]	Method	L [cm]
Vasava et al. (24)[a]	$N = 1$ (young patient)	CTA	1.8
Recruited patients	$N = 4$ (72.75 $\pm$ 9.32)	CT	2.8
Weighted average			2.6

[a]This study uses an idealized CAD model based on one patient for a CFD simulation, but the model is not available for public access.

TABLE 5 Angles of descending aorta and aortic arch.

Authors	Cohort size (age [years])	Method	β_1 [°]	β_2 [°]	β_3 [°]
Vasava et al. (24)[a]	$N = 1$ (young patient)	CTA	10	NA	NA
Recruited patients	$N = 4$ (72.75 $\pm$ 9.32)	CT	10	10	10
Weighted average			10	10	10

[a]This study uses an idealized CAD model based on one patient for a CFD simulation, but the model is not available for public access.

3.6 Diameters of aortic arch vessels

The aortic arch gives rise to several major vessels that supply blood to the head, neck, and other organs through the brachiocephalic artery (BA), left common carotid artery (LCA), and left subclavian artery (LSA) of which their diameters are shown in Figure 2 as ϕ_1, ϕ_2, and ϕ_3, respectively. In the case of the Bovine type, the BA and LCA branch out from a common trunk with a diameter of ϕ_{b1}, while the diameter of LSA is denoted as ϕ_{b2}. These three arteries, or in the case of the Bovine type aorta, the two branches, exhibit varying diameters among healthy individuals. Documenting the diameter of these branches is predominantly utilized in cardiovascular surgeries (65) such as the implementation of cerebral angiography catheter (66) as well as in procedures like radiological diagnostics and interventional radiology (67). Additionally, such diameter measurements are employed in monitoring the repair of the aortic arch following stent graft surgeries (68). The collected publications from the literature, along with the weighted averages with respect to the cohort size, are presented in Table 6. Of note, there is a limited number of studies focusing on the bovine type of aorta. It is also worth noting that in cases where the cross-sections of the aortic vessels exhibited an oval shape, the diameters are reported as the average of the larger and smaller diameters (65).

3.7 Distance between aortic arch vessels

The measurement of the spacing between the aortic arch vessels holds significant importance as a morphometric parameter within medical research. This parameter assumes crucial relevance in various aspects, including accurate diagnostics, treatment methodologies, and surgical interventions such as endovascular aortic stenting and catheterization (77). In order to provide a comprehensive understanding, a compilation of relevant parameters in the existing literature is presented in Table 7. Among the primary parameters under investigation, special attention is given to the distance between the BA and LCA arteries, denoted as d_1, as well as the distance between the LCA and LSA arteries, denoted as d_2. The distance between the first branch and the LSA artery in the Bovine type aorta is denoted as d_3. The distance from the sinotubular junction to the BA artery is also an important reference dimension that is denoted by a. All these parameters are illustrated in Figure 2.

TABLE 6 Diameters of aortic arch vessels.[e]

Authors	Cohort size (age [years])	Method	Normal Type			Bovine Type	
			ϕ_1 [cm]	ϕ_2 [cm]	ϕ_3 [cm]	ϕ_{b1} [cm]	ϕ_{b2} [cm]
Gupta and Sodhi (65)	$N = 77$ (40–70)	Cadaver	0.87	0.61	0.67	1.65[a]	0.73[a]
Shin et al. (69)	$N = 25$ (adult)	CT	1.83	0.98	1.06	NA	NA
Alsaif and Ramadan (70)	$N = 36$ (adult)	CT	1.79	0.977	1.43	NA	NA
Vasava et al. (71)[f]	N=1 (adult)	CT	0.88	0.85	0.99	NA	NA
Rengier et al. (72)	$N = 20$	CT	1.47	0.98	1.22	NA	NA
Finlay et al. (73)	$N = 45$	CT	1.57	1.01	1.35	NA	NA
Carr et al. (26)	$N = 10$ (≥ 65)	CT	1.35	0.75	1.03	NA	NA
Manole et al. (74)	$M = 24$, $F = 9$	CT	1.08	0.62	0.95	NA	NA
Osorio et al. (75)	$N = 1$ (adult)	CT	1.24	0.74	0.74	NA	NA
Wilbring et al. (68)	$N = 118$ (63 ± 15)	CT	2.05	1.38	1.43	NA	NA
Zubair et al. (63)	$N = 116$ (77.4 ± 10)	CT	1.69	1.17	1.32	NA	NA
Tapia-Nañez et al. (76)	$N = 220$ (52.7 ± 17.6)	CT	1.28	0.86	1.08	2.21[b]	1.18[b]
Recruited patients	$N = 4$ (72.75 ± 9.32)	CT	1.25[c]	0.93[c]	1.35[c]	2.0[d]	1.58[d]
Weighted average			1.47	0.97	1.14	2.18	1.07

[a]$N = 10$.
[b]$N = 30$.
[c]$N = 3$.
[d]$N = 1$
[e]Data has been reported based on the mean values and has the standard deviation range of 11-28% with respect to the mean.
[f]This study uses an idealized CAD model based on one patient for a CFD simulation, but the model is not available for public access.

TABLE 7 Distance between aortic arch vessels.[c]

Authors	Cohort size (age [years])	Method	a [cm]	Normal Type		Bovine Type
				d_1 [cm]	d_2 [cm]	d_3 [cm]
Gupta and Sodhi (65)	$N = 100$ (68)	Cadaver	NA	1.54	3.02	2.51
Finlay et al. (73)	$N = 45$ (68)	CT	7.77	1.83	4.74	NA
Wilbring et al. (68)	$N = 118$ (63 ± 15)	CT	7.7	1.69	3.31	NA
Liu et al. (78)	$N = 114$ (53.3 ± 14.4)	CT	7.82	NA	NA	NA
Zubair et al. (63)	$N = 116$ (77.4 ± 10)	CT	6.59	1.83	3.68	NA
Saade et al. (79)	$N = 75$ (69 ± 13.5)	CT	8.73	NA	NA	NA
Zerebiec et al. (66)	$N = 100$ (62)	CT	NA	1.56	3.17	NA
Recruited patients	$N = 4$ (72.75 ± 9.32)	CT	7.5	1.73[a]	3.47[a]	4.00[b]
Weighted average			7.62	1.68	3.44	2.70

[a]$N = 3$.
[b]$N = 1$.
[c]Data has been reported based on the mean values and has the standard deviation range of 23-28% with respect to the mean.

3.8 Angles of aortic arch vessels

The angle of the arch vessels is a significant morphometric parameter that plays a crucial role in hemodynamics and the potential blood clots transport to the head, especially in patients implanted with a left ventricular assist device (LVAD). Three angles are defined between the arch vessel centerline and the thoracic aorta. The angles of the BA, LCA, and LSA vessels with respect to the arch are denoted as α_1, α_2, and α_3, respectively. For the Bovine type, the corresponding angles are presented as α_{b1} and α_{b2} for the first branch and LSA artery, respectively, as shown in Figure 2. The data is shown in Table 8.

3.9 Aortic root

The aortic root serves as the anatomical connection between the left ventricle and the ascending aorta (81). The aortic valve, which normally has three leaflets (cusps), permits the passage of blood pumped from the contracting left ventricle. Its closure sustains the high pressure required in the systemic circulation. The shape and dimensions of the aortic root are adapted from Ovcharenko et al. (82) that collected data on subjects using CT and Echo image modalities, and generated an idealized aortic root model. We leveraged this study, which provided comprehensive data on parameters such as aortic root diameter, shape and depth of aortic sinuses, sinotubular junction diameter, and other relevant dimensions. This particular study is unique in the sense that its data is accessible online through the GrabCAD (83) platform, whereas the vast majority of reviewed studies do not provide any 3D segmented dataset or share a CAD file.

To ensure compatibility between the dimensions, the 3D model by Ovcharenko et al. (82) was scaled down by a factor of 0.9518 to fit into our compiled dimensions addressed in Section 3 and summarized in Table 10. This slight difference in the aortic root diameter naturally arises from different cohort sizes. The

TABLE 8 Angles of aortic arch vessels.[d]

Authors	Cohort size (age [years])	Method	α_1 [°]	α_2 [°]	α_3 [°]	α_{b1} [°]	α_{b2} [°]
Demertzis et al. (80)	$N = 92$ (69.4 ± 9.9)	CT	84.79	73.9[a]	70.16	NA	NA
Recruited patients	$N = 4$ (72.75 ± 9.32)	CT	84[b]	57[b]	59[b]	80[c]	65[c]
Weighted average			84.77	73.31	69.81	80	65

[a]$N = 83$.
[b]$N = 3$.
[c]$N = 1$.
[d]Data has been reported based on the mean values and has the standard deviation range of 12–22% with respect to the mean.

aforementioned study was also utilized as a point of reference for determining the location of the right coronary artery on the anterior coronary sinus and the left coronary artery on the left posterior aortic sinus.

3.10 Diameters of coronary arteries

The coronary artery dimension plays a significant role in diagnosing and treating various conditions such as coronary artery disease (84, 85). In surgical procedures such as percutaneous coronary intervention (PCI) and coronary artery bypass graft (CABG) surgery, the size of the coronary arteries holds particular importance (86). Typically, this size is considered independent of factors such as age and body size, except for gender (85, 87). Yet, certain studies have found no significant difference in coronary artery size based on gender (86). In both the Normal type and Bovine type aortas, the diameter of the coronary arteries is denoted as C_1 and C_2 for the right and left coronaries, respectively, as illustrated in Figure 2, and reported in Table 9.

3.11 Aortic valve

The aortic valve, typically a trileaflet valve, has not been included in the model design because it is a dynamic component of the aorta-heart. The shape and opening configuration of its leaflets vary within the cardiac cycle. The operation of the valve leaflets may also vary depending on the condition or disease being studied. Additionally, valves can be native, transcatheter, or mechanical, with either two or three cusps. Given these variations, researchers can digitally integrate their choice of valves into the proposed models for *in vitro* and *in silico* studies. Several notable studies on the aortic valves, including those involving mechanical, bioprosthetic, or idealized models, are available (3, 6, 89–95).

TABLE 9 Diameters of coronary arteries.[a]

Authors	Cohort size (age [years])	Method	C_1 [mm]	C_2 [mm]
Cavalcanti et al. (88)	$N = 51$	Cadaver	2.9	3.75
Mehrotra et al. (84)[b]	$N = 321$ (49.4 ± 11.22)	QCA	3.1	4.28
Raut et al. (86)	$N = 229$ (51.7 ± 9.35)	QCA	1.83	2.34
Recruited patients	$N = 4$ (72.75 ± 9.32)	CT	2	2
Weighted average			2.6	3.5

QCA, quantitative coronary angiography.
[a]Data has been reported based on the mean values and has the standard deviation range of 20-27% with respect to the mean.
[b]Indian population.

4 Proposed idealized aorta models

Based on the literature survey reported here, we compiled and summarized the weighted averages of all relevant dimensions of the aorta in Table 10. We then used this table to design two idealized models, following the same naming convention in the literature, for the Normal type (Type I) and the Bovine type (Type II) of the aorta as shown in Figure 2. For each model, three views are used to clearly show all the dimensions as well as the fourth view positioned with respect to the standard anatomical planes. The Bovine type shares the same statistical dimensions as the Normal type with the exception of the arch vessels and their corresponding diameters and angles.

For the purpose of CAD modeling, SolidWorks® 2022 was utilized. First, we sketched circular profiles of the aortic models in multiple cross-sections. Then, the "*loft*" feature was leveraged to create a transition between the cross-section profiles while ensuring a smooth overall shape. The sketch was started from the cross-section of the STJ location and ended with the termination circle of the descending aorta. Additional intermediate profiles (circles) were necessary to refine the final shape of the models. Two guide curves that connected the profiles were drawn using the "*spline*" feature. Due to the arch curvature with a particular radius of curvature (R), the "*3D sketch*" feature was activated before using the "*spline*" drawing tool to establish a proper out-of-plane curvature. Then, the tangency directions at spline points were adjusted based on the models' design. The arch vessels were then added to the model following the corresponding dimensions. Finally, the aortic sinuses along with the coronary arteries were added.

For each idealized aorta, we provide the CAD model for the lumen as shown in Figure 2, as well as a shell version with a thickness of 1.0 mm. The lumen model can be used in numerical simulations or to mold a phantom for experimental studies. The editable shell model with a finite wall thickness is suitable for the purpose of fabrication via additive manufacturing. All models are

10.3389/fcvm.2024.1358601

TABLE 10 A summary of the aorta dimensions derived from four recruited patients (Patients 1–4), and a summary of the weighted averages of aorta dimensions used for the two proposed idealized aorta models (Type I and Type II). Dimensions are in centimeters and angles in degrees. The cumulative number of subjects used for the weighted averages in the idealized models is denoted as N.

Models	D_1	D_2	D_3	C_1	C_2	d_1	d_2	d_3	Φ_1	Φ_2	Φ_3	Φ_{b1}	Φ_{b2}	W	H	R	L	a	α_1	α_2	α_3	α_{b1}	α_{b2}	β_1	β_2	β_3
Patient 1[a]	3.2	2.6	2.7	0.2	0.2	NA	NA	4	NA	NA	NA	2	1.58	9.2	4	9.2	2.4	8.5	NA	NA	NA	80	65	10	0	0
Patient 2[b]	3.3	2.75	2.35	0.2	0.2	1.8	3.54	NA	1.35	1	1.25	NA	NA	9.2	4	13.1	3.2	7.5	82	60	60	NA	NA	0	0	0
Patient 3[b]	3.15	2.8	2.25	0.2	0.2	1.7	3.4	NA	1.2	0.95	1.35	NA	NA	8	4	13.2	2.8	7	85	55	55	NA	NA	15	20	20
Patient 4[b]	3.15	2.7	2.25	0.2	0.2	1.7	3.4	NA	1.2	0.85	1.45	NA	NA	8	4	13.3	2.8	7	85	55	55	NA	NA	15	20	20
Average	3.2	2.7	2.4	0.2	0.2	1.73	3.47	4	1.25	0.93	1.35	2	1.58	8.6	4	12.2	2.8	7.5	84	57	59	80	65	10	10	10
Type I	3.17	2.65	2.5	0.26	0.35	1.68	3.44	NA	1.47	0.97	1.14	NA	NA	7.95	4.06	12.2	2.6	7.62	84.8	73.3	69.8	NA	NA	10	10	10
Type II	3.17	2.65	2.5	0.26	0.35	NA	NA	2.7	NA	NA	NA	2.18	1.07	7.95	4.06	12.2	2.6	7.62	NA	NA	NA	80	65	10	10	10
N	8,071	2,133	728	605	605	483	483	104	706	706	706	301	301	509	509	4	5	472	96	96	96	1	1	5	4	4

[a]Classified as Type II.
[b]Classified as Type I.

shared online in both STereoLithography (STL) and SolidWorks part (SLDPRT) file formats.

5 Hemodynamics analysis

To assess the performance of our developed idealized models, we conducted high-resolution planar PIV experiments and high-resolution CFD simulations for the two models in a left ventricular assist device (LVAD) setting, as detailed in Subsections 2.3 and 2.4. We used two Reynolds numbers for both idealized models in both CFD and PIV settings, and one Reynolds number for the four patient-specific CFD cases, totaling 12 studies combined. The CFD results are first verified against PIV experiments, as shown in Figure 3, which depicts streamlines colored by the local velocity magnitude in the CFD cases, and streamlines overlaid on the measured velocity magnitude field in the PIV cases. The velocity magnitude was normalized by the inflow bulk velocity of each case. The incoming flow in the cannula accelerates towards the superior direction as it approaches the graft location due to its strong curvature, which is consistent in all cases. The jetting flow entering the aorta induces several recirculation zones, which are observed in both types of models. At the higher Reynolds number, these zones slightly change in size or intensity, but they remain remarkably persistent. While certain minor differences in the flow topology are noticed between CFD and PIV, it is important to note that the modalities are inherently different. Streamlines in PIV are based on 2D measurements (a 2D projection of the 3D velocity field), while CFD computations are fully 3D, and streamlines are computed on a plane comparable to that of PIV. For a detailed quantitative comparison, the probability density function (PDF) of the normalized velocity magnitude in idealized models obtained by CFD and PIV is shown in Supplementary Figure S1. Additionally, the median of the quantities along with their 25% and 75% percentiles is shown in the same figure. Notably, for a fair comparison, the CFD data was extracted from a comparable plane to the PIV plane, as shown in Figure 3.

After establishing a close agreement between simulations and experiments, we compared the flow patterns in the idealized models with those in the four subjects in Subsection 2.2. Figure 4 illustrates the flow structure within the models from different perspectives. In the first row, streamlines colored by the local velocity magnitude depict the overall complex flow pattern, which is highly vortical near the aortic root. The second row illustrates the high-momentum flow structure within the cannula and the aorta using the isosurface of the velocity magnitude. We used 50% of the inflow bulk velocity as the threshold level for each isosurface. In the third row, the local wall shear stress map shows elevated values near the arch vessels, at the coronaries, and at the cannula. In the maps for the last two patients (3 and 4), an increased level of wall shear stress is also noticeable at the inferior region of the aortic arch. This is due to the different cannula angles compared to the other two patients (1 and 2) and the two idealized models. The cannula in the last two patients directs the jetting flow toward the posterior-inferior direction, where it impinges on the wall, causing an elevated wall shear stress

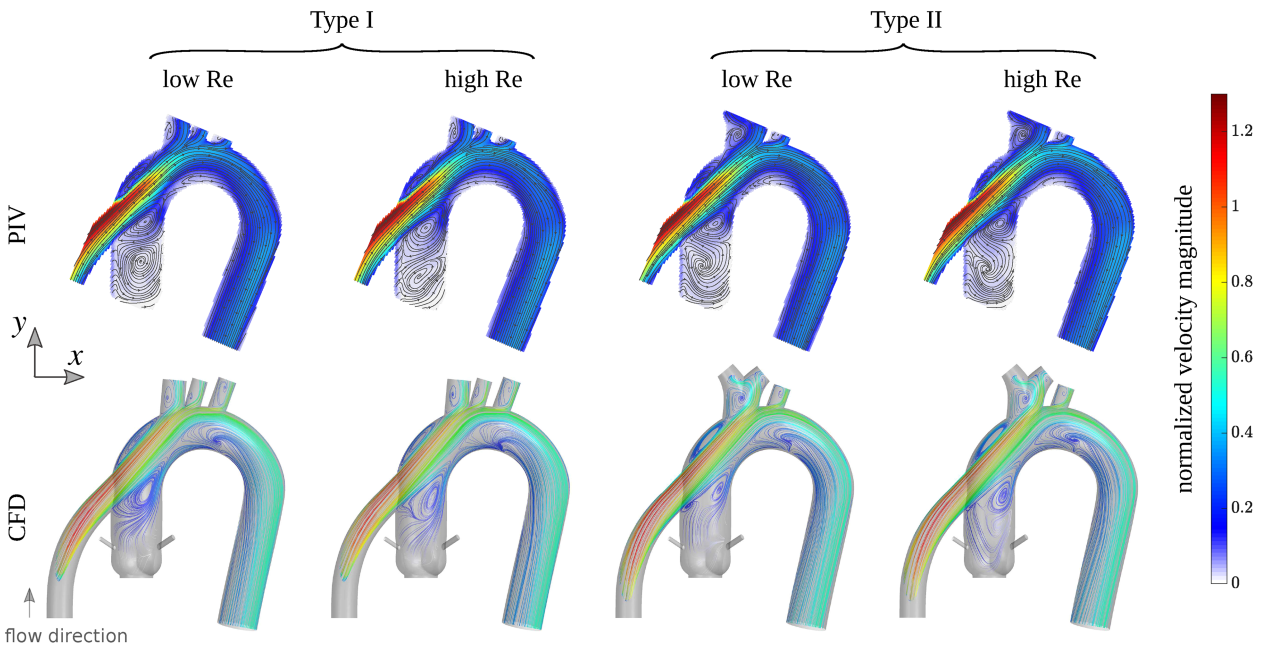

FIGURE 3
First row: streamlines overlaid on the velocity magnitude field measured by PIV for Type I and Type II idealized models grafted with the outflow of a left ventricular assist device (LVAD). Second row: streamlines from CFD colored by the velocity magnitude computed in a plane comparable to experiments. The colorbar shows the velocity magnitude normalized by the inflow bulk velocity of each case. The Reynolds number (based on the inflow bulk velocity and the cannula diameter) is approximately 1,757 and 3,163 for the low and high flow rates cases, respectively.

region. To better illustrate the flow behavior, several cross-sections were extracted at different locations, showing velocity magnitude, vorticity magnitude, and static pressure in the fourth, fifth, and sixth rows, respectively. While certain differences are observed between the idealized models and the subject-specific models (particularly for patients 3 and 4), the global flow patterns and the range of quantities are consistent. The differences in fine flow features, especially in wall shear stress, which may be sensitive to the anatomical features, are expected. Notably, the idealized models show a smaller pressure drop between the cannula inlet and the descending aorta outlet. This is perhaps due to their simpler geometry as well as greater surface smoothness. For a detailed quantitative comparison, Supplementary Figure S2 presents probability density functions and percentile plots for velocity magnitude, vorticity magnitude, wall shear stress, and static pressure for all CFD cases at the 5 LPM flow rate setting.

6 Discussion

This study highlights the scarcity of idealized models for the aorta. Among the few available, the models are typically designed for specific clinical conditions such as aortic dissection, ascending aortic aneurysm, or abdominal aortic aneurysm (18–22), and are often overly simplified reconstructions based on a single patient case. To address this research gap, we conducted a critical literature review focusing on the morphometric parameters of the healthy human aorta. The surveyed data, along with the data from four recruited subjects were compiled to present a comprehensive summary of relevant dimensions and angles. Our study illustrates the population's heterogeneity, showcasing diverse aortic types and sizes, while also highlighting the lack of data on specific dimensions such as the descending aorta angle with respect to anatomical planes and the branching angle of vessels from the aortic arch. To ensure a more realistic representation of dimensions, the average of each parameter was weighted by the study cohort size. While aortic size measurements, including those from the four recruited subjects, are derived from various imaging modalities such as CT and MRI, our review of the existing studies in Section 3 affirms that there is no significant difference between these measurements across imaging methods, which is consistent with the multi-modality assessment of thoracic aortic dimensions by Frazao et al. (96). They reported a great level of agreement in thoracic aortic measurements between CT and MRI. However, they also found that TTE significantly underestimates the maximum aortic root diameter compared to CT and MRI. In the present work, very few studies based on echo modalities were found and used in our workflow.

Subsequently, we utilized these dimensions to develop 3D CAD models of the aorta, incorporating both the Normal (Type I) and Bovine (Type II) aortic arch vessel configurations. Based on the compiled dimensions, these idealized models collectively are estimated to capture the major anatomic features found in the healthy adult aorta, represented by the two most common arch variants. Our choice of the healthy population has been inspired by the significance of aortic hemodynamics as addressed in Section 1. These CAD models are suitable for prudent use in hemodynamics and thrombi transport studies in both experimental and computational settings.

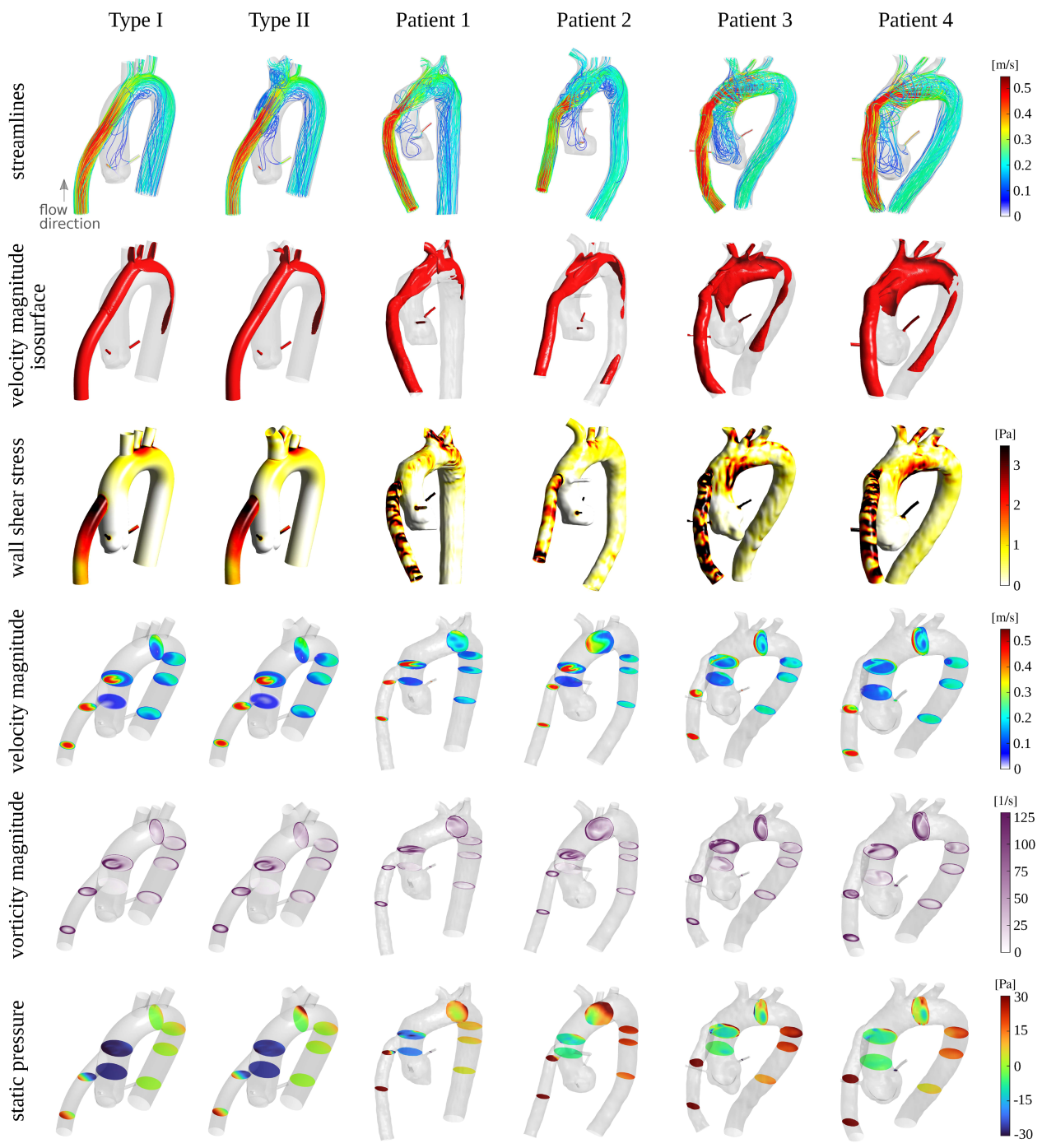

FIGURE 4
First row: streamlines colored by the local velocity magnitude. Second row: isosurface of the velocity magnitude at a threshold level of approximately 0.2 m/s corresponding to 50% of the bulk velocity at the inflow. Third row: wall shear stress map. Fourth, fifth, and sixth rows: cross-sections at different locations colored by the velocity magnitude, vorticity magnitude, and static pressure, respectively. The Reynolds number (based on the inflow bulk velocity and the cannula diameter) for all cases is approximately 1,757.

In this study, we performed an assessment of hemodynamics within the developed models in a left ventricular assist device (LVAD) setting using high-resolution CFD simulations and high-resolution planar PIV experiments. The flow pattern closely agrees between simulations and experiments at two flow conditions, as shown in the qualitative and quantitative comparisons. Additionally, we compared the flow within the idealized models with that of the four patients at an inflow condition of 5 LPM, which is the most common flow setting for the device and is also considered the cycle-averaged flow rate in a healthy cardiac cycle. The global flow features captured by the idealized models are generally representative of the patients. Notably, we did not present the results of experiments for patient-specific models due to the difficulties and challenges faced with optical imaging. Indeed, one

motivation for developing idealized models has been the difficulties that encounter with optical imaging through patient-specific models, particularly in models fabricated using the layer-by-layer process of 3D-printing. The refractive index of each layer may differ slightly from the neighboring layers and the rest of the model, leading to local amplification of optical distortion by the arbitrary shape and surface quality in subject-specific models. An idealized model, with its simpler geometry and inherently better surface smoothness, minimizes such distortions.

This study has focused on developing idealized models that capture the general anatomical features of the aorta, rather than creating customized models tailored to specific pathological conditions or individual patient characteristics. However, the proposed models serve as the base geometry and can be customized to incorporate specific dimensional parameters for achieving various morphological geometries, including models for different diseases. These open-access idealized models can be easily modified by users to accommodate aortic diseases such as abdominal aortic aneurysm (AAA), ascending aortic aneurysm, and aortic coarctation.

The present study has certain limitations, most notably the absence of a comprehensive statistical analysis within the existing literature on morphometric parameters. Performing such an analysis would require a complex regularization of measurement resolution and addressing uncertainties associated with various imaging modalities and cadaveric studies falls outside the scope of our study. Furthermore, the idealized models were constructed using compiled dimensions from different studies, each focusing on a specific part of the aorta. In an alternative approach, upon the availability of a single large dataset of CT- or MRI-based scans of the full thoracic aorta, the authors envision image segmentation (manually or using AI-assisted methods) to extract all the detailed dimensions required to develop and formulate idealized models.

Additionally, for practical reasons, the flow assessment for all the cases was performed using steady-state flow conditions and rigid vessel walls. It is acknowledged that hemodynamics in the aorta is sensitive to inflow and outflow boundary conditions as well as vessel wall compliance. Depending on the purpose and metric under study, various parameters and study strategies become important at different levels. Generally, a pulsatile flow would cause a more complex flow pattern and affect flow unsteadiness and instabilities, vortex formation, transport, and breakdown. However, there is a complex interaction between different parameters, most notably the Reynolds number, Womersley number, and Strouhal number, e.g., see Peacock et al. (97). In terms of the wall compliance, rigid models commonly tend to generate increased systolic pressure, peak velocities, and pulse wave velocity, but depending on various parameters at play, the effects may be more or less pronounced, e.g., see Zimmermann et al. (15).

7 Conclusions

Our comprehensive study integrates literature-derived model design parameters to create two CAD models representing the aorta in healthy adults, specifically focusing on Normal and Bovine variants. The hemodynamics study within our idealized models under two left ventricular assist device (LVAD) support configurations showed that the global flow patterns in the idealized models agree well both qualitatively and quantitatively between CFD simulations and PIV experiments. Additionally, the flow structure is consistent between the idealized and the patient-specific cases in CFD simulations performed at a common LVAD support setting. This verification affirms the capability of our idealized models to replicate general flow features in subject-specific geometries. These meticulously constructed CAD models, rooted in statistical data, not only serve as valuable tools for investigating hemodynamics or solid mechanics but also hold promise for applications in medical device design where anatomical statistics are needed. The work contributes a robust foundation for advancing research in cardiovascular biomechanics and has implications for clinical and engineering domains.

Data availability statement

The CAD models can be found at the link provided in the Supplementary Material. The hemodynamics data is available upon request from the corresponding author.

Ethics Statement

The requirement of ethical approval was waived by Allina Health IRB 1 (Reference Number: 1542852-1) and The University of Toledo (Reference Number: 300885) for the studies involving humans because the institutional review boards determined that this study does not meet the definition of research or research with human subjects as defined under the portions of 45 CFR 46.102. The studies were conducted in accordance with the local legislation and institutional requirements. Written informed consent for participation was not required from the participants or the participants' legal guardians/next of kin because no humans were directly involved with this study.

Author contributions

HM: Formal Analysis, Investigation, Methodology, Writing – original draft, Writing – review & editing; MK: Investigation, Writing – original draft, Writing – review & editing; RM: Conceptualization, Writing – review & editing; OA: Conceptualization, Methodology, Supervision, Writing – original draft, Writing – review & editing.

Funding

The author(s) declare financial support was received for the research, authorship, and/or publication of this article.

This work was partially supported by fellowship funding from the Scientific and Technological Research Council of Türkiye

(TÜBİTAK) under the grant number of 1059B192000179 with the 2219 programme.

Acknowledgments

The first author's tuition scholarship and teaching assistantship provided by the University of Toledo are gratefully acknowledged. Additionally, we acknowledge the computational resources provided by the Ohio Supercomputer Center (OSC).

Conflict of interest

The authors declare that the research was conducted in the absence of any commercial or financial relationships that could be construed as a potential conflict of interest.

Publisher's note

All claims expressed in this article are solely those of the authors and do not necessarily represent those of their affiliated organizations, or those of the publisher, the editors and the reviewers. Any product that may be evaluated in this article, or claim that may be made by its manufacturer, is not guaranteed or endorsed by the publisher.

Supplementary material

The Supplementary Material for this article can be found online at: https://www.frontiersin.org/articles/10.3389/fcvm.2024.1358601/full#supplementary-material

References

1. Wang J, Brown S, Tullis SW. Oscillatory blood flow in a deformable human aortic arch. In: *Summer Bioengineering Conference*. Vol. 54587. American Society of Mechanical Engineers (2011). p. 1127–8.

2. Tse KM, Chang R, Lee HP, Lim SP, Venkatesh SK, Ho P. A computational fluid dynamics study on geometrical influence of the aorta on haemodynamics. *Eur J Cardiothorac Surg*. (2013) 43:829–38. doi: 10.1093/ejcts/ezs388

3. Bao Le T, Gilmanov A, Sotiropoulos F. High resolution simulation of tri-leaflet aortic heart valve in an idealized aorta. *J Med Device*. (2013) 7:030930. doi: 10.1115/1.4024520

4. Benk C, Mauch A, Beyersdorf F, Klemm R, Russe M, Blanke P, et al. Effect of cannula position in the thoracic aorta with continuous left ventricular support: four-dimensional flow-sensitive magnetic resonance imaging in an in vitro model. *Eur J Cardiothorac Surg*. (2013) 44:551–8. doi: 10.1093/ejcts/ezt095

5. Cherry EM, Eaton JK. Shear thinning effects on blood flow in straight and curved tubes. *Phys Fluids*. (2013) 25:19. doi: 10.1063/1.4816369

6. Dasi L, Ge L, Simon H, Sotiropoulos F, Yoganathan A. Vorticity dynamics of a bileaflet mechanical heart valve in an axisymmetric aorta. *Phys Fluids*. (2007) 19:17. doi: 10.1063/1.2743261

7. De Zelicourt D, Jung P, Horner M, Pekkan K, Kanter KR, Yoganathan AP. Cannulation strategy for aortic arch reconstruction using deep hypothermic circulatory arrest. *Ann Thorac Surg*. (2012) 94:614–20. doi: 10.1016/j.athoracsur.2012.03.053

8. Eeg TB. *Fluid structure interaction simulation on an idealized aortic arch* (Master's thesis). Institutt for konstruksjonsteknikk (2012).

9. Qiao Y, Fan J, Luo K. Mechanism of blood flow energy loss in real healthy aorta using computational fluid–structure interaction framework. *Int J Eng Sci*. (2023) 192:103939. doi: 10.1016/j.ijengsci.2023.103939

10. Silveira M, Huebner R, Navarro TP. Pulsatile blood flow in the thoracic aorta and aneurysm: a numerical simulation in cad-built and patient-specific model. *J Braz Soc Mech Sci Eng*. (2017) 39:3721–8. doi: 10.1007/s40430-017-0837-2

11. Gray RA, Pathmanathan P. Patient-specific cardiovascular computational modeling: diversity of personalization and challenges. *J Cardiovasc Transl Res*. (2018) 11:80–8. doi: 10.1007/s12265-018-9792-2

12. Buchmann N, Atkinson C, Jeremy M, Soria J. Tomographic particle image velocimetry investigation of the flow in a modeled human carotid artery bifurcation. *Exp Fluids*. (2011) 50:1131–51. doi: 10.1007/s00348-011-1042-1

13. Aycock KI, Hariharan P, Craven BA. Particle image velocimetry measurements in an anatomical vascular model fabricated using inkjet 3D printing. *Exp Fluids*. (2017) 58:1–8. doi: 10.1007/s00348-017-2403-1

14. Amili O, Schiavazzi D, Moen S, Jagadeesan B, Van de Moortele P-F, Coletti F. Hemodynamics in a giant intracranial aneurysm characterized by in vitro 4D flow MRI. *PLoS One*. (2018) 13:e0188323. doi: 10.1371/journal.pone.0188323

15. Zimmermann J, Loecher M, Kolawole FO, Bäumler K, Gifford K, Dual SA, et al. On the impact of vessel wall stiffness on quantitative flow dynamics in a synthetic model of the thoracic aorta. *Sci Rep*. (2021) 11:6703. doi: 10.1038/s41598-021-86174-6

16. Falk KL, Medero R, Roldan-Alzate A. Correction: Fabrication of low-cost patient-specific vascular models for particle image velocimetry. *Cardiovasc Eng Technol*. (2023) 14:615–. doi: 10.1007/s13239-023-00655-5

17. Menichini C, Xu XY. Mathematical modeling of thrombus formation in idealized models of aortic dissection: initial findings and potential applications. *J Math Biol*. (2016) 73:1205–26. doi: 10.1007/s00285-016-0986-4

18. Peng Y, Zhang X, Li J, Zhang X, He H, Li X, et al. Enlarged lumen volume of proximal aortic segment and acute type B aortic dissection: a computer fluid dynamics study of ideal aortic models. *Int J Gen Med*. (2022) 15:535–43. doi: 10.2147/IJGM.S343403

19. Wang Y, Luo K, Qiao Y, Fan J. An integrated fluid-chemical model toward modeling the thrombus formation in an idealized model of aortic dissection. *Comput Biol Med*. (2021) 136:104709. doi: 10.1016/j.compbiomed.2021.104709

20. Liang L, Liu M, Martin C, Elefteriades JA, Sun W. A machine learning approach to investigate the relationship between shape features and numerically predicted risk of ascending aortic aneurysm. *Biomech Model Mechanobiol*. (2017) 16:1519–33. doi: 10.1007/s10237-017-0903-9

21. Speelman L, Schurink GWH, Bosboom EMH, Buth J, Breeuwer M, van de Vosse FN, et al. The mechanical role of thrombus on the growth rate of an abdominal aortic aneurysm. *J Vasc Surg*. (2010) 51:19–26. doi: 10.1016/j.jvs.2009.08.075

22. Taylor CA, Hughes TJ, Zarins CK. Effect of exercise on hemodynamic conditions in the abdominal aorta. *J Vasc Surg*. (1999) 29:1077–89. doi: 10.1016/S0741-5214(99)70249-1

23. Gao F, Watanabe M, Matsuzawa T. Stress analysis in a layered aortic arch model under pulsatile blood flow. *Biomed Eng Online*. (2006) 5:11. doi: 10.1186/1475-925X-5-25

24. Vasava P, Jalali P, Dabagh M, Kolari PJ. Finite element modelling of pulsatile blood flow in idealized model of human aortic arch: study of hypotension and hypertension. *Comput Math Methods Med*. (2012) 2012:14. doi: 10.1155/2012/861837

25. Shahcheraghi N, Dwyer H, Cheer A, Barakat A, Rutaganira T. Unsteady and three-dimensional simulation of blood flow in the human aortic arch. *J Biomech Eng*. (2002) 124:378–87. doi: 10.1115/1.1487357

26. Carr IA, Nemoto N, Schwartz RS, Shadden SC. Size-dependent predilections of cardiogenic embolic transport. *Am J Physiol Heart Circ Physiol*. (2013) 305:H732–9. doi: 10.1152/ajpheart.00320.2013

27. Mukherjee D, Jani ND, Selvaganesan K, Weng CL, Shadden SC. Computational assessment of the relation between embolism source and embolus distribution to the circle of willis for improved understanding of stroke etiology. *J Biomech Eng*. (2016) 138:081008. doi: 10.1115/1.4033986

28. Prisco AR, Aguado-Sierra J, Butakoff C, Vazquez M, Houzeaux G, Eguzkitza B, et al. Concomitant respiratory failure can impair myocardial oxygenation in patients with acute cardiogenic shock supported by VA-ECMO. *J Cardiovasc Transl Res*. (2021) 15:1–10. doi: 10.1007/s12265-021-10110-2

29. Benim A, Nahavandi A, Assmann A, Schubert D, Feindt P, Suh S. Simulation of blood flow in human aorta with emphasis on outlet boundary conditions. *Appl Math Model*. (2011) 35:3175–88. doi: 10.1016/j.apm.2010.12.022

30. Fuchs A, Berg N, Fuchs L, Prahl Wittberg L. Assessment of rheological models applied to blood flow in human thoracic aorta. *Bioengineering*. (2023) 10:1240. doi: 10.3390/bioengineering10111240

31. Liang L, Liu M, Martin C, Sun W. A deep learning approach to estimate stress distribution: a fast and accurate surrogate of finite-element analysis. *J R Soc Interface*. (2018) 15:20170844. doi: 10.1098/rsif.2017.0844

32. Plonek T, Zak M, Burzynska K, Rylski B, Gozdzik A, Kustrzycki W, et al. The combined impact of mechanical factors on the wall stress of the human ascending aorta—a finite elements study. *BMC Cardiovasc Disord*. (2017) 17:1–7. doi: 10.1186/s12872-017-0733-9

33. Reymond P, Crosetto P, Deparis S, Quarteroni A, Stergiopulos N. Physiological simulation of blood flow in the aorta: comparison of hemodynamic indices as predicted by 3-D FSI, 3-D rigid wall and 1-D models. *Med Eng Phys*. (2013) 35:784–91. doi: 10.1016/j.medengphy.2012.08.009

34. Suito H, Takizawa K, Huynh VQ, Sze D, Ueda T. Fsi analysis of the blood flow and geometrical characteristics in the thoracic aorta. *Comput Mech*. (2014) 54:1035–45. doi: 10.1007/s00466-014-1017-1

35. Aliseda A, Chivukula VK, Mcgah P, Prisco AR, Beckman JA, Garcia GJ, et al. Lvad outflow graft angle and thrombosis risk. *ASAIO J (Am Soc Artif Intern Org 1992)*. (2017) 63:14. doi: 10.1097/MAT.0000000000000443

36. Amili O, MacIver R, Coletti F. Magnetic resonance imaging based flow field and lagrangian particle tracking from a left ventricular assist device. *J Biomech Eng*. (2020) 142:19. doi: 10.1115/1.4043939

37. May-Newman K, Hillen B, Dembitsky W. Effect of left ventricular assist device outflow conduit anastomosis location on flow patterns in the native aorta. *ASAIO J*. (2006) 52:132–9. doi: 10.1097/01.mat.0000201961.97981.e9

38. Prather R, Divo E, Kassab A, DeCampli W. Computational fluid dynamics study of cerebral thromboembolism risk in ventricular assist device patients: effects of pulsatility and thrombus origin. *J Biomech Eng*. (2021) 143:091001. doi: 10.1115/1.4050819

39. Ricardo Argueta-Morales I, Tran R, Ceballos A, Clark W, Osorio R, Divo EA, et al. Mathematical modeling of patient-specific ventricular assist device implantation to reduce particulate embolization rate to cerebral vessels. *J Biomech Eng*. (2014) 136:071008. doi: 10.1115/1.4026498

40. Barmparas G, Inaba K, Talving P, David J-S, Lam L, Plurad D, et al. Pediatric vs adult vascular trauma: a national trauma databank review. *J Pediatr Surg*. (2010) 45:1404–12. doi: 10.1016/j.jpedsurg.2009.09.017

41. U.S. Department of Health and Human Services, Food and Drug Administration, Center for Drug Evaluation and Research (CDER), Center for Biologics Evaluation and Research (CBER). *Pediatric Information Incorporated into Human Prescription Drug and Biological Product Labeling Guidance for Industry*. Silver Spring, MD: Federal Register (2019).

42. Biaggi P, Matthews F, Braun J, Rousson V, Kaufmann PA, Jenni R. Gender, age, and body surface area are the major determinants of ascending aorta dimensions in subjects with apparently normal echocardiograms. *J Am Soc Echocardiogr*. (2009) 22:720–5. doi: 10.1016/j.echo.2009.03.012

43. Mao SS, Ahmadi N, Shah B, Beckmann D, Chen A, Ngo L, et al. Normal thoracic aorta diameter on cardiac computed tomography in healthy asymptomatic adults: impact of age and gender. *Acad Radiol*. (2008) 15:827–34. doi: 10.1016/j.acra.2008.02.001

44. Celikyay ZRY, Koner AE, Celikyay F, Denız C, Acu B, Firat MM. Frequency and imaging findings of variations in human aortic arch anatomy based on multidetector computed tomography data. *Clin Imaging*. (2013) 37:1011–9. doi: 10.1016/j.clinimag.2013.07.008

45. Nelson ML, Sparks CD. Unusual aortic arch variation: distal origin of common carotid arteries. *Clin Anat*. (2001) 14:62–5. doi: 10.1002/1098-2353(200101)14:1¡62::AID-CA1012¿3.0.CO;2-#

46. Nayak SR, Pai MM, Prabhu LV, D'Costa S, Shetty P. Anatomical organization of aortic arch variations in the India: embryological basis and review. *J Vasc Bras*. (2006) 5:95–100. doi: 10.1590/S1677-54492006000200004

47. Natsis KI, Tsitouridis IA, Didagelos MV, Fillipidis AA, Vlasis KG, Tsikaras PD. Anatomical variations in the branches of the human aortic arch in 633 angiographies: clinical significance and literature review. *Surg Radiol Anat*. (2009) 31:319–23. doi: 10.1007/s00276-008-0442-2

48. Jakanani G, Adair W. Frequency of variations in aortic arch anatomy depicted on multidetector CT. *Clin Radiol*. (2010) 65:481–7. doi: 10.1016/j.crad.2010.02.003

49. Dumfarth J, Chou AS, Ziganshin BA, Bhandari R, Peterss S, Tranquilli M, et al. Atypical aortic arch branching variants: a novel marker for thoracic aortic disease. *J Thorac Cardiovasc Surg*. (2015) 149:1586–92. doi: 10.1016/j.jtcvs.2015.02.019

50. Huapaya JA, Chávez-Trujillo K, Trelles M, Carbajal RD, Espadin RF. Anatomic variations of the branches of the aortic arch in a peruvian population. *Medwave*. (2015) 15:e6194. doi: 10.5867/medwave.2015.06.6194

51. Popieluszko P, Henry BM, Sanna B, Hsieh WC, Saganiak K, Pekala PA, et al. A systematic review and meta-analysis of variations in branching patterns of the adult aortic arch. *J Vasc Surg*. (2018) 68:298–306. doi: 10.1016/j.jvs.2017.06.097

52. Aronberg D, Glazer H, Madsen K, Sagel S. Normal thoracic aortic diameters by computed tomography. *J Comput Assist Tomogr*. (1984) 8(2):247–50. PMID: 6707274

53. Hager A, Kaemmerer H, Rapp-Bernhardt U, Blücher S, Rapp K, Bernhardt TM, et al. Diameters of the thoracic aorta throughout life as measured with helical computed tomography. *J Thorac Cardiovasc Surg*. (2002) 123:1060–6. doi: 10.1067/mtc.2002.122310

54. Redheuil A, Yu W-C, Mousseaux E, Harouni AA, Kachenoura N, Wu CO, et al. Age-related changes in aortic arch geometry: relationship with proximal aortic function and left ventricular mass and remodeling. *J Am Coll Cardiol*. (2011) 58:1262–70. doi: 10.1016/j.jacc.2011.06.012

55. Hannuksela M, Lundqvist S, Carlberg B. Thoracic aorta–dilated or not? *Scand Cardiovasc J*. (2006) 40:175–8. doi: 10.1080/14017430600565999

56. Wolak A, Gransar H, Thomson LE, Friedman JD, Hachamovitch R, Gutstein A, et al. Aortic size assessment by noncontrast cardiac computed tomography: normal limits by age, gender, and body surface area. *JACC Cardiovasc Imaging*. (2008) 1:200–9. doi: 10.1016/j.jcmg.2007.11.005

57. Evangelista A, Flachskampf FA, Erbel R, Antonini-Canterin F, Vlachopoulos C, Rocchi G, et al. Echocardiography in aortic diseases: EAE recommendations for clinical practice. *Eur J Echocardiogr*. (2010) 11:645–58. doi: 10.1093/ejechocard/jeq056

58. Craiem D, Chironi G, Casciaro ME, Redheuil A, Mousseaux E, Simon A. Three-dimensional evaluation of thoracic aorta enlargement and unfolding in hypertensive men using non-contrast computed tomography. *J Hum Hypertens*. (2013) 27:504–9. doi: 10.1038/jhh.2012.69

59. Davis AE, Lewandowski AJ, Holloway CJ, Ntusi NA, Banerjee R, Nethononda R, et al. Observational study of regional aortic size referenced to body size: production of a cardiovascular magnetic resonance nomogram. *J Cardiovasc Magn Reson*. (2014) 16:1–9. doi: 10.1186/1532-429X-16-9

60. Vizzardi E, Maffessanti F, Lorusso R, Sciatti E, Bonadei I, Gelsomino S, et al. Ascending aortic dimensions in hypertensive subjects: reference values for two-dimensional echocardiography. *J Am Soc Echocardiogr*. (2016) 29:827–37. doi: 10.1016/j.echo.2016.03.016

61. Guo J-p., Jia X, Sai Z, Ge Y-y., Wang S, Guo W. Thoracic aorta dimension changes during systole and diastole: evaluation with ecg-gated computed tomography. *Ann Vasc Surg*. (2016) 35:168–73. doi: 10.1016/j.avsg.2016.01.050

62. Craiem D, El Batti S, Casciaro ME, Mousseaux E, Sirieix M-E, Simon A, et al. Age-related changes of thoracic aorta geometry used to predict the risk for acute type b dissection. *Int J Cardiol*. (2017) 228:654–60. doi: 10.1016/j.ijcard.2016.11.125

63. Zubair MM, de Beaufort HW, Belvroy VM, Schwein A, Irshad A, Mohamed A, et al. Impact of cardiac cycle on thoracic aortic geometry—morphometric analysis of ecg gated computed tomography. *Ann Vasc Surg*. (2020) 65:174–82. doi: 10.1016/j.avsg.2019.10.072

64. Alhafez BA, Ocazionez D, Sohrabi S, Sandhu H, Estrera A, Safi HJ, et al. Aortic arch tortuosity, a novel biomarker for thoracic aortic disease, is increased in adults with bicuspid aortic valve. *Int J Cardiol*. (2019) 284:84–9. doi: 10.1016/j.ijcard.2018.10.052

65. Gupta M, Sodhi L. Variations in branching pattern, shape, size and relative distances of arteries arising from arch of aorta. *Nepal Med Coll J NMCJ*. (2005) 7 (1):13–7. PMID: 16295713

66. Zerebiec KW, Heidari P, D'Agostino E, Soares BP, Johnson DM, Raymond SB. Arch and great vessel geometry from a transradial angiographic approach. *Stroke Vasc Interv Neurol*. (2023) 3:e000470. doi: 10.1161/SVIN.122.000470

67. Vučurević G, Marinković S, Puškaš L, Kovačević I, Tanasković S, Radak D, et al. Anatomy and radiology of the variations of aortic arch branches in 1,266 patients. *Folia Morphol (Praha)*. (2013) 72:113–22. doi: 10.5603/FM.2013.0019

68. Wilbring M, Rehm M, Ghazy T, Amler M, Matschke K, Kappert U. Aortic arch mapping by computed tomography for actual anatomic studies in times of emerging endovascular therapies. *Ann Vasc Surg*. (2016) 30:181–91. doi: 10.1016/j.avsg.2015.07.018

69. Shin I-Y, Chung Y-G, Shin W-H, Im S-B, Hwang S-C, Kim B-T. A morphometric study on cadaveric aortic arch and its major branches in 25 Korean adults: the perspective of endovascular surgery. *J Korean Neurosurg Soc*. (2008) 44:78. doi: 10.3340/jkns.2008.44.2.78

70. Alsaif HA, Ramadan WS. An anatomical study of the aortic arch variations. *JKAU Med Sci*. (2010) 17:37–54. doi: 10.4197/Med.17-2.4

71. Vasava P, Jalali P, Dabagh M. Computational study of pulstile blood flow in aortic arch: effect of blood pressure. In: *World Congress on Medical Physics and Biomedical Engineering, September 7–12, 2009, Munich, Germany: Vol. 25/4 Image Processing, Biosignal Processing, Modelling and Simulation, Biomechanics*. Springer (2010). p. 1198–201.

72. Rengier F, Wörz S, Godinez WJ, Schumacher H, Böckler D, Rohr K, et al. Development of in vivo quantitative geometric mapping of the aortic arch for advanced endovascular aortic repair: feasibility and preliminary results. *J Vasc Interv Radiol*. (2011) 22:980–6. doi: 10.1016/j.jvir.2011.01.434

73. Finlay A, Johnson M, Forbes TL. Surgically relevant aortic arch mapping using computed tomography. *Ann Vasc Surg*. (2012) 26:483–90. doi: 10.1016/j.avsg.2011.08.018

74. Manole A, Iliescu D, Rusali A, Bordei P. Morphometry of the aortic arch and its branches. *ARS Med Tomitana*. (2013) 19:154–9. doi: 10.2478/arsm-2013-0027

75. Osorio AF, Osorio R, Ceballos A, Tran R, Clark W, Divo EA, et al. Computational fluid dynamics analysis of surgical adjustment of left ventricular assist device implantation to minimise stroke risk. *Comput Methods Biomech Biomed Eng*. (2013) 16:622–38. doi: 10.1080/10255842.2011.629616

76. Tapia-Nañez M, Landeros-Garcia G, Sada-Treviño M, Pinales-Razo R, Quiroga-Garza A, Fernandez-Rodarte B, et al. Morphometry of the aortic arch and its branches. a computed tomography angiography-based study. *Folia Morphol (Praha)*. (2021) 80:575–82. doi: 10.5603/FM.a2020.0098

77. Aboulhoda BE, Ahmed RK, Awad AS. Clinically-relevant morphometric parameters and anatomical variations of the aortic arch branching pattern. *Surg Radiol Anat*. (2019) 41:731–44. doi: 10.1007/s00276-019-02215-w

78. Liu L, Wang W, Lu Q, Jing Z, Zhang S, Xu B. Morphology of the ascending aorta: a study on 114 Chinese patients. *J Interv Med*. (2018) 1:22–7. doi: 10.19779/j.cnki.2096-3602.2018.01.06

79. Saade W, Vinciguerra M, Romiti S, Macrina F, Frati G, Miraldi F, et al. 3d morphometric analysis of ascending aorta as an adjunctive tool to predict type a acute aortic dissection. *J Thorac Dis*. (2021) 13:3443. doi: 10.21037/jtd-21-119

80. Demertzis S, Hurni S, Stalder M, Gahl B, Herrmann G, Van den Berg J. Aortic arch morphometry in living humans. *J Anat*. (2010) 217:588–96. doi: 10.1111/j.1469-7580.2010.01297.x

81. Loukas M, Bilinsky E, Bilinsky S, Blaak C, Tubbs RS, Anderson RH. The anatomy of the aortic root. *Clin Anat*. (2014) 27:748–56. doi: 10.1002/ca.22295

82. Ovcharenko E, Klyshnikov K, Vlad A, Sizova I, Kokov A, Nushtaev D, et al. Computer-aided design of the human aortic root. *Comput Biol Med*. (2014) 54:109–15. doi: 10.1016/j.compbiomed.2014.08.023

83. GrabCAD. Grabcad (2015).

84. Mehrotra S, Mohammed S, Sharma Y. Evaluation of normal coronary artery dimensions in Indian population-study from a northern Indian medical education and research institute. *Edorium J Cardiol*. (2016) 3:6–12. doi: 10.5348/C03-2016-6-OA-2

85. Reddy S, Kumar S, Kashyap JR, Rao R, Kadiyala V, Reddy H, et al. Coronary artery size in North Indian population–intravascular ultrasound-based study. *Indian Heart J*. (2019) 71:412–7. doi: 10.1016/j.ihj.2019.10.005

86. Raut BK, Patil VN, Cherian G. Coronary artery dimensions in normal Indians. *Indian Heart J*. (2017) 69:512–4. doi: 10.1016/j.ihj.2017.01.009

87. Kim EJ, Yoo JY, Cheon WS, Han SW, Choi YJ, Ryu KH, et al. Coronary artery size in Korean: normal value and its determinants. *Korean Circ J*. (2005) 35:115–22. doi: 10.4070/kcj.2005.35.2.115

88. Cavalcanti JS, Melo NCVd., Vasconcelos RSd. Morphometric and topographic study of coronary ostia. *Arq Bras Cardiol*. (2003) 81:359–62. doi: 10.1590/S0066-782X2003001200003

89. Bailoor S, Seo J-H, Dasi LP, Schena S, Mittal R. A computational study of the hemodynamics of bioprosthetic aortic valves with reduced leaflet motion. *J Biomech*. (2021) 120:110350. doi: 10.1016/j.jbiomech.2021.110350

90. Becsek B, Pietrasanta L, Obrist D. Turbulent systolic flow downstream of a bioprosthetic aortic valve: velocity spectra, wall shear stresses, and turbulent dissipation rates. *Front Physiol*. (2020) 11:577188. doi: 10.3389/fphys.2020.577188

91. Conti CA, Votta E, Della Corte A, Del Viscovo L, Bancone C, Cotrufo M, et al. Dynamic finite element analysis of the aortic root from MRI-derived parameters. *Med Eng Phys*. (2010) 32:212–21. doi: 10.1016/j.medengphy.2009.12.003

92. De Hart J, Peters G, Schreurs P, Baaijens F. A three-dimensional computational analysis of fluid–structure interaction in the aortic valve. *J Biomech*. (2003) 36:103–12. doi: 10.1016/S0021-9290(02)00244-0

93. Gharaie SH, Mosadegh B, Morsi Y. In vitro validation of a numerical simulation of leaflet kinematics in a polymeric aortic valve under physiological conditions. *Cardiovasc Eng Technol*. (2018) 9:42–52. doi: 10.1007/s13239-018-0340-7

94. Labrosse MR, Beller CJ, Robicsek F, Thubrikar MJ. Geometric modeling of functional trileaflet aortic valves: development and clinical applications. *J Biomech*. (2006) 39:2665–72. doi: 10.1016/j.jbiomech.2005.08.012

95. Seo J-H, Zhu C, Resar J, Mittal R. Flow physics of normal and abnormal bioprosthetic aortic valves. *Int J Heat Fluid Flow*. (2020) 86:108740. doi: 10.1016/j.ijheatfluidflow.2020.108740

96. Frazao C, Tavoosi A, Wintersperger BJ, Nguyen ET, Wald RM, Ouzounian M, et al. Multimodality assessment of thoracic aortic dimensions: comparison of computed tomography angiography, magnetic resonance imaging, and echocardiography measurements. *J Thorac Imaging*. (2020) 35:399–406. doi: 10.1097/RTI.0000000000000514

97. Peacock J, Jones T, Tock C, Lutz R. The onset of turbulence in physiological pulsatile flow in a straight tube. *Exp Fluids*. (1998) 24:1–9. doi: 10.1007/s003480050144

frontiers | Frontiers in Cardiovascular Medicine

TYPE Original Research
PUBLISHED 20 August 2024
DOI 10.3389/fcvm.2024.1363230

Check for updates

OPEN ACCESS

EDITED BY
Aike Qiao,
Beijing University of Technology, China

REVIEWED BY
Fraser Callaghan,
University Children's Hospital Zurich, Switzerland
Ying He,
Dalian University of Technology, China
Tinghui Zheng,
Sichuan University, China
Mingzi Zhang,
Macquarie University, Australia

*CORRESPONDENCE
Yang Liu
✉ liuyangxijing@126.com
Jian Yang
✉ yangjian1212@hotmail.com

†These authors have contributed equally to this work

RECEIVED 30 December 2023
ACCEPTED 24 June 2024
PUBLISHED 20 August 2024

CITATION
Li L, Wang Y, Jin P, Yang T, Zhu G, Li Y, Tang J, Liu Y and Yang J (2024) Hemodynamics in the treatment of pseudoaneurysm caused by extreme constriction of aortic arch with coated stent.
Front. Cardiovasc. Med. 11:1363230.
doi: 10.3389/fcvm.2024.1363230

COPYRIGHT
© 2024 Li, Wang, Jin, Yang, Zhu, Li, Tang, Liu and Yang. This is an open-access article distributed under the terms of the Creative Commons Attribution License (CC BY). The use, distribution or reproduction in other forums is permitted, provided the original author(s) and the copyright owner(s) are credited and that the original publication in this journal is cited, in accordance with accepted academic practice. No use, distribution or reproduction is permitted which does not comply with these terms.

Hemodynamics in the treatment of pseudoaneurysm caused by extreme constriction of aortic arch with coated stent

Lanlan Li[1†], Yiwei Wang[1†], Ping Jin[1†], Tingting Yang[2], Guangyu Zhu[2], Yuxi Li[3], Jiayou Tang[1], Yang Liu[1*] and Jian Yang[1*]

[1]Department of Cardiovascular Surgery, Xijing Hospital, Air Force Medical University, Xi'an, Shaanxi, China, [2]School of Energy and Power Engineering, Xi'an Jiaotong University, Xi'an, Shaanxi, China, [3]Department of Ultrasound Medicine, Xijing Hospital, Air Force Medical University, Xi'an, Shaanxi, China

Objectives: To evaluate the changes in distal vascular morphology and hemodynamics in patients with extremely severe aortic coarctation (CoA) after covered palliative (CP) stent dilation with different surgical strategies.
Materials and methods: Perioperative computed tomography angiography and digital subtraction angiography were utilized to construct three aortic models with varying stenosis rates and one follow-up model in a patient with extremely severe CoA. The models included: an idealized non-stenosed model (A: 0%), a model post initial stent deployment (B: 28%), a model post balloon expansion (C: 39%), and a model 18 months after post-balloon expansion (D: 39%). Consistent boundary conditions were applied to all models, and hemodynamic simulation was conducted using the pure fluid method.
Results: The narrowest and distal diameter of the stent increased by 34.71% and 59.29%, respectively, from model B to C. Additionally, the distal diameter of the stent increased by −13.80% and +43.68% compared to the descending aorta diameter, respectively. Furthermore, the ellipticity of the maximum cross-section of the aneurysm region in model A to D continued to increase. The oscillatory shear index at the stenosis to the region of the aneurysm were found to be higher in Models A and B, and lower in Models C and D. At the moment of maximum flow velocity, the blood flow distribution in models A and B was more uniform in the widest section of the blood vessels at the distal end of the stenosis, whereas models C and D exhibited disturbed blood flow with more than 2 eddy currents. The time-averaged wall shear stress (TAWSS) decreased in the distal and basal aneurysms, while it significantly increased at the step position. The aneurysmal region exhibited an endothelial cell activation potential value lower than 0.4 Pa^{-1}.
Conclusion: In patients with extremely severe CoA, it is crucial to ensure that the expanded diameter at both ends of the CP stent does not exceed the native vascular diameter during deployment. Our simulation results demonstrate that overdilation leads to a decrease in the TAWSS above the injured vessel, creating an abnormal hemodynamic environment that may contribute to the development and enlargement of false aneurysms in the early postoperative period.

Clinical Trial Registration: ClinicalTrials.gov, (NCT02917980).

KEYWORDS

coarctation of aorta, aortic pseudoaneurysm, hemodynamics, balloon-expandable stent, surgical strategy

Introduction

Extremely narrowed aortic arch is a rare and severe congenital heart disease in which patients often present with upper extremity hypertension, making activities limited, and stenting of the aortic arch is currently the modality of choice for the treatment of coarctation of the aorta (CoA) (1–3). When employing Cheatham Platinum (CP) stents for CoA treatment, the balloon-in-balloon (BIB) catheter is typically not inflated to the extent that it fully matches the size of the stenotic region within the vessel, which makes the mid-section of the stent present a waist sign in the postoperative period, and the stent has poor morphology and a high rate of shortening after overexpansion, which can damage the endothelium and cause iatrogenic pseudoaneurysm in the distant future of the procedure (4, 5). Therefore, how to find a more appropriate surgical strategy for patients with extreme narrowing of the aortic arch is a major clinical problem that needs to be explored and solved under the constraints of guaranteeing the safety of the procedure, the long-term effectiveness of the postoperative period, and the feasibility of the surgical program in line with the actual operation of the clinic (6–9).

It has been observed that diverse hemodynamic conditions can influence the morphological development of blood vessels. In the presence of hemodynamic irregularities within the vessel, there is a risk of aneurysm, aortic dissection, and atherosclerosis (6, 7). When the vessel undergoes an interventional procedure, the hemodynamic environment is significantly altered (7, 8). Evaluating the efficacy of stent implantation in the clinical setting involves assessing changes in pressure and flow velocity immediately post-implantation. Over the long term, the adaptation of vessels to these changes and the potential future complications can be predicted by analyzing alterations in vascular forces and blood flow patterns (8, 9). These biomechanical parameters can be determined using Computational Fluid Dynamics (CFD) numerical simulation techniques.

This study involved a retrospective analysis of a patient who had undergone CoA stenting and subsequently developed a pseudoaneurysm. Numerical simulations, utilizing multimodal images of the patient, were conducted to compare the changes in hemodynamic parameters between the anticipated ideal state and the actual intraoperative conditions post-procedure (6–8). The objective is to predict the risk factors of complications, such as pseudoaneurysm, after the treatment of extreme CoA using morphological and biomechanical analysis (9, 10). Additionally, this research methodology can aid in identifying a more suitable procedure strategy for patients with extreme aortic arch narrowing, considering both surgical safety and long-term effectiveness, while ensuring practical feasibility within clinical practice (11, 12). This will serve as a robust foundation for the future development and implementation of stent implantation strategies for aortic arch narrowing.

Materials and methods

Baseline characteristics

A male patient presenting with a narrowed aortic arch and intractable hypertension (upper extremity blood pressure of 210/110 mmHg) was selected for this study. The patient had a dissected stenosis (dissected length of 6 mm) and preoperative measurements indicating a left radial artery blood pressure of 185/110 mmHg, right femoral artery blood pressure of 75/60 mmHg, and an stenosis pressure difference of 110 mmHg.

Procedures

Intraoperatively, DSA-guided transcatheter stenting was performed using 39-mm-length overlay CP stents, along with a 20 mm Numed BiB balloon dilatation. During the procedure, the stent underwent initial balloon expansion, and angiography revealed the presence of stenosis, with the stent being well adhered to the vessel wall. Monitoring of the blood pressure using a pigtail catheter positioned at the proximal and distal ends of the stenosis yielded a maximum systolic pressure difference of 13 mm Hg. Due to the apparent stenosis and the pressure difference not meeting the standard range, the surgeon applied high pressure to the balloon for a second time to expand the stent, resulting in a reduced pressure difference of 4 mmHg. Consequently, the patient's hypertension was alleviated, and the procedure was successfully concluded.

Computed tomography angiography (CTA) images

The CTA images were acquired using a Siemens dual-source Flash CT, covering the scanning range from the skull base to the bilateral groin, with a slice thickness of 1 mm and slice spacing of 0.8 mm. The scanning direction was head to foot, with a tube voltage of 100 KV and an automatically adjusted tube current ranging from 200 mA to 600 mA. A contrast agent triphasic injection scheme was implemented as follows: I. 350 mgI 70–80 ml at a flow rate of 4–5 ml/s, II. 350 mgI 20 ml at a flow rate of 1.5 ml/s, III. saline 30–40 ml at a flow rate of 4–5 ml/s.

Geometric modeling

In this study, we acquired computed tomography angiography (CTA) images of the patient, encompassing preoperative CTA, CTA at 3 days postoperatively, and CTA at 18 months postoperatively (Figure 1). The Mimics Innovation Suite 21.0 software was utilized to interpret the patient's CTA in DICOM format. First, we developed model A, aimed at achieving perfect correction, by utilizing preoperative CTA images to replicate the stenosis location with the same diameter as the descending aorta, demonstrating a stenosis rate of 0.0%. Subsequently, model B was constructed for optimal intervention, which entailed measuring the stent height and diameters at both ends of the stent based on the digital subtraction angiography (DSA) images following the initial intraoperative balloon dilatation and comparing these measurements with those from the preoperative CTA images. After realizing that the DSA images were not scaled, the stent shape and size at different angles following the initial surgical intervention were obtained based on the

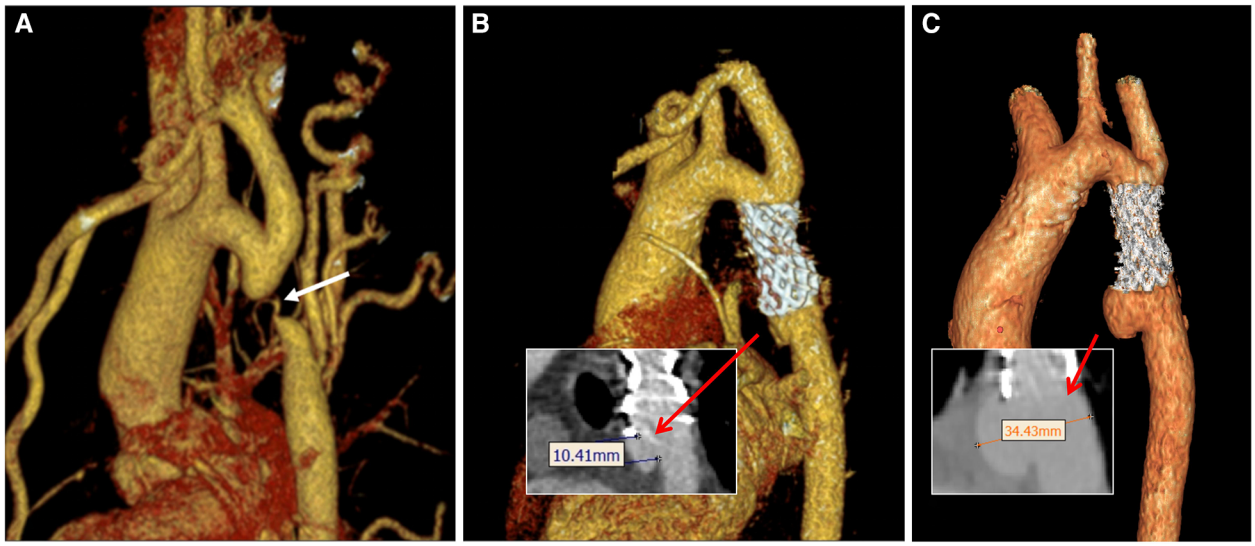

FIGURE 1
Three-dimensional images of the aorta during perioperative CTA in patient. (A) Preoperative image; (B) postoperative-3 days; (C) postoperative-18 months. The white arrow indicates the position of the stenosis. The red arrows indicate the neck of the aneurysm in B and the distance between the aneurysm dome and the parent artery in C, respectively.

intraoperative dynamic DSA images. Subsequently, Model B, with a stenosis rate of 28%, was virtually constructed using the preoperative CTA images. Subsequently, Model C was developed following the second intervention, signifying overcorrection and the conclusion of the procedure after the second balloon dilatation. Model C, representing a stenosis rate of 39% in the actual state, was constructed based on the review of CTA images at 3 days postoperatively. Lastly, a model was constructed for the patient at 18 months after the second dilatation of the stent, and a model of the patient at 18 months after the second dilatation of the stent was constructed by using the review CTA images to directly construct model D, with a stenosis rate of 39%. Model D was utilized to validate the findings of Model C and to monitor the progression of aneurysm development. It is noteworthy that the model was simplified by deleting the distal collateral vessels in the stenosis of the descending aorta (Figure 2).

Numerical simulation methods

The blood flow was modeled as an incompressible Newtonian fluid with laminar characteristics. Key parameters included a blood density of 1,150 kg/m^3, blood viscosity of 0.0035 Pa·s, and Poisson's ratio of 0.45. Both the vessel wall and stent position were treated as rigid walls with no slippage. Pure fluid analysis was conducted using the CFX module in Ansys 2021 R1 software, with a boundary layer of 8. Additionally, tetrahedral meshers were created in the fluid domain using Ansys ICEM CFD (10, 11). As depicted in Figure 3, boundary conditions were established based on postoperative ultrasound and monitoring, enabling the determination of flow velocity at the center point of the ascending aorta (AA), brachiocephalic trunk (BCA), left common carotid artery (LCCA), and left subclavian artery (LSA) (13). At the same time, a 5F pigtail catheter with a pressure sensor was inserted into the distal end of the descending aorta (DA) through the femoral artery. The pressure waveform of the outlet DA and the heart rate (75 beats/min, corresponding to a cardiac cycle of 0.8 s) were recorded using an ECG monitor (14). The transient simulations demonstrated that the model achieved convergence in calculating the results for three cardiac cycles. As a result, the findings of the fourth cycle were extracted for analysis in this study. (The measurement data for all models, including boundary, stenosis position, aneurysm diameter, stenosis rate, ellipticity, etc., are presented in Table 1. The corresponding measurement positions for each parameter are illustrated in Figure 3.)

The post-processing data extraction

The post-processing software CFD-Post 2021 R1 was utilized to calculate essential parameters such as Time-Averaged Wall Shear Stress (TAWSS), Oscillatory Shear Index (OSI), Endothelial Cell Activation Potential (ECAP) (12), velocity, and others. These parameters were displayed using contours, vector diagrams, and various other visualization methods. The pertinent mechanical parameter are provided in Equations (1), (2), and (3), respectively:

$$\mathrm{TAWSS} = \frac{1}{T}\int_0^T |\mathbf{WSS}|\mathrm{d}t \tag{1}$$

$$\mathrm{OSI} = \frac{1}{2}\left(1 - \frac{\left|\frac{1}{T}\int_0^T \mathbf{WSS}\mathrm{d}t\right|}{\frac{1}{T}\int_0^T |\mathbf{WSS}|\mathrm{d}t}\right) \tag{2}$$

$$\mathrm{ECAP} = \frac{\mathrm{OSI}}{\mathrm{TAWSS}} \tag{3}$$

10.3389/fcvm.2024.1363230

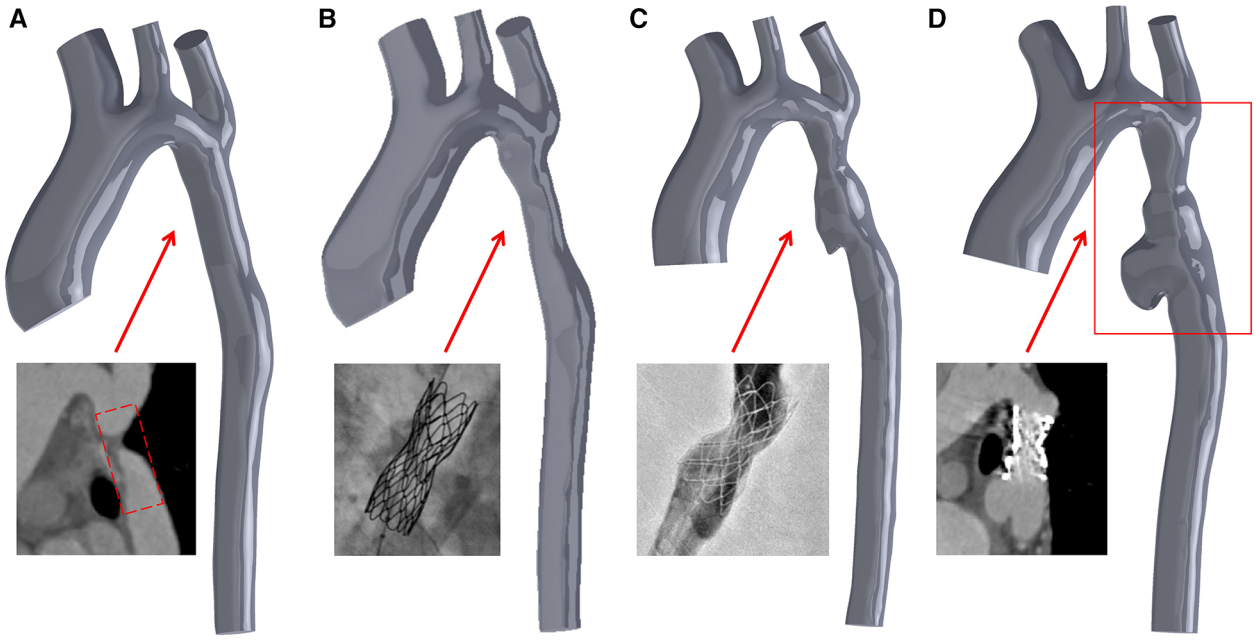

FIGURE 2
Three-dimensional digital models were constructed based on CTA and DSA images. Model A represents the idealized expansion of the stent to match the vessel diameter; model B signifies the initial partial expansion of the stent; model C portrays the subsequent over-expansion of the stent; and model D showcases the vessel model 18 months after the second over-expansion of the stent. Specifically, model C corresponds to a 3-day postoperative model depicted in Figure 1B, while model D corresponds to the 3D CTA images shown in Figure 1C.

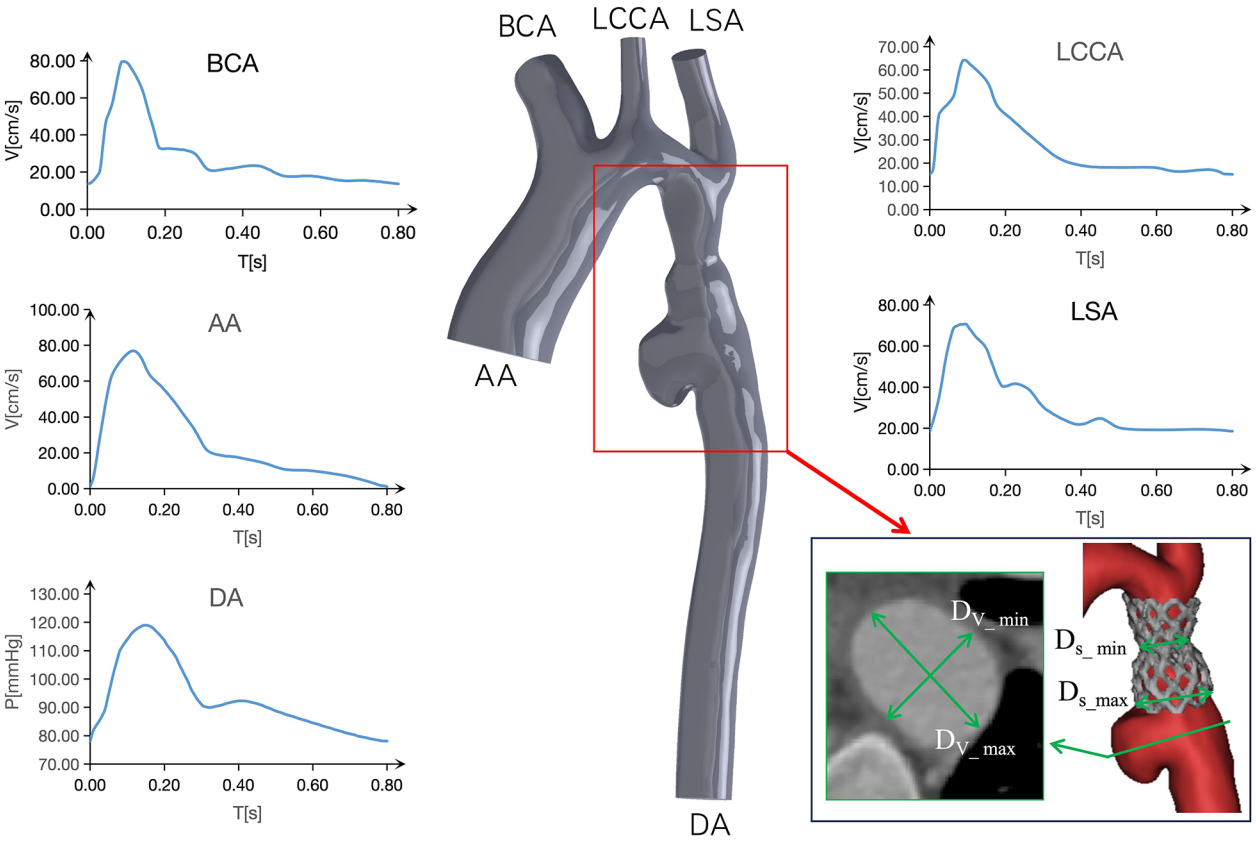

FIGURE 3
Boundary conditions of models and schematic representation of the plane of correlation analysis.

TABLE 1 The diameters of aortic at baseline and follow-up.

Model	A (control)	B (1st-expansion)	C (2nd-expansion)	D (Postoperative-18 months)
$D_{\_AA}$(mm)	27.94	27.73	28.41	30.81
$D_{\_BCA}$(mm)	19.51	19.46	16.39	15.47
$D_{\_LCCA}$(mm)	10.02	10.03	8.39	7.37
$D_{\_LSA}$(mm)	13.37	13.48	11.82	10.28
$D_{\_DA}$(mm)	14.77	14.85	14.19	16.36
D_{S_min}(mm)	18.32	9.22	12.42	11.94
D_S(mm)	18.32	12.80	20.39	19.67
Percentage of stent stenosis	0%	28%	39%	39%
D_{V_max}(mm)	18.45	18.78	23.73	34.43
D_{V_min}(mm)	18.30	18.30	18.53	22.76
Ellipticity	1.01	1.03	1.28	1.51

Wall Shear Stress (WSS) refers to the tangential force exerted on a vessel due to pulsatile blood flow. In formulas (1) and (2), **WSS** represents the instantaneous WSS vector, and T denotes the integration period, specifically referring to a cardiac cycle. TAWSS denotes the average integral value of WSS during a cardiac cycle. Inadequately low WSS can lead to intimal inflammation and platelet deposition, while excessively high WSS can damage the blood vessel wall. OSI is utilized to assess WSS volatility, primarily measuring the degree of WSS direction change during the cardiac cycle. The value ranges from 0 to 0.5, where 0 indicates stable WSS direction throughout the cardiac cycle, and 0.5 indicates significant changes in WSS direction, representing purely oscillatory flow. ECAP serves to characterize the potential for local mural thrombosis in aneurysms. A higher ECAP suggests a greater likelihood of thrombosis, and a value of 1.4 Pa-1 is generally considered critical (15). Therefore, these hemodynamic parameters can be employed to analyze the development of vascular aneurysms and associated complications (16).

Results

Morphological feature

Initially, anatomical measurements indicated a progressive decrease in the diameters of the three branch vessels of the aortic arch post-surgery. Notably, at the 18-month mark, the BCA, LCCA, and LSA exhibited reductions of 20.71%, 26.45%, and 23.11%, respectively, compared to their preoperative measurements. In contrast, the diameters of the aortic AA and descending aortic DA increased by 10.27% and 10.77%, respectively, during the same period.

From model B to model C during the two intraoperative interventions, it can be seen that the diameter of the narrowest stenosis position of CoA patients increased from 9.22 mm to 12.42 mm, that is, the diameter of the stenosis position of the stent increased by 34.71% after expansion. The diameter of the distal stent at the stenosis site expanded from 12.80 mm to 20.39 mm, an increase of 59.29%. However, for CP stents, the stenosis rate at the CoA lesion site increased from 28% to 39%. Meanwhile, relative to the diameter of the descending aorta, the diameter of the distal end of the stent decreased by 13.80% in model B and increased by 43.68% in model C (Table 1).

Figures 1, 2 show that following the second intervention, an asymmetrical "step" pattern emerged on the inner curvature of the aorta, located 10.41 mm from the distal end of the stent. The angle formed at this position became increasingly sharper over the 18 months after surgery. The DSA image reveals a deepening of the angiographic development at the top of the "step". According to the two follow-up examinations, the vascular wall in this region continues to locally expand, leading to the formation of aneurysms. The maximum aneurysm diameter (DV_max), measured as the distance between the aneurysm dome and the parent artery, gradually increases from Model A to Model D, with growth rates of 1.79%, 26.36%, and 45.09%, respectively. The narrowest diameter (DV_min) grew more slowly, with growth rates of 0%, 1.26%, and 22.83%. Concurrently, the ellipticity of the blood vessels at this cross-section increased by 1.98%, 24.27%, and 17.97% across the models.

Hemodynamic characteristics

TAWSS: As depicted in Figure 4, the TAWSS of the vascular wall in the aneurysm region in models C and D, reviewed after surgery, was higher compared to the ideal Model A and Model B, which exhibited insufficient stent expansion during the initial intervention. In model C, the TAWSS on both sides of the short axis of the aneurysm fell within the range of normal vascular stress, while the local TAWSS at this position in Model D was in the 5~6 Pa range, slightly higher than the normal value. At 18 months post-surgery, the TAWSS at the distal end of the long axis of the aneurysm and at the lowest end of the aneurysm in Model C was lower than 1 Pa, whereas in Model D, it was within the normal range of 1~4 Pa. With the growth of the aneurysm, the TAWSS at the "step" position in Model D increased significantly, with an area of more than 5 Pa expanding. Furthermore, in Model C, characterized by excessive stent expansion during the second intervention, a step-type aneurysm structure emerged in the blood vessels at the distal end of the stent, leading to an overall increase in TAWSS at this position, particularly at the step-type location.

OSI and Velocity: In Figure 5, following the initial intervention (Model B), the OSI value at the distal stent closely approximates that of an idealized normal individual (Model A), ranging from 0.30 to 0.45. However, at 3 days (Model C) and 18 months (Model D) after overdilation, the blood vessels downstream of the stent

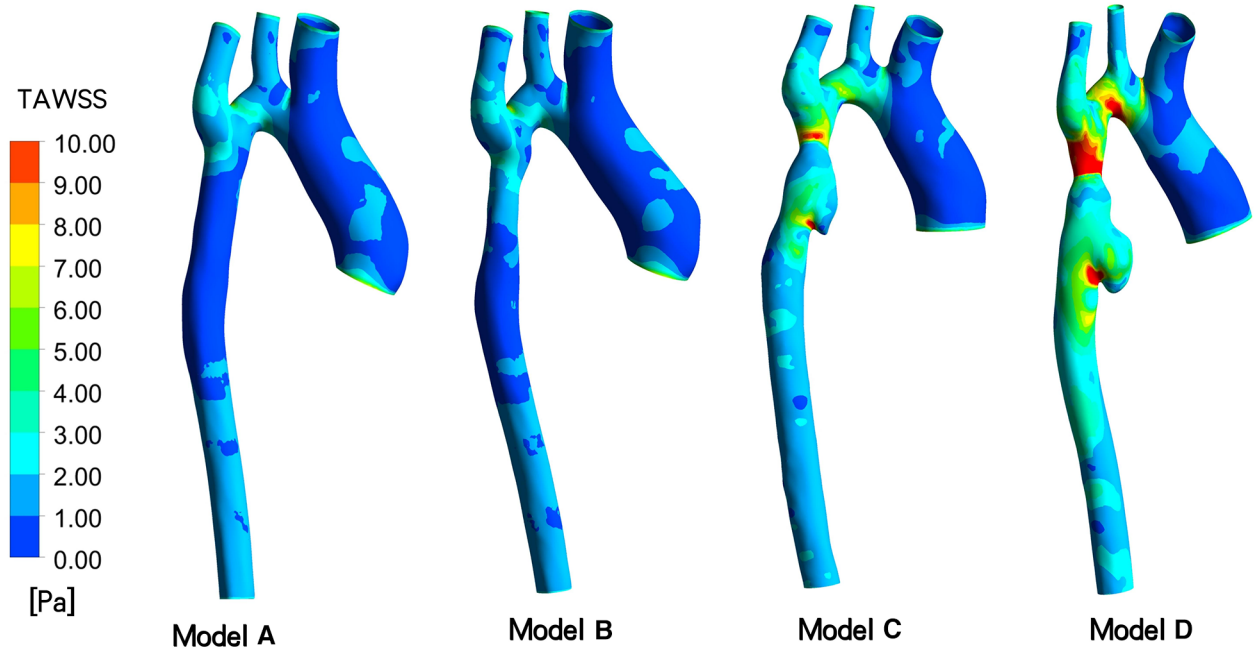

FIGURE 4
Depicts time-averaged wall shear stress (TAWSS) contour of models A to D indicated in different follow-up.

continue to dilate. Consequently, the OSI at the aneurysm gradually decreased. in model C, the OSI is primarily concentrated at 0.06–0.12, and in model D, it ranges from 0.00 to 0.09. The maximum inlet flow velocity occurs at t = 0.096 s during one cardiac cycle. The velocity distribution appears more uniform in model A and B, model C shows mild blood flow disturbance, and in model D, up to three instances of rotational flow are observed in this cross-section.

ECAP, which represents the ratio of two parameters, OSI and TAWSS, serves as an indicator for assessing the susceptibility to thrombosis in aneurysms (12). As depicted in Figure 6, the distribution of ECAP in the distal aneurysm region of the stent varies across the four models. Results from two postoperative follow-up visits reveal a gradual decrease in vascular wall ECAP in this area over time, with values lower than those observed during the initial intraoperative intervention and in the ideal stenosis-free model. Moreover, the ECAP value in all models is consistently below 1.4 Pa-1. Specifically, in the ideal model A, the ECAP is primarily concentrated in the range of 0.42 to 0.75 Pa^{-1}, while in model B, it ranges from 0.20 to 0.80 Pa^{-1}. Additionally, model C exhibits a focus on 0.05–0.35 Pa^{-1}, and model D is concentrated in the range of 0.00–0.15 Pa^{-1}.

Discussion

Coarctation of the aorta (CoA) is a prevalent congenital heart condition that prompts the development of robust collateral circulation in the descending aorta to ensure adequate blood supply to the lower limbs. Unlike typical patients with constricted arches, the distal end of the stenosis did not exhibit dilation due to the collateral blood supply. Consequently, the CP stent and BIB were chosen based on the diameter at the distal end of the stenosis to address this unique characteristic.

In large arterial vessels, the normal WSS typically falls within the range of 1–5 Pa (7). When this range is exceeded, the vessel's anti-inflammatory and anti-thrombotic responses can be altered. Particularly in cases of arterial stenosis, the vessels downstream of the stenosis may facilitate aneurysm dilation due to the elevated WSS (17, 18). A comprehensive evaluation of the risk of associated complications under various CoA stent implantation strategies necessitates careful consideration of hemodynamic alterations. Given that aneurysm dilation, rupture, and thrombosis are attributed to the collective hemodynamic effects occurring throughout the cardiac cycle, it is essential to concurrently assess multiple parameters such as TAWSS, OSI, and ECAP for comprehensive risk evaluation (19–22).

In the specific case under consideration, as observed in the DSA image, the second balloon expansion resulted in the stent becoming shorter and wider, during the shortening process, it is prone to causing damage to the intima. The results presented in Table 1 and Figure 4 illustrate the evolving regional morphology and local TAWSS of the aneurysms over time. The aneurysm exhibited slight dilation in the short axis direction and significant growth in the long axis direction. This phenomenon can be attributed to the low TAWSS of the vessel wall in the long axis direction of the aneurysm at 3 days post-surgery (Model C), while the TAWSS at this location in Model D returned to the normal range at 18 months post-surgery. This discrepancy led to rapid expansion of the aneurysm in the long axis direction in the early stage, potentially resulting in relative stability in the long

10.3389/fcvm.2024.1363230

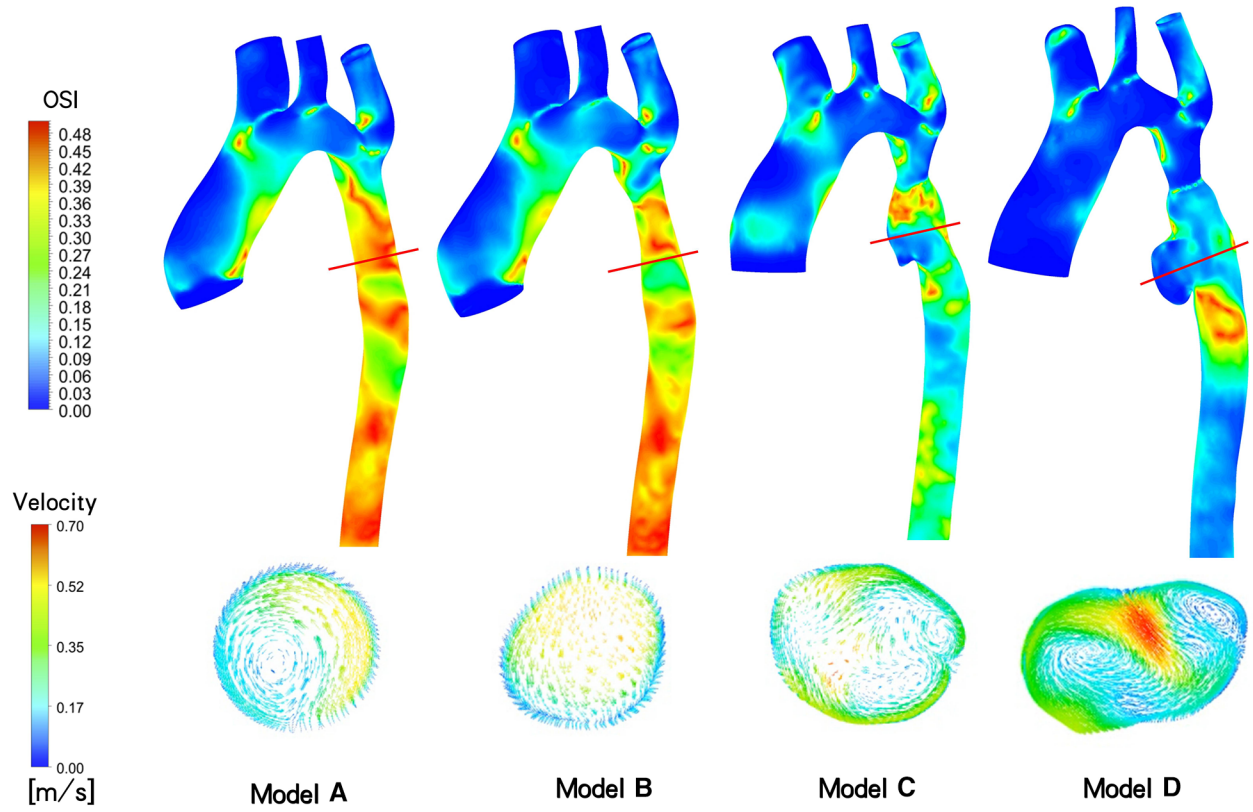

FIGURE 5
Aortic Oscillatory Shear Index (OSI) contour and cross-sectional velocity vectors at the site of aneurysm generation of maximum flow rate at different follow-up time (t = 0.096s).

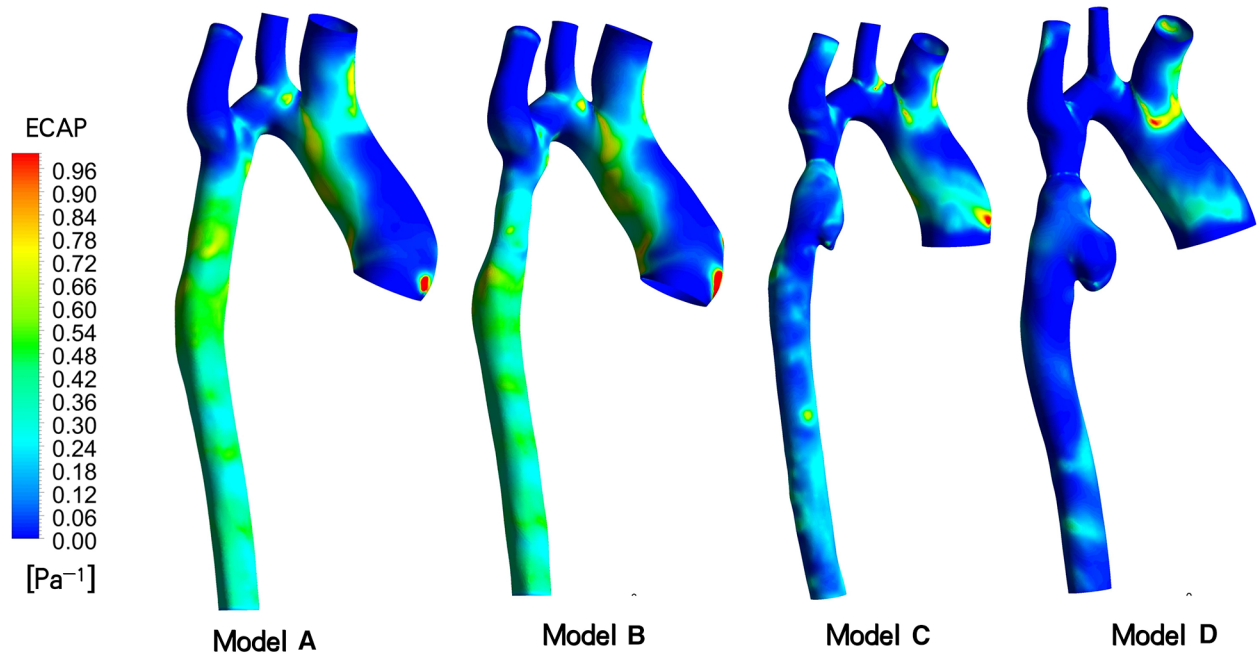

FIGURE 6
Endothelial cell activation potential (ECAP) contour models A to D indicated different follow-up time.

term. In contrast, the TAWSS of the artery wall in the short axis direction of the aneurysm only marginally increased at 18 months post-surgery, contributing to the gradual expansion of the aneurysm in the short axis direction (23–25).

Several studies have indicated a correlation between localized aneurysm dilation and the rapid growth of intraluminal thrombus within the aneurysm (26). As depicted in Figure 5, aneurysms developed in the narrow distal blood vessels following overexpansion of the CP stent, with the OSI in this area significantly lower than that of model B, which underwent incomplete initial dilation. Multiple eddy currents were observed in the aneurysm region, potentially contributing to the low OSI. Subsequent imaging revealed no thrombosis in the patient's aneurysm region. However, while numerous studies suggest a noteworthy negative correlation between intravascular OSI and thrombus aggregation in aneurysms, indicating that low OSI regions may promote thrombosis (27, 28), other studies argue that the relationship between intra-aneurysm OSI and thrombus deposition cannot be solely determined based on OSI (29). Consequently, it is challenging to employ OSI and eddy currents conjointly to evaluate aneurysm thrombosis in this case.

Considering the prevailing viewpoint that TAWSS and OSI collectively contribute to thrombosis formation, we introduce the related parameter ECAP for analysis. Generally, an ECAP value exceeding 1.4Pa-1 is indicative of a high probability of thrombosis. Simulation results for this patient indicate that the ECAP value in the distal vascular region of these stent models remains below this critical threshold, irrespective of the initial incomplete stent dilation or subsequent excessive dilation. Consequently, we posit that the risk of thrombosis in aneurysms is low. The factors contributing to rapid aneurysm dilation demonstrate limited correlation with thrombus formation.

Study limitations

The present study utilized a simplified shell unit model and conducted a pure fluid analysis without considering the vessel wall thickness and its elastic structure beyond the point of coated stent implantation. Notably, the vessel wall typically comprises three layers - endothelium, midthelium, and ectothelium - each with unique properties. Furthermore, the patient's endothelium experienced minor rupturing during surgery, giving rise to a medically originated pseudoaneurysm with distinct vascular properties compared to other segments of the vessel wall. There is potential for predicting the growth rate and morphology of pseudoaneurysms through fluid-solid coupling (30, 31). Additionally, we implemented standardized boundary conditions to alleviate the impact of these variables, allowing for a more focused comparison of hemodynamic differences within the lesion area. However, this approach may introduce some bias in interpreting the results. Specifically, despite the thick side branch of the descending aorta distal to the stenosis of the aortic arch, which contributes to lower limb blood flow. Upon removal of these collateral vessels, blood flow and WSS in the abdominal aorta at and below this location will decrease, leading to a reduction in intracranial eddy currents to some extent. However, given the focus of this paper, the alteration in the hemodynamic environment of the thoracic aorta will not be addressed. For patients with extremely severe CoA, the blood supply to the descending aorta will no longer primarily rely on collateral vessels post-stenting. Consequently, based on the postoperative reexamination images of the patients, the collateral vessels also adaptively diminish in size, thereby reducing their original blood supply function. Hence, it is reasonable to disregard the influence of collateral vessels on the hemodynamic environment of aneurysms in the simplified model presented in this paper.

Conclusions

Our model demonstrated that after the initial moderate stent expansion, the hemodynamic parameters of Model B were very close to those of the idealized normal Model A, suggesting a low risk of serious complications following the procedure. In contrast, when the diameter of both ends of the CP stent significantly exceeded that of the descending aorta due to overexpansion, the resulting asymmetric aneurysm exhibited low TAWSS and ECAP in the distal vascular wall. This scenario would likely promote the rapid expansion and growth of pseudoaneurysms in the early stage. Notably, the distribution range of TAWSS along the vascular wall provides important guidance for predicting the potential for aneurysm expansion.

Data availability statement

The original contributions presented in the study are included in the article/Supplementary Material, further inquiries can be directed to the corresponding author.

Ethics statement

The studies involving humans were approved by Xijing Hospital (approval number: KY-20192138-C-1). The studies were conducted in accordance with the local legislation and institutional requirements. Written informed consent for participation was not required from the participants or the participants' legal guardians/next of kin in accordance with the national legislation and institutional requirements. Written informed consent was obtained from the individual(s) for the publication of any potentially identifiable images or data included in this article.

Author contributions

LL: Conceptualization, Methodology, Writing – original draft. YW: Conceptualization, Data curation, Investigation, Writing – review & editing. PJ: Conceptualization, Data curation, Supervision, Writing – review & editing. TY: Data curation,

Formal Analysis, Resources, Writing – review & editing. GZ: Conceptualization, Data curation, Investigation, Software, Supervision, Writing – review & editing. YuL: Data curation, Formal Analysis, Methodology, Supervision, Writing – review & editing. JT: Investigation, Supervision, Visualization, Writing – review & editing. YaL: Data curation, Funding acquisition, Investigation, Validation, Visualization, Writing – review & editing. JY: Conceptualization, Funding acquisition, Supervision, Validation, Writing – review & editing.

Funding

The author(s) declare financial support was received for the research, authorship, and/or publication of this article.

This work was supported by the Development and Transformation of New Technology and Construction of Precision Diagnosis and Treatment System for Transcatheter Interventional Diagnosis and Treatment of Structural Heart Diseases (2022YFC2503400); Research on Key Techniques of Minimally Invasive Treatment for Valvular Heart Diseases (2023-YBSF-105); National Key Research and Development Programs (2022YFC2503402); National Natural Science Foundation of China (82370375, 82270526)

Conflict of interest

The authors declare that the research was conducted in the absence of any commercial or financial relationships that could be construed as a potential conflict of interest.

Publisher's note

All claims expressed in this article are solely those of the authors and do not necessarily represent those of their affiliated organizations, or those of the publisher, the editors and the reviewers. Any product that may be evaluated in this article, or claim that may be made by its manufacturer, is not guaranteed or endorsed by the publisher.

References

1. O'Brien P, Marshall AC. Coarctation of the aorta. *Circulation*. (2015) 131 (9):363–5. doi: 10.1161/CIRCULATIONAHA.114.008821

2. Sadeghipour P, Mohebbi B, Firouzi A, Khajali Z, Saedi S, Shafe O, et al. Balloon-Expandable cheatham-platinum stents versus self-expandable nitinol stents in coarctation of aorta: a randomized controlled trial. *JACC Cardiovasc Interv*. (2022) 15(3):308–17. doi: 10.1016/j.jcin.2021.11.025

3. Stout KK, Daniels CJ, Aboulhosn JA, Bozkurt B, Broberg CS, Colman JM, et al. 2018 AHA/ACC guideline for the management of adults with congenital heart disease: a report of the American College of Cardiology/American Heart Association Task Force on clinical practice guidelines. *J Am Coll Cardiol*. (2019) 73(12):e81–e192. doi: 10.1016/j.jacc.2018.08.1029

4. Alvarez-Fuente M, Ayala A, Garrido-Lestache E, Bermudez-Cañete R, Garcia-De Vicente A, Toledano M, et al. Long-term complications after aortic coarctation stenting. *J Am Coll Cardiol*. (2021) 77(19):2448–50. doi: 10.1016/j.jacc.2021.03.303

5. Brown ML, Burkhart HM, Connolly HM, Dearani JA, Hagler DJ, Schaff HV. Late outcomes of reintervention on the descending aorta after repair of aortic coarctation. *Circulation*. (2010) 122(11 Suppl):S81–S4. doi: 10.1161/CIRCULATIONAHA.109.925172

6. Staarmann B, Smith M, Prestigiacomo CJ. Shear stress and aneurysms: a review. *Neurosurg Focus*. (2019) 47(1):E2. doi: 10.3171/2019.4.FOCUS19225

7. Ene-Iordache B, Remuzzi A. Disturbed flow in radial-cephalic arteriovenous fistulae for haemodialysis: low and oscillating shear stress locates the sites of stenosis. *Nephrol Dial Transpl*. (2012) 27(1):358–68. doi: 10.1093/ndt/gfr342

8. Rezaeitaleshmahalleh M, Lyu Z, Mu N, Zhang X, Rasmussen TE, McBane RD, et al. Characterization of small abdominal aortic aneurysms' growth status using spatial pattern analysis of aneurismal hemodynamics. *Sci Rep*. (2023) 13(1):13832. doi: 10.1038/s41598-023-40139-z

9. Qiao Y, Mao L, Wang Y, Luan J, Chen Y, Zhu T, et al. Hemodynamic effects of stent-graft introducer sheath during thoracic endovascular aortic repair. *Biomech Model Mechanobiol*. (2022) 21(2):419–31. doi: 10.1007/s10237-021-01542-5

10. Al-Rawi M, Al-Jumaily AM, Belkacemi D. Non-invasive diagnostics of blockage growth in the descending aorta-computational approach. *Med Biol Eng Comput*. (2022) 60(11):3265–79. doi: 10.1007/s11517-022-02665-2

11. Aristokleous N, Kontopodis NG, Tzirakis K, Ioannou CV, Papaharilaou Y. Hemodynamic impact of abdominal aortic aneurysm stent-graft implantation-induced stenosis. *Med Biol Eng Comput*. (2016) 54(10):1523–32. doi: 10.1007/s11517-015-1425-1

12. Di Achille P, Tellides G, Figueroa C, et al. A haemodynamic predictor of intraluminal thrombus formation in abdominal aortic aneurysms. *Proc R Soc A Math Phys Eng Sci*. (2014) 470(2172):20140163. doi: 10.1016/j.clinbiochem.2012.04.020

13. Dai Y, Qian Y, Zhang M, Li Y, Lv P, Tang X, et al. Associations between local haemodynamics and carotid intraplaque haemorrhage with different stenosis severities: a preliminary study based on MRI and CFD. *J Clin Neurosci*. (2019) 66:220–5. doi: 10.1016/j.jocn.2019.05.041

14. Zhang M, Liu J, Zhang H, Verrelli DI, Wang Q, Hu L, et al. CTA-based non-invasive estimation of pressure gradients across a CoA: a validation against cardiac catheterisation. *J Cardiovasc Transl*. (2021) 14(5):873–82. doi: 10.1007/s12265-020-10092-7

15. Kelsey LJ, Powell JT, Norman PE, Miller K, Doyle BJ. A comparison of hemodynamic metrics and intraluminal thrombus burden in a common iliac artery aneurysm. *Int J Numer Meth Bio*. (2016) 33(5). doi: 10.1002/cnm.2821

16. Martufi G, Forneris A, Appoo JJ, Di Martino ES. Is there a role for biomechanical engineering in helping to elucidate the risk profile of the thoracic aorta? *Ann Thorac Surg*. (2016) 101(1):390–8. doi: 10.1016/j.athoracsur.2015.07.028

17. Lu Z, Li S, Tang H, Zhu S, Liu P, Lv N, et al. Effect of proximal parent artery stenosis on the outcomes of posterior communicating artery aneurysms: a preliminary study based on case-specific hemodynamic analysis. *World Neurosurg*. (2022) 164:e349–57. doi: 10.1016/j.wneu.2022.04.101

18. Kono K, Fujimoto T, Terada T. Proximal stenosis may induce initiation of cerebral aneurysms by increasing wall shear stress and wall shear stress gradient. *Int J Numer Meth Bio*. (2014) 30(10):942–50. doi: 10.1002/cnm.2637

19. Mutlu O, Salman HE, Al-Thani H, El-Menyar A, Qidwai UA, Yalcin HC. How does hemodynamics affect rupture tissue mechanics in abdominal aortic aneurysm: focus on wall shear stress derived parameters, time-averaged wall shear stress, oscillatory shear index, endothelial cell activation potential, and relative residence time. *Comput Biol Med*. (2023) 154:106609. doi: 10.1016/j.compbiomed.2023.106609

20. Cebull HL, Rayz VL, Goergen CJ. Recent advances in biomechanical characterization of thoracic aortic aneurysms. *Front Cardiovasc Med*. (2020) 7:75. doi: 10.3389/fcvm.2020.00075

21. Gao JP, Guo W. Mechanisms of abdominal aortic aneurysm progression: a review. *Vasc Med*. (2022) 27(1):88–96. doi: 10.1177/1358863X211021170

22. Boyd AJ, Kuhn DC, Lozowy RJ, Kulbisky GP. Low wall shear stress predominates at sites of abdominal aortic aneurysm rupture. *J Vasc Surg*. (2016) 63 (6):1613–9. doi: 10.1016/j.jvs.2015.01.040

23. Boyd AJ, Kuhn DC, Lozowy RJ, Kulbisky GP. High WSS or low WSS? Complex interactions of hemodynamics with intracranial aneurysm initiation, growth, and rupture: toward a unifying hypothesis. *AJNR Am J Neuroradiol*. (2014) 35(7):1254–62. doi: 10.3174/ajnr.A3558

24. Dolan JM, Kolega J, Meng H. High wall shear stress and spatial gradients in vascular pathology: a review. *Ann Biomed Eng*. (2013) 41(7):1411–27. doi: 10.1007/s10439-012-0695-0

25. Zambrano BA, Gharahi H, Lim C, Jaberi FA, Choi J, Lee W, et al. Association of intraluminal thrombus, hemodynamic forces, and abdominal aortic aneurysm expansion using longitudinal CT images. *Ann Biomed Eng*. (2016) 44(5):1502–14. doi: 10.1007/s10439-015-1461-x

26. Metaxa E, Kontopodis N, Tzirakis K, Ioannou CV, Papaharilaou Y. Effect of intraluminal thrombus asymmetrical deposition on abdominal aortic aneurysm growth rate. *J Endovasc Ther*. (2015) 22(3):406–12. doi: 10.1177/1526602815584018

27. Arzani A, Suh GY, Dalman RL, Shadden SC. A longitudinal comparison of hemodynamics and intraluminal thrombus deposition in abdominal aortic aneurysms. *Am J Physiol Heart Circ Physiol*. (2014) 307(12):H1786–95. doi: 10.1152/ajpheart.00461.201428

28. Qiu Y, Wang Y, Fan Y, Peng L, Liu R, Zhao J, et al. Role of intraluminal thrombus in abdominal aortic aneurysm ruptures: a hemodynamic point of view. *Med Phys*. (2019) 46(9):4263–75. doi: 10.1002/mp.13658

29. Lozowy RJ, Kuhn DC, Ducas AA, Boyd AJ. The relationship between pulsatile flow impingement and intraluminal thrombus deposition in abdominal aortic aneurysms. *Cardiovasc Eng Technol*. (2016) 8(1):57–69. doi: 10.1007/s13239-016-0287-5

30. Sheidaei A, Hunley SC, Zeinali-Davarani S, Raguin LG, Baek S. Simulation of abdominal aortic aneurysm growth with updating hemodynamic loads using a realistic geometry. *Med Eng Phys*. (2011) 33(1):80–8. doi: 10.1016/j.medengphy.2010.09.012

31. Geng J, Wang Y, Ji Z, Wang W, Yin Y, Yang G, et al. Advantages of 3D registration technology (3DRT) in clinical application of unruptured intracranial aneurysm follow-up: a novel method to judge aneurysm growth. *J Neuroradiol*. (2023) 50(2):209–16. doi: 10.1016/j.neurad.2022.08.004

frontiers | Frontiers in Cardiovascular Medicine

TYPE Original Research
PUBLISHED 23 August 2024
DOI 10.3389/fcvm.2024.1384977

Check for updates

OPEN ACCESS

EDITED BY
Hitomi Anzai,
Tohoku University, Japan

REVIEWED BY
Eugenio Vocaturo,
National Research Council (CNR), Italy
Chang Won Jeong,
Wonkwang University, Republic of Korea
Nikolaos Papandrianos,
University of Thessaly, Greece

*CORRESPONDENCE
Feng Li
✉ 1575054688@qq.com
Jing Guan
✉ guanjingishere@126.com

†These authors have contributed equally to this work and share first authorship

RECEIVED 11 February 2024
ACCEPTED 07 August 2024
PUBLISHED 23 August 2024

CITATION
Duan M, Mao B, Li Z, Wang C, Hu Z, Guan J and Li F (2024) Feasibility of tongue image detection for coronary artery disease: based on deep learning.
Front. Cardiovasc. Med. 11:1384977.
doi: 10.3389/fcvm.2024.1384977

COPYRIGHT
© 2024 Duan, Mao, Li, Wang, Hu, Guan and Li. This is an open-access article distributed under the terms of the Creative Commons Attribution License (CC BY). The use, distribution or reproduction in other forums is permitted, provided the original author(s) and the copyright owner(s) are credited and that the original publication in this journal is cited, in accordance with accepted academic practice. No use, distribution or reproduction is permitted which does not comply with these terms.

Feasibility of tongue image detection for coronary artery disease: based on deep learning

Mengyao Duan[1†], Boyan Mao[2†], Zijian Li[1], Chuhao Wang[2], Zhixi Hu[3], Jing Guan[1*] and Feng Li[1*]

[1]School of Traditional Chinese Medicine, Beijing University of Chinese Medicine, Beijing, China, [2]School of Life Science, Beijing University of Chinese Medicine, Beijing, China, [3]School of Traditional Chinese Medicine, Hunan University of Chinese Medicine, Changsha, China

Aim: Clarify the potential diagnostic value of tongue images for coronary artery disease (CAD), develop a CAD diagnostic model that enhances performance by incorporating tongue image inputs, and provide more reliable evidence for the clinical diagnosis of CAD, offering new biological characterization evidence.
Methods: We recruited 684 patients from four hospitals in China for a cross-sectional study, collecting their baseline information and standardized tongue images to train and validate our CAD diagnostic algorithm. We used DeepLabV3 + for segmentation of the tongue body and employed Resnet-18, pretrained on ImageNet, to extract features from the tongue images. We applied DT (Decision Trees), RF (Random Forest), LR (Logistic Regression), SVM (Support Vector Machine), and XGBoost models, developing CAD diagnostic models with inputs of risk factors alone and then with the additional inclusion of tongue image features. We compared the diagnostic performance of different algorithms using accuracy, precision, recall, F1-score, AUPR, and AUC.
Results: We classified patients with CAD using tongue images and found that this classification criterion was effective (ACC = 0.670, AUC = 0.690, Recall = 0.666). After comparing algorithms such as Decision Tree (DT), Random Forest (RF), Logistic Regression (LR), Support Vector Machine (SVM), and XGBoost, we ultimately chose XGBoost to develop the CAD diagnosis algorithm. The performance of the CAD diagnosis algorithm developed solely based on risk factors was ACC = 0.730, Precision = 0.811, AUC = 0.763. When tongue features were integrated, the performance of the CAD diagnosis algorithm improved to ACC = 0.760, Precision = 0.773, AUC = 0.786, Recall = 0.850, indicating an enhancement in performance.
Conclusion: The use of tongue images in the diagnosis of CAD is feasible, and the inclusion of these features can enhance the performance of existing CAD diagnosis algorithms. We have customized this novel CAD diagnosis algorithm, which offers the advantages of being noninvasive, simple, and cost-effective. It is suitable for large-scale screening of CAD among hypertensive populations. Tongue image features may emerge as potential biomarkers and new risk indicators for CAD.

KEYWORDS

coronary artery disease, deep learning, hypertension, tongue image, early diagnosis

1 Introduction

The World Health Organization (WHO) has declared that cardiovascular disease (CVD), particularly coronary artery disease (CAD), is the leading cause of death due to illness globally, accounting for 17.9 million fatalities per year, representing 32% of all deaths caused by disease (1). This significant public health challenge places a significant

financial burden on national health budgets (2). Hypertension is an important independent risk factor for the development of CAD (3). Relevant studies have shown that patients with hypertension have a higher risk of developing CAD, and when the two diseases coexist, there is a significant increase in the risk of cardiovascular death (4, 5). Early diagnosis and prompt treatment of patients with CAD have been shown to significantly improve outcomes and reduce treatment costs (3). However, the gold standard for diagnosing CAD is invasive coronary angiography, which is expensive and can cause complications (6). It is not suitable for early diagnosis and disease risk assessment. Finding non-invasive, cost-effective and efficient methods for early CAD diagnosis is crucial in global public health.

The rapid development of artificial intelligence in recent years has provided new insights into the exploration of non-invasive diagnostic methods for CAD. Clinical data exhibit complex and multidimensional characteristics, in which machine learning (ML) demonstrates advantages over traditional statistical methods (7). ML involves the selection and integration of multiple models. When confronted with the complex nonlinear relationships in clinical data, traditional statistical methods often struggle to accomplish modeling tasks. However, ML algorithms can automatically learn to handle nonlinear relationships and select useful predictive features. These algorithms can more effectively reveal hidden relationships within data and has been increasingly utilized for the diagnosis and risk prediction of clinical diseases.

Some scholars have already utilized ML to develop diagnostic models for CAD, with the predictive variables primarily being clinical risk factors (8–10). These studies demonstrate the promising application prospects of ML in clinical diagnostic tasks. Recent research has found that, in addition to risk factors, other biological information may also hold significant importance for the diagnosis of CAD, such as facial images and pulse waves (11, 12). In clinical diagnosis, the primary focus is on the patient's symptoms and signs.Traditional Chinese Medicine (TCM) employs unique and effective diagnostic strategies, particularly in observing the external conditions of patients. TCM theory posits that "internal diseases manifest externally," thereby allowing practitioners to gauge the severity of illnesses through observation. Tongue diagnosis is a critical component of the TCM observation process. The appearance of the tongue, including its color, shape, and coating, has long been utilized in TCM to diagnose various health conditions. From a biomedical perspective, the tongue is a highly vascular organ closely related to the cardiovascular system. Changes in blood circulation and overall systemic health often manifest as observable alterations in the tongue's appearance. Many studies have proven the effectiveness of diagnosing diseases through tongue observation (references 14–27), and we have compiled these studies into Table 1 and provided commentary on each. From a biomedical standpoint, the tongue contains rich physiological and pathological information. It is an important terminal organ with abundant blood supply, closely linked to the cardiovascular system. When there are issues with blood circulation, the tongue's appearance often changes (27, 28). Biomedical research suggests that hypoxemia can lead to changes in tongue color and is associated with various cardiovascular diseases (29). In the case of CHD, the narrowing of the coronary arteries restricts blood flow to the heart, potentially causing systemic changes in overall circulation and oxygenation levels, which manifest on the tongue. Despite this, the tongue has not been effectively utilized in the actual diagnosis process of CAD. Recent advancements in artificial intelligence and deep learning have made it possible to extract and analyze subtle features from medical images, including tongue images, which were previously difficult to quantify. By leveraging these technologies, it is possible to detect patterns and features in tongue images associated with CAD, providing a non-invasive, cost-effective, and accessible diagnostic tool. Therefore, what exactly is the diagnostic value of the tongue for CAD? Can tongue images become a crucial basis for optimizing non-invasive diagnosis of CAD? This is precisely the question this study aims to explore.

To this end, we conducted a multi-center cross-sectional clinical study, utilizing deep learning methods to explore the potential connection between tongue image features and CAD. Additionally, we aimed to investigate the feasibility of optimizing CAD diagnostic models by incorporating tongue image features as risk factors. Meanwhile, we also hope to present a new and effective biomarker for the clinical diagnosis of CAD.

2 Materials and methods

2.1 Study population and ethical statement

From March 2019 to November 2022, hypertensive patients aged 18–85 were recruited from the cardiology departments of Dongzhimen Hospital, Dongfang Hospital, the Third Affiliated Hospital of Beijing University of Chinese Medicine, and the First Affiliated Hospital of Hunan University of Chinese Medicine. All participants signed an informed consent form, and the study was conducted in accordance with the Declaration of Helsinki. The ethical review of this study was carried out and approved by the Institutional Review Board (IRB) of Shuguang Hospital affiliated with Shanghai University of Traditional Chinese Medicine (IRB number: 2018-626-55-01), with the clinical trial registration number ChiCTR1900026008. All source codes and data analyzed in this study can be obtained from the corresponding author upon reasonable request.

The diagnostic criteria for hypertension refer to the "Chinese Guidelines for the Prevention and Treatment of Hypertension," which define hypertension as a systolic blood pressure ≥140 mmHg or diastolic blood pressure ≥90 mmHg, or currently undergoing treatment with antihypertensive medication (30). The diagnosis of CAD is based on the patient's CAG results, that is, a narrowing of the inner diameter of at least one of the coronary arteries (left anterior descending, left circumflex, right coronary artery, or left main) by ≥50%. Initially, 684 patients were recruited, with the following exclusion criteria: (1) patients whose tongue appearance was altered by medications or food, (2) no definitive diagnosis related to CAD, prior percutaneous coronary intervention (PCI) or coronary artery bypass grafting (CABG); (3) those with a severe

TABLE 1 Research on tongue image-assisted disease diagnosis in the past 3 years.

Study name	Year	Authors	Main findings	Comments	Diagnosis method
Improvement in tongue color image analysis for disease identification using deep learning based depthwise separable (13)	2021	Rajakumaran S, Sasikala J	Deep learning-based depthwise separable method enhances disease identification through tongue color image analysis.	Novel method with potential applications, needs more research.	Deep Learning and Tongue Color Image Analysis
Application of computer tongue image analysis technology in the diagnosis of NAFLD (14)	2021	Jiang T, Guo X, Tu L, et al.	Computer tongue image analysis aids in non-invasive diagnosis of NAFLD.	Effective for NAFLD, could be adapted for heart disease diagnosis.	Computer Tongue Image Analysis
Internet of things and synergic deep learning based biomedical tongue color image analysis for disease diagnosis and classification (15)	2021	Mansour RF, Althobaiti MM, Ashour AA	IoT and synergic deep learning based tongue color image analysis improves disease diagnosis.	Combines IoT and deep learning for enhanced	Using IoT and synergistic deep learning for tongue image analysis
Establishment of noninvasive diabetes risk prediction model based on tongue features and machine learning techniques (16)	2021	Li J, Chen Q, Hu X, Yuan P, et al.	Noninvasive risk prediction model for diabetes based on tongue features and ML techniques.	Promising noninvasive risk prediction.	Noninvasive Risk Prediction Model based on tongue image
Intelligent deep learning based disease diagnosis using biomedical tongue images (17)	2022	Thanikachalam V, Shanthi S, Kalirajan K,et al	Deep learning-based analysis of biomedical tongue images aids in the diagnosis of multiple diseases including coronary heart disease.	Promising results but requires large-scale validation.	Deep Learning and Biomedical Tongue Images
Deep Learning Multi-label Tongue Image Analysis and Its Application in a Population Undergoing Routine Medical Checkup (18)	2022	Jiang T, Lu Z, Hu X,et al	Deep learning multi-label tongue image analysis is effective for routine medical checkups.	Tongue images based on deep learning can assist in medical examinations.	Multilabel tongue images processed based on deep learning
A multi-step approach for tongue image classification in patients with diabetes (19)	2022	Li J, Huang J, Jiang T, et al	Multi-step approach enhances tongue image classification for diabetes patients.	Effective for patient-specific diagnosis.	Multi-Step Classification Approach based on tongue image
Simulated Annealing with Deep Learning Based Tongue Image Analysis for Heart Disease Diagnosis (20)	2023	Sivasubramaniam S, Balamurugan SP	Tongue image analysis using deep learning and simulated annealing improves heart disease diagnosis.	Effective but needs further clinical validation.	Tongue Image Analysis and Deep Learning
Multiple color representation and fusion for diabetes mellitus diagnosis based on back tongue images (21)	2023	Zhang N, Jiang Z, Li JX, et al	Multiple color representation and fusion improve diabetes diagnosis based on tongue images.	Enhanced diabetes diagnosis with feature fusion.	Multicolor representation and fusion methods for processing tongue images
Development of a tongue image-based machine learning tool for the diagnosis of gastric cancer: a prospective multicentre clinical cohort study (22)	2023	Yuan L, Yang L, Zhang S, Xu Z, et al.	Tongue image-based machine learning tool developed for gastric cancer diagnosis in a multicentre clinical cohort study.	Validated in multi-center studies, this method shows potential for application to other diseases.	Tongue Image-Based Machine Learning Tool
Reliability of non-contact tongue diagnosis for Sjögren's syndrome using machine learning method (23)	2023	Noguchi K, Saito I, Namiki T, Yoshimura Y, et al.	Non-contact tongue diagnosis for Sjögren's syndrome is reliable using machine learning.	Tongue images can be used for contactless diagnosis of Sjögren's syndrome.	Tongue Diagnosis and machine learning
A lung cancer risk warning model based on tongue images (24)	2023	Shi Y, Guo D, Chun Y, et al.	Tongue image analysis can provide early warning for lung cancer risk.	Promising for early detection and risk assessment.	Tongue Image Analysis and Machine Learning
Application of intelligent tongue image analysis in Conjunction with microbiomes in the diagnosis of MAFLD (25)	2024	Dai S, Guo X, Liu S, et al.	Intelligent tongue image analysis combined with microbiome data improves diagnosis of MAFLD.	The potential of using the tongue for disease diagnosis based on deep learning has been demonstrated.	Intelligent Tongue Image Analysis and Microbiomes
Machine learning aided non-invasive diagnosis of coronary heart disease based on tongue features fusion (26)	2024	Duan M, Zhang Y, Liu Y, et al.	Tongue features fusion with machine learning aids non-invasive coronary heart disease diagnosis.	Feature fusion method improves diagnosis accuracy.	Tongue Features Fusion and Machine Learning

10.3389/fcvm.2024.1384977

lack of relevant clinical pathophysiological information; (4) those with poor quality tongue images.

2.2 Data collection

Trained research physicians conducted interviews and took tongue photographs of participants following a standardized collection process. The interviews gathered baseline data on general conditions, socioeconomic status, lifestyle (alcohol consumption, smoking, insomnia), and clinical manifestations. Tongue photographs were collected using a TFDA-1 tongue diagnosis instrument (Figure 1), two hours after breakfast or lunch. The specific steps for image collection are as follows: (1) Power on the Instrument after inspection and adjust the camera parameters. (2) Disinfect the areas of the instrument that may come into direct contact with the participant using 75% alcohol. (3) Instruct the patient to place their face on the chin rest, relax, and stick out their tongue flatly. (4) Turn on the built-in ring light source and complete the image capture. (5) Check the photo; if it is satisfactory, the collection is complete; if not, retake the photo until the image quality meets the standard. Qualification criteria for photo quality: no problems such as occlusion, blurring, fogging, overexposure, or underexposure; the tongue should be relaxed and flattened with no twisting or tension; there should be no foreign objects, staining, or other conditions affecting the appearance of the tongue surface.

2.3 Data preprocessing

Patients were divided into two groups based on whether they were diagnosed with CAD: the hypertension group and the

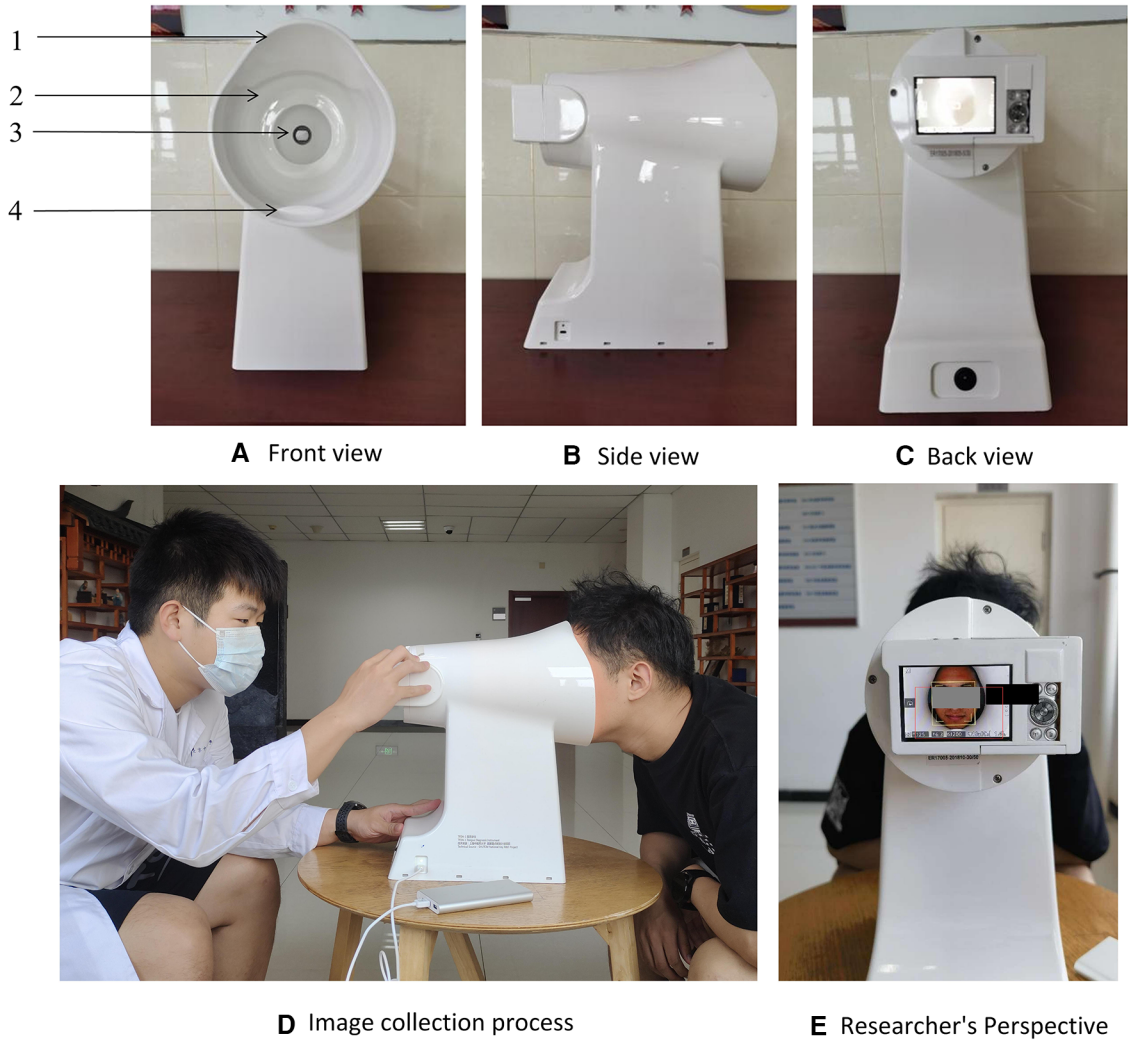

FIGURE 1
The tongue diagnosis instrument and collection process. 1: lens hood, 2: LED light resource, 3: high-definition camera, 4: chin support plate. Note. Use fixed standard camera parameters when shooting: the color temperature is 5,000 k, the color rendering index is 97, the frame rate is 1/125 s, the aperture is F/6.3, the exposure indicator scale is 0 or ±1. **(A)** Front view of the device; **(B)** Side view of the device; **(C)** Rear view of the device; **(D)** Schematic of the image acquisition process; **(E)** Perspective of the operator.

hypertension combined with CAD group, with the labels recorded as 0 and 1, respectively.

Considering that tongue images also contain other facial information, which is superfluous for this study, we built a deep learning model for semantic segmentation of the tongue body using the DeepLabV3 + framework (Figure 2A). We used 500 images from a national key research and development program tongue image database for model training, implementing a phased training strategy. In the first 50 epochs of training (Figure 2B), the backbone of the model was frozen to focus on fine-tuning the tail end of the network, with a batch size set to 8. Subsequently, in the unfreezing phase, all network layers were involved in training, with the batch size adjusted to 4 and the learning rate set to 0.01. After completing the segmentation of the tongue body, the image size was uniformly cropped and adjusted to 256×256 pixels (Figure 2C). Additionally, due to our overall small sample size, data augmentation was performed on the images through rotation, flipping, and translation.

For the baseline data of patients obtained through interviews, there was only a minimal amount of missing data (less than 5% missing). Various interpolation methods were used to fill in the missing data. For discrete variables in the baseline data, such as gender and ethnicity, one-hot encoding was employed for data preprocessing.

2.4 Development of a CAD diagnostic algorithm

The customization of a CAD diagnostic algorithm primarily encompasses two core steps: the classification of images using deep learning frameworks, and the construction of diagnostic models utilizing common ML techniques. In this study, we utilized the ResNet-18 network (Figure 3A), pretrained on the ImageNet dataset, as the foundation for our deep learning architecture. As a deep residual network, ResNet-18 effectively mitigates the vanishing gradient problem encountered in training deep networks through residual learning, making it widely applicable in image recognition, especially in the field of medical image processing. It has demonstrated excellent performance in various tongue image processing tasks.

During the training process, we chose to freeze the first and second layers (layer1 and layer2) of the model, training only the parameters of the third and fourth layers (layer3 and layer4) along with the fully connected layer. This strategy not only helps prevent overfitting, which might arise due to the small size of the dataset, but also further enhances the model's ability to learn representations. Stochastic Gradient Descent (SGD) was employed as the optimizer, with cross-entropy loss function used as the loss function. Upon convergence, the output of the penultimate layer of the model forms a 512-dimensional deep

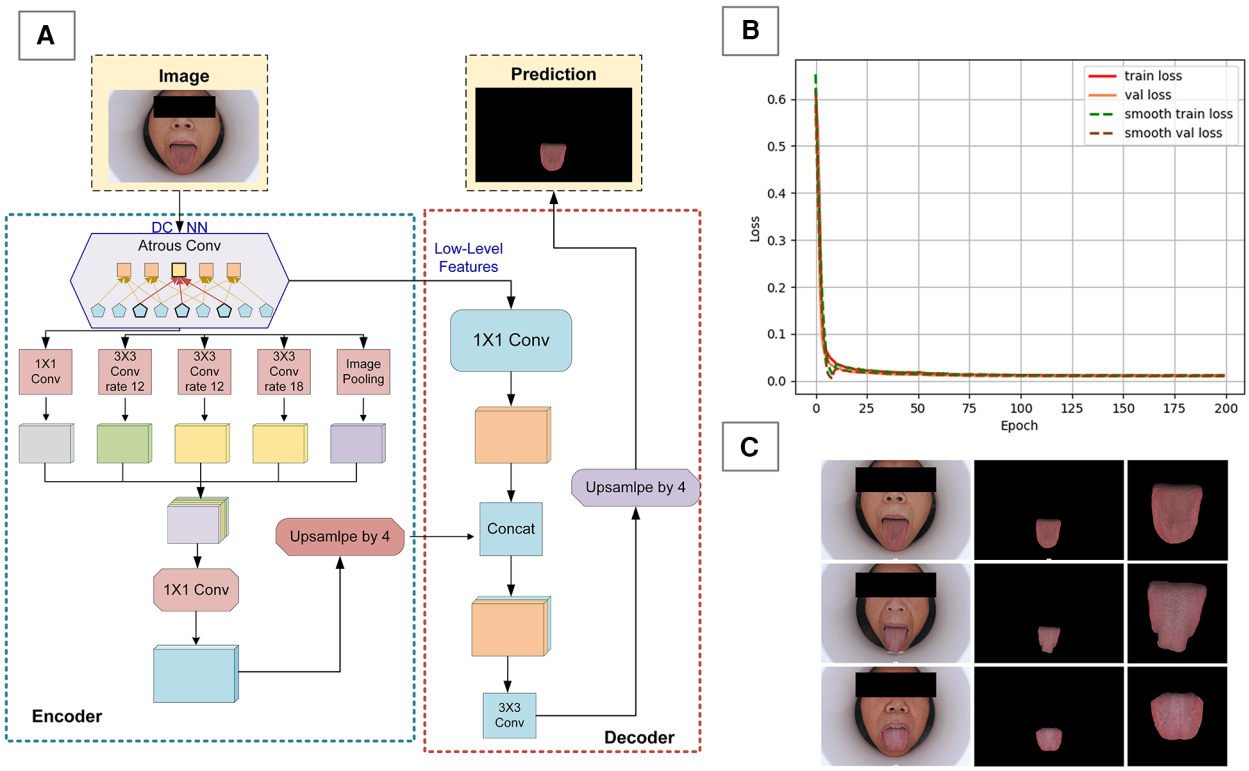

FIGURE 2
Data preprocessing for tongue images. (A) DeepLabV3 + framework diagram, (B) model training loss function graph, (C) preprocessing effect on tongue image.

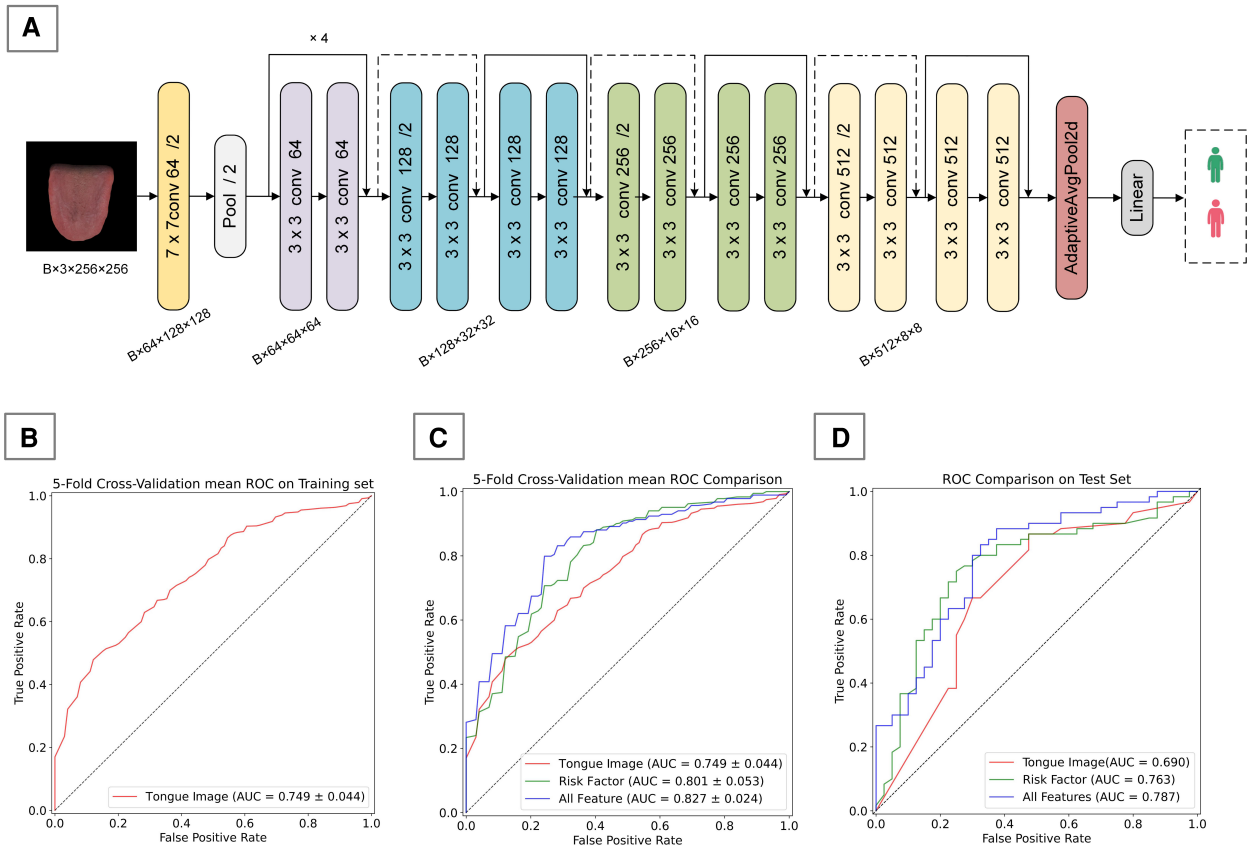

FIGURE 3
Tongue image-based CAD diagnostic algorithm. **(A)** ResNet-18 framework used in this study, **(B)** 5-fold cross-validation mean ROC on training set, **(C)** 5-fold cross-validation mean ROC Comparison on training set, **(D)** performance comparison of different feature inputs on the validation set.

feature vector, which is then linked to a binary classification output layer to produce probabilities.

After extracting the deep feature vectors, we constructed a CAD diagnostic model that integrates tongue image feature vectors with risk factors. To optimize the model's performance, we explored a variety of common ML algorithms, including Random Forest (RF), Support Vector Machine (SVM), Decision Trees (DT), Logistic Regression (LR), and XGBoost, all of which are widely used in disease classification and risk prediction. By comparing the performance of these algorithms, we will select the one with the best performance as the core algorithm for our final CAD diagnostic model.

2.5 Statistical analysis

Using SPSS 27 and Python 3.8 as statistical tools, we processed and analyzed the data. For data that followed a normal distribution, we employed descriptive statistics using $\bar{X} \pm SD$, along with one-way ANOVA to explore differences between groups. Before conducting the one-way ANOVA, we performed a homogeneity of variance test, such as Levene's test, to ensure that the variances across groups were roughly equal. For data not meeting the normal distribution criteria, we opted for quartile descriptions and employed the Kruskal–Wallis H test to compare differences between two groups. Additionally, we conducted an in-depth analysis of potential risk factors for CAD using binary logistic regression, presenting the results with adjusted odds ratios (adjusted OR) and their 95% confidence intervals (CI). Throughout the analysis, differences were considered statistically significant when the p-value < 0.05.

2.6 Performance evaluation standard

To evaluate the algorithm's performance, we calculated the Accuracy, Precision, Recall, F-1 Score, AUC (Area Under the Curve), and AUPR (Area Under the Precision-Recall Curve) (Equations 1–4) (31).

$$\text{Accuracy} = \frac{TP + TN}{TP + FN + FP + TN} \quad (1)$$

$$\text{Precision} = \frac{TP}{TP + FP} \quad (2)$$

$$\text{Recall} = \frac{TP}{TP + FN} \quad (3)$$

$$F1 = 2 \times \frac{\text{Precision} \times \text{Recall}}{\text{Precision} + \text{Recall}} \quad (4)$$

For binary classification problems, examples can be divided into four categories based on the combination of their true labels and the predictions made by the classifier: True Positives (TP), False Positives (FP), True Negatives (TN), and False Negatives (FN). In addition, we performed a 5-fold cross-validation on the training set to evaluate the model's effectiveness.

We evaluated the segmentation results of the DeepLabV3 + model using Pixel Accuracy (PA) and Mean Intersection over Union (MIoU) (Equations 5, 6). The formulas for calculating PA and MIoU are as follows, where k represents the number of categories excluding the background, and p_{ij} denotes the number of pixels of class i predicted to be class j (32):

$$PA = \frac{\sum_{i=0}^{k} p_{ii}}{\sum_{i=0}^{k} \sum_{j=0}^{k} p_{ij}} \quad (5)$$

$$MIoU = \frac{1}{k+1} \sum_{i=1}^{k} \frac{p_{ii}}{\sum_{j=0}^{k} p_{ij} + \sum_{j=0}^{k} p_{ji} - p_{ii}} \quad (6)$$

3 Results

3.1 Patient recruitment and data analysis

As shown in Figure 4, we recruited a total of 511 hypertension patients from the cardiology departments of Dongzhimen Hospital, Dongfang Hospital, and the Third Affiliated Hospital of Beijing University of Chinese Medicine, and an additional 173 patients from the First Affiliated Hospital of Hunan University of Chinese Medicine. These patients underwent interviews and had standard tongue photographs taken. After screening, we excluded 60 patients (8.77%) with disqualifying tongue images, 164 patients (23.98%) with more than 5% missing data, and 88 patients (12.87%) without a coronary CAD record and who could not be definitively ruled out for CAD. Ultimately, we included a total of 244 hypertension patients and 166 patients with hypertension combined with CAD in our study.

Table 2 provides detailed baseline information for both patient groups. Upon analysis, we found significant differences between groups in terms of age, BMI, and the duration of hypertension across the training, validation, and test sets. To further explore potential risk factors, we analyzed the data from the training and validation sets using logistic regression (Table 3). The results

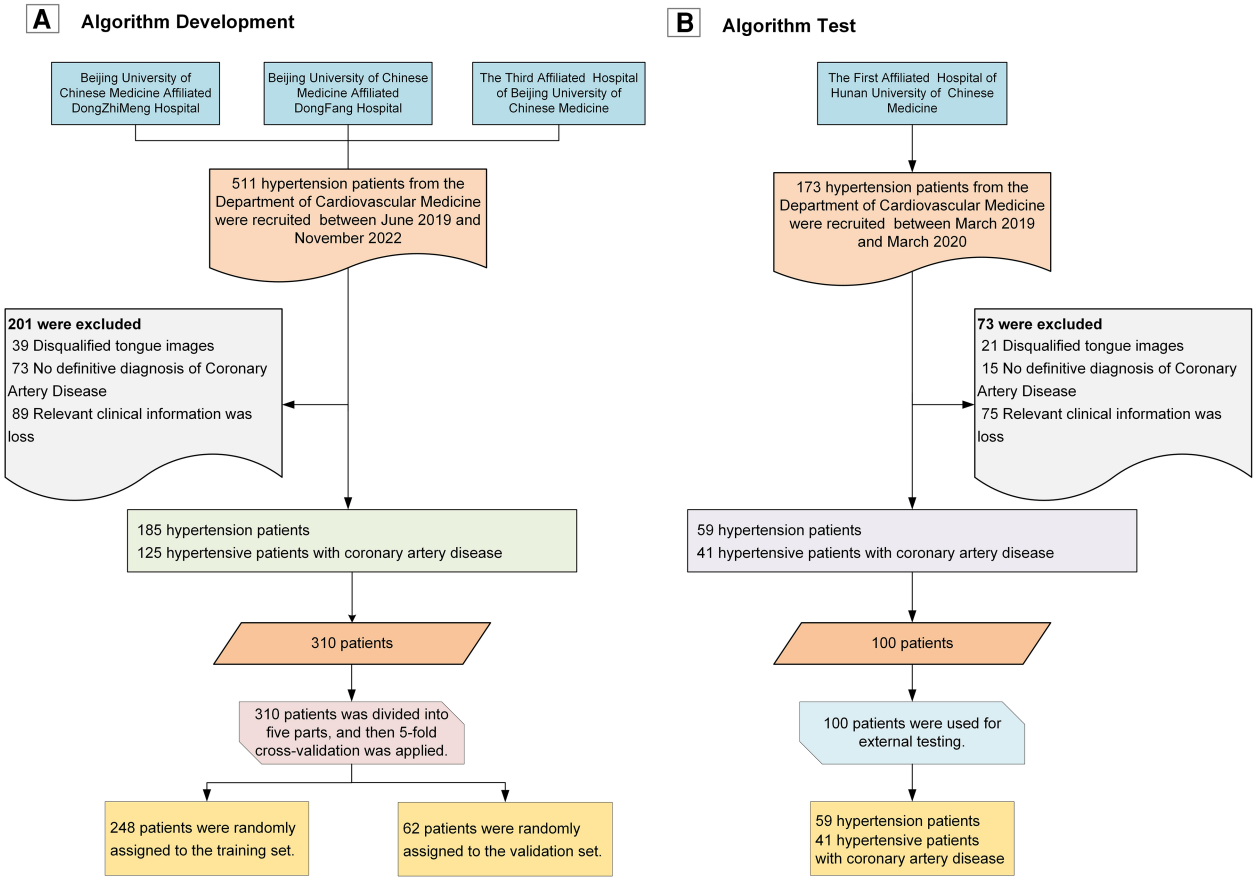

FIGURE 4
Study flowchart. **(A)** Workflow for algorithm development; **(B)** Workflow for algorithm validation.

TABLE 2 Basic information of three groups.

Groups	*n*	Age	Male	BMI	Course of hypertension (year)
Training group					
Hypertension	149	66.51 (64.84–68.18)	62	25.97 ± 3.54	15.62 (13.63–17.60)
Hypertension with CAD	99	69.38 (67.14–71.63)	51	25.54 ± 4.39	15.71 (13.03–18.40)
Validation group					
Hypertension	37	68.14 (63.64–72.64)	21	24.18 ± 4.46	14.66 (11.12–18.21)
Hypertension with CAD	25	69.35 (63.99–71.71)	12	26.75 ± 3.60	18.29 (12.34–24.24)
Test group					
Hypertension	59	69.17 (64.33–71.22)	31	24.64 ± 3.67	9.12 (6.88–14.07)
Hypertension with CAD	41	69.62 (64.14–72.16)	21	25.34 ± 4.12	13.17 (7.36–17.85)
***P*-value**		**0.007**	0.399	**0.009**	**< 0.001**

Results with $P < 0.05$ are bolded.

TABLE 3 Binary logistic regression results of the main coronary artery disease risk factors.

Variables	Adjusted OR (95% CI)	*P*-value
Age	1.04 (1.01–1.06)	**0.009**
Male	2.24 (0.90–5.53)	**0.027**
BMI	1.06 (0.97–1.16)	0.194
Course of hypertension (year)	1.00 (0.98–1.02)	0.863
Education		
Less than high school	1.28 (0.63–2.62)	0.500
University	0.12 (0.03–1.06)	**0.004**
Lifestyle		
Alcohol(>2 times/week, >1 year)	0.59 (0.23–1.53)	0.279
Smoking(>2 times/day, >1 year)	0.54 (0.22–1.35)	0.187
Insomnia (>2 times/week)	0.89 (0.44–1.79)	**0.041**
Family history of CAD	1.63 (0.94–2.82)	0.079
Work status		
Work <4 h/day	0.53 (0.15–1.86)	0.317
4–10 h/day	0.76 (0.21–2.78)	0.676
>10 h/day	0.97 (0.45–2.46)	0.432
Hyperlipidemia	4.28 (1.92–9.50)	**<0.001**
Diabetes	0.72 (0.35–1.48)	0.377
Chronic renal disease	0.39 (0.14–1.10)	0.393
Antihypertensive medication	0.56 (0.32–1.01)	**0.049**

Results with $P < 0.05$ are bolded.

indicated that older age, male gender, and having hyperlipidemia are risk factors for CAD, while having a higher education, Insomnia, and using antihypertensive medication were considered protective factors.

3.2 Performance of tongue feature extraction algorithm

In the task of semantic segmentation of the tongue body, we employed a customized algorithm based on the Deeplab V3 + framework, which demonstrated outstanding performance. The overall accuracy exceeded 99%, with a Mean Intersection over Union (mIoU) for the tongue segmentation task reaching 98.77%, and the Mean Pixel Accuracy (mPA) was as high as 99.45%. Such results fully attest to the effectiveness and accuracy of our algorithm in the task of tongue body semantic segmentation.

We developed a CAD diagnostic algorithm based on the ResNet-18 framework, which uses tongue images as input. On the training set, the algorithm showed a mean accuracy of 0.690, a mean AUC value of 0.749, and a mean recall rate of 0.842 (Table 4); on the test set, it achieved an accuracy of 0.670, an AUC value of 0.690, and a recall rate of 0.666 (Table 5). As shown in Figures 3A,C, the algorithm demonstrates certain classification capabilities on both the training and test sets, indicating that tongue images indeed possess classification value for the diagnosis of CAD in patients with hypertension.3.3 Performance of CAD Diagnostic Algorithm.

We developed two types of CAD diagnostic models: one based solely on CAD risk factors and the other combining risk factors with deep features of tongue images. To determine the optimal ML approach, we compared the performance of various algorithms, all utilizing risk factors and deep features of tongue images as inputs. Results on the training set showed that different ML algorithms could effectively complete the classification task, with XGBoost exhibiting the best performance (Table 6). Therefore, we ultimately selected XGBoost as the method for algorithm customization. Moreover, we compared algorithm customized only with risk factors to those incorporating tongue image features, it was found that the inclusion of tongue image features significantly enhanced algorithm performance, indicating that adding tongue features as input variables positively contributes to algorithm optimization (Figure 3B; Table 4).

We also evaluated the performance of different ML algorithms on the test set (Table 7), and the results were broadly consistent with those on the validation set. Although there was a slight decrease in performance, the algorithms still demonstrated good classification capabilities, with XGBoost continuing to show the best performance. Additionally, we compared algorithms developed solely based on risk factors with those that integrate both risk factors and tongue image features, using the test set for evaluation (Figure 3C; Table 5). This finding confirms the practical diagnostic value of tongue images for CAD and also indicates the potential of tongue images to enhance the efficacy of current diagnostic models for the condition.

To more comprehensively evaluate the algorithm's applicability and performance across different populations, we subdivided the test set according to age, gender, and the number of risk factors, and presented the algorithm's performance across various subgroups. As shown in Figure 5, in terms of age distribution, the algorithm demonstrated superior diagnostic ability in the elderly population aged 65 and above. Regarding gender, our algorithm demonstrated relatively stable performance between men and women, with no significant differences. In terms of risk factors, the algorithm's judgment ability significantly improved when the number of risk factors reached or exceeded three; however, with fewer risk factors, the algorithm's performance was comparatively weaker.

TABLE 4 Performance of 5-fold cross-validation with different feature inputs.

Input features	Mean accuracy	Mean precision	Mean recall	Mean F-1 score	Mean AUC	Mean AUPR
Tongue feature	0.690	0.699	0.842	0.763	0.749	0.807
Risk factors	0.761	0.778	0.837	0.806	0.801	0.842
Risk factors & tongue feature	0.794	0.795	0.886	0.836	0.827	0.865

TABLE 5 Performance on the test Set with different feature inputs.

Input features	Accuracy	Precision	Recall	F-1 score	AUC	AUPR
Tongue feature	0.670	0.754	0.666	0.708	0.690	0.717
Risk factors	0.730	0.811	0.717	0.761	0.763	0.800
Risk factors & tongue feature	0.760	0.773	0.850	0.809	0.786	0.845

TABLE 6 Comparison of 5-fold cross-validation results across different algorithms.

Algorithm	Mean accuracy	Mean precision	Mean recall	Mean F-1 score	Mean AUC	Mean AUPR
DT	0.745	0.802	0.778	0.783	0.760	0.791
RF	0.777	0.793	0.848	0.817	0.818	0.851
SVM	0.742	0.753	0.859	0.799	0.799	0.856
LR	0.761	0.786	0.826	0.804	0.817	0.851
XGBoost	0.794	0.795	0.886	0.836	0.825	0.865

TABLE 7 The performance comparison of different algorithm on the test set.

Algorithm	Accuracy	Precision	Recall	F-1 score	AUC	AUPR
DT	0.710	0.738	0.800	0.768	0.708	0.785
RF	0.740	0.774	0.800	0.786	0.781	0.843
SVM	0.720	0.742	0.793	0.767	0.742	0.790
LR	0.750	0.769	0.833	0.800	0.751	0.823
XGBoost	0.760	0.773	0.850	0.809	0.786	0.845

4 Discussion

Hypertensive patients constitute a large patient population and are an important risk factor for coronary heart disease. When the two conditions occur simultaneously, they can result in a higher burden of disease and accidental risks (4). Therefore, this study selected hypertensive patients as the target population. Tongue diagnosis is an important diagnostic method in TCM, closely related to the cardiovascular blood flow status. However, it has been largely overlooked in the actual diagnosis of CAD. In recent years, there have been many studies on constructing artificial intelligence diagnostic models for CAD, but none have attempted to utilize the tongue, a biological marker of the human body. We conducted a multi-center cross-sectional study, customizing a CAD diagnostic algorithm that integrates risk factors and tongue features based on clinically accessible data, achieving moderate performance. We innovated a method using deep learning to optimize CAD diagnosis through tongue images. This method has the advantages of being non-invasive, low-cost, and easy to operate compared to coronary angiography, and it exhibits better diagnostic performance than traditional CAD diagnostic algorithms that use risk factors. Our results affirm the practical diagnostic value of the tongue for CAD and demonstrate the feasibility of enhancing CAD diagnostic algorithm performance with tongue images.

For the development of a CAD diagnostic model, the rational use of clinical risk factors is of great importance. Various CAD diagnostic and prediction models, such as the Framingham (33) and the Systematic Coronary Risk Evaluation (SCORE) (34) heavily rely on clinical risk factors as a crucial basis. Inspired by this approach, our study first analyzed potential clinical risk factors for CAD. In our dataset, not all known CAD risk factors played a risk role, and insomnia, previously considered a risk factor (35) acted as a protective factor. We developed a CAD diagnostic algorithm that uses clinical risk factors as inputs, which exhibited moderate diagnostic performance (ACC = 0.770). Diagnostic models developed in other studies based on clinical risk factors showed similar performance (36–38). Although the performance of our non-invasive diagnostic model still needs further improvement, which may be related to the grouping method, sample size, and model construction approach, our results still demonstrate the potential of using tongue images for non-invasive diagnosis of CAD. Based on this, we attempted to incorporate tongue image features as inputs to develop a new CAD diagnostic algorithm. To accurately and objectively explore the value of tongue images for CAD diagnosis, we used the

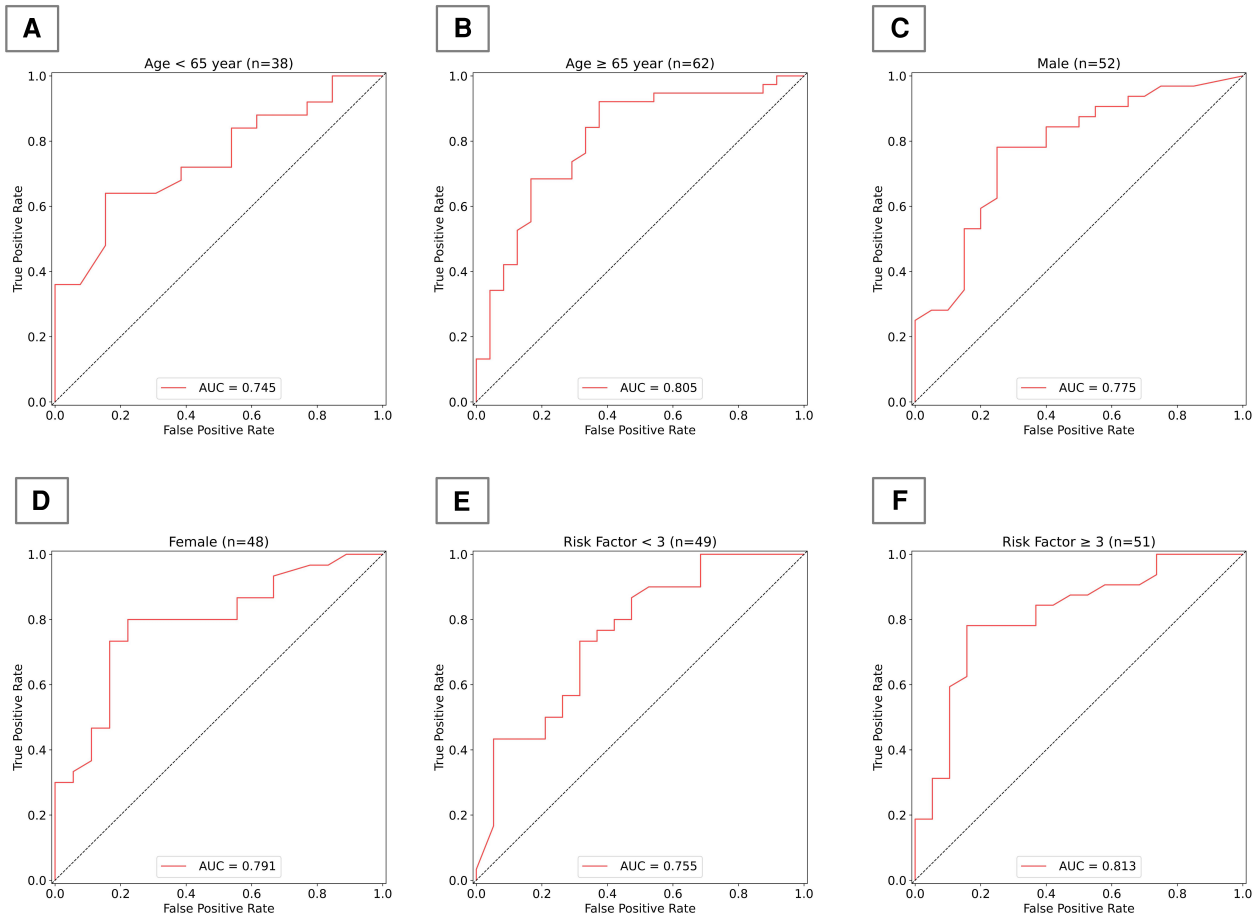

FIGURE 5
Algorithm performance in subgroups of test group. **(A)** AUC for the model in individuals under 65 years old; **(B)** AUC for the model in individuals 65 years and older; **(C)** AUC for the model in males; **(D)** AUC for the model in females; **(E)** AUC for the model in individuals with fewer than 3 risk factors; **(F)** AUC for the model in individuals with 3 or more risk factors.

TFDA-1 tongue diagnosis instrument for image capture and established a standardized data collection process. We eliminated potential interference from other facial information through tongue body semantic segmentation and image cropping. In customizing the algorithm for diagnosing CAD with tongue images, we employed the Resnet-18 as the deep learning framework. Resnet-18 is a type of deep residual network (39) that has consistently shown good performance in past studies on tongue images (40–42). In the analysis of tongue image features using traditional feature engineering, medical prior knowledge is often borrowed to define features based on the color, shape, and texture of the tongue, ensuring that the features possess good interpretability and medical significance.

That is precisely why our research opted for deep learning instead of traditional feature engineering. Despite the complexity and lack of explainability in the decision-making process of deep learning, this method simplifies the feature extraction process compared to traditional tongue image feature extraction engineering (43). It eliminates the need for extensive manual labeling of image features and enables fast and efficient automatic learning of complex feature representations in images, uncovering hidden information. The results indicate that, although there was a slight decline in the algorithm's performance on the test set compared to the validation set, the algorithm still retains certain classification capabilities overall. This suggests that tongue images have a definite diagnostic value for CAD, making the tongue an effective biological marker for CAD diagnosis.

Ultimately, we incorporated both risk factors and tongue image features as inputs and developed a new CAD diagnostic algorithm using XGBoost. This algorithm demonstrates superior performance compared to those utilizing single-type features as inputs. This part of the work validates the practical effectiveness of tongue images in enhancing the performance of CAD diagnostic algorithms, proving the feasibility of supplementing clinical diagnosis with TCM diagnostic theories. It offers a new perspective on integrating traditional medical knowledge with modern technology. Additionally, we also focused on the algorithm's performance across different demographic subgroups. The results indicate that the algorithm has better diagnostic capability in elderly populations aged 65 years and above, which may be related to the higher prevalence of CAD in older individuals. The algorithm performs similarly in both men and women, indicating that our developed algorithm has commendable generalization capability across genders. The model exhibits higher accuracy in judgments when the number of risk factors is three or more,

highlighting the importance of considering multiple risk factors in the diagnosis of CAD. This approach enhances our understanding of the model's generalizability, revealing its applicability to patient groups with varying demographic and clinical profiles. It holds significant value for clinical practice, offering a reference for tailoring diagnostic methods based on demographic characteristics to improve diagnostic accuracy. By evaluating the model's performance in different subgroups, we can identify potential biases that might affect accuracy, thereby rendering it more reliable in clinical settings.

Although this study identified the potential value of the tongue in diagnosing CAD, it also has some limitations. Firstly, despite being a multi-center study, there are only four hospitals from two regions involved in the sub-centers, lacking subjects from different ethnicities and countries. Secondly, this study is focused solely on hypertensive populations, and the overall sample size is relatively small, which may limit the possibility of applying the CAD diagnostic algorithm to a wider population. Thirdly, while this study employed standardized tongue image collection equipment to minimize interference from other factors during image capture, it also restricts the application of the model in different scenarios and with different collection devices. Although this study explores the potential value of tongue diagnosis for CAD, future research needs to further validate and optimize our diagnostic model in a wider and larger population, carrying out prospective studies. We also experimented with using different types of cameras, various light sources, and even mobile portable devices for image collection, to further expand the model's applicability and enhance its generalization capability. In future research, we can expect more optimized and interpretable deep learning models to enhance the study results, capturing finer changes in tongue images more accurately, thus further optimizing the findings of this study. Additionally, tongue diagnosis is only an essential component of TCM diagnosis, and we can further focus on the integration of multimodal data, considering the fusion of other biomarkers with tongue images to build a more comprehensive and integrated CAD diagnostic model.

5 Conclusion

Exploring an inexpensive, non-invasive diagnostic tool that can be used for early-stage and large-scale screening of CAD is essential. In this study, we analyzed potential risk factors for CAD, extracted potential diagnostic features from tongue images, and developed a new, well-performing CAD diagnostic algorithm based on these findings. Our work introduces a novel perspective, suggesting that tongue images have applicable diagnostic value for CAD diagnosis. Tongue image features could become new risk indicators for CAD, demonstrating the feasibility of integrating TCM theories with modern technology.

Data availability statement

The raw data supporting the conclusions of this article will be made available by the authors, without undue reservation.

Ethics statement

The studies involving humans were approved by Shuguang Hospital affiliated with Shanghai University of Traditional Chinese Medicine (IRB number: 2018-626-55-01). The studies were conducted in accordance with the local legislation and institutional requirements. The participants provided their written informed consent to participate in this study.

Author contributions

MD: Data curation, Funding acquisition, Investigation, Methodology, Project administration, Software, Validation, Writing – original draft, Writing – review & editing. BM: Funding acquisition, Methodology, Software, Validation, Writing – original draft, Writing – review & editing. ZL: Data curation, Formal Analysis, Writing – original draft, Writing – review & editing. CW: Data curation, Methodology, Writing – original draft, Writing – review & editing. ZH: Data curation, Methodology, Writing – original draft, Writing – review & editing. JG: Data curation, Investigation, Supervision, Validation, Writing – original draft, Writing – review & editing. FL: Conceptualization, Data curation, Funding acquisition, Investigation, Supervision, Validation, Writing – original draft, Writing – review & editing.

Funding

The author(s) declare financial support was received for the research, authorship, and/or publication of this article.

Our Study was supported by Beijing Municipal Education Science Planning Project [grant numbers CDAA21037]; the China Postdoctoral Science Foundation [grant numbers 2024M750261]; the Postdoctoral Fellowship Program of CPSF [grant numbers GZC20230323]; the Ministry of Science and Technology of the People's Republic of China [grant numbers 2017FYC1703301]; National Natural Science Foundation of China [grant numbers 12102064].

Acknowledgments

We would like to thank all participants and their family members for being willing to participate in this study.

Conflict of interest

The authors declare that the research was conducted in the absence of any commercial or financial relationships that could be construed as a potential conflict of interest.

Publisher's note

All claims expressed in this article are solely those of the authors and do not necessarily represent those of their affiliated organizations, or those of the publisher, the editors and the reviewers. Any product that may be evaluated in this article, or claim that may be made by its manufacturer, is not guaranteed or endorsed by the publisher.

References

1. World Health Organization. *Cardiovascular Diseases (CVDs)*. Geneva, Switzerland: World Health Organization (2019). Available online at: https://www.who.int/news-room/fact-sheets/detail/cardiovascular-diseases-(cvds)

2. Roth GA, Mensah GA, Johnson CO, Addolorato G, Ammirati E, Baddour LM, et al. Global burden of cardiovascular diseases and risk factors, 1990–2019: update from the GBD 2019 study. *J Am Coll Cardiol*. (2020) 76(25):2982–3021. doi: 10.1016/j.jacc.2020.11.010

3. Meng H, Ruan J, Yan Z, Chen Y, Liu J, Li X, et al. New progress in early diagnosis of atherosclerosis. *Int J Mol Sci*. (2022) 23(16):8939. doi: 10.3390/ijms23168939

4. Charchar FJ, Prestes PR, Mills C, Ching SM, Neupane D, Marques FZ, et al. Lifestyle management of hypertension: international society of hypertension position paper endorsed by the world hypertension league and European society of hypertension. *J Hypertens*. (2024) 42(1):23–49. doi: 10.1097/HJH.0000000000003563

5. Berge CA, Eskerud I, Almeland EB, Larsen TH, Pedersen ER, Rotevatn S, et al. Relationship between hypertension and non-obstructive coronary artery disease in chronic coronary syndrome (the NORIC registry). *PLoS One*. (2022) 17(1): e0262290. doi: 10.1371/journal.pone.0262290

6. Truesdell AG, Alasnag MA, Kaul P, Rab ST, Riley RF, Young MN, et al. Intravascular imaging during percutaneous coronary intervention: JACC state-of-the-art review. *J Am Coll Cardiol*. (2023) 81(6):590–605. doi: 10.1016/j.jacc.2022.11.045

7. Suri JS, Bhagawati M, Paul S, Protogeron A, Sfikakis PP, Kitas GD, et al. Understanding the bias in machine learning systems for cardiovascular disease risk assessment: the first of its kind review. *Comput Biol Med*. (2022) 142:105204. doi: 10.1016/j.compbiomed.2021.105204

8. Tao S, Yu L, Yang D, Yao R, Zhang L, Huang L, et al. Development and validation of a clinical prediction model for detecting coronary heart disease in middle-aged and elderly people: a diagnostic study. *Eur J Med Res*. (2023) 28(1):375. doi: 10.1186/s40001-023-01233-0

9. Mirjalili SR, Soltani S, Heidari Meybodi Z, Marques-Vidal P, Kraemer A, Sarebanhassanabadi M. An innovative model for predicting coronary heart disease using triglyceride-glucose index: a machine learning-based cohort study. *Cardiovasc Diabetol*. (2023) 22(1):200. doi: 10.1186/s12933-023-01939-9

10. Wang Z, Sun Z, Yu L, Wang Z, Li L, Lu X. Machine learning-based prediction of composite risk of cardiovascular events in patients with stable angina pectoris combined with coronary heart disease: development and validation of a clinical prediction model for Chinese patients. *Front Pharmacol*. (2024) 14:1334439. doi: 10.3389/fphar.2023.1334439

11. Lin S, Li Z, Fu B, Chen S, Li X, Wang Y, et al. Feasibility of using deep learning to detect coronary artery disease based on facial photo. *Eur Heart J*. (2020) 41 (46):4400–11. doi: 10.1093/eurheartj/ehaa640

12. Wang S, Wu D, Li G, Song X, Qiao A, Li R, et al. A machine learning strategy for fast prediction of cardiac function based on peripheral pulse wave. *Comput Methods Programs Biomed*. (2022) 216:106664. doi: 10.1016/j.cmpb.2022.106664

13. Rajakumaran S, Sasikala J. Improvement in tongue color image analysis for disease identification using deep learning based depthwise separable convolution model. *Indian J Comput Sci Eng*. (2021) 12(1):21–32. doi: 10.21817/indjcse/2021/v12i1/211201082

14. Jiang T, Guo X, Tu L, Lu Z, Cui J, Ma X, et al. Application of computer tongue image analysis technology in the diagnosis of NAFLD. *Comput Biol Med*. (2021) 135:104466. doi: 10.1016/j.compbiomed.2021.104466

15. Mansour RF, Althobaiti MM, Ashour AA. Internet of things and synergic deep learning based biomedical tongue color image analysis for disease diagnosis and classification. *IEEE Access*. (2021) 9:1. doi: 10.1109/ACCESS.2021.3094226

16. Li J, Chen Q, Hu X, Yuan P, Cui L, Tu L, et al. Establishment of noninvasive diabetes risk prediction model based on tongue features and machine learning techniques. *Int J Med Inform*. (2021) 149:104429. doi: 10.1016/j.ijmedinf.2021.104429

17. Thanikachalam V, Shanthi S, Kalirajan K, Abdel-Khalek S, Omri M, Ladhar LM. Intelligent deep learning based disease diagnosis using biomedical tongue images. *CMC Computers Mater Continua*. (2022) 3:15. doi: 10.32604/cmc.2022.020965

18. Jiang T, Lu Z, Hu X, Zeng L, Ma X, Lu Z, et al. Deep learning multi-label tongue image analysis and its application in a population undergoing routine medical checkup. *Evid Based Complement Alternat Med*. (2022) 2022:3384209. doi: 10.1155/2022/3384209

19. Li J, Huang J, Jiang T, Tu L, Cui L, Cui J, et al. A multi-step approach for tongue image classification in patients with diabetes. *Comput Biol Med*. (2022) 149:105935. doi: 10.1016/j.compbiomed.2022.105935

20. Sivasubramaniam S, Balamurugan SP. Simulated annealing with deep learning based tongue image analysis for heart disease diagnosis. *Intell Autom Soft Comput*. (2023) 37(1):111–26. doi: 10.32604/iasc.2023.035199

21. Zhang N, Jiang Z, Li JX, Zhang D. Multiple color representation and fusion for diabetes mellitus diagnosis based on back tongue images. *Comput Biol Med*. (2023) 155:106652. doi: 10.1016/j.compbiomed.2023.106652

22. Yuan L, Yang L, Zhang S, Xu Z, Qin J, Liu X, et al. Development of a tongue image-based machine learning tool for the diagnosis of gastric cancer: a prospective multicentre clinical cohort study. *EClinicalMedicine*. (2023) 57:101834. doi: 10.1016/j.eclinm.2023.101834

23. Noguchi K, Saito I, Namiki T, Yoshimura Y, Nakaguchi T. Reliability of non-contact tongue diagnosis for Sjögren's syndrome using machine learning method. *Sci Rep*. (2023) 13(1):1334. doi: 10.1038/s41598-023-27764-4

24. Shi Y, Guo D, Chun Y, Liu J, Liu L, Tu L, et al. A lung cancer risk warning model based on tongue images. *Front Physiol*. (2023) 14:1154294. doi: 10.3389/fphys.2023.1154294

25. Dai S, Guo X, Liu S, Tu L, Hu X, Cui J, et al. Application of intelligent tongue image analysis in conjunction with microbiomes in the diagnosis of MAFLD. *Heliyon*. (2024) 10(7):e29269. doi: 10.1016/j.heliyon.2024.e29269

26. Duan M, Zhang Y, Liu Y, Mao B, Li G, Han D, et al. Machine learning aided non-invasive diagnosis of coronary heart disease based on tongue features fusion. *Technol Health Care*. (2024) 32(1):441–57. doi: 10.3233/THC-230590

27. Skalidis E, Zacharis E, Hamilos M, Skalidis I, Anastasiou I, Parthenakis F. Transient lingual ischemia complicating coronary angiography. *J Invasive Cardiol*. (2019) 31(3):E51. https://www.researchgate.net/publication/331730352_Transient_Lingual_Ischemia_Complicating_Coronary_Angiography

28. Chang FY, Natesan S, Goh WY, Anerdis JLD. An elderly woman with tongue ischemia. *J Am Geriatr Soc*. (2016) 64(10):e111–2. doi: 10.1111/jgs.14395

29. Hamaoka T, McCully KK. Review of early development of near-infrared spectroscopy and recent advancement of studies on muscle oxygenation and oxidative metabolism. *J Physiol Sci*. (2019) 69:799–811. doi: 10.1007/s12576-019-00697-2

30. Writing Group of 2018 Chinese Guidelines for the Management of Hypertension, Chinese Hypertension League, Chinese Society of Cardiology. 2018 Chinese guidelines for the management of hypertension. *Chin J Cardiovasc Med*. (2019) 24:24–56.

31. Olaniran OR, Alzahrani ARR, Alzahrani MR. Eigenvalue distributions in random confusion matrices: applications to machine learning evaluation. *Mathematics*. (2024) 12(10):1425. doi: 10.3390/math12101425

32. He J, Cheng Y, Wang W, Ren Z, Zhang C, Zhang W. A lightweight building extraction approach for contour recovery in complex urban environments. *Remote Sens*. (2024) 16(5):740. doi: 10.3390/rs16050740

33. Mahmood SS, Levy D, Vasan RS, Wang TJ. The framingham heart study and the epidemiology of cardiovascular disease: a historical perspective. *Lancet*. (2014) 383 (9921):999–1008. doi: 10.1016/S0140-6736(13)61752-3

34. Conroy RM, Pyörälä K, Fitzgerald AP, Sans S, Menotti A, De Backer G, et al. Estimation of ten-year risk of fatal cardiovascular disease in Europe: the SCORE project. *Eur Heart J*. (2003) 24(11):987–1003. doi: 10.1016/s0195-668x(03)00114-3

35. Javaheri S, Redline S. Insomnia and risk of cardiovascular disease. *Chest*. (2017) 152(2):435–44. doi: 10.1016/j.chest.2017.01.026

36. Huang Y, Ren Y, Yang H, Ding Y, Liu Y, Yang Y, et al. Using a machine learning-based risk prediction model to analyze the coronary artery calcification score and predict coronary heart disease and risk assessment. *Comput Biol Med*. (2022) 151(Pt B):106297. doi: 10.1016/j.compbiomed.2022.106297

37. Zhang L, Niu M, Zhang H, Wang Y, Zhang H, Mao Z, et al. Nonlaboratory-based risk assessment model for coronary heart disease screening: model development and validation. *Int J Med Inform*. (2022) 162:104746. doi: 10.1016/j.ijmedinf.2022.104746

38. Li D, Xiong G, Zeng H, Zhou Q, Jiang J, Guo X. Machine learning-aided risk stratification system for the prediction of coronary artery disease. *Int J Cardiol*. (2021) 326:30–4. doi: 10.1016/j.ijcard.2020.09.070

39. He KM, Zhang X, Ren SQ, Sun J. *Deep residual learning for image recognition. 2016 IEEE Conference on Computer Vision and Pattern Recognition (CVPR)* (2016). p. 770–8. doi: 10.1109/cvpr.2016.90

40. Ma C, Zhang P, Du S, Li Y, Li S. Construction of tongue image-based machine learning model for screening patients with gastric precancerous lesions. *J Pers Med*. (2023) 13(2):271. doi: 10.3390/jpm13020271

41. Li J, Yuan P, Hu X, Huang J, Cui L, Cui J, et al. A tongue features fusion approach to predicting prediabetes and diabetes with machine learning. *J Biomed Inform*. (2021) 115:103693. doi: 10.1016/j.jbi.2021.103693

42. Okawa J, Hori K, Izuno H, Fukuda M, Ujihashi T, Kodama S, et al. Developing tongue coating status assessment using image recognition with deep learning. *J Prosthodont Res*. (2023) 68(3):425–31. doi: 10.2186/jpr.JPR_D_23_00117

43. Bhatnagar V, Bansod PP. Challenges and solutions in automated tongue diagnosis techniques: a review. *Crit Rev Biomed Eng*. (2022) 50(1):47–63. doi: 10.1615/CritRevBiomedEng.2022044392

Frontiers in
Cardiovascular Medicine

Innovations and improvements in cardiovascular treatment and practice

Focuses on research that challenges the status quo of cardiovascular care, or facilitates the translation of advances into new therapies and diagnostic tools.

Discover the latest Research Topics

See more →

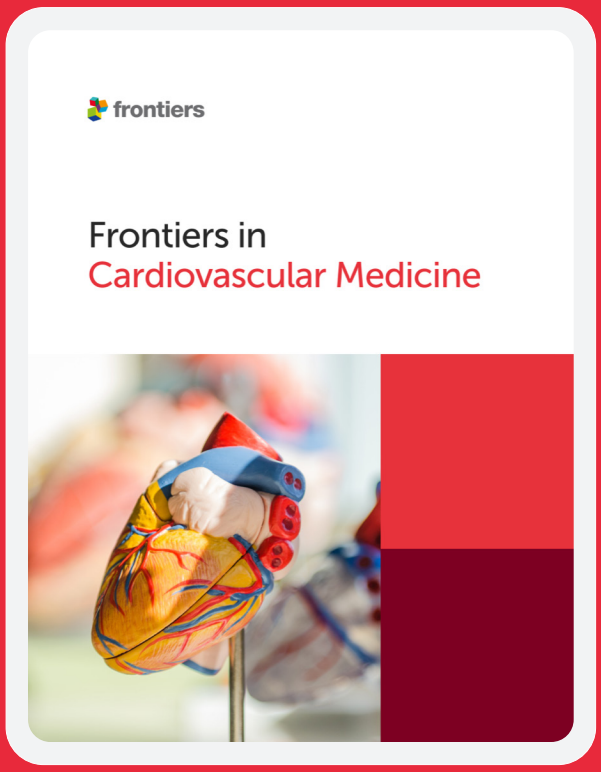

Frontiers

Avenue du Tribunal-Fédéral 34
1005 Lausanne, Switzerland
frontiersin.org

Contact us

+41 (0)21 510 17 00
frontiersin.org/about/contact